



Luminosity determination in pp collisions at $\sqrt{s} = 13$ TeV using the ATLAS detector at the LHC

ATLAS Collaboration*

CERN, 1211 Geneva 23, Switzerland

Received: 20 December 2022 / Accepted: 17 March 2023
© CERN for the benefit of the ATLAS collaboration 2023

Abstract The luminosity determination for the ATLAS detector at the LHC during Run 2 is presented, with pp collisions at a centre-of-mass energy $\sqrt{s} = 13$ TeV. The absolute luminosity scale is determined using van der Meer beam separation scans during dedicated running periods in each year, and extrapolated to the physics data-taking regime using complementary measurements from several luminosity-sensitive detectors. The total uncertainties in the integrated luminosity for each individual year of data-taking range from 0.9% to 1.1%, and are partially correlated between years. After standard data-quality selections, the full Run 2 pp data sample corresponds to an integrated luminosity of $140.1 \pm 1.2 \text{ fb}^{-1}$, i.e. an uncertainty of 0.83%. A dedicated sample of low-pileup data recorded in 2017–2018 for precision Standard Model physics measurements is analysed separately, and has an integrated luminosity of $338.1 \pm 3.1 \text{ pb}^{-1}$.

Contents

1	Introduction
2	Methodology and datasets
3	Luminosity detectors and algorithms
3.1	LUCID Cherenkov detector
3.2	Beam conditions monitor
3.3	Track-counting algorithms
3.4	Calorimeter-based algorithms
4	Absolute luminosity calibration in vdM scans
4.1	vdM formalism
4.2	vdM scan datasets
4.3	Scan curve fitting
4.4	Bunch population measurement
4.5	Orbit drift corrections
4.6	Non-factorisation effects
4.7	Beam–beam interactions
4.8	Emittance growth corrections
4.9	Length scale determination

4.10	Magnetic non-linearity
4.11	Consistency checks
5	Calibration transfer to high-luminosity running
5.1	Comparison of luminosity measurements at high pileup
5.2	Performance of track-counting algorithms
5.3	LUCID correction strategy
6	Calibration transfer uncertainties
6.1	Tile calorimeter activation model
6.2	Comparisons of TileCal and track-counting measurements: direct approach
6.3	Comparisons of calorimeter and track-counting measurements: ladder approach
7	Long-term stability
8	Uncertainties and results
8.1	Uncertainty correlations between years
8.2	Results for the $\sqrt{s} = 13$ TeV Run 2 dataset
8.3	Comparison with Z -counting measurements
9	Luminosity calibration for low-pileup datasets
10	Conclusions
	References

1 Introduction

A precise measurement of the integrated luminosity is a key component of the ATLAS physics programme at the CERN Large Hadron Collider (LHC), in particular for cross-section measurements where it is often one of the leading sources of uncertainty. Searches for new physics phenomena beyond those predicted by the Standard Model also often require accurate estimates of the luminosity to determine background levels and sensitivity. This paper describes the measurement of the luminosity of the proton–proton (pp) collision data sample delivered to the ATLAS detector at a centre-of-mass energy of $\sqrt{s} = 13$ TeV during Run 2 of the LHC in the years 2015–2018. The measurement builds on the experience and techniques developed for Run 1 and documented extensively in Refs. [1–3], where uncertainties in the total

*e-mail: atlas.publications@cern.ch

integrated luminosities of $\Delta\mathcal{L}/\mathcal{L} = 1.8\%$ for $\sqrt{s} = 7\text{TeV}$ and 1.9% for $\sqrt{s} = 8\text{TeV}$ were achieved.

The luminosity measurement is based on an absolute calibration of the primary luminosity-sensitive detectors in low-luminosity runs with specially tailored LHC conditions using the van der Meer (vdM) method [4,5]. A calibration transfer procedure was then used to transport this calibration to the physics data-taking regime at high luminosity. The vdM calibration was performed in dedicated fills once per year during Run 2, and relative comparisons of the luminosities measured by different detectors were used to set limits on any possible change in the calibration during the year. Finally, the integrated luminosity and uncertainty for the whole Run 2 data-taking period was derived, taking into account correlations between the uncertainties in each of the component years.

The structure of this paper mirrors the calibration process. After a brief introduction to the methodology and the Run 2 dataset in Sect. 2, the various luminosity-sensitive detectors are described in Sect. 3, the absolute vdM calibration in Sect. 4, the calibration transfer procedure in Sects. 5 and 6, the long-term stability studies in Sect. 7 and the correlations and combination in Sect. 8. The latter also contains a summary (Table 8) of the contributing uncertainties in all individual years and the combination. A dedicated luminosity calibration for special datasets recorded for precision W/Z physics with low numbers of pp interactions per bunch crossing is described in Sect. 9. Conclusions are given in Sect. 10.

2 Methodology and datasets

The instantaneous luminosity \mathcal{L}_b produced by a single pair of colliding bunches can be expressed as

$$\mathcal{L}_b = \frac{R}{\sigma} \quad (1)$$

where R is the rate of a particular process with cross-section σ . In the case of inelastic pp collisions with cross-section σ_{inel} , Eq. (1) becomes

$$\mathcal{L}_b = \frac{\mu f_r}{\sigma_{\text{inel}}} \quad (2)$$

where the pileup parameter μ is the average number of inelastic interactions per bunch crossing, and f_r is the LHC bunch revolution frequency (11,246 Hz for protons). The total instantaneous luminosity is given by

$$\mathcal{L}_{\text{inst}} = \sum_{b=1}^{n_b} \mathcal{L}_b = n_b \langle \mathcal{L}_b \rangle = n_b \frac{\langle \mu \rangle f_r}{\sigma_{\text{inel}}}$$

where the sum runs over the n_b bunch pairs colliding at the interaction point (IP), $\langle \mathcal{L}_b \rangle$ is the mean per-bunch luminosity

and $\langle \mu \rangle$ is the pileup parameter averaged over all colliding bunch pairs.

The instantaneous luminosity can be measured by monitoring μ_{vis} , the visible interaction rate per bunch-crossing for a particular luminosity algorithm, based on a chosen luminosity-sensitive detector.¹ The per-bunch luminosity can be written in analogy with Eqs. (1) and (2) as

$$\mathcal{L}_b = \frac{\mu_{\text{vis}} f_r}{\sigma_{\text{vis}}} \quad (3)$$

where the algorithm-specific visible cross-section is a calibration constant which represents the absolute luminosity calibration of the given algorithm, and can be determined via the vdM calibration method discussed in Sect. 4. Once σ_{vis} is known, the pileup parameter μ can be determined from $\mu = \mu_{\text{vis}} \sigma_{\text{inel}} / \sigma_{\text{vis}}$. Since σ_{inel} is not precisely known, a reference value of $\sigma_{\text{inel}} = 80\text{mb}$ is used by convention by all LHC experiments for pp collisions at $\sqrt{s} = 13\text{TeV}$. The values of μ and its bunch-averaged counterpart $\langle \mu \rangle$ are important parameters for characterising the performance of the LHC machine and detectors, but the luminosity calibration based on σ_{vis} is independent of the chosen reference value of σ_{inel} .

Provided the calibration constant σ_{vis} is stable in time, and does not depend on the LHC conditions (e.g. the number of bunches or value of $\langle \mu \rangle$), the measurement of μ_{vis} at any moment is sufficient to determine the per-bunch instantaneous luminosity at that time. In practice, no luminosity algorithm is perfectly stable in time and independent of LHC conditions, and comparisons between many different algorithms and detectors, each with their own strengths and weaknesses, are essential to produce a precise luminosity measurement with a robust uncertainty estimate.

In ATLAS, the rate μ_{vis} is measured over a finite time interval called a luminosity block (LB), during which data-taking conditions (including the instantaneous luminosity) are assumed to remain stable. The start and end times of each LB are defined by the ATLAS central trigger processor, and the normal duration during Run 2 data-taking was 1 min, sometimes cut short if a significant change of conditions such as a detector problem occurred. The instantaneous luminosity for each LB was calculated from the sum of per-bunch luminosities, each derived using Eq. (3) and the per-bunch μ_{vis} values measured within the LB, modified by the calibration transfer corrections discussed in Sect. 5. The integrated luminosity was then obtained by multiplying $\mathcal{L}_{\text{inst}}$ by the duration of the LB, and these values were stored in the ATLAS conditions database [6]. The data-taking is organised into a series of ‘runs’ of the ATLAS data acquisition system,

¹ The term ‘luminosity algorithm’ refers to the measurement of a quantity proportional to the instantaneous luminosity, e.g. a counting rate or electrical current, using a procedure or set of selection criteria specific to a particular luminosity detector.

each of which normally corresponds to an LHC fill, including the periods outside stable beam collisions such as LHC injection, acceleration and preparation for collisions. ATLAS physics analyses are based on a ‘good runs list’ (GRL), a list of runs and LBs within them with stable beam collisions and where all the ATLAS subdetectors were functioning correctly according to a standard set of data-quality requirements [7]. The integrated luminosity corresponding to the GRL can be calculated as the sum of the integrated luminosities of all LBs in the GRL, after correcting each LB for readout dead-time. If the trigger used for a particular analysis is prescaled, the effective integrated luminosity is reduced accordingly [8].

The data-taking conditions evolved significantly during Run 2, with the LHC peak instantaneous luminosity at the start of fills ($\mathcal{L}_{\text{peak}}$) increasing from 5 to $19 \times 10^{33} \text{ cm}^{-2} \text{ s}^{-1}$ as the number of colliding bunch pairs n_b and average current per bunch were increased during the course of each year. In addition, progressively stronger focusing in the ATLAS and CMS interaction regions (characterised by the β^* parameter, the value of the β function at the interaction point [9]) was used in each successive year, leading to smaller transverse beam sizes and higher per-bunch instantaneous luminosity. Table 1 shows an overview of typical best parameters for each year, together with the total delivered integrated luminosity. All this running took place with long ‘trains’ of bunches featuring 25 ns bunch spacing within the trains, except for the second part of 2017, where a special filling pattern with eight filled bunches separated by 25 ns followed by a four bunch-slot gap (denoted ‘8b4e’) was used. This bunch pattern mitigated the enhancement of electron-cloud induced instabilities caused by a vacuum incident. The luminosity was levelled by partial beam separation at the beginning of such 8b4e LHC fills to give a maximum pileup parameter of $\langle \mu \rangle \approx 60$, whereas the maximum $\langle \mu \rangle$ achieved in standard 25 ns running was about 55 in 2018. These values are significantly larger than the maximum $\langle \mu \rangle$ of around 40 achieved with 50 ns bunch spacing in Run 1 [3], and posed substantial challenges to the detectors.

3 Luminosity detectors and algorithms

The ATLAS detector [10–13] consists of an inner tracking detector surrounded by a thin superconducting solenoid producing a 2 T axial magnetic field, electromagnetic and hadronic calorimeters, and an external muon spectrometer incorporating three large toroidal magnet assemblies.² The

ATLAS luminosity measurement relies on multiple redundant luminosity detectors and algorithms, which have complementary capabilities and different systematic uncertainties. For LHC Run 2, the primary bunch-by-bunch luminosity measurement was provided by the LUCID2 Cherenkov detector [14] in the far forward region, upgraded from its Run 1 configuration and referred to hereafter as LUCID. This was complemented by bunch-by-bunch measurements from the ATLAS beam conditions monitor (BCM) diamond detectors, and from offline measurements of the multiplicity of reconstructed charged particles in randomly selected colliding-bunch crossings (track counting). The ATLAS calorimeters provided bunch-integrated measurements (i.e. summed over all bunches) based on quantities proportional to instantaneous luminosity: liquid-argon (LAR) gap currents in the case of the endcap electromagnetic (EMEC) and forward (FCal) calorimeters, and photomultiplier currents from the scintillator-tile hadronic calorimeter (TileCal). All these measurements are discussed in more detail below.

3.1 LUCID Cherenkov detector

The LUCID detector contains 16 photomultiplier tubes (PMTs) in each forward arm of the ATLAS detector (side A and side C), placed around the beam pipe in different azimuthal ϕ positions at approximately $z = \pm 17 \text{ m}$ from the interaction point and covering the pseudorapidity range $5.561 < |\eta| < 5.641$. Cherenkov light is produced in the quartz windows of the PMTs, which are coated with ^{207}Bi radioactive sources that provide a calibration signal. Regular calibration runs were performed between LHC fills, allowing the high voltage applied to the PMTs to be adjusted so as to keep either the charge or amplitude of the calibration pulse constant over time. The LUCID detector was read out with dedicated electronics which provided luminosity counts for each of the 3564 nominal LHC bunch slots. These counts were integrated over the duration of each luminosity block, and over shorter time periods of 1–2 s to provide real-time feedback to the LHC machine for beam optimisation.

Several algorithms were used to convert the raw signals from the PMTs to luminosity measurements, using a single PMT or combining the information from several PMTs in various ways. The simplest algorithm uses a single PMT, and counts an ‘event’ if there is a signal in the PMT above a given threshold (a ‘hit’), corresponding to one or more inelastic pp interactions detected in a given bunch crossing. Assuming that the number of inelastic pp interactions in a

² ATLAS uses a right-handed coordinate system with its origin at the nominal interaction point in the centre of the detector, and the z axis along the beam line. The x axis points from the nominal interaction point to the centre of the LHC ring, and the y axis points upwards. The two sides of the detector are denoted A (corresponding to $z > 0$) and C

Footnote 2 continued

($z < 0$). Pseudorapidity is defined in terms of the polar angle θ as $\eta = -\ln \tan \theta/2$, and transverse momentum and energy are defined relative to the beam line as $p_T = p \sin \theta$ and $E_T = E \sin \theta$. The azimuthal angle around the beam line is denoted by ϕ .

Table 1 Selected LHC parameters for pp collisions at $\sqrt{s} = 13$ TeV in 2015–2018. The values shown are representative of the best accelerator performance during normal physics operation. In 2017, the LHC was run in two modes: standard 25 ns bunch train operation with long trains, and ‘8b4e’, denoting a pattern of eight bunches separated by 25 ns fol-

lowed by a four bunch-slot gap. Values are given for both configurations. The instantaneous luminosity was levelled by beam separation to about $\mathcal{L}_{\text{peak}} = 16 \times 10^{33} \text{ cm}^{-2} \text{ s}^{-1}$ for part of the 8b4e period. The 0.1 fb^{-1} of physics data delivered during 2015 with 50 ns bunch spacing is not included

Parameter	2015	2016	2017	2018
Maximum number of colliding bunch pairs (n_b)	2232	2208	2544/1909	2544
Bunch spacing [ns]	25	25	25/8b4e	25
Typical bunch population [10^{11} protons]	1.1	1.1	1.1/1.2	1.1
β^* [m]	0.8	0.4	0.3	0.3–0.25
Peak luminosity $\mathcal{L}_{\text{peak}}$ [$10^{33} \text{ cm}^{-2} \text{ s}^{-1}$]	5	13	16	19
Peak number of inelastic interactions/crossing ($\langle\mu\rangle$)	~ 16	~ 41	$\sim 45/60$	~ 55
Luminosity-weighted mean inelastic interactions/crossing	13	25	38	36
Total delivered integrated luminosity [fb^{-1}]	4.0	39.0	50.6	63.8

bunch crossing follows a Poisson distribution, the probability for such an event P_{evt} is given in terms of the single-PMT visible interaction rate $\mu_{\text{vis}} = \epsilon\mu$ by

$$P_{\text{evt}} = \frac{N_{\text{evt}}}{N_{\text{BC}}} = 1 - e^{-\mu_{\text{vis}}}$$

where N_{evt} is the number of events counted in the luminosity block and N_{BC} is the number of bunch crossings sampled (equal for a single colliding bunch pair to $f_r \Delta t$ where Δt is the duration of the luminosity block). The μ_{vis} value is then given by $\mu_{\text{vis}} = -\ln(1 - P_{\text{evt}})$, from which the instantaneous luminosity can be calculated via Eq. (3) once σ_{vis} is known. Several PMTs can be combined in an ‘EventOR’ (hereafter abbreviated to EvtOR) algorithm by counting an event if any of a group of PMTs registers a hit in a given bunch crossing. Such an algorithm has a larger efficiency and σ_{vis} than a single-PMT algorithm, giving a smaller statistical uncertainty at low bunch luminosity. However, at moderate single-bunch luminosity ($\mu > 20$ – 30), it already suffers from ‘zero starvation’, when for a given colliding-bunch pair, all bunch crossings in the LB considered contain at least one hit. In this situation, there are no bunch crossings left without an event, making it impossible to determine μ_{vis} . LUCID EvtOR algorithms were therefore not used for standard high-pileup physics running during Run 2. The ‘HitOR’ algorithm provides an alternative method for combining PMTs at high luminosity. For N_{PMT} PMTs, the average probability P_{hit} to have a hit in any given PMT during the N_{BC} bunch crossings of one luminosity block is inferred from the total number of hits summed over all PMTs N_{hit} by

$$P_{\text{hit}} = \frac{N_{\text{hit}}}{N_{\text{BC}} N_{\text{PMT}}} = 1 - e^{-\mu_{\text{vis}}}, \quad (4)$$

which leads for the HitOR algorithm to $\mu_{\text{vis}} = -\ln(1 - P_{\text{hit}})$. Per-bunch LB-averaged event and hit counts from a variety of PMT combinations were accumulated online in the LUCID readout electronics.

Both the configuration of LUCID and the LHC running conditions evolved significantly over the course of Run 2, and different algorithms gave the best LUCID offline luminosity measurement in each data-taking year. These algorithms are summarised in Table 2, together with the corresponding visible cross-sections derived from the vdM calibration, the peak (μ) value and the corresponding fraction of bunch crossings which do not have a PMT hit. The latter fell below 1% at the highest instantaneous luminosities achieved in 2017 and 2018. Where possible, HitOR algorithms were used, as the averaging over multiple PMTs reduces systematic uncertainties due to drifts in the calibration of individual PMTs, and also evens out the asymmetric response of PMTs in different ϕ locations due to the LHC beam crossing angle used in bunch train running. The BiHitOR algorithm, which combines four bismuth-calibrated PMTs on the A-side of LUCID with four more on the C-side using the HitOR method, was used in both 2016 and 2017. Some PMTs were changed during each winter shutdown, so the sets of PMTs used in the two years were not exactly the same. In 2015, nearly all PMTs suffered from long-term timing drifts due to adjustments of the high-voltage settings, apart from one PMT on the C-side (C9), and the most stable luminosity measurement (determined from comparisons with independent measurements from other detectors) was obtained from the single-PMT algorithm applied to PMT C9. In 2015 and 2016, the bismuth calibration signals were used to adjust the PMT gains so as to keep the mean charge recorded by the PMT constant over the year. However, the efficiencies of the hit-counting algorithms depend primarily on the pulse amplitude. Additional offline corrections were therefore applied to the LUCID data in these years to correct for this imperfect calibration. In 2017 and 2018, the gain adjustments were made using the amplitudes derived from the calibration signals, and so these corrections were not needed. In 2018, a significant number of PMTs stopped working during the course of the data-taking year,

Table 2 LUCID algorithms used for the baseline luminosity determination in each year of Run 2 data-taking, together with the visible cross-sections σ_{vis} determined from the absolute vdM calibration (see Sect. 4), the peak $\langle\mu\rangle$ value taken from Table 1, and the fraction of bunch crossings $f_{\text{no-hit}}$ which do not have a PMT hit at this $\langle\mu\rangle$ value. For the HitOR algorithms, this fraction represents an average over all the contributing PMTs

Year	Algorithm	σ_{vis} [mb]	Peak $\langle\mu\rangle$	$f_{\text{no-hit}}$ [%]
2015	PMT C9	6.540	16	27.0
2016	BiHitOR	6.525	41	3.5
2017	BiHitOR	6.706	60	0.6
2018	PMT C12	6.860	55	0.9

and a single PMT on the C-side (C12) was used for the final offline measurement, as it showed good stability throughout the year and gave results similar to those of a more complicated offline HitOR-type combination of the remaining seven working PMTs. In all years, other LUCID algorithms were also available, and were studied as part of the vdM and stability analyses. These algorithms include Bi2HitOR, an alternative to BiHitOR using an independent set of eight PMTs with four on each side of the detector, single-sided HitOR and EvtOR algorithms, EvtAND algorithms requiring a coincidence of hits on both sides, and single-PMT algorithms based on individual PMTs.

3.2 Beam conditions monitor

The BCM detector consists of four $8 \times 8 \text{ mm}^2$ diamond sensors arranged around the beam pipe in a cross pattern at $z = \pm 1.84 \text{ m}$ on each side of the ATLAS interaction point [15]. The BCM mainly provides beam conditions information and beam abort functionality to protect the ATLAS inner detector, but it also gives a bunch-by-bunch luminosity signal with sub-nanosecond timing resolution. Various luminosity algorithms are available, combining hits from individual sensors in different ways with EvtOR and EvtAND algorithms in the same way as for LUCID. The BCM provided the primary ATLAS luminosity measurement during most of Run 1 [2, 3] but performed much less well in the physics data-taking conditions of Run 2, with 25 ns bunch spacing and higher pileup, due to a combination of radiation damage, charge-pumping effects [2] and bunch-position-dependent biases along bunch trains. Its use in the Run 2 analysis was therefore limited to consistency checks during some vdM scan periods with isolated bunches and low instantaneous luminosity, and luminosity measurement in heavy-ion collisions.

3.3 Track-counting algorithms

The track-counting luminosity measurement determines the per-bunch visible interaction rate μ_{vis} from the mean number

Table 3 Track-selection criteria for the different working points used in the track-counting luminosity measurement, applied in addition to the basic TightPrimary selection of Ref. [16]. Selection A was used for the baseline track-counting luminosity measurement

Criterion	Selection A	Selection B	Selection C
p_T [GeV]	> 0.9	> 0.9	> 0.9
$ \eta $	< 1.0	< 2.5	< 1.0
$N_{\text{hits}}^{\text{Si}}$	≥ 9	≥ 9 if $ \eta < 1.65$ else ≥ 11	≥ 10
$N_{\text{holes}}^{\text{Pix}}$	≤ 1	$= 0$	≤ 1
$ d_0 /\sigma_{d_0}$	< 7	< 7	< 7

of reconstructed tracks per bunch crossing averaged over a luminosity block. The measurement was derived from randomly sampled colliding-bunch crossings, where only the data from the silicon tracking detectors (i.e. the SCT and pixel detectors, including a new innermost layer, the ‘insertable B-layer’ (IBL) [11, 12] added before Run 2) were read out, typically at 200 Hz during normal physics data-taking and at much higher rates during vdM scans and other special runs. These events were saved in a dedicated event stream, which was then reconstructed offline using special track reconstruction settings, optimised for luminosity monitoring. All reconstructed tracks used in the track-counting luminosity measurement were required to satisfy the TightPrimary requirements of Ref. [16], and to have transverse momentum $p_T > 0.9 \text{ GeV}$ and a track impact parameter significance of $|d_0|/\sigma_{d_0} < 7$, where d_0 is the impact parameter of the track with respect to the beamline in the transverse plane, and σ_{d_0} the uncertainty in the measured d_0 , including the transverse spread of the luminous region. Several different track selection working points, applying additional criteria on top of these basic requirements, were used, as summarised in Table 3. The baseline selection A uses tracks only in the barrel region of the inner detector ($|\eta| < 1.0$), requires at least nine silicon hits $N_{\text{hits}}^{\text{Si}}$ (counting both pixel and SCT hits), and requires at most one pixel ‘hole’ ($N_{\text{holes}}^{\text{Pix}}$), i.e. a missing pixel hit where one is expected, taking into account known dead modules. Selection B extends the acceptance into the endcap tracking region, with tighter hit requirements for $|\eta| > 1.65$, and does not allow any pixel holes. Selection C is based on selection A, with a tighter requirement of at least ten silicon hits. Selection A was used as the baseline track-counting luminosity measurement, and the other selections were used to study systematic uncertainties.

The statistical precision of the track-counting luminosity measurement is limited at low luminosity, making it impractical to calibrate it directly using vdM scans. Instead, the working points were calibrated to agree with LUCID luminosity measurements in the same LHC fills as the vdM scans, utilising periods with stable, almost constant lumi-

osity where the beams were colliding head-on in ATLAS, typically while vdM scans were being performed at the CMS interaction point. The average number of selected tracks per $\sqrt{s} = 13$ TeV inelastic pp collision was about 1.7 for selections A and C, and about 3.7 for selection B, which has a larger acceptance in $|\eta|$.

3.4 Calorimeter-based algorithms

The electromagnetic endcap calorimeters are sampling calorimeters with liquid argon as the active medium and lead/stainless-steel absorbers, covering the region $1.5 < |\eta| < 3.2$ on each side of the ATLAS detector. Ionisation electrons produced by charged particles crossing the LAr-filled gaps between the absorbers draw a current through the high-voltage (HV) power supplies that is proportional to the instantaneous luminosity, after subtracting the electronics pedestal determined from the period without collisions at the start of each LHC fill. A subset of the EMEC HV lines are used to produce a luminosity measurement, independently from the A- and C-side EMEC detectors. A similar measurement is available from the forward calorimeters that cover the region $3.2 < |\eta| < 4.9$ with longitudinal segmentation into three modules. The first module has copper absorbers, optimised for the detection of electromagnetic showers, and the HV currents from the 16 azimuthal sectors are combined to produce a luminosity measurement, again separately from the A- and C-side calorimeters. Since both the EMEC and FCal luminosity measurements rely on ‘slow’ ionisation currents, they cannot resolve individual bunches and therefore give bunch-integrated measurements which are read out every few seconds and then averaged per luminosity block. They have insufficient sensitivity at low luminosity to be calibrated during vdM scans, so they were cross-calibrated to track-counting measurements in high-luminosity physics fills as discussed in Sect. 7.

The event-by-event ‘energy flow’ through the cells of the LAr calorimeters, as read out by the standard LAr pulse-shaping electronics, provides another potential luminosity measurement. However, the long LAr drift time and bipolar pulse shaping [17] wash out any usable signal during running with bunch trains. Only the EMEC and FCal cells have short enough drift times to yield useful measurements in runs with isolated bunches separated by at least 500 ns. Under these conditions, the total energy deposited in a group of LAr cells and averaged over a luminosity block is proportional to the instantaneous luminosity (after pedestal subtraction). A dedicated data stream reading out only the LAr calorimeter data in randomly sampled bunch crossings was used in certain runs with isolated bunches to derive a LAr energy-flow luminosity measurement. This was exploited to constrain potential non-linearity in the track-counting luminosity measurement as discussed in Sect. 6.3.

The TileCal hadronic calorimeter uses steel absorber plates interleaved with plastic scintillators as the active medium, read out by wavelength-shifting fibres connected to PMTs [18]. It is divided into a central barrel section covering $|\eta| < 1.0$, and an extended barrel on each side of the detector (A and C) covering $0.8 < |\eta| < 1.7$. Both the barrel and extended barrels are segmented azimuthally into 64 sectors, and longitudinally into three sections. The current drawn by each PMT (after pedestal correction) is proportional to the total number of particles traversing the corresponding TileCal cell, and hence to the instantaneous luminosity. In principle, all TileCal cells can be used for luminosity measurement, but the D-cells, located at the largest radius in the last longitudinal sampling, suffer least from variations in response over time due to radiation damage. The D6 cells, at the highest pseudorapidity in the extended barrels on the A- and C-sides, were used for the primary TileCal luminosity measurements in this analysis, with other D-cells at lower pseudorapidity being used for systematic comparisons. Changes in the gains of the PMTs with time were monitored between physics runs using a laser calibration system which injects pulses directly into the PMTs, and the response of the scintillators was also monitored once or twice per year using ^{137}Cs radioactive sources circulating through the calorimeter cells during shutdown periods. The TileCal D-cells have insufficient sensitivity to be calibrated during vdM scans, so they were cross-calibrated to track-counting in the same way as for the EMEC and FCal measurements.

The TileCal system also includes the E1 to E4 scintillators, installed in the gaps between the barrel and endcap calorimeter assemblies, and designed primarily to measure energy loss in this region. Being much more exposed to particles from the interaction point than the rest of the TileCal scintillators (which are shielded by the electromagnetic calorimeters) the E-cells (in particular E3, and E4 which is closest to the beamline) are sensitive enough to make precise luminosity measurements during vdM fills. They play a vital role in constraining the calibration transfer uncertainties, as discussed in Sect. 6. However, their response changes rapidly over time due to radiation damage, so they cannot be used for long-term stability studies. The high currents drawn by the E-cell PMTs also cause the PMT gains to increase slightly at high luminosity, resulting in an overestimation of the actual luminosity. This effect was monitored during collision data-taking by firing the TileCal calibration laser periodically during the LHC abort gap—a time window during each revolution of the LHC beams, in which no bunches pass through the ATLAS interaction point, and which is left free for the duration of the rise time of the LHC beam-dump kicker magnets. By comparing, in 2018 data, the response of the E-cell PMTs to the laser pulse with that of the D6-cell PMTs (the gain of which remains stable thanks to the much lower currents), a correction to the E-cell PMT gain was

derived, reducing the reported luminosity in high-luminosity running by up to 1% for the E4 cells, and somewhat less for E3. This correction is applied to all the TileCal E-cell data shown in this paper.

4 Absolute luminosity calibration in vdM scans

The absolute luminosity calibration of LUCID and BCM, corresponding to the determination of the visible cross-section σ_{vis} for each of the LUCID and BCM algorithms, was derived using dedicated vdM scan sessions during special LHC fills in each data-taking year. The calibration methodology and main sources of uncertainty are similar to those in Run 1 [2,3], but with significant refinements in the light of Run 2 experience and additional studies. The improvements especially concern the scan-curve fitting, the treatment of beam-beam and emittance growth effects, and the potential effects of non-linearity from magnetic hysteresis in the LHC steering corrector magnets used to move the beams in vdM scans. These aspects are given particular attention below. The uncertainties related to each aspect of the vdM calibration are discussed in the relevant subsections, and listed for each data-taking year in Table 8 in Sect. 8.

4.1 vdM formalism

The instantaneous luminosity for a single colliding bunch pair, \mathcal{L}_b , is given in terms of LHC beam parameters by

$$\mathcal{L}_b = \frac{f_r n_1 n_2}{2\pi \Sigma_x \Sigma_y} \tag{5}$$

where f_r is the LHC revolution frequency, n_1 and n_2 are the numbers of protons in the beam-1 and beam-2 colliding bunches, and Σ_x and Σ_y are the convolved beam sizes in the horizontal and vertical (transverse) planes [5]. In the vdM method, the uncalibrated instantaneous luminosity or counting rate $R(\Delta x)$ is measured as a function of the nominal separation Δx between the two beams in the horizontal plane, given by

$$\Delta x = x_{\text{disp},1} - x_{\text{disp},2}$$

where $x_{\text{disp},i}$ is the displacement of beam i from its initial position (corresponding to $x_{\text{disp},i} = 0$) with approximately head-on collisions (i.e. no nominal transverse separation). These initial positions were established by optimising the luminosity as a function of separation in each plane before starting the first vdM scan in a session. The separation was then varied in steps by displacing the two beams in opposite directions ($x_{\text{disp},2} = -x_{\text{disp},1}$), starting with the maximum negative separation, moving through the peak and onward to maximum positive separation, and measuring the instantaneous luminosity $R(\Delta x)$ at each step. The procedure was

then repeated in the vertical plane (varying Δy and keeping $\Delta x = 0$) to measure $R(\Delta y)$, completing an x - y scan pair. The quantity Σ_x is then given by

$$\Sigma_x = \frac{1}{\sqrt{2\pi}} \frac{\int R(\Delta x) d\Delta x}{R(\Delta x^{\text{max}})} \tag{6}$$

i.e. the ratio of the integral over the horizontal scan to the instantaneous luminosity $R(\Delta x^{\text{max}})$ on the peak of the scan at $\Delta x^{\text{max}} \approx 0$, and similarly for Σ_y with a vertical scan.

If the form of $R(\Delta x)$ is Gaussian, Σ_x is equal to the standard deviation of the distribution, but the method is valid for any functional form of $R(\Delta x)$. However, the formulation does assume that the particle densities in each bunch can be factorised into independent functions of x and y . The effect of violations of this assumption (i.e. of non-factorisation) is quantified in Sect. 4.6 below. Since the normalisation of $R(\Delta x)$ cancels out in Eq. (6), any quantity proportional to luminosity can be used to determine the scan curve. The calibration of a given algorithm (i.e. its σ_{vis} value) can then be determined by combining Eqs. (3) and (5) to give

$$\sigma_{\text{vis}} = \mu_{\text{vis}}^{\text{max}} \frac{2\pi \Sigma_x \Sigma_y}{n_1 n_2} \tag{7}$$

where $\mu_{\text{vis}}^{\text{max}}$ is the visible interaction rate per bunch crossing at the peak of the scan curve. In practice, the vdM scan curve was analysed in terms of the specific visible interaction rate $\bar{\mu}_{\text{vis}}$, the visible interaction rate μ_{vis} divided by the bunch population product $n_1 n_2$ measured at each scan step, as discussed in Sect. 4.4. This normalisation accounts for the small decreases in bunch populations during the course of each scan. The specific interaction rate in head-on collisions $\bar{\mu}_{\text{vis}}^{\text{max}}$ was determined from the average of the rates fitted at the peaks of the x and y scan curves $\bar{\mu}_{\text{vis},x}^{\text{max}}$ and $\bar{\mu}_{\text{vis},y}^{\text{max}}$, so Eq. (7) becomes

$$\sigma_{\text{vis}} = \frac{1}{2} \left(\bar{\mu}_{\text{vis},x}^{\text{max}} + \bar{\mu}_{\text{vis},y}^{\text{max}} \right) \cdot 2\pi \Sigma_x \Sigma_y. \tag{8}$$

A single pair of x - y vdM scans suffices to determine σ_{vis} for each algorithm active during the scan. Since the quantities entering Eq. (8) may be different for each colliding bunch pair, it is essential to perform a bunch-by-bunch analysis to determine σ_{vis} , limiting the vdM absolute calibration in ATLAS to the LUCID and BCM luminosity algorithms. Track-counting cannot be used since only a limited rate of bunch crossings can be read out for offline analysis,³ and the calorimeter algorithms only measure bunch-integrated luminosity.

³ At $\sqrt{s} = 8$ TeV, track-counting algorithms were calibrated in vdM scans [3], but trigger-rate and dataflow limitations restricted this calibration to a small subset of the colliding bunch pairs. A more precise calibration can be achieved by cross-calibrating to LUCID algorithms as discussed in Sect. 3.3.

4.2 vdM scan datasets

In order to minimise both instrumental and accelerator-related uncertainties [5], $\sqrt{s} = 13$ TeV vdM scans were not performed in standard physics conditions, but once per year in dedicated low-luminosity vdM scan fills using a special LHC configuration. Filling schemes with 44–140 isolated bunches in each beam were used, so as to avoid the parasitic encounters between incoming and outgoing bunches that occur in normal bunch train running. This allowed the beam crossing angle to be set to zero, reducing orbit drift and beam–beam-related uncertainties. The parameter β^* was set to 19.2 m rather than the 0.25–0.8 m used during normal physics running, and the injected beam emittance was increased to 3–4 $\mu\text{m}\text{-rad}$. These changes increased the RMS transverse size of the luminous region to about 60 μm , thus reducing vertex-resolution uncertainties in evaluating the non-factorisation corrections discussed below. The longitudinal size of the luminous region was typically around 45 mm, corresponding to an RMS bunch length of 64 mm. Special care was taken in the LHC injector chain to produce beams with Gaussian-like transverse profiles [19], a procedure that also minimises non-factorisation effects in the scans. Finally, bunch currents were reduced to $\sim 0.8 \times 10^{11}$ protons/bunch, minimising bunch-current normalisation uncertainties. When combined with the enlarged emittance, this also reduces beam–beam biases. These configurations typically resulted in $\langle\mu\rangle \approx 0.5$ at the peak of the scan curves, whilst maintaining measurable rates in the tails of the scans at up to $6\sigma_{\text{nom}}^{\text{b}}$ separation, where $\sigma_{\text{nom}}^{\text{b}} \approx 100 \mu\text{m}$ is the nominal single-beam size at the interaction point.

The vdM scan datasets are listed in Table 4. Several pairs of on-axis x – y scans were performed in each session, spaced through one or more fills in order to study reproducibility. One or two pairs of off-axis scans, where the beam was scanned in x with an offset in y of e.g. 300 μm (and vice versa) were also included, to study the beam profiles in the tails in order to constrain non-factorisation effects. A diagonal scan varying x and y simultaneously was also performed in 2016. A typical scan pair took 2×20 min for x and y , scanning the beam separation between $\pm 6\sigma_{\text{nom}}^{\text{b}}$ in 25 steps of $0.5\sigma_{\text{nom}}^{\text{b}}$. Length scale calibration (LSC) scans were also performed in the vdM or nearby fills, as described in Sect. 4.9. A vdM fill lasted up to one day, with alternating groups of scans in ATLAS and CMS, and the beams colliding head-on in the experiment which was not performing scans.

4.3 Scan curve fitting

Typical vdM scan curves from the 2017 and 2018 datasets using the LUCID BiHitOR and C12 algorithms are shown in Fig. 1. The $\bar{\mu}_{\text{vis}}$ distributions were fitted using an analytic function (e.g. a Gaussian function multiplied by a poly-

Table 4 Summary of the $\sqrt{s} = 13$ TeV pp vdM scan fills used in the ATLAS Run 2 vdM analysis, showing the dates, LHC fill numbers, numbers of bunches in each beam (n_{tot}), numbers of bunch pairs colliding in ATLAS (n_{b}), and the individual x – y scan pairs performed in each fill (S1, S2, etc., including off-axis scans denoted ‘Sn-off’, a diagonal x y scan in 2016 denoted ‘S5-diag’ and length scale calibration scans denoted LSC). All fills used the dedicated vdM optics with $\beta^* = 19.2$ m, with zero beam crossing angle and only isolated bunches

Date	Fill	n_{tot}	n_{b}	Scans
24/8/2015	4266	44	30	S1, S2, S3-off
25/8/2015	4269	51	8	S4, LSC
17/5/2016	4937	55	11	LSC
18/5/2016	4945	52	32	S1,S2, S3-off, S4, S5-diag
27/5/2016	4954	52	32	S6
28/7/2017	6016	52	32	S1, S2, S3-off, S4, S5, LSC
29/6/2018	6864	70	58	LSC
30/6/2018	6868	140	124	S1, S2, S3-off, S4, S5-off, S6

nomial), after subtraction of backgrounds. For the LUCID algorithms, the background is dominated by noise from the ^{207}Bi calibration source, which was estimated by subtracting the counting rate measured in the preceding bunch slot. The latter was always empty in the LHC filling patterns used for vdM scans, which only include isolated bunches separated by at least 20 unfilled bunch slots. This procedure also subtracts the smaller background due to ‘afterglow’ from photons produced in the decay of nuclei produced in hadronic showers initiated by the pp collisions. This background scales with the instantaneous luminosity at each scan point, and decays slowly over the bunch slots following each filled bunch slot. A further small background comes from the interaction of the protons in each beam with residual gas molecules in the beam pipe, and scales with the bunch population n_1 or n_2 . It was estimated using the counting rate in the bunch slots corresponding to ‘unpaired’ bunches, where a bunch from one beam passes through the ATLAS interaction point without meeting a bunch travelling in the opposite direction.

Since the visible interaction rate is only sampled at a limited number of scan points, the choice of fit function is crucial in order to ensure unbiased estimates of $\mu_{\text{vis}}^{\text{max}}$ and $\Sigma_{x,y}$. Fitting the scan curves to a Gaussian function multiplied by a fourth-order polynomial (referred to as GP4) gives a good general description of the shape, but was found to systematically overestimate the peak of the scan curves by about 0.5%, biasing $\bar{\mu}_{\text{vis}}^{\text{max}}$. Better results were achieved by adding a second Gaussian function to the GP4 function for the five central scan points, flattening the scan curve at the peak.⁴ This GP4+G function was used for the baseline σ_{vis} results. The

⁴ The second Gaussian function introduces discontinuities into the fitting function just outside the five central points, but the results were

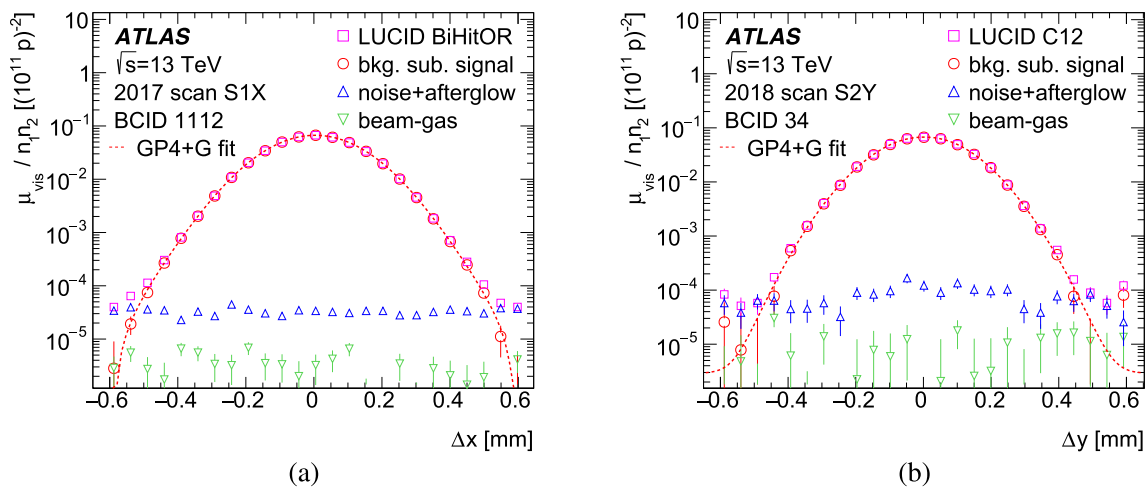


Fig. 1 Visible interaction rate μ_{vis} per unit bunch population product $n_1 n_2$ (i.e. $\bar{\mu}_{\text{vis}}$) vs. beam separation in (a) the horizontal plane for bunch slot (BCID) 1112 in scan 1 of 2017, using the LUCID BiHitOR algorithm, and (b) the vertical plane for BCID 34 in scan 2 of 2018, using the LUCID C12 PMT algorithm. The measured rate is shown by the pink squares, the background-subtracted rate by the red circles, the estimated background from noise and afterglow by the blue upward-

pointing triangles and that from beam–gas interactions by the green downward-pointing triangles. The error bars show the statistical uncertainties, which are in some cases smaller than the symbol sizes. The fits to a Gaussian function multiplied by a fourth-order polynomial (GP4) plus an additional Gaussian function in the central region and a constant term (see text) are shown by the dashed red lines

statistical uncertainties from the fit are smaller than 0.1% in all years, and are listed as ‘Statistical uncertainty’ in Table 8. A Gaussian function multiplied by a sixth-order polynomial (GP6) was found to give a similar goodness-of-fit to GP4+G, and the difference between the σ_{vis} obtained from these two functions was used to define the ‘Fit model’ uncertainty shown for each data-taking year in Table 8. In all cases, a constant term was also included in the fit function, and the integrals to determine $\Sigma_{x,y}$ (Eq. (6)) were truncated at the limits of the scan range. The constant term improves the fit stability and the description of the tails.

To estimate the uncertainty due to the background subtraction procedure, alternative fits were performed to the data without subtracting the estimates of the noise and beam–gas components, instead using the constant term to account for their contributions, and implicitly assuming that the backgrounds do not depend on beam separation. In this case, the constant term was not included in the evaluation of $\Sigma_{x,y}$ and $\mu_{\text{vis}}^{\text{max}}$. The resulting difference in σ_{vis} was used to define the ‘Background subtraction’ uncertainty in Table 8.

The vdM scan curve fits were performed for all available LUCID and BCM algorithms, and the results are compared in Sect. 4.11. However, most of the systematic uncertainty studies detailed below were only performed with a single ‘reference’ algorithm for each year of data-taking. For 2016–2018, this is the algorithm listed in Table 2 and used for the baseline luminosity determination; however for 2015, the

LUCID BiEvtORA algorithm, using four PMTs on the A-side of LUCID in an EvtOR combination, was used as the reference algorithm instead.

4.4 Bunch population measurement

The determination of the bunch populations n_1 and n_2 was based on the LHC beam instrumentation, using the methods discussed in detail in Ref. [3]. The total intensity in each beam was measured by the LHC DC current transformers (DCCT), which have an absolute precision of better than 0.1% but lack the ability to resolve individual bunches. The per-bunch intensities were determined from the fast beam-current transformers (FBCT), which can resolve the current in each of the 3564 nominal 25 ns bunch slots in each beam. The FBCT measurements were normalised to the DCCT measurement at each vdM scan step, and supplemented by measurements from the ATLAS beam-pickup timing system (BPTX), which can also resolve the relative populations in each bunch.

Both the FBCT and BPTX systems suffer from non-linear behaviour, which can be parameterised as a constant offset between the measured and true beam current, assuming the measurement is approximately linear near the average bunch currents \bar{n}_1 and \bar{n}_2 for the two beams. For the BPTX measurements, these offsets were determined for each x – y scan pair from the data by minimising the differences between the corrected σ_{vis} values measured for all bunches, defining a χ^2

found not to depend on whether the discontinuities were placed close to the central points or close to the next two scan points at larger $|\Delta x|$.

by

$$\chi^2(\bar{\sigma}_{\text{vis}}, b_1, b_2) = \sum_i \left(\frac{S(\bar{\sigma}_{\text{vis}}, b_1, b_2, n_1^i, n_2^i) - \sigma_{\text{vis}}^{\text{meas},i}}{\Delta\sigma_{\text{vis}}^{\text{meas},i}} \right)^2$$

where $\sigma_{\text{vis}}^{\text{meas},i}$ is the uncorrected measured visible cross-section for colliding bunch pair i and $\Delta\sigma_{\text{vis}}^{\text{meas},i}$ its statistical error, and S represents the modified visible cross-section which would be measured for bunch pair i , given a true average visible cross-section $\bar{\sigma}_{\text{vis}}$ and bunch current offsets b_1 and b_2 for the two beams. The quantity S is given by

$$S(\bar{\sigma}_{\text{vis}}, b_1, b_2, n_1^i, n_2^i) = \bar{\sigma}_{\text{vis}} \cdot \left(\frac{n_1^i + b_1(n_1^i - \bar{n}_1)}{n_1^i} \right) \left(\frac{n_2^i + b_2(n_2^i - \bar{n}_2)}{n_2^i} \right)$$

where the two terms in brackets represent the bunch-dependent biases in the measured σ_{vis} values caused by the non-linearity in the BPTX bunch current measurements. The values of b_1 and b_2 were determined separately for each scan in each year by minimising the χ^2 as a function of b_1 , b_2 and $\bar{\sigma}_{\text{vis}}$ [20], and have typical sizes of a few percent. In all vdM datasets, this correction reduces the apparent dependence of the σ_{vis} measured for each bunch pair on the BPTX bunch-population product $n_1 n_2$.

The FBCT uses independent electronics channels with separate scales and offsets for the even- and odd-numbered bunch slots, making it difficult to apply the above procedure to the FBCT measurements. Instead, the uncorrected FBCT measurements in each scan were fitted to a linear function of the offset-fit-corrected BPTX measurements, deriving parameters p_0^j and p_1^j , where $j = 1$ for odd and 2 for even bunch pairs. These parameters, derived from separate fits to the odd and even bunches within each scan, were used to determine corrected FBCT populations $n_1^{i,j,\text{FBCT-corr}}$ from the uncorrected measurements $n_1^{i,j,\text{FBCT-uncorr}}$ via

$$n_1^{i,j,\text{FBCT-corr}} = (n_1^{i,j,\text{FBCT-uncorr}} - p_0^j) / p_1^j$$

and similarly for $n_2^{i,j,\text{FBCT-corr}}$. This correction procedure reduced the $n_1 n_2$ dependence of the σ_{vis} values measured using the FBCT, with residual variations contributing to the bunch-by-bunch consistency uncertainty discussed in Sect. 4.11 below. The FBCT bunch population measurements (corrected using the BPTX offset fit) were used for the baseline σ_{vis} results, with the alternative BPTX-only results used to define the ‘FBCT bunch-by-bunch fractions’ uncertainty in Table 8, which is below 0.1% for all years. The changes in σ_{vis} resulting from these corrections amount to about +0.4% in 2015 and less than $\pm 0.05\%$ in all other years.

The DCCT measurement used to normalise the BPTX and FBCT results summed over all filled bunches is also sensitive to additional contributions to the total circulating beam currents from ghost charge and satellite bunches. Ghost charge

refers to circulating protons present in nominally unfilled bunch slots, which are included in the DCCT reading but are typically below the FBCT or BPTX threshold. Their contribution was measured by comparing the rate of beam–gas vertices reconstructed by the LHCb experiment in nominally empty bunch slots with the rate in those bunch slots containing an unpaired bunch [21].

Satellite bunches are composed of protons present in a nominally filled bunch slot, but which are captured in a radio-frequency (RF) bucket at least one RF period (2.5 ns) away from the nominally filled bucket. Their current is included in the FBCT reading, but because collisions between satellite bunches in each beam make a negligible contribution to the nominal luminosity signal at the interaction point, their contributions to the FBCT measurements must be estimated and subtracted. Satellite populations were measured using the LHC longitudinal density monitor [22]. At zero crossing angle, longitudinally displaced collisions between a satellite bunch and the opposing in-time nominal bunch can contribute to the measured luminosity signal in the corresponding bunch slot. The magnitude of this additional contribution is proportional to the sum of the fractional satellite populations in the two beams, and also depends on the emittance of the satellite bunch, on the number of RF buckets by which it is offset from the nominal bunch, and on the longitudinal location and time acceptance of the luminosity detector considered. The fractional satellite contribution summed over both beams is at most 0.02%, 0.03%, 0.02% and 0.09% in each of the datasets from 2015 to 2018, and these values were conservatively taken as uncertainties in σ_{vis} due to the additional luminosity produced by nominal–satellite collisions.

The combined effects of ghost and satellite charges on the bunch-population measurement lead to positive corrections to σ_{vis} of 0.1–0.4%, depending on the vdM fill in question, with uncertainties that are an order of magnitude smaller. The corresponding uncertainty in Table 8 also includes the effect of nominal–satellite collisions.

A further uncertainty of 0.2% arises from the absolute calibration of the DCCT current measurements, derived from a precision current source. The uncertainty takes into account residual non-linearities, long-term stability and dependence on beam conditions, and was derived using the procedures described in Ref. [23].

4.5 Orbit drift corrections

Gradual orbit drifts of up to $O(10 \mu\text{m})$ in the positions of one or both beams have been observed during the course of a single vdM scan. These drifts change the actual beam separation from the nominal one produced by the LHC steering corrector magnets, and were monitored using two independent beam position monitor (BPM) systems. The DOROS BPM

system⁵ uses pickups located at the inner (i.e. closest to the IP) ends of the LHC final-focus quadrupole triplet assemblies at $z = \pm 21.7$ m on each side of the IP, allowing the beam position at the IP to be determined by averaging the measurements from each side. Since these BPMs are located closer to ATLAS than the steering correctors used to move the beams during vdM scans, they also see the beam displacements during scans. The arc BPMs are located at intervals throughout the LHC magnetic arcs, and the measurements from those close to ATLAS can be extrapolated to give the beam position at the IP. The arc BPMs do not see the displacement during scans, apart from any residual effects leaking into the LHC arcs due to non-closure of the orbit bumps around the IP. For both BPM systems, the beam positions in both planes were measured at the zero nominal beam separation points immediately before and after each single scan (x or y), and any changes were interpolated linearly as a function of time within the scan to give corrections $\delta_1^{x,y}(t)$ and $\delta_2^{x,y}(t)$ for beams 1 and 2.

The dominant effect on the vdM analysis comes from in-plane drifts, defined as horizontal (vertical) drifts during a horizontal (vertical) scan. They distort the beam-separation scale in Fig. 1, changing the values of $\Sigma_{x,y}$ obtained from Eq. (6). These drifts were taken into account by correcting the separation at each scan step to include the interpolated orbit drifts:

$$\Delta x^{\text{corr}} = \Delta x^{\text{nominal}} + \delta_1^x - \delta_2^x$$

and similarly for y , before fitting the scan curves.

A subdominant effect is caused by out-of-plane drifts between the peaks of the x and y scans (including during any pause between the two scans). A horizontal orbit drift between the x -scan peak (where the beams are perfectly centred horizontally by definition) and the y -scan peak (where they may no longer be), would lead to an underestimate of the visible interaction rate at the peak of the y scan, and hence of $\bar{\mu}_{\text{vis},y}^{\text{max}}$ in Eq. (8). Similarly, a vertical orbit drift causes an underestimate of the peak interaction rate in the x scan.⁶ Approximate corrections for out-of-plane drifts were made using the differences in horizontal and vertical orbit drifts δx^0 and δy^0 between the peaks of the x and y scan curves:

$$\delta x^0 = \delta_1^x(t_y^0) - \delta_2^x(t_y^0) - \delta_1^y(t_x^0) + \delta_2^y(t_x^0)$$

⁵ Named for the DOROS (Diode ORbit and Oscillation System) front-end electronics, which can separate the close-in-time signals from the bunches circulating in opposite directions in the same beam pipe close to the IP.

⁶ Strictly speaking, what matters is the cumulative effect on the collision rate of the change in horizontal (vertical) beam separation, relative to that at the peak of the x (y) scan, from the beginning to the end of the y (x) scan. If the orbit drift rate is constant in time during the individual x and y scans, the cumulative effect on $\bar{\mu}_{\text{vis}}^{\text{max}}$ is equivalent to that evaluated from the scan peaks alone.

$$\delta y^0 = \delta_1^y(t_x^0) - \delta_2^y(t_x^0) - \delta_1^x(t_y^0) + \delta_2^x(t_y^0)$$

where the central (zero nominal separation) points of the x and y scan curves occur at times t_x^0 and t_y^0 . It can be shown [24] that the visible cross-section defined in Eq. (8) and corrected for out-of-plane orbit drifts is given by

$$\sigma_{\text{vis}} = 4\pi \Sigma_x \Sigma_y \frac{\mathcal{G}_x(\Delta x^{\text{max}}) \mathcal{G}_y(\Delta y^{\text{max}})}{\mathcal{G}_x(\delta x^0) + \mathcal{G}_y(\delta y^0)}$$

where $\mathcal{G}_x(\Delta x)$ and $\mathcal{G}_y(\Delta y)$ denote the functions of nominal separation fitted to the normalised vdM scan curves $\bar{\mu}_{\text{vis}}(\Delta x)$ and $\bar{\mu}_{\text{vis}}(\Delta y)$, and Δx^{max} and Δy^{max} are the fitted nominal beam separations at the peaks of these functions, i.e. $\mathcal{G}_x(\Delta x^{\text{max}}) = \bar{\mu}_{\text{vis},x}^{\text{max}}$ and $\mathcal{G}_y(\Delta y^{\text{max}}) = \bar{\mu}_{\text{vis},y}^{\text{max}}$. This formalism corrects for both out-of-plane orbit drifts and any imperfect initial alignment in the non-scanning plane.

A third effect is associated with the potential change in Σ_x due to drifts in the y (i.e. non-scanning) plane during the x scan, and similarly for Σ_y due to drifts in x during the y scan. This effect is distinct from the effects of out-of-plane drifts on $\bar{\mu}_{\text{vis}}^{\text{max}}$ discussed above. However, since the beams were reasonably well-centred on each other before each scan started (as ensured by the scan protocol), these effects are negligible for the orbit drifts observed in the non-scanning plane during on-axis scans.

Large orbit drift corrections were seen for scan S4 in 2015 (shifting σ_{vis} by 2.6%), S1 in 2017 (1.1%) and S4 in 2018 (−0.8%), mainly due to drift in the horizontal plane. All other scans have orbit drift corrections at the level of $\pm 0.5\%$ or less. Applying the corrections always improved the scan-to-scan consistency within each year. The baseline corrections were evaluated using the DOROS BPM system, and using the arc BPMs gave similar results. The ‘Orbit drift correction’ uncertainties in Table 8 were calculated as the fractional scan-averaged difference between the σ_{vis} values determined using the DOROS and arc BPM corrections, and are smaller than 0.1% in all years.

Short-term movements of the beams during the 30 s duration of a single vdM scan step may lead to fluctuations in the luminosity, distorting the measured scan curve. The potential effect of this beam position jitter was characterised by studying the distribution of the individual arc BPM beam position extrapolations, which were sampled every 5–7 s, i.e. several times per scan step. All measurements in a single x or y scan were fitted as a function of time to a second-order polynomial, and the RMS of the residuals of the individual measurements with respect to this fit were taken to be representative of the random beam jitter. Data from the y scan (where the beams are stationary in x) were used to measure the jitter in the x -direction, and vice versa, giving RMS values in the range 0.5–1.0 μm , typically larger in the horizontal plane than the vertical. One thousand simulated replicas of each real data scan were created, applying Gaussian smearing to the beam

positions (and hence the separation) at each step according to the RMS of the arc BPM fit residuals, coherently for the data from all colliding bunch pairs. The RMS of the σ_{vis} values obtained from these fits, averaged over all scans in a year, is typically around 0.2%. No correction was made for this effect, but the RMS was used to define the ‘Beam position jitter’ uncertainty in Table 8.

4.6 Non-factorisation effects

The vdM formalism described by Eqs. (5–7) assumes that the particle density distributions in each bunch can be factorised into independent horizontal and vertical components, such that the term $1/2\pi \Sigma_x \Sigma_y$ in Eq. (5) fully describes the overlap integral of the two beams. Evidence of non-factorisation was clearly seen during Run 1 [3], especially when dedicated beam tailoring in the LHC injector chain was not used. Such beam tailoring, designed to produce Gaussian-like beam profiles in x and y , was used for all $\sqrt{s} = 13$ TeV vdM scan sessions during Run 2, and information derived from the distribution of primary collision vertices reconstructed by the ATLAS inner detector in both on- and off-axis scans was used to constrain the possible residual effect of non-factorisation on the σ_{vis} determination, following the procedure of Ref. [3].

In more detail, combined fits were performed to the beam-separation dependence of both the LUCID luminosity measurements and the position, orientation and shape of the luminous region, characterised by the three-dimensional (3D) spatial distribution of the primary collision vertices formed from tracks reconstructed in the inner detector (i.e. the beamspot) [25]. Since this procedure requires a large number of reconstructed vertices per scan step, it was carried out for only a handful of colliding bunch pairs, whose tracking information was read out at an enhanced rate. Non-factorisable single-beam profiles (each composed of a weighted sum of three 3D Gaussian distributions $G(x, y, z)$ with arbitrary widths and orientations) were fitted to these data. These profiles were then used in simulated vdM scans to determine the ratio R of the apparent luminosity scale which would be extracted using the standard factorisable vdM formalism to the true luminosity scale determined from the full 3D beam overlap integral. This procedure was carried out both for each on-axis x – y scan in each vdM dataset, and with fits combining each off-axis (and in 2016, diagonal) scan with the closest-in-time on-axis scan. The resulting R values for the 2016 and 2017 datasets are shown in Fig. 2. In general, the results from on-axis and combined fits are similar, although there is significant scatter between bunches and scans.

The ratio R was used to correct the visible cross-section measured by the standard factorised vdM analysis for the measured non-factorisation: $\sigma_{\text{vis}}^{\text{corr}} = \sigma_{\text{vis}}/R$. Since the evaluation of R only sampled a small fraction of the colliding

bunch pairs, the error-weighted average of R over this subset of bunches was taken as representative of the complete set, and applied to the bunch-averaged σ_{vis} , giving corrections of $R = 1.006 \pm 0.003$ for 2016, 0.998 ± 0.001 for 2017 and 1.003 ± 0.003 for 2018, where the uncertainties were defined as the RMS of the individual R values for all available bunches and scans in each year. In 2015, the same method gave a central value of $R = 0.995$ but with a poor fit to the offset scan S3-off. An alternative method, fitting a non-factorisable function of both x and y to the x and y scan curves simultaneously, but without the use of beamspot data, gave a central value of $R = 1.006$. For the 2015 dataset, a value of $R = 1.000 \pm 0.006$ was used, i.e. no correction but an uncertainty that spans the range of central values from the two methods.

4.7 Beam–beam interactions

The mutual electromagnetic interaction between colliding bunches produces two effects that may bias their overlap integral, and that depend on the beam separation: a transverse deflection that induces a non-linear distortion of the intended separation, and a defocusing of one beam by the other that not only modulates the optical demagnification from the LHC arcs to the interaction point, but also modifies the shape of the transverse bunch profiles.

The beam–beam deflection can be modelled as a kick produced by a small dipole magnet, i.e. for a horizontal scan as an angular deflection $\theta_{x,i}$ that results in a horizontal beam displacement or orbit shift $\delta x_{\text{bb},i}^{\text{IP}}$ of each beam i at the IP. In the round-beam approximation, the deflection of a beam-1 bunch during a horizontal on-axis scan is given by [26]

$$\theta_{x,1} = \frac{2r_p n_2}{\gamma_1 \Delta x} \left[1 - \exp(-\Delta x^2 / (2\Sigma_x^2)) \right]; \quad \theta_{x,2} \approx -\theta_{x,1} \quad (9)$$

where $r_p = e^2 / (4\pi\epsilon_0 m_p c^2)$ is the classical proton radius, $\gamma_1 = E_1 / m_p$ is the Lorentz factor of the beam-1 particles with energy E_1 and mass m_p , n_2 is the charge of the beam-2 bunch, Δx is the nominal beam separation produced by the steering corrector magnets, and Σ_x is the transverse convolved beam size defined in Eq. (6). The induced single-beam displacement at the interaction point is proportional to $\theta_{x,i}$, and is given by

$$\delta x_{\text{bb},i}^{\text{IP}} = \theta_{x,i} \frac{\beta_x^*}{2 \tan(\pi Q_x)}; \quad \delta x_{\text{bb},2}^{\text{IP}} \approx -\delta x_{\text{bb},1}^{\text{IP}}$$

where β_x^* is the value of the horizontal β -function at the IP and Q_x is the horizontal tune.⁷ Similar formulae apply to a vertical scan. The beam–beam deflection at each scan point,

⁷ The tune of a storage ring is defined as the betatron phase advance per turn, equivalent to the number of betatron oscillations over one full ring circumference.

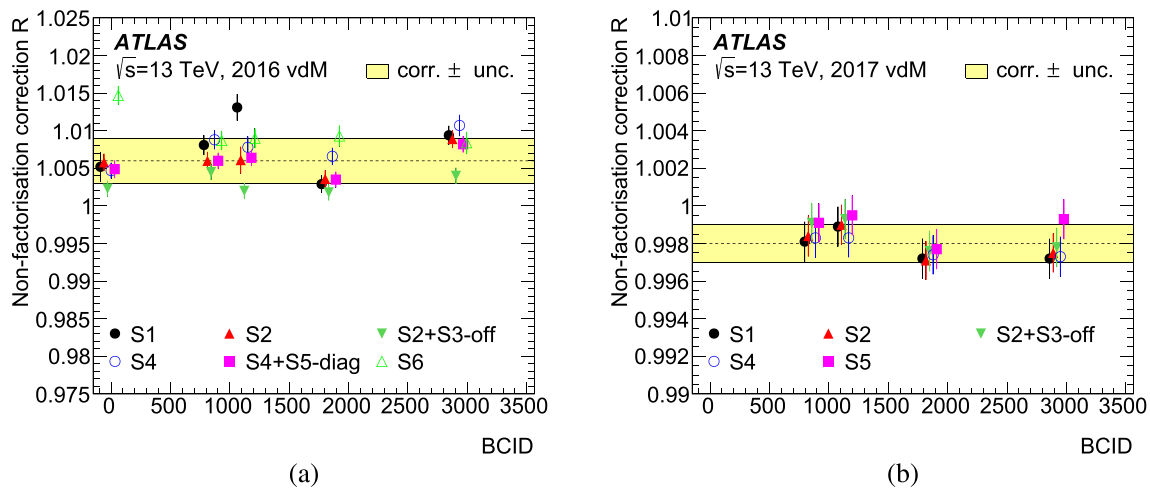


Fig. 2 Non-factorisation correction factors R for several colliding bunch pairs (BCID) and vdM scan sets in the (a) 2016 and (b) 2017 vdM sessions. The results were extracted from combined fits to the vdM luminosity scan curves and reconstructed primary vertex data, using either on-axis scans alone or combined fits to an on-axis scan and an off-axis

or diagonal scan. The uncertainties are statistical. The dashed horizontal lines show the error-weighted mean corrections, and the yellow bands the uncertainties assigned from the RMS of the measured R values. The results from the different scans for each colliding bunch pair are slightly offset on the horizontal axis for clarity

and its impact on the corresponding beam separation, can be calculated analytically from the measured bunch currents and $\Sigma_{x,y}$ values using the Bassetti–Erskine formula for elliptical beams [27]. An example for one colliding bunch pair in the 2017 scan S1X (i.e. the x -scan of S1) is shown in Fig. 3(a). The change of separation is largest for $|\Delta x| \approx 200 \mu\text{m}$, where it amounts to almost $\pm 2 \mu\text{m}$, and decreases to around $\pm 1 \mu\text{m}$ in the tails of the scan. Beam–beam deflections were taken into account on a bunch-by-bunch basis, by correcting the nominal separation at each scan step by the calculated orbit shifts for both beams

$$\Delta x^{\text{corr}} = \Delta x + \delta x_{\text{bb},1}^{\text{IP}} - \delta x_{\text{bb},2}^{\text{IP}}$$

then refitting the vdM-scan curves and updating $\Sigma_{x,y}$. This orbit-shift correction causes a 1.7–2.2% increase in σ_{vis} , depending on the bunch parameters.

In the Run-1 luminosity calibrations [2,3], the defocusing effect was estimated using the MAD-X optics code [28], giving a negative optical-distortion correction of 0.2–0.3% in σ_{vis} , and thereby cancelling out a small fraction of the orbit-shift correction. However, this calculation implicitly neglected the fact that the gradient of the beam–beam force is different for the particles in the core of the bunch than it is for those in the tails. Recent studies [29] using two independent multiparticle simulation codes, B*B [30] and COMBI [31], have shown that the linear-field approximation used by MAD-X is inadequate, and that the actual optical-distortion correction is larger than previously considered.

Starting from the assumption of two initially round Gaussian proton bunches, with equal populations ($n_1 = n_2$) and sizes ($\sigma_{x,1} = \sigma_{x,2} = \sigma_{y,1} = \sigma_{y,2}$), that collide at a sin-

gle interaction point with zero crossing angle and the same β -function ($\beta_x^* = \beta_y^* = \beta^*$), Ref. [29] demonstrates that the optical-distortion correction at each nominal beam separation Δx can be characterised by a reduction in luminosity $L_{\text{no-bb}}/L$ parameterised as a function of Δx , the non-colliding tunes⁸ $Q_{x,y}$ and the round-beam equivalent beam–beam parameter ξ_R :

$$\frac{L_{\text{no-bb}}}{L}(\Delta x) = f(\Delta x, Q_x, Q_y, \xi_R)$$

with

$$\xi_R = \frac{r_p \bar{n} \beta^*}{2\pi \gamma \Sigma_x \Sigma_y}. \tag{10}$$

At each given nominal separation Δx , $L_{\text{no-bb}}$ is the luminosity in the absence of (or equivalently, after correction for) optical-distortion effects, L is the uncorrected (i.e. measured) luminosity, $\bar{n} = (n_1 + n_2)/2$ is the average number of protons per bunch, r_p is the common classical particle radius, and γ is the common Lorentz factor. For the Run 2 $\sqrt{s} = 13 \text{ TeV}$ vdM scans, the parameter ξ_R varies from 3×10^{-3} to 4×10^{-3} . Reference [29] provides a polynomial parameterisation of the correction $L_{\text{no-bb}}/L$ obtained from the full B*B and COMBI simulations, valid for the range of beam parameters typical of LHC vdM scans.

An additional complication arises from the effects of collisions at ‘witness IPs’, i.e. at interaction points other than that of ATLAS. Studies with COMBI simulations [29] showed

⁸ The non-colliding tunes refer to the tunes in the absence of collisions at any of the four LHC IPs.

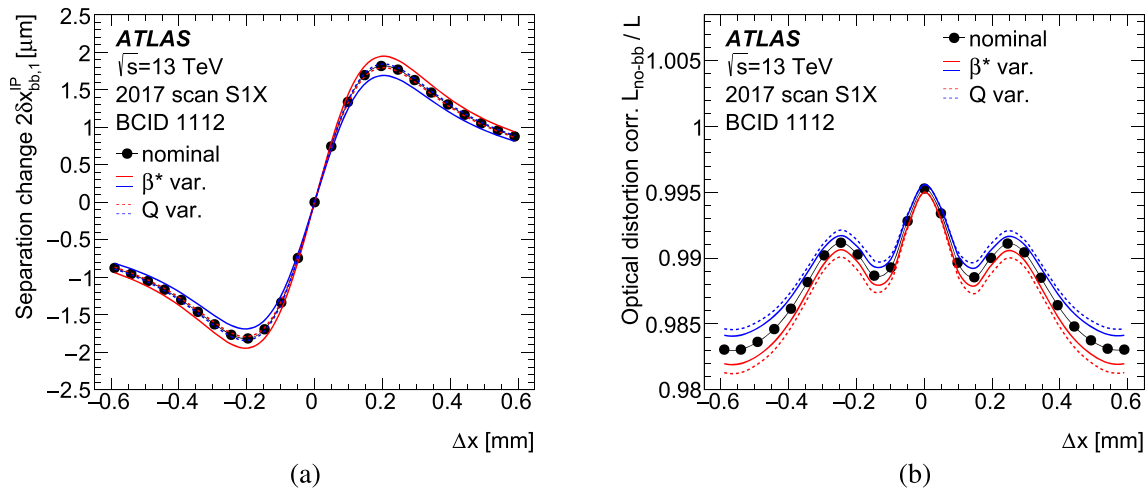


Fig. 3 (a) Calculated change in beam separation due to the beam–beam deflection (orbit shift) and (b) optical-distortion correction, as functions of the nominal beam separation in the horizontal plane, for bunch slot (BCID) 1112 in the horizontal scan 1 of the 2017 vdM session. The

nominal values are shown by the black points and curve. The solid and dashed lines illustrate the impact of varying the β^* values by $\pm 10\%$ or the non-colliding tunes Q by ± 0.002 , in each case for both beams and both planes simultaneously

that the effect on the beam–beam corrections can be adequately modelled by an ad-hoc shift $\Delta Q_{x,y}$ in the non-colliding tune values that are input to the single-IP parameterisation

$$\Delta Q_{x,y} = p_1(n_w) \xi_R$$

that accounts for the average beam–beam tune shift induced by collisions at interaction points other than the one where the scan is taking place. Here, n_w is the number of witness IP collisions for the colliding bunch pair in question, incremented by one half for each additional collision that each separate bunch experiences around the LHC ring, and $p_1(n_w)$ is a first-order polynomial function of n_w . Since all bunches that collide in ATLAS also collide in CMS, $n_w \geq 1$. Depending on the LHC filling pattern, some bunches also experience collisions in either LHCb or ALICE, leading to some bunch pairs with $n_w = 1.5$ or $n_w = 2$, especially in 2018.

The resulting optical-distortion correction for one particular colliding bunch pair in the 2017 scan S1X is shown in Fig. 3(b); the luminosity is reduced by 0.5% at the peak and almost 2% in the tails, depending slightly on the β^* and tune values. This correction was applied to the measured luminosities (and hence $\bar{\mu}_{vis}$ values) at each scan point, reducing σ_{vis} by around 1.5%. The values of the orbit-shift, optical-distortion and total beam–beam corrections, averaged over all colliding bunch pairs, are shown for each scan in each year in Fig. 4. The revised optical-distortion correction cancels out a much larger fraction of the orbit-shift correction than predicted by the original linear treatment.

The systematic uncertainty affecting the magnitude of the beam–beam corrections [29] is dominated by the tunes. An uncertainty of 0.002 is assigned to the non-colliding tunes,

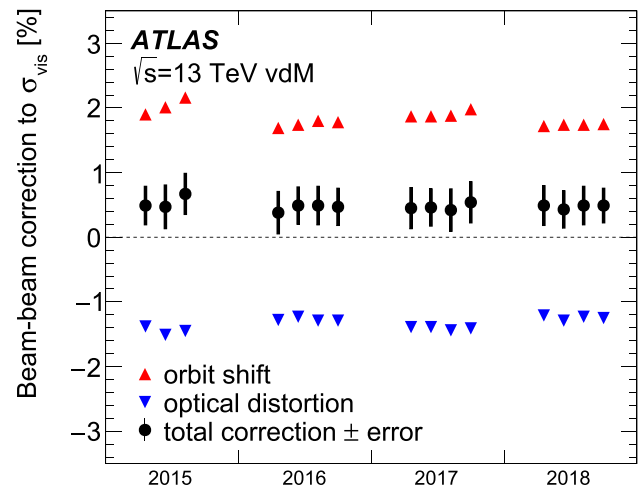


Fig. 4 Bunch-averaged corrections to σ_{vis} due to the orbit shift and optical distortion caused by the mutual electromagnetic interaction of the two beams, calculated for all Run 2 $\sqrt{s} = 13$ TeV on-axis vdM scans, showing the two effects separately, and their total. The error bars show the uncertainties of the total correction

correlated between beams and planes; an additional uncertainty of 0.001 in the mean tunes input to the parameterisation accounts for the approximate modelling of the effect of witness-IP collisions on the unperturbed-tune⁹ spectra. The uncertainty in the actual value of β^* (which is difficult to

⁹ The unperturbed tunes are the values of the horizontal and vertical tunes with the beam–beam interaction ‘switched off’ at the IP where the scans are taking place (whether or not the beams are colliding at other IPs). Physically, these correspond to the mean tune values that would be measured, for the bunch pair under study, before the beams are brought into collision at this IP.

measure precisely) is conservatively taken as 10%, uncorrelated between the two beams but correlated between x and y ; it directly translates into an uncertainty in the value of ξ_R defined in Eq. (10). A number of additional uncertainties, detailed below, arise due to the assumptions made in the evaluation of the combination of the orbit-shift and optical-distortion corrections [29]. An uncertainty of 0.1% results from potential non-Gaussian tails in the initial unperturbed transverse beam profiles. Other effects, such as the departure from round beams (i.e. $\Sigma_x \neq \Sigma_y$), unequal transverse beam sizes, limitations in the parameterisation of optical distortions, uncertainties in the modelling of witness-IP effects, magnetic lattice non-linearity, and the effects of a residual beam crossing angle, each lie below 0.1%. Most of the uncertainties are either correlated or anticorrelated between the orbit-shift and optical-distortion corrections; their effects were therefore evaluated taking this into account. The total beam–beam uncertainty in σ_{vis} in Table 8 is less than 0.3% for all years.

4.8 Emittance growth corrections

The determination of σ_{vis} from Eq. (8) implicitly assumes that the convolved beam sizes $\Sigma_{x,y}$ (and therefore the transverse emittances [5] of the two beams) remain constant both during a single x or y scan and between the peaks of the two scans. The result may be biased if the beam sizes (and hence also the peak interaction rates) change during or between x and y scans.

The evolution of the emittances during the vdM scan sessions was studied by comparing the values of $\Sigma_{x,y}$ obtained from the different on-axis scans in each vdM fill. These studies showed that Σ_x generally increases through the fill at rates of 0.2–0.6 $\mu\text{m}/\text{h}$, whereas Σ_y decreases at around 0.8–1.3 $\mu\text{m}/\text{h}$, due to synchrotron-radiation damping [9]. The peak interaction rates (after correcting for out-of-plane orbit drifts as discussed in Sect. 4.5) also increase with time, consistent with the larger change of emittance in the y plane (as a decrease in emittance should correspond to an increase in peak rate). The effect of emittance growth on the estimate of $\Sigma_{x,y}$ from a single x or y scan was studied by fitting simulated scan curves, described by Gaussian distributions whose widths changed during the scan according to the observed rates. The largest bias was found to be 0.03%, with typical values being an order of magnitude smaller, and this effect was thus neglected.

Much larger potential biases in σ_{vis} arise from the evaluation of the x - and y -related quantities in Eq. (8) at different times. Making the time-dependence explicit, Eq. (8) can be rewritten as

$$\sigma_{vis}(t_x, t_y) = \frac{1}{2} \left(\bar{\mu}_{vis,x}^{\max}(t_x) + \bar{\mu}_{vis,y}^{\max}(t_y) \right) \cdot 2\pi \Sigma_x(t_x) \Sigma_y(t_y)$$

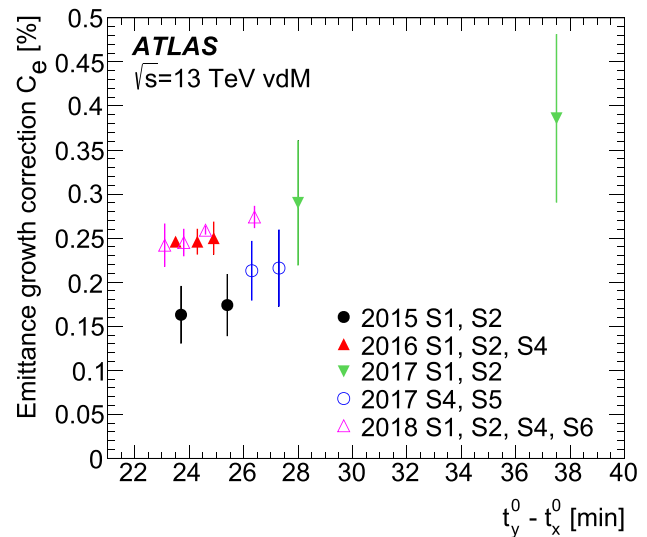


Fig. 5 Emittance growth correction C_e for each vdM scan in fills with more than one scan, shown as a function of the elapsed time between the peaks of the x and y scans. The corrections were evaluated by determining the rate of change of emittances during the sequences of scans given in the legend, dividing the 2017 scans into two groups. The error bars show the total uncertainties, including the statistical uncertainties from the linear fits and the systematic uncertainty due to the mismatch between the $\Sigma_{x,y}$ and peak-rate evolution

where the x -related quantities are evaluated at time t_x and the y -related quantities at time t_y . These quantities can be translated to a common time $t_{mid} = (t_x^0 + t_y^0)/2$ midway between the peaks of the x and y scans at t_x^0 and t_y^0 , using linear fits of the evolution of $\Sigma_{x,y}$ and peak rates with time (this procedure is only possible for fills which have more than one on-axis scan). The emittance growth correction C_e can then be defined as

$$C_e = \frac{\sigma_{vis}(t_{mid}, t_{mid})}{\sigma_{vis}(t_x^0, t_y^0)} - 1$$

correcting the measured visible cross-section for the bias caused by evaluating the x - and y -scan quantities at different times: $\sigma_{vis}^{corr} = (1 + C_e) \sigma_{vis}$. Since the visible cross-section should not depend on the choice of t_{mid} , C_e was also evaluated by evolving all quantities to $t = t_x^0$ or $t = t_y^0$, taking the largest difference as the uncertainty in C_e due to the linear evolution model. This uncertainty also accounts for the small inconsistencies observed between the evolution of the measured $\bar{\mu}_{vis}^{\max}$ and that predicted from the measured evolution of $\Sigma_{x,y}$.

The corrections for each scan recorded in a fill with more than one on-axis scan are shown as a function of the elapsed time between the x and y scan peaks in Fig. 5, together with the systematic uncertainty from the fit model combined with the statistical uncertainties from the linear fits. The corrections increase σ_{vis} , typically by 0.15–0.3%, except for scan

S1 in 2017, where there was a delay between the x and y scans, and hence a larger correction of 0.39%. Although all four 2017 scans were performed in the same fill, there was a 6-h gap between S1+S2 and S4+S5. The two pairs of scans have different emittance growth rates, so they were analysed separately. Scans S4 in 2015 and S6 in 2016 were performed in separate LHC fills (see Table 4) with only a single on-axis scan, so they were assigned the average correction for other scans in that year. In all cases, the corrections were calculated using the bunch-averaged $\Sigma_{x,y}$ and $\bar{\mu}_{\text{vis}}^{\text{max}}$, but a bunch-by-bunch analysis showed very similar results, the emittance growing at similar rates in all bunches. The final uncertainties due to emittance growth corrections shown in Table 8 are smaller than 0.1% for all years.

4.9 Length scale determination

The $\Sigma_{x,y}$ measurements require knowledge of the length scale, i.e. the actual beam displacements (and hence beam separation) produced by the settings of the LHC steering magnets intended to produce a given nominal displacement. This was determined using length scale calibration (LSC) scans, separately for each beam and plane (x and y). In each scan, the target beam being calibrated was moved successively to five equally spaced positions within $\pm 3\sigma_{\text{nom}}^{\text{b}}$, and its position measured using the luminous centroid (or beamspot) position fitted from primary collision vertices reconstructed in the ATLAS inner detector when the two beams were in head-on collision. Since the alignment of the inner detector is very well understood [32], the beamspot gives a measurement of the beam displacement that is accurate at the 0.1% level over the scanning range. In practice, the requirement for the two beams to be in head-on collision was satisfied by performing a three-point miniscan of the non-target beam around the target beam nominal position at each step, fitting the resulting curve of luminosity vs. beamspot position, and interpolating the beamspot position to that of maximum luminosity and beam overlap. As shown in Fig. 6(a), the slope of a linear fit of the beamspot position vs. the nominal position gives the linear length scale M_1 , i.e. the ratio of actual to nominal beam movement for each beam and plane (the offset of this fit depends on the relation between the LHC beam and ATLAS coordinate systems). Orbit drifts can influence the measured values of M_1 , and were corrected using arc BPM data, interpolating the difference in beam positions measured directly before and after each scan linearly in time through the scan, in a procedure similar to that described for the vdM scans in Sect. 4.5.

The four length scales for B1X (i.e. beam 1 in the x -direction), B1Y, B2X and B2Y were measured in turn in the LSC scans for each year, which were always performed with the same machine optics as, and close in time to, the vdM scans. The resulting values of M_1 for all four quanti-

ties are shown in Fig. 6(b), and are always within $\pm 0.4\%$ of unity. However, apart from B1Y, the length scales differ significantly between years, despite the same nominal machine configuration being used. In 2015–2017, all four scans were performed from negative to positive displacement, meaning that beam 1 moved in the same direction as in the vdM scans, but beam 2 moved in the opposite direction. In 2018, the beam-2 LSC scans were performed from positive to negative displacement, so both beams were calibrated by moving them in the same direction as in the vdM scans.

The measured $\Sigma_{x,y}$ values from Eq. (6) must be corrected by the average of the beam-1 and beam-2 length scales M_1 in each plane, leading to a correction L_{xy} to the visible cross-section $\sigma_{\text{vis}}^{\text{corr}} = L_{xy}\sigma_{\text{vis}}$, where the length scale product L_{xy} is given by

$$L_{xy} = (M_1^{x,1} + M_1^{x,2})(M_1^{y,1} + M_1^{y,2})/4$$

and $M_1^{x|y,i}$ is the measured linear length scale for the x or y plane and beam i . The statistical uncertainty from the beamspot position measurements is shown as the ‘Length scale calibration’ uncertainty in Table 8, and is below 0.1%. A further uncertainty of 0.12% arises from uncertainties in the absolute length scale of the inner detector, determined from simulation studies of various realistic misalignment scenarios as described in Ref. [2]. The studies were updated to use scenarios appropriate to the Run 2 detector, including the impact of the precise measurements from the innermost pixel layer, the IBL.

4.10 Magnetic non-linearity

The fit residuals shown in the lower panel of Fig. 6(a) suggest that, in this particular scan, the actual beam movement is not perfectly linear with respect to the nominal position, at the level of $1\ \mu\text{m}$ in $\pm 300\ \mu\text{m}$ of displacement. The residuals from some of the other $\sqrt{s} = 13\ \text{TeV}$ LSC scans show similar hints of systematic non-linear behaviour; some are more scattered, and some appear consistent with a purely linear dependence. The $\sqrt{s} = 8\ \text{TeV}$ LSC data from 2012 are also suggestive of non-linear behaviour [3]. More recent data are available to study these effects further. For five days in October 2018, the LHC delivered pp collisions at $\sqrt{s} = 900\ \text{GeV}$ in support of the forward-physics programme. As part of this run, a vdM scan session, including a length scale calibration, took place with $\beta^* = 11\ \text{m}$, a configuration in which the transverse beam sizes (and hence scan ranges) are around three times larger than in the vdM optics used at $\sqrt{s} = 13\ \text{TeV}$. As well as the length scale calibration, a total of seven x - y vdM scans were performed over four fills spanning a three-week period, as shown in the top part of Table 5. The residuals from the length scale calibration are shown in Fig. 7, and show a clear deviation from linear-

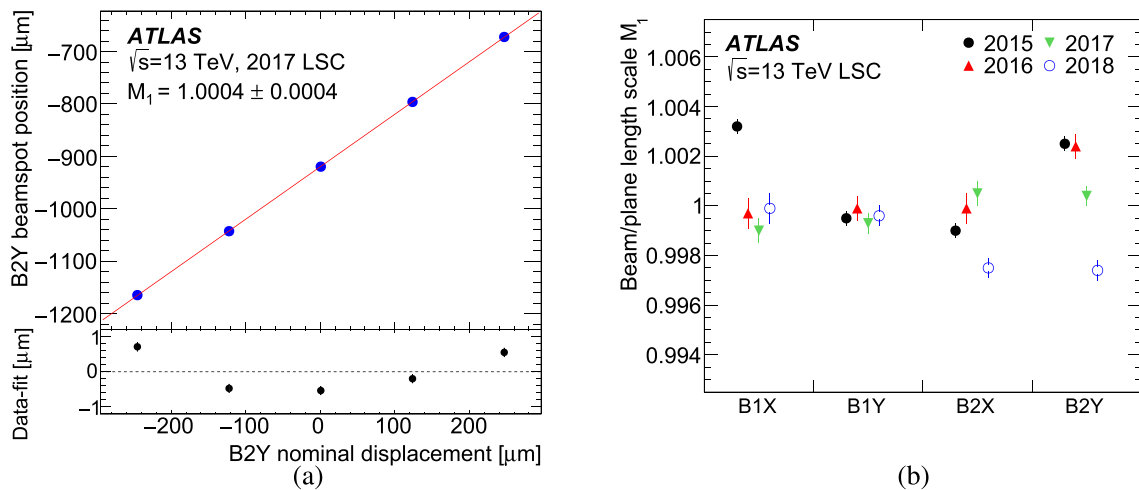


Fig. 6 (a) Length scale calibration for the y direction of beam 2 in the 2017 measurement, showing the beamspot position vs. the nominal displacement of the target beam, together with a linear fit giving the slope parameter M_1 . The lower plot shows the fit residuals, with the error

bars indicating the statistical uncertainties of the beamspot positions. These residuals are discussed further in Sect. 4.10. (b) Measurements of the linear length scale M_1 for each beam and plane measured in the calibration for each year of data-taking

ity, of up to $\pm 3 \mu\text{m}$ over a $\pm 900 \mu\text{m}$ scan range. The shape of the residual curve is approximately inverted for beam 2 compared to beam 1 in both planes. As the two beams were moved in opposite directions during the LSC, this suggests the non-linearity may come from hysteresis effects in the steering corrector magnets.

The beamspot positions measured during the $\sqrt{s} = 900 \text{ GeV}$ LSC scans provide unambiguous evidence of non-linearity, but have limited granularity (only five points per scan) and do not address reproducibility, as only one scan was performed per beam/plane. The multiple vdM scans per session have 25 points per scan and so can potentially address these issues, but since the beams move in opposite directions, the beamspot position remains approximately stationary, only moving slightly if the two beams are of unequal sizes. The DOROS BPMs measure the displacements of each beam separately during vdM scans, and can be used to study magnetic non-linearity effects. However, they suffer from short-term variations in their calibration, and must also be corrected for the effects of beam–beam deflections.

The differences between the beam position at the interaction point determined from the uncalibrated DOROS BPM measurements, and the nominal beam-1 displacements, are shown during the $\sqrt{s} = 900 \text{ GeV}$ x scans from 2018 in Fig. 8(a). The residuals are shown after subtracting an offset from the BPM such that the residual with the beam at the nominal head-on position, immediately before the start of each scan, is zero. A significant slope is visible, indicating a miscalibration of the length scale of the BPM. The residuals are slightly negative at the nominal central point of the scan, suggesting magnetic hysteresis. The curves also have

an ‘S’ shape, due to the beam–beam deflection already discussed in Sect. 4.7. As well as the true beam displacement at the interaction point, the DOROS BPMs also measure an additional apparent displacement from half the angular kick $\theta_{x,i}$ projected over the distance $L_{\text{doros}} = 21.7 \text{ m}$ between the IP and the BPM.¹⁰ With $\theta_{x,i}$ given by Eq. (9), the apparent displacement $\delta x_{\text{bb},i}^{\text{doros}}$ of beam i at the IP as measured by the DOROS BPMs is

$$\begin{aligned} \delta x_{\text{bb},1}^{\text{doros}} &= \theta_{x,1} \left(\frac{\beta^*}{2 \tan(\pi Q_x)} + \frac{L_{\text{doros}}}{2} \right); \\ \delta x_{\text{bb},2}^{\text{doros}} &= -\delta x_{\text{bb},1}^{\text{doros}}. \end{aligned} \tag{11}$$

The expected apparent horizontal beam–beam displacements for beam 1 in these scans, calculated using the measured $\Sigma_{x,y}$ and beam currents, are shown in Fig. 8(b) and reach $\pm 15 \mu\text{m}$ at $\pm 250 \mu\text{m}$ single-beam displacement (corresponding to a separation $\Delta x = 500 \mu\text{m}$). The displacements for the off-axis scans S2 and S7 are smaller, and were calculated using a generalisation of Eq. (9) that also takes into account the constant beam separation in the non-scanning plane.

The miscalibration and offset of the DOROS BPM measurement visible in Fig. 8(a) can be corrected by replacing the initial DOROS estimate of the beam position at the IP $x_{D,i}$ by $D_{x,i}^{\text{cal}} x_{D,i} - D_{x,i}^{\text{ofs}}$, where $D_{x,i}^{\text{cal}} \approx 1$ is the DOROS length scale and $D_{x,i}^{\text{ofs}}$ the offset at the central scan point. Using the calibrated DOROS measurement, together with the nominal beam displacement $x_{\text{nom},i}$ scaled by its length scale $M_{1,i}$ and the estimate of the apparent beam–beam deflection $\delta x_{\text{bb},i}^{\text{doros}}$

¹⁰ The factor of one-half arises because in the new closed orbit, both the incoming and outgoing beams are deviated from their initial trajectories by $\theta_{x,1}/2$, giving a total angular deflection of $\theta_{x,1}$ at the IP.

Table 5 Summary of the $\sqrt{s} = 900$ GeV vdM scan fills used in the study of magnetic non-linearity, showing the dates, LHC fill numbers, total numbers of bunches in each beam (n_{tot}) and colliding in ATLAS (n_b), and the individual scans performed in each fill. In the first group of scans performed in 2018, each scan consisted of an x - y vdM scan pair

Date	Fill	n_{tot}	n_b	Scans
14/10/2018	7299	152	150	S1, S2-off, S3
14/10/2018	7300	152	150	LSC, S4
5/11/2018	7406	152	150	S5
5/11/2018	7407	152	150	S6, S7-off
28/10/2021	7516	4	2	S1xsep, S2xpar, S3ypar, S4ysep, S5ypar, S6xB1, S7xB2, S8ypar
30/10/2021	7524	3	0	S1xpar, S2xpar, S3xsep, S4xpar, S5ypar, S6ypar, S7ysep, S8ypar
30/10/2021	7525	3	3	S1xpar, S2xsep, S3ypar, S4ysep, S5yB1, S6yb2, S6xB1, S7xB2

(S1, S3 etc.), an off-axis scan (S2-off) or a length scale calibration scan (LSC). The second group of scans was performed during the LHC beam test in October 2021, and individual x or y scans are listed separately, as parallel (par), separation (sep) or single-beam (B1 or B2) scans

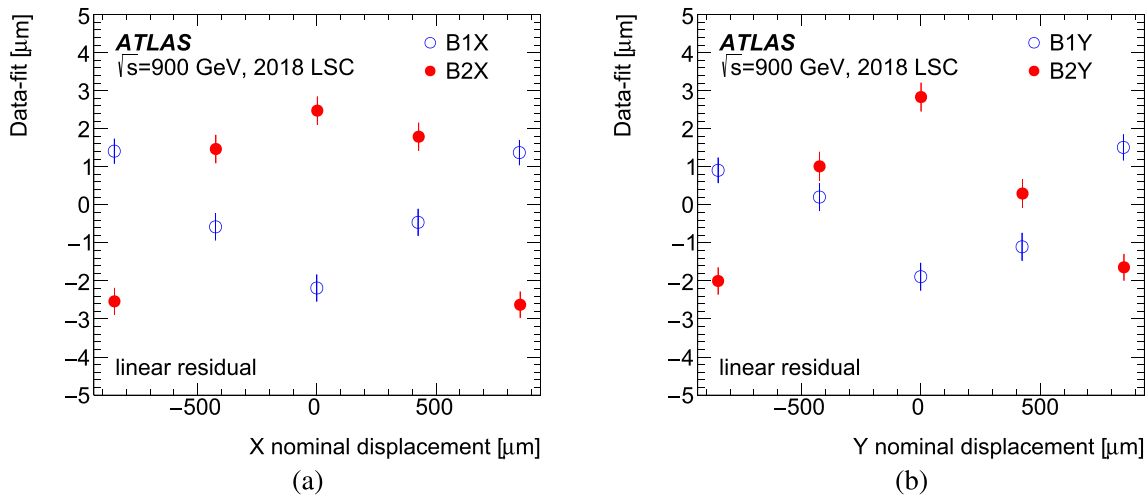


Fig. 7 Residuals of the beamspot position with respect to a linear fit of the beamspot position vs. nominal displacement of the target beam in the length scale calibration of the 2018 $\sqrt{s} = 900$ GeV vdM session, for

(a) the x and (b) the y plane, for beam 1 (blue open points) and beam 2 (red filled points). The error bars show the statistical uncertainties from the beamspot position measurements

from Eq. (11) scaled by a parameter α , the residual between the calibrated DOROS measurement and the nominal beam displacement for beam i at a particular scan point is given by

$$\Delta x_i^{\text{doros}} = D_{x,i}^{\text{cal}} x_{D,i} - D_{x,i}^{\text{ofs}} - M_{1,i} x_{\text{nom},i} - \alpha \delta x_{\text{bb},i}^{\text{doros}}. \quad (12)$$

These residuals were used to define a χ^2 summed over all the scan points in a single scan or set of scans for one beam and plane:

$$\chi_{\text{doros}}^2 = \sum \left(\frac{\Delta x_i^{\text{doros}}}{s_{\text{doros}} \sigma_{\text{doros}}} \right)^2 \quad (13)$$

where the statistical uncertainties in the DOROS BPM measurements σ_{doros} were determined from the spread of individual measurements over the duration of one LB, and s_{doros} is a scale factor with nominal value $s_{\text{doros}} = 1$. The χ^2 was minimised, allowing the values of $D_{x,i}^{\text{cal}}$, $D_{x,i}^{\text{ofs}}$ and α to be determined. The length scale M_1 cannot be determined from this

fit (as it is almost degenerate with $D_{x,i}^{\text{cal}}$), but was determined within the same framework by using the residuals between the beamspot and nominal beam positions in the LSC scan to define an additional χ^2 term constraining M_1 :

$$\chi_{\text{lsc}}^2 = \sum \left(\frac{x_{\text{bs}} - M_{1,i} x_{\text{nom},i}}{\sigma_{x,\text{bs}}} \right)^2 \quad (14)$$

where x_{bs} is the beamspot position measurement at maximum beam overlap derived from each LSC miniscan and $\sigma_{x,\text{bs}}$ its uncertainty, and the sum is taken over the five LSC scan points.¹¹ A combined fit to all seven vdM scans and the LSC was performed separately for each beam and plane to determine $D_{x,i}^{\text{cal}}$, $D_{x,i}^{\text{ofs}}$, M_1 and α . Separate values of $D_{x,i}^{\text{cal}}$ and $D_{x,i}^{\text{ofs}}$ were fitted in each scan, and these were found to dif-

¹¹ This χ^2 minimisation to determine M_1 is equivalent to the linear fit shown in Fig. 6(a).

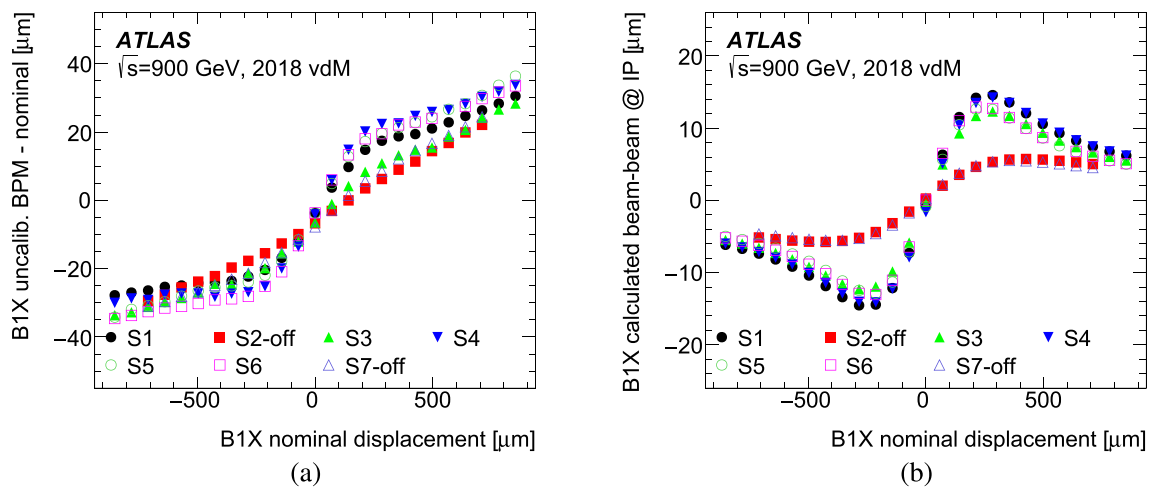


Fig. 8 Details of the analysis of beam-1 DOROS BPM residuals in the x scans of the 2018 $\sqrt{s} = 900$ GeV vdM scan session: (a) residuals between the uncalibrated BPM measurements and the nominal beam

displacement as a function of the nominal displacement; (b) apparent beam–beam-induced displacement at the IP as seen by the DOROS BPMs, calculated using the measured beam parameters

fer scan-to-scan with RMS values of 0.3–0.4% (the DOROS BPM responses are not expected to be stable in time, due to temperature variations in their electronics). For each beam and plane, a common α value was fitted for all scans, and these values differed from unity by up to 17%.

The resulting DOROS residuals from Eq. (12) are shown for each beam and plane in Fig. 9, together with the beamspot residuals from the LSC scan that were also shown in Fig. 7. In both x and y planes for beam 2, the residuals from all scans are similar, and close to those from the LSC scan, suggesting a non-linearity that is largely reproducible between scans, and present whether the beam displacements are measured with DOROS BPM or beamspot data. The situation for beam 1 appears more complex: the DOROS residuals broadly follow the beamspot data, but several scans exhibit residual S-shaped wiggles even after subtracting the scaled beam–beam displacement, suggesting that the magnitude of the apparent beam–beam displacement has been overestimated or underestimated. Allowing the value of α to be different for each scan (as well as for each plane) significantly improved the fits, giving residuals for beam 1 that resemble the beam-2 curves, although inverted due to the opposite scan direction. However, the fitted α values scatter between 0.5 and 1.2, typically being smaller for beam 1 than for beam 2. This large range of fitted α values suggests that although the separation-dependence of the beam–beam displacement seen by the DOROS BPMs is well predicted by Eqs. (9) and (11), its magnitude is not.

The non-linearity between the nominal and actual beam displacements $x_{\text{nom},i}$ and $x_{\text{disp},i}$ was parameterised as

$$x_{\text{disp},i} = M_{1,i}x_{\text{nom},i} + M_{2,i}r_i^2 + M_{3,i}r_i^3 \tag{15}$$

where $M_{1,i}$ is the linear length scale, and $M_{2,i}$ and $M_{3,i}$ are the coefficients of quadratic and cubic terms in the reduced beam separation $r = x_{\text{nom},i}/x_{\text{max}}$, where $x_{\text{max}} = 850 \mu\text{m}$ is the maximum beam displacement in a $\sqrt{s} = 900$ GeV scan. The corresponding non-linear terms were added to Eqs. (12) and (14), and the fits repeated, also allowing α to be different in each scan. The resulting residuals are typically smaller than $0.5 \mu\text{m}$ and without significant structure, demonstrating that the non-linearity seen in both DOROS BPM and beamspot measurements can be reasonably well parameterised by Eq. (15). The fitted values of M_1 , M_2 and M_3 for both beams and planes are shown in Table 6, together with the M_1 values from linear fits to the LSC scan only, analogous to that shown in Fig. 6. The significant quadratic terms of $|M_2| \approx 4 \mu\text{m}$, with opposite signs for the two beams, account for the symmetric distortions seen in Fig. 9. The cubic M_3 terms account for any distortions that are asymmetric between positive and negative beam displacements, and their fitted values are all smaller than $1 \mu\text{m}$ and consistent with zero. However, the M_3 and M_1 terms are anticorrelated, and the M_1 values also change slightly between the linear and non-linear fits.

The effect of the non-linear terms on the length scale product was estimated by modelling the scan curves as single Gaussian functions with RMS equal to the $\Sigma_{x,y}$ averaged over all scans, and calculating the change in the integrals of Eq. (6) from the distortions in Δx and Δy when using the non-linear instead of the linear length scale. For the 2018 $\sqrt{s} = 900$ GeV scans L_{xy} changes from 1.0071 ± 0.0003 to 1.0075 ± 0.0004 , a change of only 0.04%. Although the M_2 terms are large, they have no effect on L_{xy} , because e.g. a decrease of the integral for $\Delta x < 0$ is compensated by an

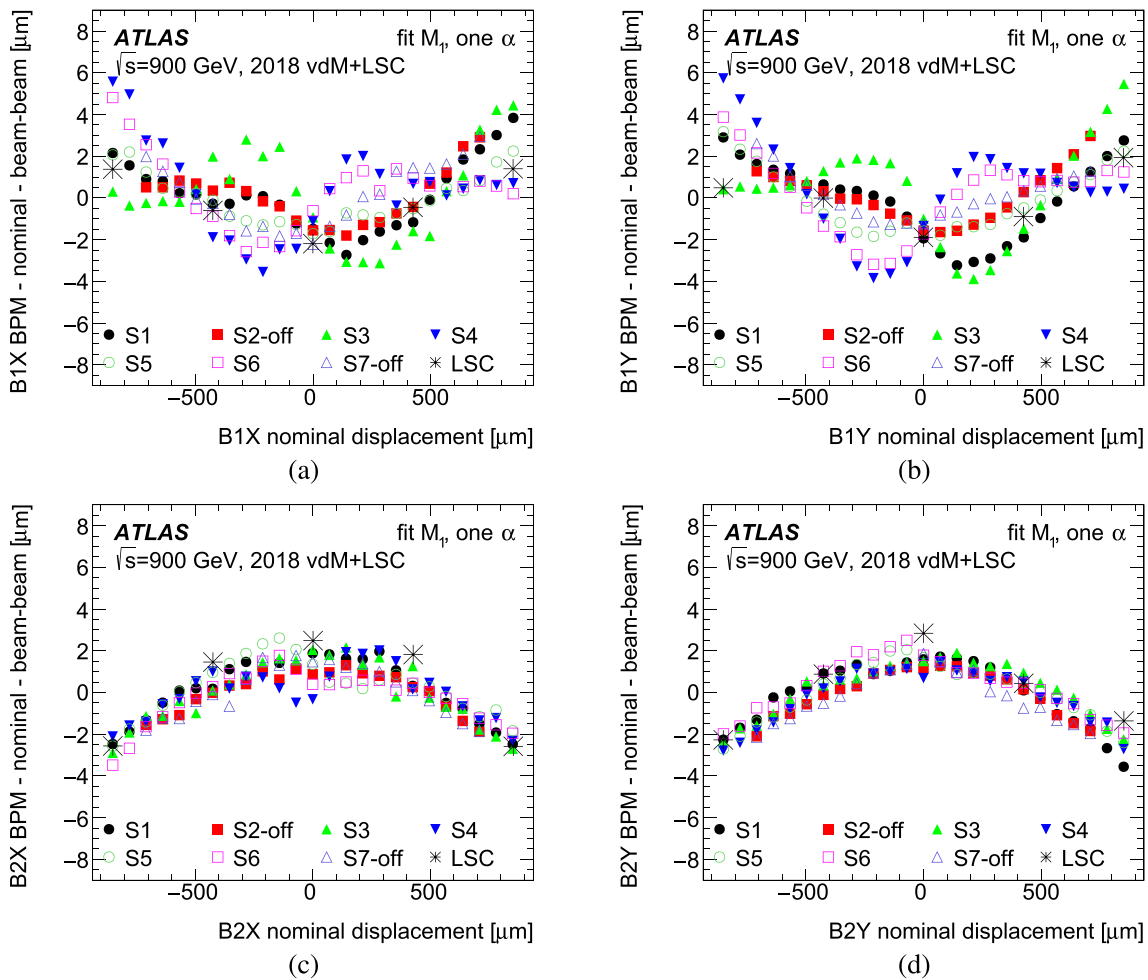


Fig. 9 Residuals between the beam displacement at the interaction point inferred from the calibrated DOROS BPM measurement corrected for the beam–beam-induced displacement, and the nominal beam displacement, during vdM scans at $\sqrt{s} = 900$ GeV in 2018, using a fit with a linear magnetic model and a single beam–beam deflection scaling parameter α per beam and plane. The four plots show (a) B1X, (b)

B1Y, (c) B2X and (d) B2Y. The residuals for the seven scans are shown separately by the different coloured markers. The black stars show the differences between the beamspot position and the nominal beam displacement measured in the length scale calibration scan and plotted on the same axes

equal increase for $\Delta x > 0$, and only the small changes in M_1 and M_3 have any effect.

Since the non-linear effects seen in the $\sqrt{s} = 900$ GeV scans were unexpected, two additional studies were made to probe the interpretation in terms of non-linearity of the steering magnets. Firstly, the magnetic fields produced by two spare LHC corrector dipoles were precisely measured on a test bench, with both standard magnetic cycles covering the full operating range, and test cycles replaying the powering history during vdM scans at $\sqrt{s} = 13$ TeV from fill 6016 in 2017 [33]. These studies showed that, in the laboratory environment, the magnetic fields are highly reproducible (to better than 10^{-4}), but that there is a significant hysteresis effect depending on whether the magnet current is being

increased or decreased (and hence on the direction of beam movement in a vdM scan).

Secondly, a series of test scans were performed at $\sqrt{s} = 900$ GeV during the October 2021 LHC pilot run, as shown in the lower part of Table 5. The DOROS BPM data were analysed in the same way as for the 2018 $\sqrt{s} = 900$ GeV scans, but keeping $M_1 = 1$ and $M_{2,3} = 0$, and without additional constraints from beamspot data. Figure 10(a, b) show the residuals from the two beams in a series of y-plane scans in fill 7524. In this fill, the three bunches in each beam were positioned around the LHC ring such that none collided in ATLAS, eliminating beam–beam deflections. Two consecutive parallel scans were performed, in which both beams were moved from negative to positive displacement. These were followed by a separation scan in which beam 2

Table 6 Fitted values of the length scale M_1 from a linear fit to the LSC scan data only (left column) and the parameters M_1 , M_2 and M_3 from the non-linear fit to vdM and LSC scan data (right columns), for each beam and plane in the 2018 $\sqrt{s} = 900$ GeV vdM scan session

	M_1 (linear LSC)	M_1	M_2 [μm]	M_3 [μm]
B1X	1.0044 ± 0.0003	1.0046 ± 0.0006	3.7 ± 0.2	-0.2 ± 0.5
B1Y	1.0064 ± 0.0003	1.0067 ± 0.0003	4.5 ± 0.1	-0.3 ± 0.2
B2X	1.0022 ± 0.0003	1.0024 ± 0.0006	-4.2 ± 0.2	-0.1 ± 0.5
B2Y	1.0012 ± 0.0003	1.0014 ± 0.0003	-4.2 ± 0.2	-0.2 ± 0.2

was moved in the opposite direction (positive to negative) to beam 1, as in a vdM scan, and then a further parallel scan. The offsets between the DOROS BPM and nominal displacements were determined separately for each scan, so that they are zero at the nominal zero displacement just before each scan started. These residuals are not affected by beam–beam displacements, and clearly show that the non-linearity at $\sqrt{s} = 900$ GeV is highly reproducible from scan to scan, with the opposite sign for beam 2 in the separation scan where it moves in the opposite direction.

Figure 10(c, d) show results from fill 7525, where all three bunches were colliding in ATLAS, and parallel and separation scans were followed by scans where only one beam was moved and the other remained stationary (and is hence not plotted). The beam–beam displacement was calculated using the Σ_y value obtained from the separation scan S4ysep, and subtracted from the residuals after being scaled by a fitted parameter α , the same for all scans but different for the two beams. The fitted values of α are within 10% of unity, validating the modelling of the beam–beam displacement as seen by the DOROS BPMs for the case where all bunches are colliding in ATLAS. The residuals are again similar for all three scans for beam 1, and for the separation and single-beam scans in beam 2 where it moves in the same direction.

Figure 10(e, f) show results from fill 7516, with four bunches in each beam, and only two colliding in ATLAS. This was fitted in the same way as for fill 7525, but the fitted α values are much smaller, 0.07 for beam 1 and 0.15 for beam 2. After subtracting this scaled beam–beam displacement, the residuals are again very reproducible between scans and similar to those in the other fills. In such a fill, the DOROS BPMs see a mixture of colliding bunches that are deviated by the beam–beam interaction, and non-colliding bunches that are not deviated. The response of the DOROS electronics is known to depend both on the time structure of the bunch pattern, and the relative intensity of the bunches, and in this case the sensitivity to the beam–beam displacement is reduced by much more than the $\alpha = 0.5$ which would be expected from the fraction of bunches that were colliding.

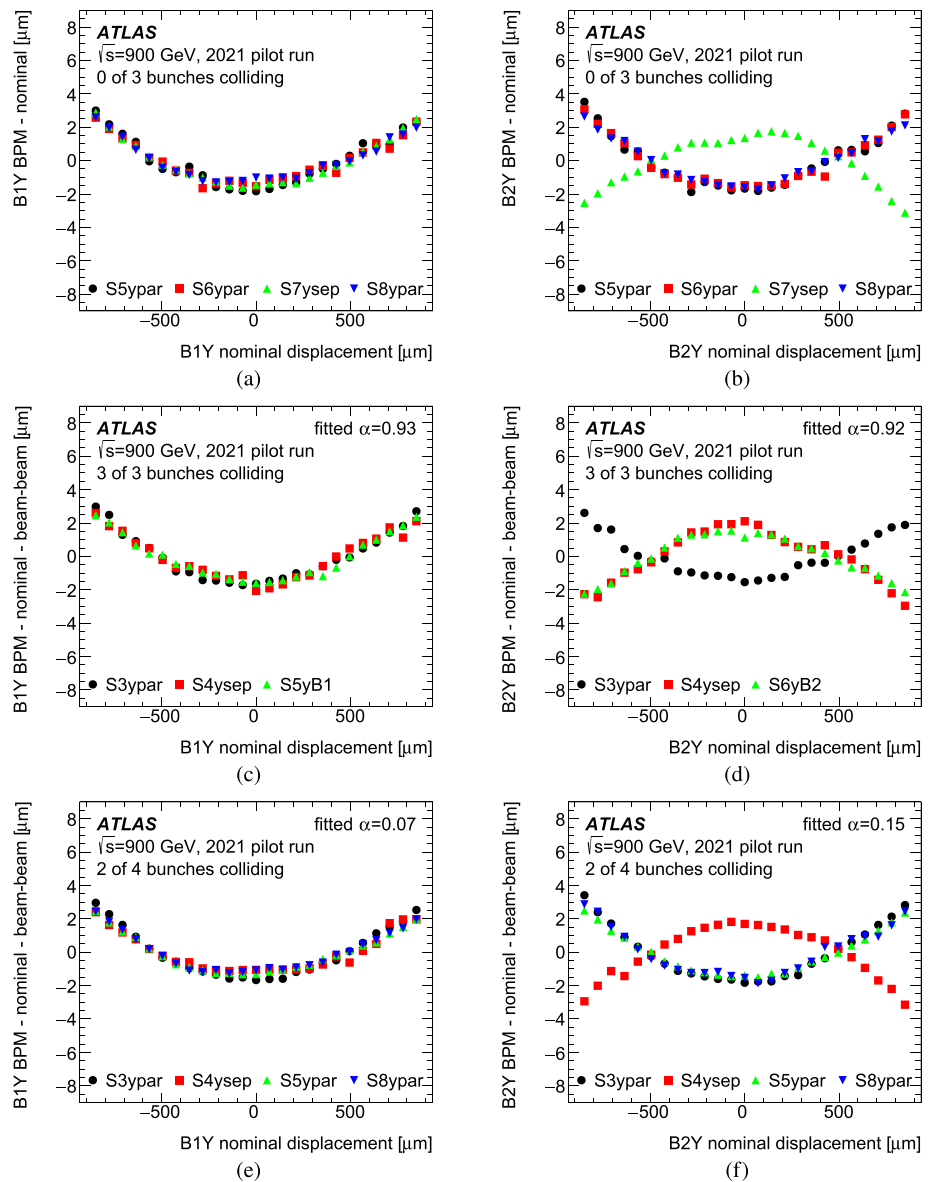
Qualitatively similar results were obtained in the x -plane, though with a larger scatter of residuals. These studies confirm that the non-linearity in the beam displacements appears to originate from hysteresis in the LHC steering magnets, and

is highly reproducible from scan to scan. The effect of beam–beam deflections can be modelled by Eqs. (9) and (11), after empirical scaling by the factor α which must be determined from data.

To estimate the potential effect of magnetic non-linearity on the length scale at $\sqrt{s} = 13$ TeV, the data from each year’s vdM and LSC scans were fitted in the same way as at $\sqrt{s} = 900$ GeV, fitting $M_{1,2,3}$ and α for each beam and plane separately in each year. However, due to the smaller beam displacements compared to the BPM and beamspot resolution, the results were less conclusive. The residual distributions for some scan sessions showed shapes reminiscent of the non-linearities seen at $\sqrt{s} = 900$ GeV, and which could be eliminated by adding M_2 and M_3 terms to the basic linear length scale. Others, particularly 2016, showed no significant non-linearity, and some scans in 2015 showed evidence of higher-order structure. In most datasets, the fitted values of α are close to the naive expectation of $\alpha \approx n_b/n_{\text{tot}}$, assuming the DOROS position readings correspond to an unweighted average over all bunches. The resulting values of M_2 and M_3 for each beam, plane and year are shown in Fig. 11. Significant M_2 and M_3 terms were fitted for many of the datasets, but with magnitudes that typically do not exceed $1 \mu\text{m}$. For a given beam and plane, the results for different years are often very different, for both M_2 and M_3 . This may reflect the fact that the LHC orbit was set up independently in each year, leading to potentially different corrector magnet currents and hence hysteresis effects for the same scan patterns in different years.

The baseline fit was performed with a common value of α for all scans for each individual beam and plane, and with the factor s_{doros} of Eq. (13) set to $s_{\text{doros}} = 2$, rather than $s_{\text{doros}} = 1$ as used at $\sqrt{s} = 900$ GeV. This was required to get χ_{doros}^2 values close to one per degree of freedom, suggesting that the DOROS BPM errors estimated from the spread within each luminosity block do not fully capture the measurement uncertainties. Alternative fits with $s_{\text{doros}} = 1$, or allowing α to vary per scan, were also considered. Since in the LSC scans of 2015–2017, beam 2 was moved in the opposite direction to that in the vdM scans, the baseline fits were performed with the signs of M_2 and M_3 reversed in the LSC compared to the vdM scans, reflecting the scan direction dependence

Fig. 10 Residuals between the beam displacement at the interaction point inferred from the calibrated DOROS BPM measurement and the nominal beam displacement, during scans at $\sqrt{s} = 900$ GeV in the October 2021 LHC pilot run. The left column shows B1Y and the right column B2Y; the results in the x -plane are similar. The three rows show (a, b) a fill with no bunches colliding at the ATLAS IP, (c, d) all three bunches colliding at ATLAS, and (e, f) a ‘mixed’ configuration with two out of four bunches colliding at ATLAS. The beam–beam displacement was subtracted in plots (c–f), scaled by the parameter α whose fitted values are given in the legends



suggested by Figs. 7, 9 and 10. An alternative fit without these sign reversals was also considered in these cases.

Given the lack of conclusive evidence for magnetic non-linearity at $\sqrt{s} = 13$ TeV, the baseline L_{xy} values were taken from the linear fits described in Sect. 4.9, and the largest deviations from any of the non-linear fits were considered to define a (symmetric) systematic uncertainty added in quadrature to the statistical uncertainty from the linear fits. This procedure assumes that any significant non-linearity can be adequately described by a cubic parameterisation determined from the combined fit to vdM and LSC scans, but does not attempt to correct it. The resulting L_{xy} values are shown in the rightmost panel of Fig. 11, together with the L_{xy} values from the baseline non-linear fits. The magnetic non-linearity uncertainty varies from 0.1% in 2016 to 0.6% in 2018, reflecting the fitted values of M_3 shown in Fig. 11.

4.11 Consistency checks

Since the value of σ_{vis} for a given luminosity algorithm should not depend on beam parameters, the ability to determine it separately from each colliding bunch pair and x - y scan set allows the stability and reproducibility of the calibrations to be checked. Figure 12 shows the σ_{vis} values measured for each bunch pair and scan in each vdM scan session. The values are shown after all corrections have been applied, normalised to the error-weighted mean over all bunch pairs and scans in each year. Within one scan, the spread of σ_{vis} values over all bunch pairs (after subtracting in quadrature the expected spread given the average statistical error of the individual measurements) is a measure of potential systematic bunch-to-bunch inconsistencies in the absolute luminosity scale. The largest such value for each year was taken as the ‘Bunch-by-bunch σ_{vis} consistency’ uncertainty in Table 8.

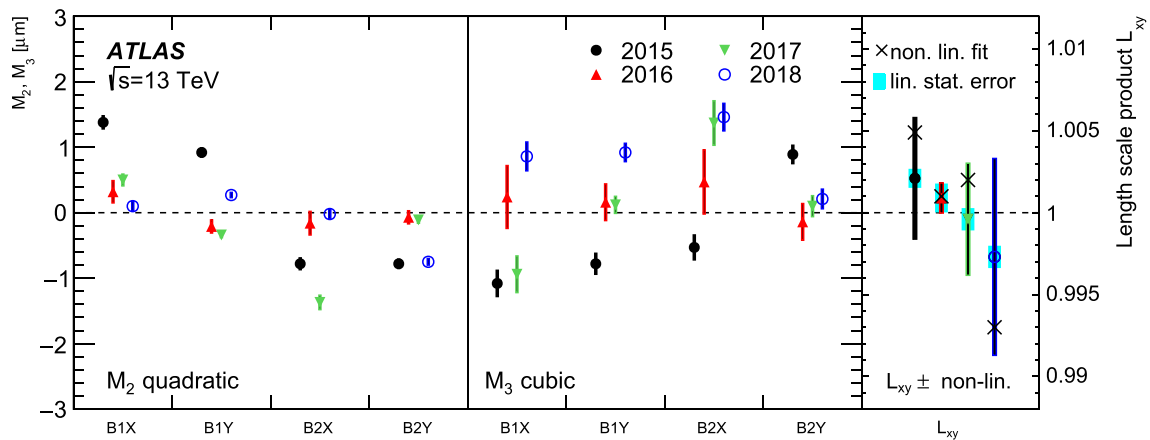


Fig. 11 Summary of the non-linear length scale determination for the $\sqrt{s} = 13$ TeV vdM+LSC datasets. The left and middle panels show the quadratic M_2 and cubic M_3 terms fitted for each beam and plane from the combined vdM and LSC data for each data-taking year, with error bars indicating the statistical uncertainties. The right panel shows the

linear length scale product L_{xy} for each year, together with its statistical error (cyan band), the central value of the baseline non-linear fit incorporating the M_2 and M_3 terms (black cross), and the total uncertainty in L_{xy} encompassing the central values of the baseline and alternative non-linear fits (see text)

These uncertainties are at most 0.4% (in 2015), and zero in 2018, where the spread was consistent with the expected bunch-to-bunch statistical fluctuations, which are larger than in other years due to the use of a single LUCID PMT as reference algorithm.

The differences in bunch-averaged σ_{vis} between scans give an indication of the reproducibility of the calibration on a timescale of hours, or longer in 2015 and 2016 where the scans were distributed over several LHC fills (Table 4). The sampling-corrected standard deviation of these values was used to define the ‘Scan-to-scan reproducibility’ uncertainty in Table 8, which is 0.3% or less in all years except in 2017, where significant inconsistencies between scans are apparent, reflected in the larger uncertainty of 0.7% that dominates the vdM calibration uncertainty for that dataset. The average of the σ_{vis} values from all scans in one year was finally used as the central value of the calibration result for that year.

In each year, the vdM calibration procedure was used to determine σ_{vis} for all available LUCID and BCM algorithms. Since the acceptance of each algorithm is different, the σ_{vis} values are also different, but all algorithms should agree on the values of $\Sigma_{x,y}$ and hence on the specific luminosity \mathcal{L}_{spec} for each colliding bunch pair, given by

$$\mathcal{L}_{spec} = \frac{\mathcal{L}_b}{n_1 n_2} = \frac{f_r}{2\pi \Sigma_x \Sigma_y}$$

and obtained from the vdM scan curves using the luminosity measurements of each individual algorithm. The consistency of the different algorithms was quantified by calculating the per-bunch-pair and per-scan relative deviation of \mathcal{L}_{spec} for each algorithm compared to the average over all algorithms, and then averaging this deviation over all bunch pairs and scans in each year. Systematic deviations from this aver-

age are sensitive to problems with individual algorithms that may bias $\Sigma_{x,y}$, such as detector non-linearity, short-term efficiency drifts or background subtraction issues. The resulting relative deviations of \mathcal{L}_{spec} for all considered LUCID and BCM algorithms in each year are shown in Fig. 13, with the reference algorithm shown in red. The set of available algorithms evolved during Run 2, as the LUCID configuration changed and progressively more PMTs were equipped with bismuth calibration sources. The BCM algorithms were not considered for the 2018 analysis, as they showed significant instabilities during the vdM fill due to radiation-ageing effects caused by the accumulated dose. The largest deviation from the average in each year was used to determine the ‘Reference specific luminosity’ uncertainty in Table 8, which is at most 0.31%. The reference algorithm has an \mathcal{L}_{spec} close to the average of all algorithms in all years except 2018, where the single-PMT algorithm C12 has an \mathcal{L}_{spec} 0.31% higher than average. However, this algorithm was chosen for the baseline luminosity measurement due to its availability and stability throughout the year, as discussed in Sect. 3.1. The full difference between the C12 and average \mathcal{L}_{spec} values is covered by the 2018 reference specific luminosity uncertainty.

The total uncertainties in the absolute vdM calibration are listed in the ‘Subtotal vdM calibration’ row of Table 8, and range from 0.7% to 1.0% across the years of Run 2 data-taking. The largest individual uncertainties come from a variety of sources—non-factorisation effects in 2015 and 2016, scan-to-scan reproducibility in 2017 and magnetic non-linearity in 2018. All other individual sources are smaller than 0.5% in all years.

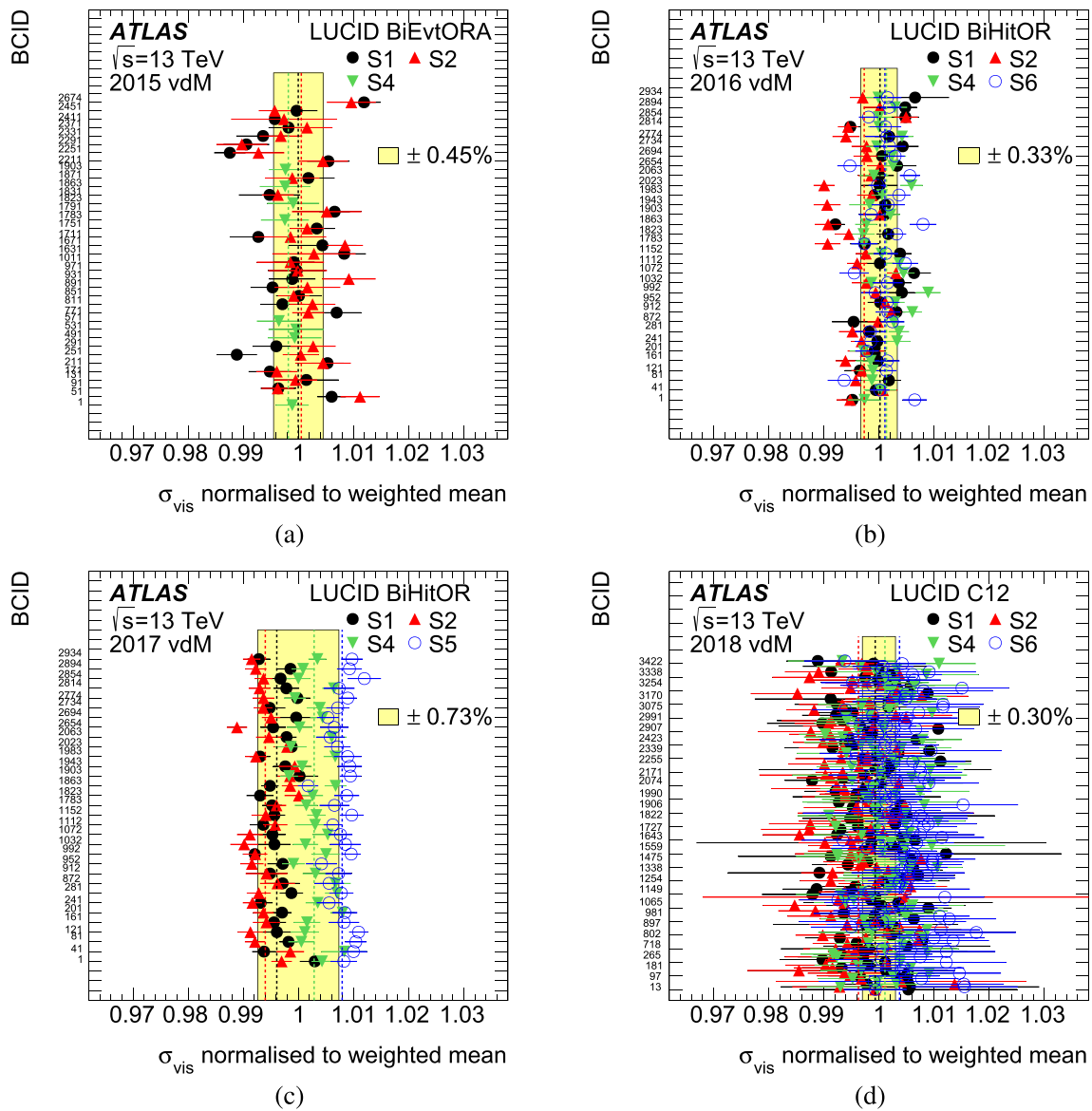


Fig. 12 Ratio of bunch-by-bunch visible cross-sections σ_{vis} to the weighted mean of σ_{vis} for all colliding bunch pairs in all on-axis scans in the vdM scan sessions from each year of data-taking, using the reference LUCID algorithm in each case. The vertical dashed lines show the mean σ_{vis} for all bunches in each individual scan set. The uncer-

tainties are statistical, and are larger for 2018 due to the use of the C12 single-PMT algorithm rather than a multi-PMT OR algorithm as used in 2015–2017. The yellow bands show the combination of bunch-to-bunch and scan-to-scan consistency uncertainties in each year, with the numerical values indicated in the legends

5 Calibration transfer to high-luminosity running

The procedures described above provide the absolute calibration of the LUCID and BCM luminosity measurements for low- μ data-taking with a limited number of isolated bunches, where the instantaneous luminosities are at least three orders of magnitude smaller than those typical of normal physics running with bunch trains. The LUCID detector suffers from significant non-linearity, and requires a downward correction of $O(10\%)$ in the physics data-taking regime. This correction

was derived using track-counting luminosity measurements and validated with calorimeter measurements, in particular those from the TileCal E-cell scintillators. The calibration transfer procedures, and their corresponding uncertainties, are discussed in detail below.

5.1 Comparison of luminosity measurements at high pileup

The natural luminosity decay during a long LHC physics fill, where the luminosity, and hence bunch-averaged pileup

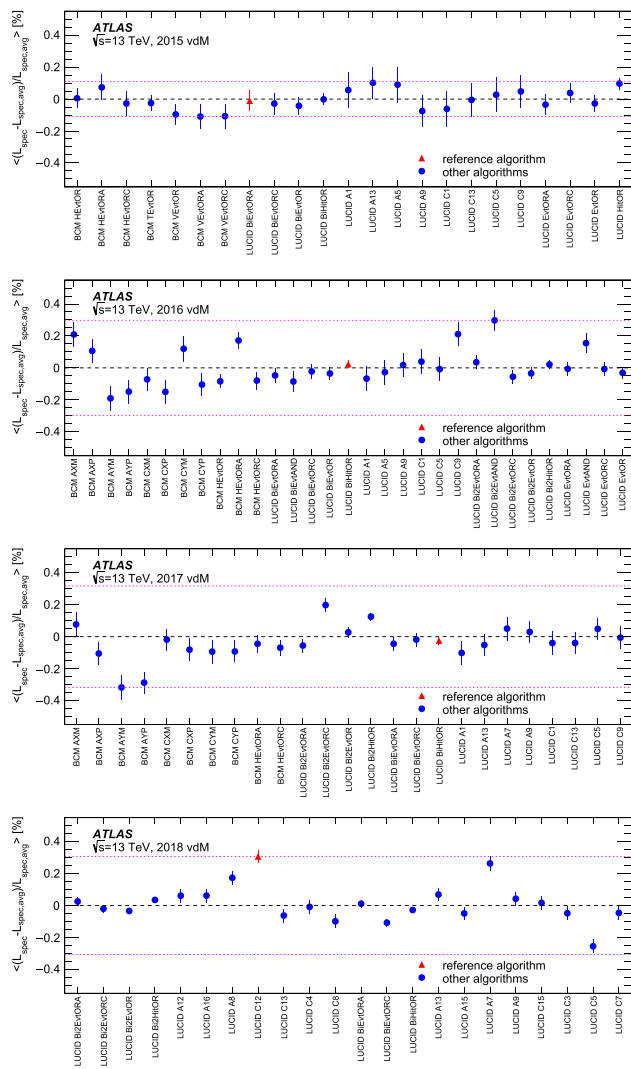


Fig. 13 Relative deviations of the specific luminosity measured by each algorithm L_{spec} from the average over all algorithms $L_{\text{spec,avg}}$, averaged over all colliding bunch pairs and scans in the vdM session of each year. The uncertainties indicated by the error bars are statistical, and the symmetric uncertainty bands encompassing all algorithms in each year are shown by the purple dotted lines. The reference algorithm for each year is indicated by the red triangle

$\langle \mu \rangle$, decrease by a factor of two or three, provides a way to study the relative responses of the different luminosity measurements as a function of $\langle \mu \rangle$. Figure 14 shows the ratios of track-counting luminosity to several other measured luminosities in two long physics fills in 2017 and 2018, plotted as a function of $\langle \mu \rangle$, which decreases steadily as the fills proceed. The ratios of track-counting to TileCal D6-cell luminosities change by at most 0.3% as the instantaneous luminosity decreases by a factor of three. The EMEC measurements include a contribution from material activation, which builds up over the first few hours of the fill to eventually contribute about 0.5% of the luminosity signal, leading to a somewhat larger decrease in the track-counting to EMEC ratio of

about 0.7% over the course of these long fills. In contrast, the track-counting/LUCID ratios are $O(10\%)$ smaller than unity at the start of physics fills, and exhibit a strong dependence on $\langle \mu \rangle$ which is well-described by a linear function, with different slopes in each year of data-taking. Although the track-counting measurement was normalised to agree with LUCID in the head-on parts of the corresponding vdM fills in each year, extrapolating the track-counting/LUCID ratios to $\langle \mu \rangle = 0.5$ from the fits shown in Fig. 14 gives ratios which differ from unity by $O(1\%)$, suggesting that the relative response of the two detectors may also be affected by running with bunch trains, and with a crossing angle between the colliding beams. The level of agreement between the luminosities measured by track-counting, EMEC and TileCal, and the strong disagreement between track-counting and LUCID, suggest that residual μ -dependencies in the track-counting, TileCal and EMEC measurements are at the percent level or less, and that LUCID overestimates the luminosity in physics conditions by $O(10\%)$, with a strong pileup dependence.

The relative dependence of the LUCID and track-counting luminosity measurements was further studied by performing μ -scans, where the luminosity was varied between zero and the maximum achievable, by partially separating the beams in the transverse plane at the ATLAS IP. Since both LUCID and track-counting measure μ for individual bunches, the performance as a function of the LHC bunch pattern and of the position of individual bunches within a bunch train could also be investigated. Figure 15 shows results from a special fill (6194) recorded in 2017, where the LHC filling pattern contained three isolated bunches, two 48-bunch trains with 25 ns spacing and two 56-bunch 8b4e trains with a repeating pattern of eight bunches separated by 25 ns followed by four empty bunch-slots. During the μ -scan, the ATLAS luminosity block boundaries were synchronised to the steps in LHC beam separation, such that each LB corresponds to a period with constant instantaneous luminosity at a different μ value. The LBs where the luminosity was varying as the beam separation was changed were discarded. Figure 15(a) shows the ratio of μ from track-counting to that from LUCID averaged over the three isolated bunches, as a function of μ_{LUCID} . There is a significant negative slope (indicating that LUCID overestimates the luminosity compared to track-counting at high pileup), but the slope is several times smaller than those seen in Fig. 14. Figure 15(b) shows the same ratio averaged over all the bunches in the 25 ns and 8b4e trains separately. Here, the slopes are larger, demonstrating a larger μ -dependence in train bunches, which is slightly stronger for 25 ns than 8b4e bunch trains. Deviations from the linear slope are also visible at the lower and upper ends of the μ range. Due to the spread in the bunch intensities and emittances produced by the LHC injector chain, the μ range sampled for 8b4e trains is slightly larger than that for 25 ns trains, and the isolated bunches extend almost

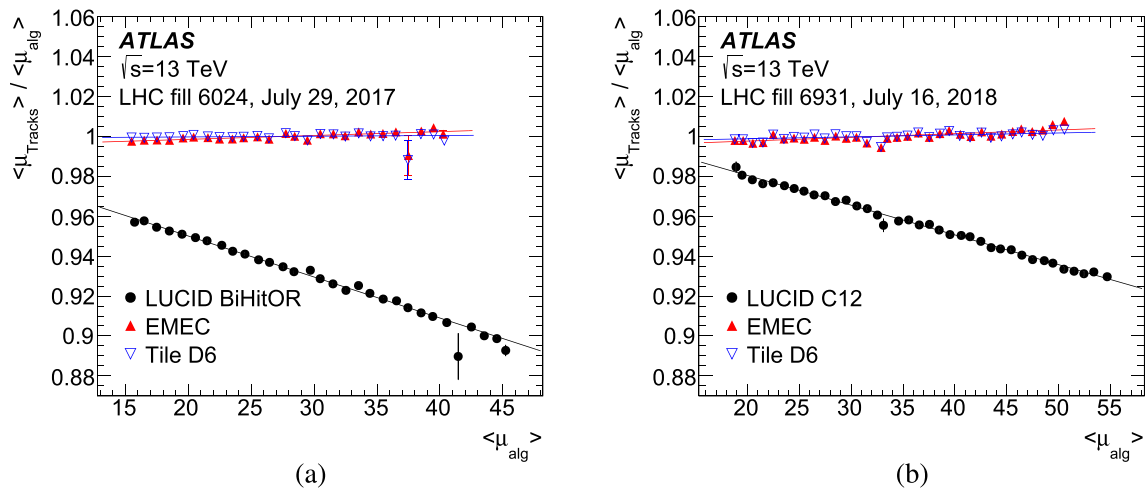


Fig. 14 Ratios of $\langle \mu \rangle$ (equivalent to ratios of instantaneous luminosity) measured by track-counting to that measured by LUCID (black points), EMEC (red filled triangles) and TileCal D6 (blue open inverted triangles) as a function of the mean number of interactions per bunch crossing $\langle \mu \rangle$ measured by the latter algorithms in two long LHC physics fills in (a) 2017 and (b) 2018. The track-counting luminosity measurements are normalised to those from LUCID in the head-on parts of

the corresponding vdM runs at low luminosity, and the calorimeter measurements are normalised to give the same integrated luminosity as track-counting in the two physics fills. The lines show linear fits through each set of points. The error bars show the statistical uncertainties in the track-counting measurements. Time progresses from right to left in these plots as $\langle \mu \rangle$ decreases through the fill

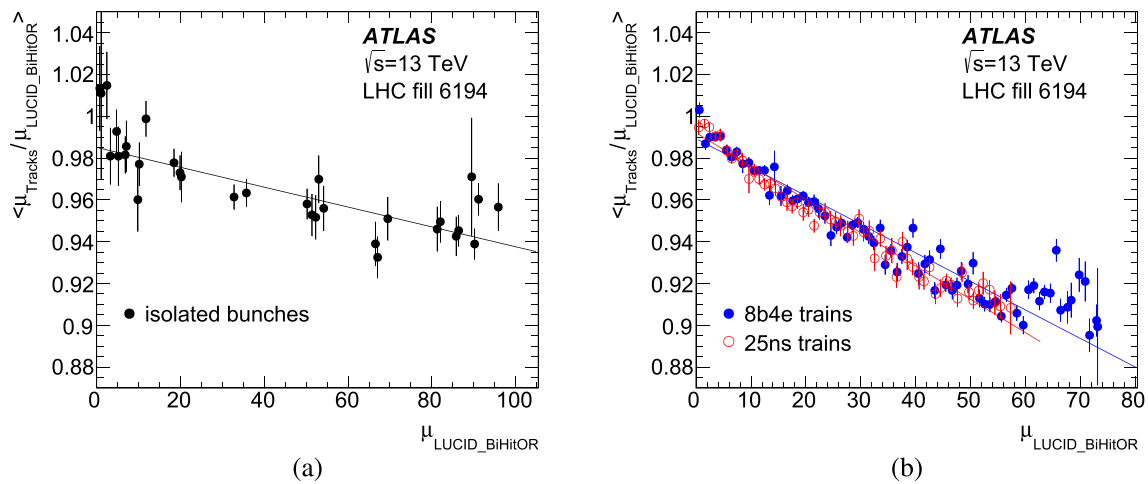


Fig. 15 Mean values of the bunch-by-bunch ratio of μ measured by track-counting and LUCID as a function of the μ measured by LUCID from the μ -scan in LHC fill 6194 with a mixture of isolated bunches, 25ns and 8b4e trains. The ratios are shown separately for (a) isolated

bunches and (b) the two types of bunch trains. The lines show linear fits through each set of points. The error bars show the uncertainties in the track-counting measurements

to $\mu = 100$, much larger values than those encountered in normal LHC fills during Run 2.

The μ -ratios between track-counting and LUCID were also analysed as a function of bunch position b within the train, fitting the ratio $R^b = \mu_{\text{Tracks}}^b / \mu_{\text{LUCID}}^b$ as a function of μ_{LUCID} to a linear function with intercept p_0^b and slope p_1^b . The resulting fitted parameters are shown separately for the 25 ns and 8b4e bunches in Fig. 16. Whilst the intercepts p_0 are similar in isolated bunches and both types of train

bunches, and do not depend significantly on train position, the slopes p_1 show significant structure. The first bunch of a 25 ns train has a similar p_1 (and hence μ -dependence) to that of isolated bunches. The subsequent bunches show increasingly negative p_1 (and larger μ -dependence), reaching a plateau about six bunches into the train, after which there is a slight recovery to a constant value through the bulk of the train. The 8b4e trains show a similar initial behaviour, but the four bunch-slot gap is enough for the ratio to ‘recover’, and the

first bunch of the next eight-bunch subtrain again behaves similarly to an isolated bunch. This structure is consistent with the slightly smaller μ -dependence for 8b4e compared to 25 ns trains seen in Fig. 15.

Since the calorimeter measurements cannot resolve the luminosity of individual bunches, the bunch-by-bunch stability of track-counting measurements cannot be validated except by ‘internal’ comparisons of different track-counting working points (see Sect. 5.2 below). However, given the small relative μ -dependence between the bunch-integrated track-counting measurements and the EMEC and TileCal calorimeter measurements shown in Fig. 14, it is reasonable to attribute the bulk of the effects seen in Figs. 15 and 16 to LUCID. A likely contributor is ‘signal migration’ [14], the overlap of several below-threshold signals in the same LUCID PMT from different pp interactions, which combine to produce an above-threshold signal which gets counted as a hit, causing deviations from the Poisson assumption in Eq. (4). These effects become more likely for higher μ values, leading to an overestimate of the luminosity at high pileup. The structures seen in Fig. 16 also suggest that particles from previous bunch crossings can contribute to this signal migration, making the overestimate worse for bunches further from the start of the train.

5.2 Performance of track-counting algorithms

The performance of the track-counting luminosity measurements was studied using the standard ATLAS detector simulation [34] based on GEANT4 [35]. A sample of events containing multiple overlaid inelastic pp collisions was generated with PYTHIA 8.186 [36] and the A3 set of tuned parameter values [37], with a flat μ profile in the range $0 < \mu < 100$. The sample included the simulation of bunch trains, with 53 trains each containing 48 colliding-bunch pairs with 25 ns spacing, simulating some of the effects of in-time and out-of-time pileup. These events were processed using the same dedicated track reconstruction settings as used for the track-counting event stream in real data, only making use of information from the pixel and SCT detectors. Figure 17a shows the efficiency to reconstruct a track and select it using each of the working points (normalised to the true number of tracks satisfying the p_T and $|\eta|$ requirements for each working point shown in Table 3), as a function of μ . For the baseline selection A, the efficiency decreases by only about 0.3% between $\mu = 0$ and $\mu = 100$. The efficiencies for the other two working points decrease faster, reflecting the more stringent hit requirements (see Table 3). Figure 17b shows the fraction of fake tracks (tracks which cannot be matched to a generator-level track with a hit-based matching probability $P_{\text{match}} > 0.5$ as defined in Ref. [16]), which is around 0.1% at $\mu = 50$ for selection A, rising non-linearly to about 1% at $\mu = 90$ as the detector occupancy increases. Here, the

alternative selections show smaller fake-track rates, again reflecting the more stringent hit requirements. The simulation includes some of the effects which lead to a loss of performance at high pileup, such as the ‘01X’ hit pattern definition in the SCT, which requires that there be no hit on a strip in the immediately preceding bunch-crossing for a valid hit to be read out. However, it does not include an inefficiency in the pixel detector due to time-over-threshold effects, where a pixel which is hit again whilst the decaying signal from an initial hit is still over the readout threshold will not record the second hit. This leads to an inefficiency which may last for tens of bunch-crossings, and particularly affects selection B, which rejects tracks with a missing pixel hit where one is expected.

The efficiencies of the track-selection working points were also studied using $Z \rightarrow \mu\mu$ events in data, where both muons were reconstructed as isolated ‘combined’ muons with $p_T > 20$ GeV, consisting of matched tracks in the ATLAS inner detector and muon spectrometer [38]. The fraction of the inner detector tracks associated with these muons that pass the track-counting selections, which only rely on criteria related to the inner detector, gives a measure of the inner detector track selection efficiency relative to the inclusive initial selection. The latter just requires a very loose reconstructed track passing p_T and $|\eta|$ requirements, together with minimal requirements on the number of inner detector hits to ensure the track can be reconstructed [39]. Figure 18a shows the resulting efficiencies measured in 2018 data for the different working points. The efficiency for selection A is reasonably stable with μ , decreasing by about 0.4% between $\mu = 0$ and $\mu = 60$, a decrease which is however larger than that seen in simulation. The efficiencies of the other selections show much stronger dependence on μ , especially for selection B. Figure 18b shows the efficiencies measured in part of the 2017 8b4e data-taking period as a function of the bunch position along the train. Again, the selection A working point is rather stable, decreasing by about 0.2% along the eight-bunch subtrains, whilst selection B shows $O(1\%)$ effects. Although these efficiencies are measured for muons with $p_T > 20$ GeV, simulation studies showed that they also capture the main effects for the track-counting selections, which are dominated by hadrons with lower p_T .

Figure 19 shows the selection efficiencies measured using $Z \rightarrow \mu\mu$ events as a function of time over the entire 2018 dataset. Selections A and C are very stable, changing by less than 0.2% during the course of the year. Selection B is much less stable, with about a 1% lower efficiency in the first few weeks. This was traced to an incorrect masking of inactive pixel modules in the track reconstruction, leading to more tracks with unexpected pixel holes. Since this early data also had atypically high $\langle\mu\rangle$ values, this effect also causes the decrease in efficiency for $\langle\mu\rangle > 50$ visible for selection B in Fig. 18a. Similar levels of stability for the selection A work-

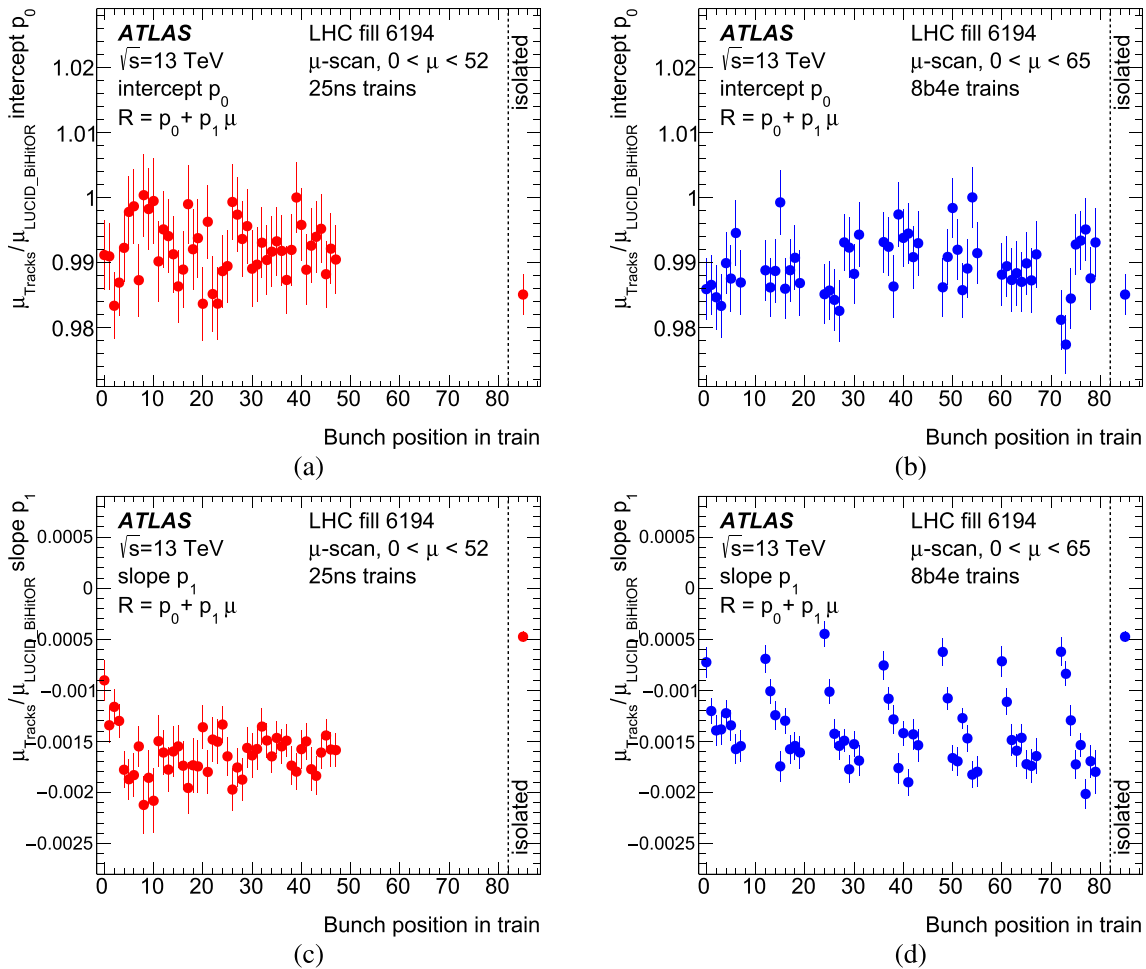


Fig. 16 Fitted intercept p_0 (upper plots) and slope parameter p_1 (lower plots) for the track-counting/LUCID μ ratios in LHC fill 6194 as a function of position within the bunch train, counting the first bunch in the train as position zero. The left plots show the results for the 48-bunch 25 ns trains, and the right plots those for the 56-bunch 8b4e trains with

eight colliding bunches separated by 25 ns followed by a four bunch-slot gap. The right-most points in each plot show the corresponding values for isolated bunches. The error bars show the statistical uncertainties from the track-counting measurements

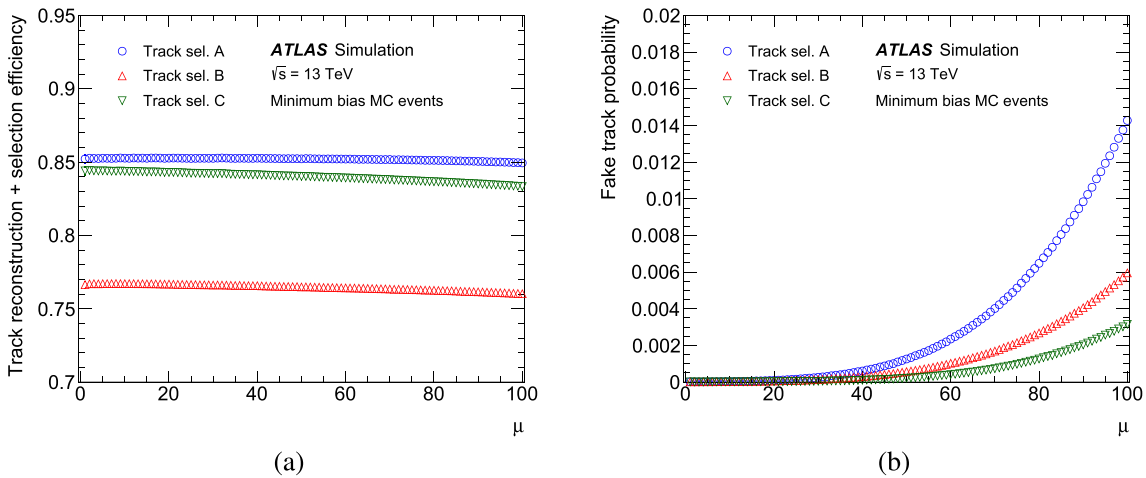


Fig. 17 Performance of the different track-selection working points for the track-counting luminosity measurement in simulation as a function of μ , showing (a) combined track reconstruction and selection efficiency, and (b) fake-track probability

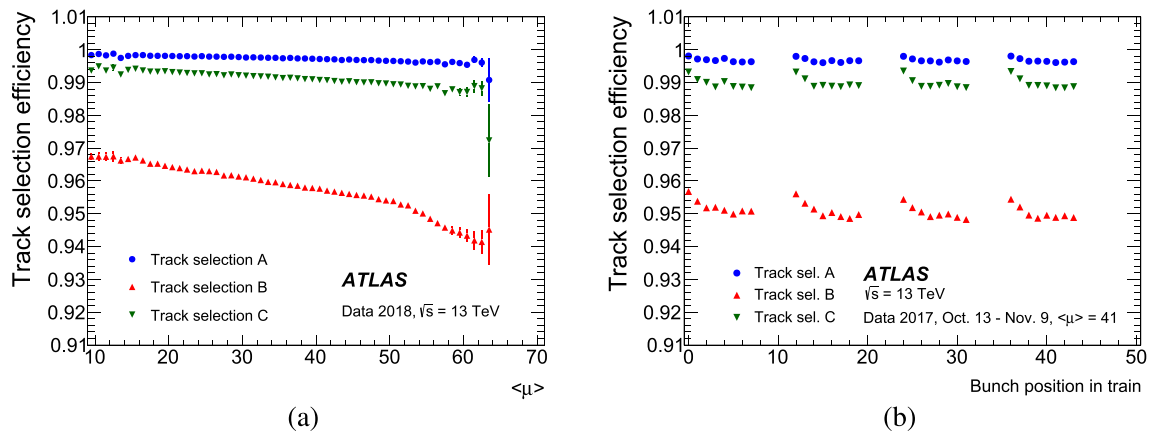


Fig. 18 Track-selection efficiency for the track-counting luminosity measurement determined using $Z \rightarrow \mu\mu$ events in data: (a) Efficiencies for the different selections as a function of $\langle\mu\rangle$ in 2018 data; (b)

Efficiencies for data recorded during part of the 8b4e collision period as a function of the position of the bunch within the 8b4e train, numbering the first bunch as position zero

ing point were seen for the datasets from other data-taking years within Run 2. Given these observations, no attempt was made to use the Z -based efficiency measurements to correct the track-counting luminosity as a function of time during each year.

These results using both simulation and real collision data demonstrate that the track-counting luminosity measurement with the selection A working point is much more robust than the LUCID luminosity measurements against variations of μ and bunch position. The track-counting measurement also shows excellent stability in time, and can thus be used as a reliable relative reference to calibrate other luminosity algorithms, once its absolute calibration has been determined by normalisation to LUCID in the vdM run.

5.3 LUCID correction strategy

Exploiting the excellent stability of the track-counting luminosity measurement, the non-linearity in LUCID was corrected as a function of $\langle\mu\rangle$ using one or more long high-luminosity reference fills in each year of data-taking. Each reference fill was used to derive a correction of the form

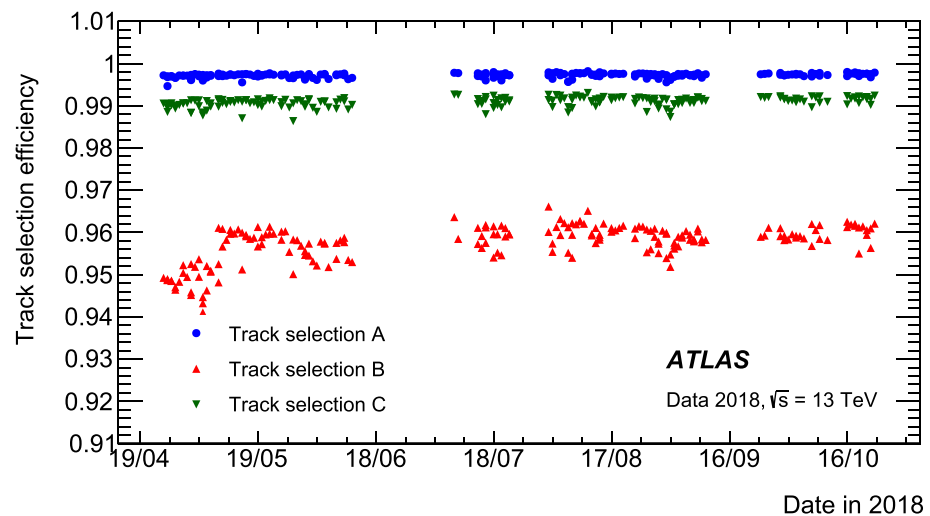
$$\langle\mu_{\text{corr}}\rangle = p_0\langle\mu_{\text{uncorr}}\rangle + p_1(\langle\mu_{\text{uncorr}}\rangle)^2 \tag{16}$$

where $\langle\mu_{\text{uncorr}}\rangle$ is the uncorrected and $\langle\mu_{\text{corr}}\rangle$ the corrected LUCID $\langle\mu\rangle$ value. The parameters p_0 and p_1 were obtained from a linear fit to the ratio of $\langle\mu\rangle$ values measured by track-counting and LUCID, $R = \langle\mu_{\text{Tracks}}\rangle/\langle\mu_{\text{LUCID}}\rangle$, as a function of $\langle\mu_{\text{uncorr}}\rangle$, as shown in Fig. 14. The track-counting luminosity was first normalised to the absolute luminosity measured by LUCID in parts of the vdM fill with stable head-on collisions at ATLAS, ensuring that $R = 1$ at low pileup ($\mu \approx 0.5$) with isolated bunches. This correction also absorbs the $O(1\%)$ change in the LUCID calibration caused by the

non-zero LHC beam crossing angle used in physics runs, and the $O(0.2\%)$ afterglow contribution to the LUCID luminosity signal in bunch train running. In principle, Eq. (16) could also be written in terms of the bunch-by-bunch μ , correcting the LUCID measurement as a function of the instantaneous luminosity in each individual bunch and potentially compensating for the bunch-to-bunch variations seen in Fig. 16. However, since ATLAS physics analyses make use of the data from all LHC bunches, an average correction based on $\langle\mu_{\text{uncorr}}\rangle$ is sufficient, and a more complex bunch-position-dependent correction scheme was not used.

The correction of Eq. (16) ensures that the LUCID luminosity agrees well with track-counting throughout the reference fill. If the LUCID response has no time dependence, a single reference fill and correction would be adequate for a whole year of data-taking. The regular PMT high-voltage adjustment based on the LUCID ^{207}Bi calibration signals ensures that this is approximately the case, but comparisons with track-counting show some residual variations, particularly during the first few weeks of data-taking in each year, when the number of colliding bunches and instantaneous luminosity increased during the LHC intensity ramp-up phase. Better agreement with track-counting throughout the year was therefore obtained by dividing each year into several correction periods, or epochs, with a long LHC fill representative of each epoch being used as a reference run. The change from 25 ns to 8b4e bunch trains in 2017 also required separate epochs for the two periods (the 8b4e epoch also includes a period of unstable 25 ns running with a reduced number of bunches and many short fills immediately preceding the change to 8b4e). One epoch in 2015, three epochs in each of 2016 and 2017, and two in 2018 were used in order to achieve good agreement between LUCID and track-counting throughout each year. Figure 20 shows

Fig. 19 Track-selection efficiency for the track-counting luminosity measurement determined using $Z \rightarrow \mu\mu$ events as a function of time within the entire 2018 high-luminosity physics dataset. The efficiencies of the different track selection working points are shown separately



the resulting level of agreement between track-counting and LUCID for each data-taking run (normally equivalent to one LHC fill), in terms of the relative differences of the per-run integrated luminosities measured by the two algorithms. The differences are plotted as a function of cumulative integrated luminosity through the year normalised to the per-year total, giving a fraction which increases monotonically from zero to one as a function of time within the year. In all years, the run-integrated LUCID and track-counting measurements typically agree to better than 0.5%, and at least about 70% of the data in each year is covered by a single correction epoch.

6 Calibration transfer uncertainties

The LUCID correction strategy discussed in Sect. 5.3 implicitly assumes that the track-counting measurement with selection A suffers from no significant non-linearity between the low-luminosity vdM and high-luminosity physics regimes, in particular as a function of $\langle\mu\rangle$, bunch structure or LHC crossing angle, which all change between the two regimes. The results shown in Sects. 5.1 and 5.2 suggest that any such non-linearity is smaller than 1%, but a more robust validation using independent detectors is essential for a high-precision luminosity measurement. Comparisons between track-counting, TileCal D-cells and EMEC (Fig. 14) can probe down to the smallest instantaneous luminosities exploited in normal physics running, but these luminosities are still $O(10^3)$ times larger than those in the vdM regime, where the EMEC and TileCal D6 measurements lose sensitivity. The only other measurements which have enough dynamic range to span from the vdM to physics regimes are those from the TileCal E-cell gap scintillators, in particular those from E3 and E4. Comparisons of the luminosity ratios $R_{\text{Tile-E/Trk}}$ in the head-on parts of the vdM fills with the equivalent ratios in nearby physics fills quantify any relative non-linearity between the TileCal E-cell and track-counting

luminosity measurements, and can thus be used to probe potential non-linearity in the track-counting measurement. Deviations of the double ratio

$$R_{\text{Tile-E/Trk}}^{\text{phys/vdM}} = \frac{R_{\text{Tile-E/Trk}}(\text{physics})}{R_{\text{Tile-E/Trk}}(\text{vdM})} \quad (17)$$

from unity, where each ratio is integrated over the vdM- or physics-like running period within a fill, can therefore be interpreted as a reasonable upper limit on the change in track-counting luminosity response between the vdM and physics regimes, and hence as an uncertainty in the calibration transfer correction applied to LUCID.

In principle, these double ratios can be measured using the vdM fills combined with any suitable physics fill close in time either before or after the vdM fill, limited by the rapid ageing of the scintillators due to radiation damage in high-luminosity running. Unfortunately, the TileCal E-cell measurements also suffer from significant contributions from activation of the surrounding material. These contributions have magnitudes of up to about 1% of the primary luminosity signal, and decay with various time constants from minutes to tens of hours. The residual activation from a high-luminosity physics fill produces a TileCal E-cell luminosity signal which is initially of a similar magnitude to the typical luminosity in a vdM fill, and which takes several days to decay to a negligible level. Wherever possible, the vdM fills were scheduled immediately after pauses in the LHC running schedule (e.g. after a technical stop) to minimise this activation, and TileCal luminosity data was recorded before and after the vdM fills to allow the activation contributions to be fitted and subtracted. The details of this activation modelling are described in Sect. 6.1.

In 2017 and 2018, additional ‘vdM-like’ fills with only 140 isolated colliding bunch pairs were scheduled after periods without high-luminosity running, to provide further constraints. These dedicated calibration transfer (CT) fills used standard low- β^* physics optics with a beam crossing angle,

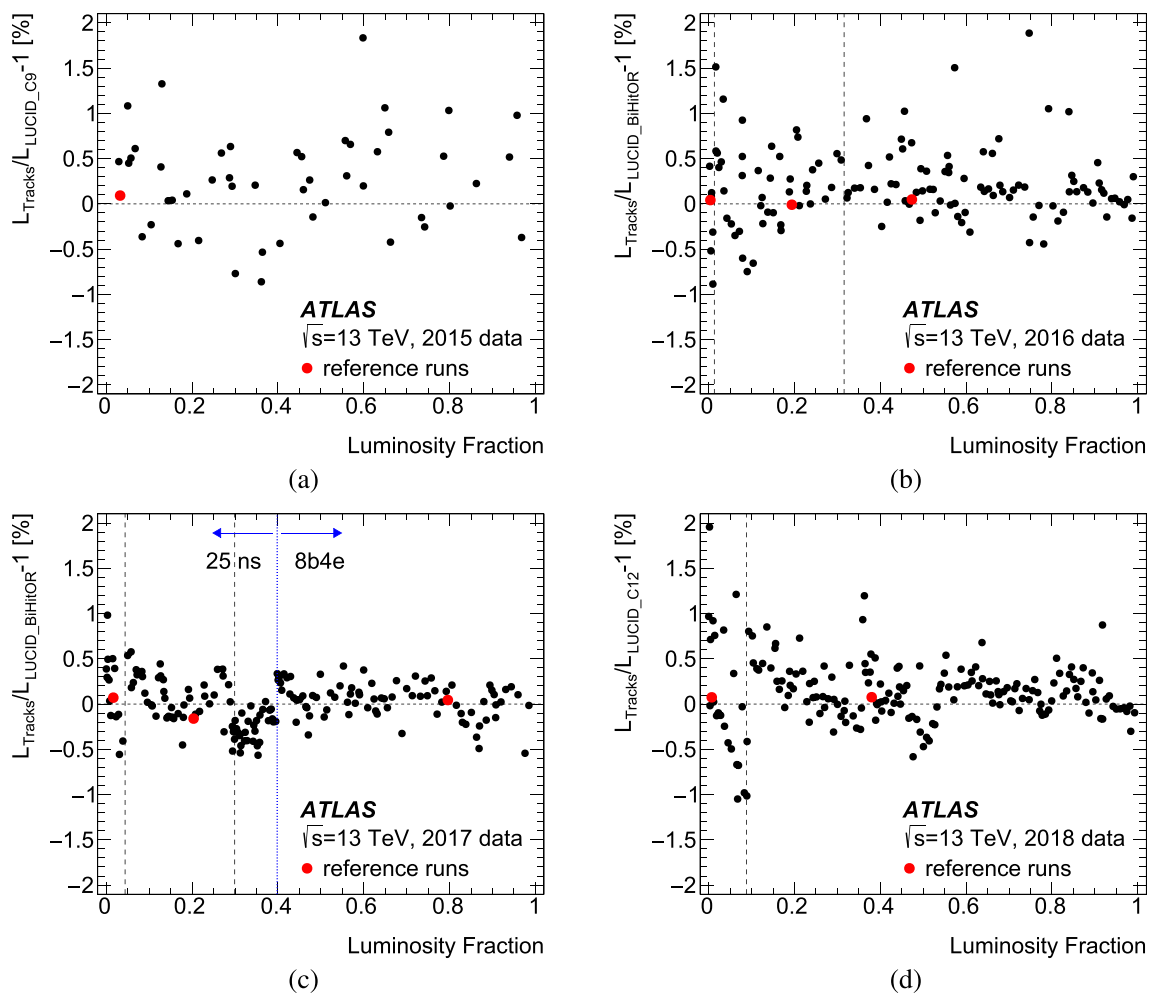


Fig. 20 Fractional differences in run-integrated luminosity between the track-counting and corrected LUCID luminosity algorithms, plotted as functions of cumulative delivered luminosity in each data-taking year. The division of the data into multiple epochs is shown by the vertical dashed lines (except in 2015), the separation of 25 ns and 8b4e

running periods in 2017 is shown by the blue dotted line, and the reference runs used to derive LUCID μ -corrections are shown by the red points. Only runs with at least 500 colliding-bunch pairs and 1 h of data-taking are shown

but the beams were partially separated for the first 2 h of running to give $\langle\mu\rangle \approx 0.5$, the same as in vdM fills. After approximately 2 h in this configuration, a μ -scan up to head-on collisions and back to separated beams was performed, followed by a period of head-on collisions to give high-pileup running with isolated bunches. The $R_{\text{Tile-E/Trk}}$ ratios in both the low and high- μ periods of these runs could then be compared with $R_{\text{Tile-E/Trk}}$ in the following physics fills to give additional constraints on the calibration transfer systematics. These studies are described in Sect. 6.2.

A further study was performed using data taken in June 2018, during the LHC intensity ramp-up after a one-week technical stop (TS1). After the 140 colliding bunch fill mentioned above, a series of relatively short physics fills with increasing numbers of bunches took place before the 2018 vdM run, with a further two fills coming after a one-

week period of low-luminosity high- β^* running for the LHC forward-physics programme that immediately followed the vdM run. This sequence of fills allowed the evolution of the $R_{\text{Tile-E/Trk}}$ ratios to be studied from vdM-like conditions, through high-pileup data with isolated bunches and then increasing numbers of bunches in trains, in a step-by-step ‘ladder’ approach discussed in Sect. 6.3. Along with some analogous fills in 2017, it also allowed the calibration transfer uncertainties for $\mu \approx 2$ running with bunch trains to be assessed, as discussed in Sect. 9 below.

6.1 Tile calorimeter activation model

The activation signal in the TileCal E-cells was described using an empirical model based on multiple components, each representing a contribution from a distinct radioactive

isotope with lifetime τ , produced in the interaction of primary or secondary collision particles with the detector material, and decaying some time t later giving a contribution to the luminosity signal in the detector. For a short pulse of real instantaneous luminosity $L_{\text{inst}}^{\text{ref}}$ of duration Δt at time $t = 0$, the resulting apparent instantaneous luminosity $L_{\text{inst}}^{\text{act}}$ from activation at some later time t is given by

$$L_{\text{inst}}^{\text{act}} = \Delta t L_{\text{inst}}^{\text{ref}} \frac{f e^{-t/\tau}}{\tau} \quad (18)$$

where the fraction f characterises the strength of the activation-induced luminosity signal with respect to the source luminosity $L_{\text{inst}}^{\text{ref}}$. The model consists of several such components i , each with their own parameters f_i and τ_i which can be fitted from data.

Periods without collisions are particularly useful in characterising the activation contributions to the TileCal E-cell measurements. Figure 21(a) shows the instantaneous luminosity measured in the A-side E3 and E4 cells in the 45 min after the beam dump in the 140 colliding bunch fill 6847 in 2018. The instantaneous luminosity just before the beam dump was about $880 \times 10^{30} \text{ cm}^{-2} \text{ s}^{-1}$, and immediately afterwards the E3 cells measured a residual luminosity of about 1% of this value due to activation, which subsequently decayed away. The activation fits well to the sum of two decaying exponential functions as shown. The measurements from E4 show about a factor two smaller activation, which decays with similar time constants. The fitted lifetimes are close to those of ^{28}Al and ^{39}Cl ($\tau = 194$ and 4934 s), two isotopes which are expected to be present in the nearby cryostats and LAr of the electromagnetic calorimeters. Figure 21(b) shows analogous measurements from the period before collisions in fill 6336 from 2017, during the time when the ATLAS data acquisition was running but there were not yet collisions in the LHC. The data-taking run started 12 h after the previous high-luminosity fill was dumped, so the relatively short lifetime components shown in Fig. 21(a) would have decayed to a negligible level, but a residual component, with a lifetime of about 12 h, can clearly be seen in both E3 and E4 measurements, again with a larger amplitude in E3 than E4.

These studies, together with similar analyses from other LHC fills, allow the time constants τ_i of the activation components in Eq. (18) to be determined, but not the fractions f_i . The latter can only be determined from knowledge of the luminosity history leading to the activation at any particular time. If the luminosity history preceding the time t is known, the activation corresponding to any given set of (τ_i, f_i) parameters can be calculated by integration, and compared with data. In practice, the activation is dominated by the relatively short-lived components shown in Fig. 21(a), and only their excitation within the fill under consideration needs to be taken into account. The long-lifetime component shown in Fig. 21(b) is only relevant for low-luminosity vDM

and CT fills which followed soon after a high-luminosity physics fill, and this component can be normalised with a free parameter representing the residual activation at the start of the data-taking run, without knowledge of the luminosity structure in the previous fill(s) that produced it.

This procedure was implemented using the LUCID luminosity measurements (including the μ -correction of Eq. (16)) for $L_{\text{inst}}^{\text{ref}}$ in Eq. (18) to derive a prediction for the contribution $L_{\text{int}}^{\text{act}}$ to the integrated luminosity measured by TileCal in each LB within a data-taking run. The corrected TileCal luminosity $L_{\text{int}}^{\text{corr}}$ is then given by

$$L_{\text{int}}^{\text{corr}} = L_{\text{int}}^{\text{calo}} - L_{\text{int}}^{\text{act}} - P \Delta t$$

where $L_{\text{int}}^{\text{calo}}$ is the uncorrected TileCal measurement and P is a pedestal correction to the instantaneous luminosity, multiplied by the luminosity block duration Δt . This correction was taken to be a constant or a linear function of time to account for slow drifts. The activation correction $L_{\text{int}}^{\text{act}}$ implicitly depends on the LUCID luminosity history and the parameters (τ_i, f_i) .

The relation between the corrected TileCal and track-counting luminosities was assumed to be a linear function of $\langle \mu \rangle$:

$$L_{\text{int}}^{\text{corr}} = L_{\text{int}}^{\text{trk}}(p_0 + \langle \mu \rangle p_1) \quad (19)$$

where $L_{\text{int}}^{\text{trk}}$ is the track-counting integrated luminosity in the LB and $\langle \mu \rangle$ is measured using track-counting. Finally, a χ^2 was defined from the comparison of corrected TileCal and track-counting measurements in each luminosity block, i.e.

$$\chi^2 = \sum \left(\frac{(L_{\text{int}}^{\text{calo}} - L_{\text{int}}^{\text{act}} - P \Delta t - L_{\text{int}}^{\text{trk}}(p_0 + \langle \mu \rangle p_1))^2}{\sigma_{L_{\text{int}}^{\text{calo}}}^2 + \sigma_{L_{\text{int}}^{\text{trk}}}^2} \right) \quad (20)$$

where the terms $\sigma_{L_{\text{int}}^{\text{calo}}}$ and $\sigma_{L_{\text{int}}^{\text{trk}}}$ represent the per-LB uncertainties in the luminosity measurements, and the sum is taken over all LBs where both the calorimeter and tracking information are available. The calorimeter uncertainties were estimated empirically from the spread of the differences between the A- and C-side measurements in each luminosity block, and parameterised as linear functions of luminosity. The χ^2 was then minimised to determine the best values of the activation model parameters (τ_i, f_i) , together with p_0 , p_1 and the pedestal parameters. Periods without collisions were also included in the χ^2 , assuming the track-counting luminosity to be zero, but periods with collisions but no track-counting or calorimeter measurements (e.g. before stable beams when the tracking detectors are not yet active) were excluded. However, the LUCID luminosity measurements (which are also available outside stable beam periods) were still used to follow the build-up of calorimeter activation during these times.

Figure 22 illustrates this fit procedure for LHC fill 6336, the 140 colliding bunch CT fill recorded in November 2017.

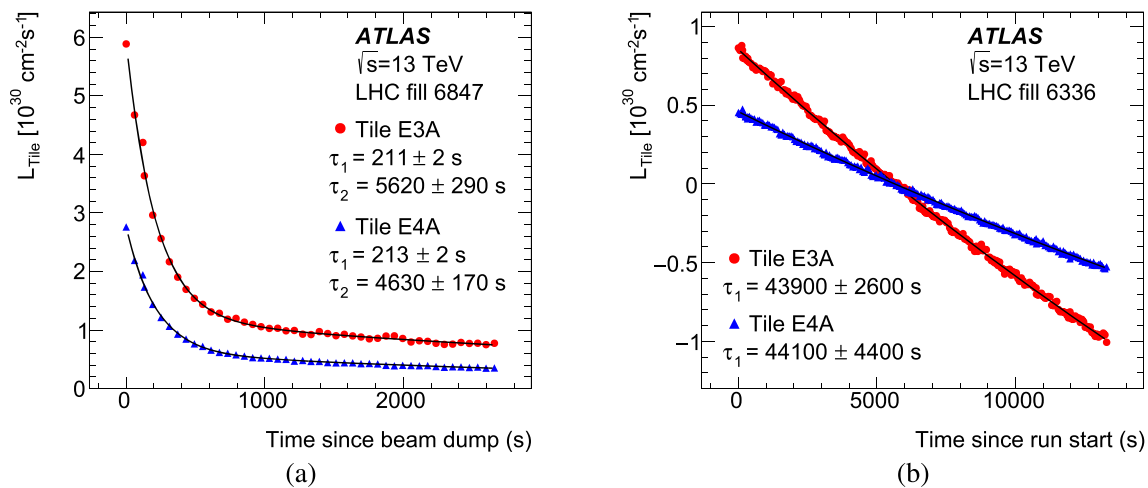


Fig. 21 Instantaneous luminosity measured by the A-side TileCal E3 and E4 cells as functions of time in (a) the period after the beam dump in fill 6847 from 2018, and (b) the period before collisions in fill 6336 from 2017. The measurements are fitted to the sum of two exponential functions in (a), and one exponential function plus a constant in (b), with the fitted lifetimes and their uncertainties shown in the legends.

Figure 22(a) shows the luminosity history of the fill as measured by LUCID: after a 4-h period before collisions, the beams were brought into head-on collision at LB 231 before being separated to give 2 h at $10 \times 10^{30} \text{ cm}^{-2} \text{ s}^{-1}$ and $\langle \mu \rangle = 0.5$, a short period with the beams separated in both planes to give almost-zero luminosity, a μ -scan in LB 428–475 (preceded by a short aborted μ -scan starting at LB 386), and finally a short period of head-on running, after which the beams were dumped and the data-taking continued for another 80 min to monitor the TileCal activation decay. Figure 22(b) shows the fitted activation contributions after minimising the χ^2 of Eq. (20); the lifetimes of the three fitted components are mainly constrained from the periods before and after collisions, whilst the fractions are also constrained from the evolution during collisions. The fractions corresponding to the $\tau \approx 200 \text{ s}$ component are around 1% for E3 and 0.5% for E4, and the longer $\tau \approx 5000 \text{ s}$ component has fitted fractions of 0.2% for E3 and less than 0.1% for E4. For this fit, the long $\tau \approx 45000 \text{ s}$ component was only used to fit the initial activation from previous running, and any activation of this component within the low-luminosity fill 6336 was neglected (i.e. f was fixed to zero). The offset of the activation contribution is arbitrary, and has been set so the activation is zero at the end of the data-taking period. The short-lifetime activation produced by the high-luminosity periods of the fill (the initial ‘spike’ when the beams were brought into collision, the μ -scan and the head-on period) is clearly visible above the background from the slow decay of the residual long-lifetime component.

The uncertainties in the individual TileCal measurements are smaller than the marker sizes and were derived from the RMS of the differences between A- and C-side measurements in each luminosity block. The pedestal offset in (b) is arbitrary, and has been set so that the mean of the measurements is zero in the pre-collision period. The measurements from the C-side cells are similar

Figure 22(c, d) show the TileCal/track-counting instantaneous luminosity ratios during the low- μ separated-beam and high- μ head-on periods of fill 6336. The uncorrected ratios (shown by the open circles) are far from unity and vary by 5–10% during the low- μ period due to the changing offset caused by the slowly decaying $\tau \approx 45000 \text{ s}$ activation component. The activation-corrected ratios are much closer to unity, although a small downward slope is still visible for E3A, perhaps due to residual imperfections in the activation modelling. During the high- μ period with $\mathcal{L}_{\text{inst}} = 900 \times 10^{30} \text{ cm}^{-2} \text{ s}^{-1}$, the uncorrected and corrected ratios are similar and much closer to unity, because the long-lifetime activation contributions are relatively much less important. The remaining deviation from unity reflects the absolute normalisation of the initial TileCal E-cell measurements, which was determined from the following high-luminosity fill without taking activation effects into account. The fitted p_1 parameters from Eq. (19) for the four cell families E3A, E3C, E4A and E4C are all small, between zero and -1×10^{-4} , and show that the corrected ratios are in good agreement between the low- and high- μ periods. These p_1 values correspond to a maximum change of -0.5% in the TileCal/track-counting ratio between $\langle \mu \rangle = 0.5$ and $\langle \mu \rangle = 50$, giving a strong constraint on the maximum non-linearity of the track-counting measurement between low- μ and high- μ isolated bunches. Similar results were obtained from the analogous 140 colliding bunch CT fill 6847 in 2018.

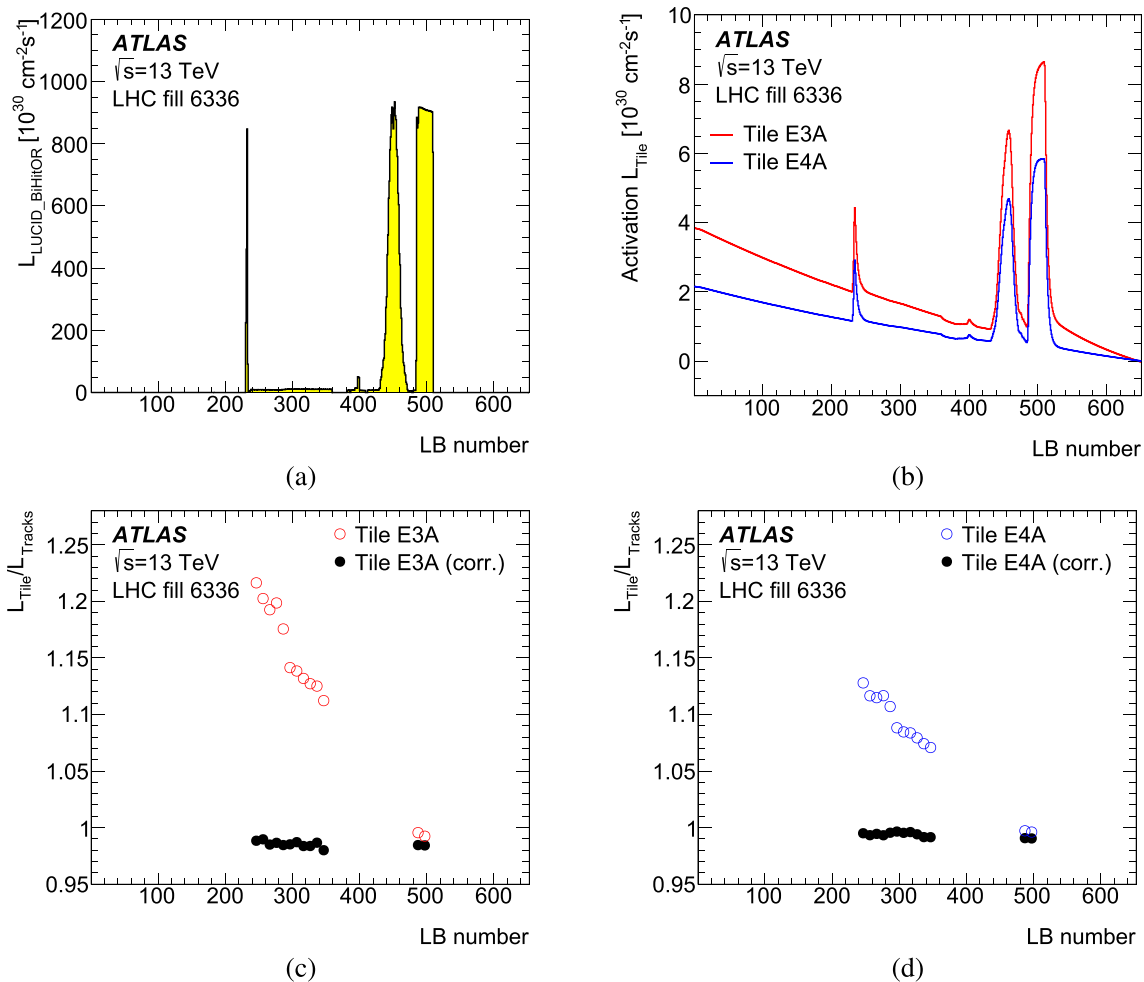


Fig. 22 Details of the TileCal E-cell activation analysis for fill 6336 from 2017 with 140 colliding bunch pairs: **(a)** luminosity profile as measured by LUCID as a function of LB number (see text); **(b)** fitted activation contributions to the A-side TileCal E3 and E4 measurements; **(c)**, **(d)** ratios of uncorrected (red or blue open circles) and activation-

corrected (black filled circles) TileCal E-cell luminosity measurements to those from track-counting for E3 and E4 in the periods with steady-state running at low and high pileup, excluding the μ -scan. The ratios have been averaged over ten consecutive luminosity blocks. The results for the C-side measurements are similar

6.2 Comparisons of TileCal and track-counting measurements: direct approach

The activation model described above was used to derive corrected TileCal E3- and E4-cell measurements for the vdM fills in 2016, 2017 and 2018, and the dedicated 140 colliding bunch CT fills in 2017 and 2018. Each such fill was paired with a nearby high-luminosity fill in order to derive the double ratios $R_{\text{Tile-E/Trk}}^{\text{phys/vdM}}$ defined in Eq. (17). For consistency, the activation model was also applied to correct the TileCal luminosity measurements in the high-luminosity fills, using the (τ_i, f_i) parameters derived from the corresponding low-luminosity fill. The datasets and results are summarised in Table 7, including comparisons between low- and high- μ isolated bunches within each of the two CT fills. The double ratios are given averaged over the A- and C-sides, but

separately for E3 and E4 cells. More details are given in Fig. 23, which shows the TileCal E-cell/track-counting single ratios as a function of luminosity block number in a continuous series for each pair of low- and high-luminosity runs, normalising the ratios so that the integrals of TileCal and track-counting luminosities agree in the low-luminosity runs. The stability of the ratios vs. time demonstrates the quality of the activation modelling; as can be seen from Fig. 22(c, d), these corrections can be of $O(10)\%$, but the corrected TileCal/track-counting ratios for low and high luminosity agree to within 0.5% for all the comparisons shown in Table 7 and Fig. 23. There are some systematic differences for the ratios involving E3 and E4 cells—the E3/track-counting ratios, which require larger activation corrections, are generally closer to unity, but all the E4 double-ratios are also within $\pm 0.5\%$ of unity. There is no systematic difference

Table 7 Pairs of vdM-like and physics-like fills used to measure the TileCal E3- and E4-cell/track-counting double ratios $R_{\text{Tile-E/Trk}}^{\text{phys/vdM}}$ in order to study the calibration transfer uncertainty in 2016–2018 data. For each fill, the LHC fill number and number of colliding bunches in ATLAS n_b are given. The vdM-like fills had only isolated bunches with

$\langle\mu\rangle = 0.5 - 0.6$, with (y) or without (n) a crossing angle at the ATLAS interaction point. The physics-like fills all have a crossing angle, and (apart from the high- μ parts of fills 6336 and 6847) a filling scheme with bunch trains. The rightmost columns show the integrated double ratios, including the effects of activation corrections

Year	vdM-like fill			Physics-like fill			Double ratios	
	Fill	n_b	X-angle	Fill	n_b	$\langle\mu\rangle$	$R_{\text{Tile-E3/Trk}}^{\text{phys/vdM}}$	$R_{\text{Tile-E4/Trk}}^{\text{phys/vdM}}$
2016 vdM	4954	32	n	4958	1453	21	1.002	1.003
2017 vdM	6016	32	n	6024	2544	40	1.000	0.997
2017 CT	6336	140	y	6336	140	46	0.998	0.996
2017 CT	6336	140	y	6337	1866	45	1.002	1.000
2017 CT	6336	140	y	6337	1866	58	1.002	1.000
2018 CT	6847	140	y	6847	140	45	1.000	0.999
2018 CT	6847	140	y	6850	590	60	1.004	1.002
2018 vdM	6868	124	n	6860	2448	51	0.998	0.995

between the comparisons where the low-luminosity fill is a vdM fill (without an LHC beam crossing angle) or a CT fill using physics optics with a crossing angle, suggesting that the track-counting measurement does not have a crossing-angle dependence. The 2016 dataset included a second vdM fill (4945) which showed larger deviations of up to 1% with respect to nearby physics fills. However, the TileCal laser calibration corrections in this period were not fully understood, and there were inconsistencies between the A- and C-side measurements, so this dataset was discarded.

Figure 24 shows the integrated TileCal E-cell/track-counting double ratios as functions of the $\langle\mu\rangle$ and n_b values in the physics-like fills, exploiting the variety of conditions sampled over the three years. No strong correlations with either quantity are visible, suggesting that the $\pm 0.5\%$ maximum deviation from unity is valid for all the conditions encountered in high-pileup physics running with bunch trains during Run 2.

Limited additional studies were performed using the TileCal A13 and A14 cells, located in the first longitudinal sampling of the extended barrel calorimeter. These cells have poorer sensitivity in vdM runs than E3 and E4, but suffer less from radiation-induced ageing and have smaller activation corrections. The activation was studied and corrections were made using the techniques described in Sect. 6.1, suggesting activation components with lifetimes of $\tau \approx 300, 5800$ and 12000 s, though the lower sensitivity of the A-cells makes it hard to determine the (τ_i, f_i) parameters unambiguously. The 2016 vdM and 2018 CT periods were studied, and the resulting $R_{\text{Tile-A/Trk}}$ ratios are shown in Fig. 25, to be compared with Fig. 23(a, e) for the E3 and E4 cells. The 2016 vdM dataset shows differences below 0.3% between the physics and vdM runs for both A13 and A14, whereas the 2018 CT dataset shows larger shifts, and results for A13

and A14 that differ by around 0.5% at high- μ , both for 140 isolated bunches and 590 bunches in trains. However, even in this dataset, the average of A13 and A14 cells shows shifts within 0.5% of unity between the low- μ and high- μ regimes.

6.3 Comparisons of calorimeter and track-counting measurements: ladder approach

The ladder approach considers the transition from the vdM to physics regimes in three steps, low- μ to high- μ isolated bunches, high- μ isolated bunches to high- μ bunch trains, then an increasing number of bunches in trains until the LHC ring is full. The first step was already addressed by the studies within the 140 colliding bunch fills 6336 and 6847 shown in Table 7 and Fig. 23(c, e), which suggest a small decrease of at most 0.4% in $R_{\text{Tile-E/Trk}}$ when going from low- to high- μ with isolated bunches. This transition was also studied using the μ -scans carried out in both fills between the low- μ and high- μ periods, as shown for the 2017 fill in Fig. 22(a). The analysis of the TileCal E-cell data again uses the activation model described in Sect. 6.1, which is particularly important in the second part of the μ -scan when the luminosity is decreasing at each step, increasing the relative importance of activation from the preceding luminosity blocks with higher instantaneous luminosities. The ratios $R_{\text{Tile-E/Trk}}$ from the A-side E3 and E4 cells are shown as a function of $\langle\mu\rangle$ for the 2017 140 colliding bunch fill in Fig. 26(a, b), and for the analogous 2018 fill in Fig. 26(c, d). Although the precision is limited in the low- μ region by the statistical uncertainties in the track-counting measurements, and the linear fits are not perfect, the general trends are clear, and similar between 2017 and 2018. The $R_{\text{Tile-E/Trk}}$ ratios slightly decrease with increasing $\langle\mu\rangle$, with negative gradients of up to 1×10^{-4} , corresponding to a double ratio $R_{\text{Tile-E/Trk}}^{\text{phys/vdM}}$ up to 0.5% below

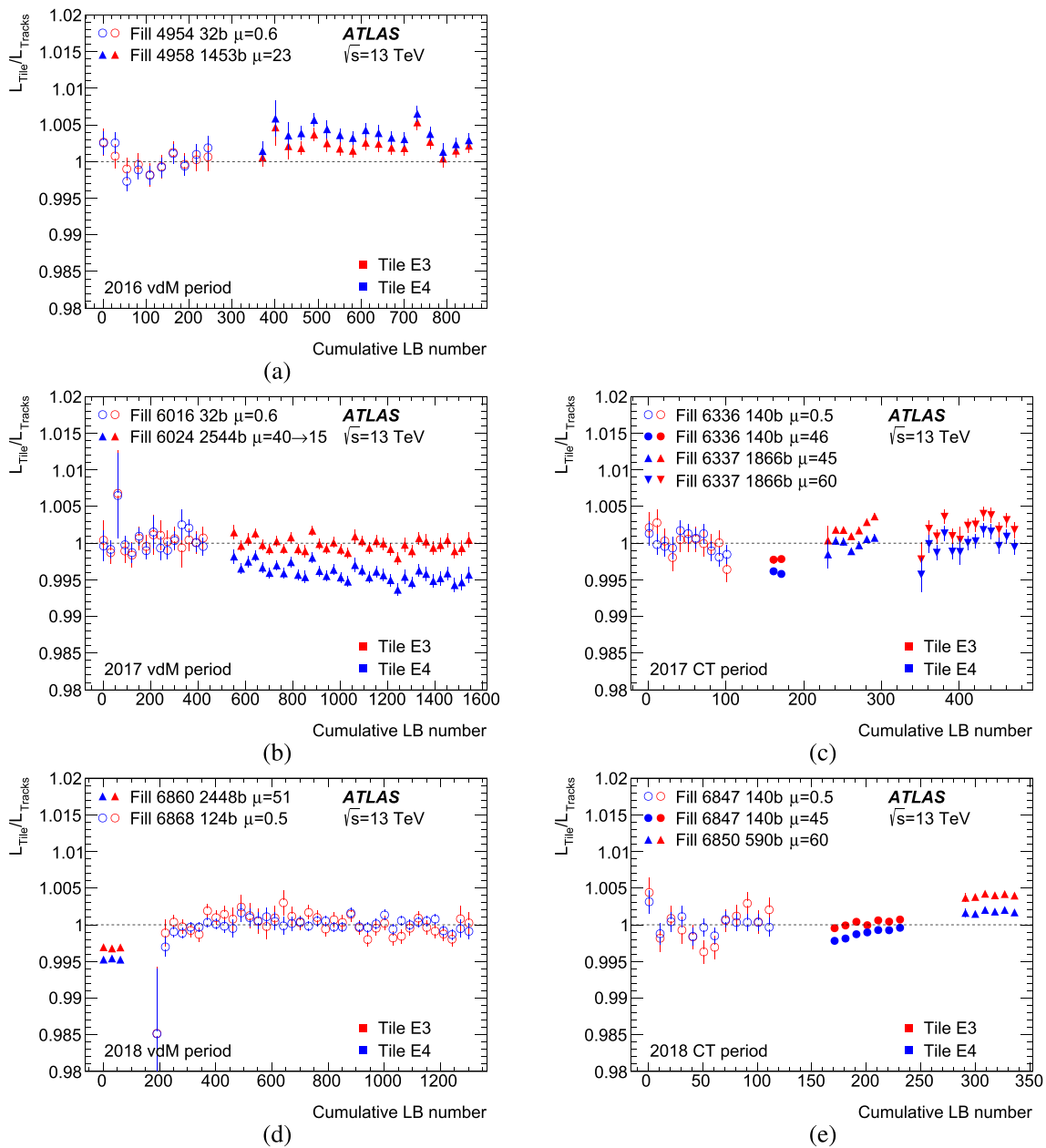


Fig. 23 Ratios of luminosity measured by the TileCal E-cells to that measured by track-counting for sequences of fills under various LHC conditions in the 2016–2018 calibration transfer studies. The ratios are averaged over the A- and C-side measurements and over 30 (vdM and related fills, left column) or 10 (CT periods, right column) luminosity blocks, separately for the E3 (red) and E4 (blue) cells. The uncertainties indicated by the error bars are dominated by the statistical uncertainties from the track-counting measurements. Within each plot, the ratios are shown as a function of luminosity block number, with gaps between fills

to give a continuous sequence over related fills. Periods with no ratio measurements within fills (e.g. during vdM scans) are not shown, and are omitted in the luminosity block numbering. The ratios have been renormalised separately for E3 and E4 cells in each sequence so that the integrated ratios in the low-luminosity vdM-like periods are unity. The numbers of colliding bunch pairs in ATLAS and the typical μ values are indicated for each fill, and the various fill periods are plotted with different marker styles

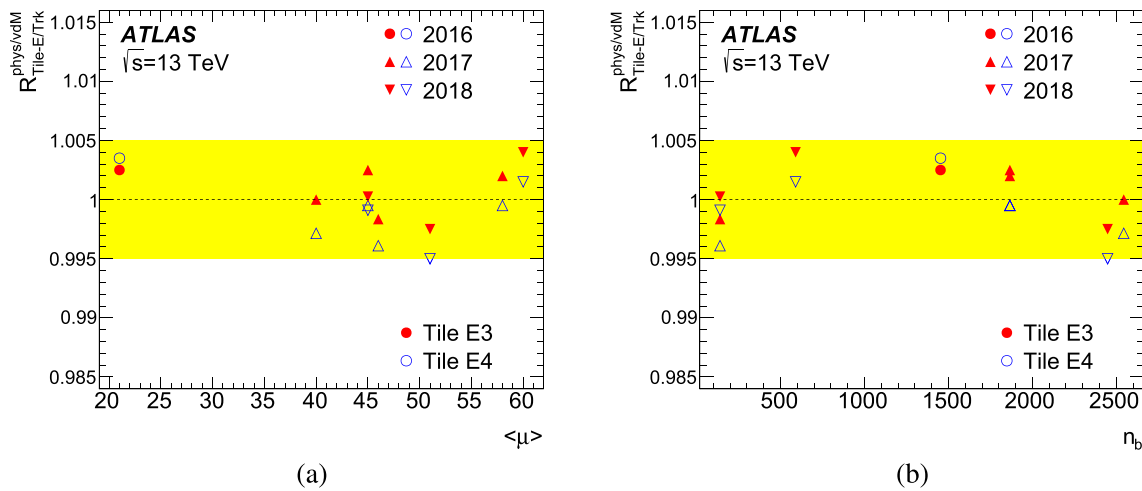


Fig. 24 Double ratios $R_{\text{Tile-E/Trk}}^{\text{phys/vdM}}$ of integrated luminosity measured by the TileCal E3 (filled red points) and E4 (open blue points) cells to that measured by track-counting in physics runs with bunch trains vs. vdM-like runs for the pairs of runs shown in Table 7, shown as a

function of (a) $\langle\mu\rangle$ in the physics run and (b) the number of colliding bunch pairs n_b in the physics run. The yellow band indicates a range of $\pm 0.5\%$

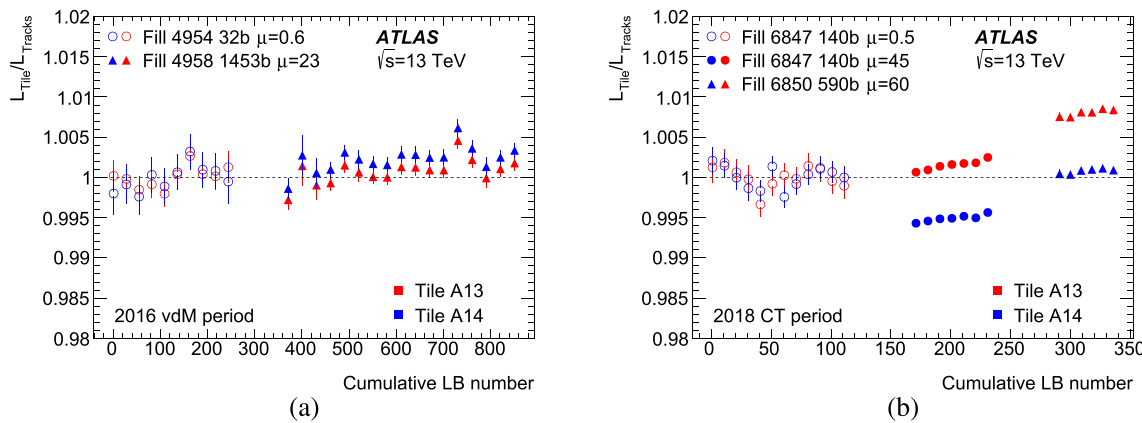


Fig. 25 Ratios of luminosity measured by the TileCal A-cells to that measured by track-counting for sequences of fills in the 2016 and 2018 calibration transfer studies. The ratios are averaged over the A- and C-side measurements and over 30 (2016 vdM period) or 10 (2018 CT period) luminosity blocks, separately for the A13 (red) and A14 (blue) cells. The uncertainties indicated by the error bars are dominated by the statistical uncertainties from the track-counting measurements. Within each plot, the ratios are shown as a function of luminosity block number,

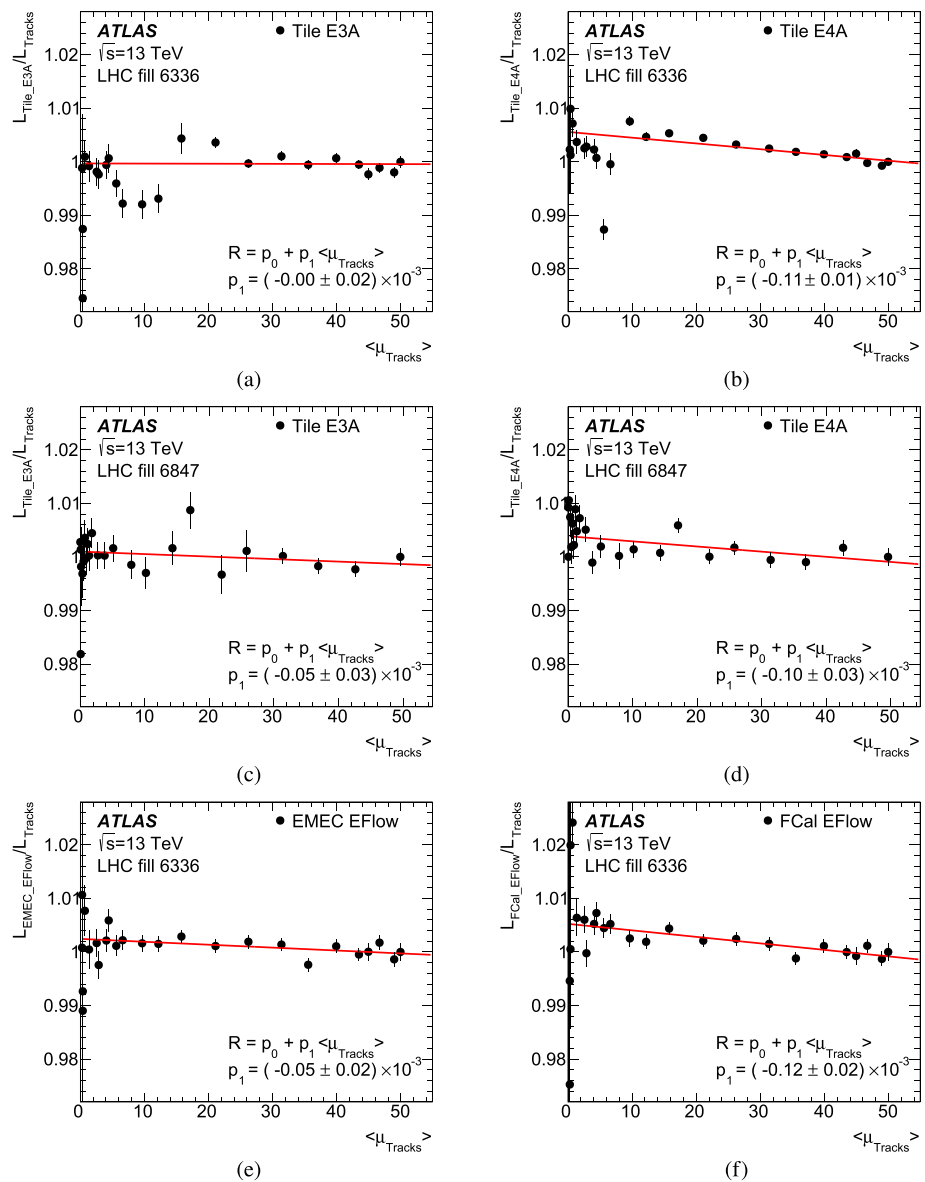
with gaps between fills to give a continuous sequence over related fills. Periods with no ratio measurements within fills (e.g. during vdM scans) are not shown, and are omitted in the luminosity block numbering. The ratios have been renormalised separately for A13 and A14 cells in each sequence so that the integrated ratios in the low-luminosity vdM-like periods are unity. The numbers of colliding bunch pairs in ATLAS and the typical μ values are indicated for each fill, and the various fill periods are plotted with different marker styles

unity for $\langle\mu\rangle \approx 50$, consistent with the results from comparing the extended low- and high- μ periods in these fills.

The LAr energy-flow luminosity measurements from EMEC and FCal were also studied in these μ -scans, determining the pedestals from the separated-beam period with almost-zero luminosity immediately before the μ -scans, and for the 2018 fill, a second separated-beam period immediately after. The resulting $R_{\text{EFlow/Trk}}$ ratios for the 2017 fill, where all colliding bunches were sampled in the special data stream, are shown in Fig. 26(e, f). They show a behaviour

very similar to that of the $R_{\text{Tile-E/Trk}}$ ratios, with small negative slopes corresponding to a negative deviation of up to 0.5% at $\langle\mu\rangle \approx 50$. Similar results were obtained for the 2018 fill, this time only sampling two of the 140 colliding bunch pairs with higher rate. These results, which use in-time event-by-event information (thus eliminating any activation contributions) from an independent detector, provide a powerful confirmation that the track-counting non-linearities between low- and high- μ in isolated bunches are smaller than 0.5%. Unfortunately the LAr signal-shaping electronics and

Fig. 26 Ratios of luminosity measured by the TileCal E-cells or LAr energy-flow to that measured by track-counting as a function of $\langle\mu\rangle$, determined from μ -scans recorded in the 140 colliding bunch fills 6336 in 2017 and 6847 in 2018: (a), (b) ratios using the A-side TileCal E3- and E4-cells in fill 6336; (c), (d) ratios using the A-side TileCal E3- and E4-cells in fill 6847; (e) ratios using the EMEC energy-flow measurement in fill 6336, (f) ratios using the FCal energy-flow measurements in fill 6336. The ratios are normalised such that the point at highest $\langle\mu\rangle$ is at unity, and the uncertainties are dominated by the statistical uncertainties in the track-counting measurements. The red lines show linear fits through the points, and the p_1 slope parameters are indicated in the legends. For the TileCal measurements, the results from the C-side E3 and E4 cells are similar



the long drift times do not allow the LAr energy-flow analysis to be extended to fills with bunch trains.

The second and third steps of the uncertainty ladder were addressed by comparing calorimeter/track-counting integrated luminosity ratios in the high- μ part of the 140 colliding-bunch fill with those in a sequence of short fills with bunch trains and increasing total numbers of bunches. The 2018 intensity ramp-up included fills with 590, 1214 (two consecutive fills) and 2448 colliding bunches before the vdM fill, and 978 and 2448 colliding-bunch fills about one week later. The resulting ratios are shown as a function of n_b for the TileCal E3 and E4 cells in Fig. 27(a). The luminosity in the 140 colliding-bunch fill is high enough that the TileCal D cells and EMEC also become sensitive, and the ratios for TileCal D5, TileCal D6 and EMEC are shown in Fig. 27(b). All ratios show a positive step of around 0.5% when going from isolated bunches to trains. Given

that this step is observed in the ratios obtained using different calorimeter technologies, it is most likely to originate from a decrease in the track-counting response in bunch-train running, e.g. because of the time-over-threshold effect in the pixel detector discussed in Sect. 5.2. As the number of bunches increases further, the ratios involving TileCal E-cells decrease, whereas those involving D-cells or EMEC remain stable within 0.1–0.2%. This is attributed to scintillator ageing in the TileCal E-cells as the accumulated luminosity increases through the intensity ramp-up period, and suggests that the track-counting response does not change significantly with increasing number of bunches, once the transition from isolated bunches to trains has been made.

Combining all steps, the ladder approach based on comparisons with TileCal D- and E-cell PMT current measurements, and LAr HV-current and energy-flow measurements, implies that the track-counting luminosity response increases

by up to 0.5% when going from low- μ to high- μ isolated bunches, and then decreases by about 0.5% going from high- μ isolated bunches to bunch trains. This is compatible with the $\pm 0.5\%$ overall shift determined from the direct approach in Sect. 6.2.

Therefore, an overall uncertainty of 0.5% was assigned to the calibration transfer correction derived from the track-counting luminosity measurements and applied to LUCID via Eq. (16). Since the same track-counting selection working point was used for all years, and no significant year-dependence was seen e.g. in Fig. 24, the same calibration transfer uncertainty was applied to all the Run 2 datasets (including 2015 where no dedicated studies were performed), and considered to be correlated between years.

7 Long-term stability

The LUCID correction strategy described in Sect. 5.3 results in a calibrated LUCID luminosity measurement for every luminosity block in every physics run. However, drifts in the response of LUCID over time that are not fully corrected by the ^{207}Bi calibration system, or drifts in the track-counting measurement used to determine the corrections to LUCID in the reference runs, could still result in a time-dependent bias in the baseline LUCID luminosity measurement. These potential biases were studied by comparing the run-integrated luminosity measurements from LUCID with independent measurements from the EMEC, FCal and TileCal D6-cell calorimeter algorithms, for every physics run in the standard GRL. Since the calorimeter measurements cannot be calibrated at low luminosity in the vdM run, they were normalised, or ‘anchored’ to agree with the run-integrated track-counting measurements in up to ten physics runs close to the vdM fill, such that discrepancies between the LUCID and calorimeter measurements in physics runs far from the vdM fill are indicative of long-term drifts in either the LUCID or calorimeter measurements.

Studies of the ratios of the FCal luminosity measurements to those from track-counting, EMEC and TileCal D6 cells as a function of the bunch-integrated instantaneous luminosity $\mathcal{L}_{\text{inst}}$ within individual runs, and comparisons of runs with different numbers of colliding bunches, showed that the FCal measurements suffer from a reproducible non-linearity that strongly depends on $\mathcal{L}_{\text{inst}}$. Compared to track counting, the FCal response increases by about 2% when the luminosity decreases from 15×10^{33} to $5 \times 10^{33} \text{ cm}^{-2}\text{s}^{-1}$; the lower the luminosity, the steeper the increase in FCal response. Over the luminosity range of interest for the physics data-taking (excluding the vdM regime and the low- μ data discussed in Sect. 9), the evolution of the uncorrected FCal/track-counting luminosity ratio is well described by a quadratic function of the uncorrected FCal instantaneous luminosity. Since the

studies in Sect. 6 showed that non-linearity in the track-counting measurement is small, the FCal data were corrected as a function of instantaneous luminosity so as to agree with track-counting in a single reference fill. For 2017–2018 FCal data, the correction parameters were derived from a single long physics fill recorded in 2017, and the 2015–2016 data were similarly corrected using a single fill from 2016. These corrections significantly improved the consistency of FCal and track-counting measurements throughout the data-taking period, and are applied to all the FCal data shown below. In addition, significant discrepancies were found between A- and C-side FCal data in 2015–2016, with C-side data agreeing much better with other luminosity measurements. The A-side data were therefore discarded, and only the C-side data used in the analysis below. In 2017–2018, the two sides agree well, and their average was used in the comparison with other luminosity measurements.

The calibration anchoring procedure, which was carried out after correcting the FCal measurements, is illustrated in Fig. 28. It shows the per-run integrated luminosity ratios between calorimeter and track-counting measurements for the selected physics runs close to the vdM fill, normalised so that their unweighted average¹² over all selected runs is unity. Only fills with at least 500 colliding bunch pairs (400 in 2015) and at least 1 h of data-taking were considered. The RMS of each set of calorimeter/track-counting ratios gives a measure of the short-term variability for each calorimeter, and is shown in the legend. These variations are caused partly by differences in the characteristics of each physics fill, in particular the fill duration, which affects the importance of activation build up, especially in the EMEC and FCal. The variations translate into ambiguities in the calorimeter luminosity normalisation, and were reduced by averaging over ten fills. In 2015 and 2016, the vdM fill was performed early in the running period, before the LHC intensity ramp-up to the full number of colliding bunches had been completed. In 2015, the first three fills have only 446 or 447 colliding bunches, compared to 1021 at the end of the sequence. The instantaneous luminosity in the first three fills is atypically low, below the range covered by the FCal intensity correction derived from 2016 data, and leads to the anomalously high FCal/track-counting ratios in these fills. In 2016, the number of colliding bunches increased from 589 to 1740, but the per-bunch instantaneous luminosity was also higher, leading to smaller variations. To account for the residual uncertainties in normalising the calorimeter luminosity measurements, the largest RMS value from any calorimeter/track-counting calibration seen in each year (excluding the FCal data in 2015)

¹² Since the intention is to smooth out possible run-to-run variations in the calorimeter/track-counting luminosity ratios, the measurements were not weighted according to the integrated luminosity in each run.

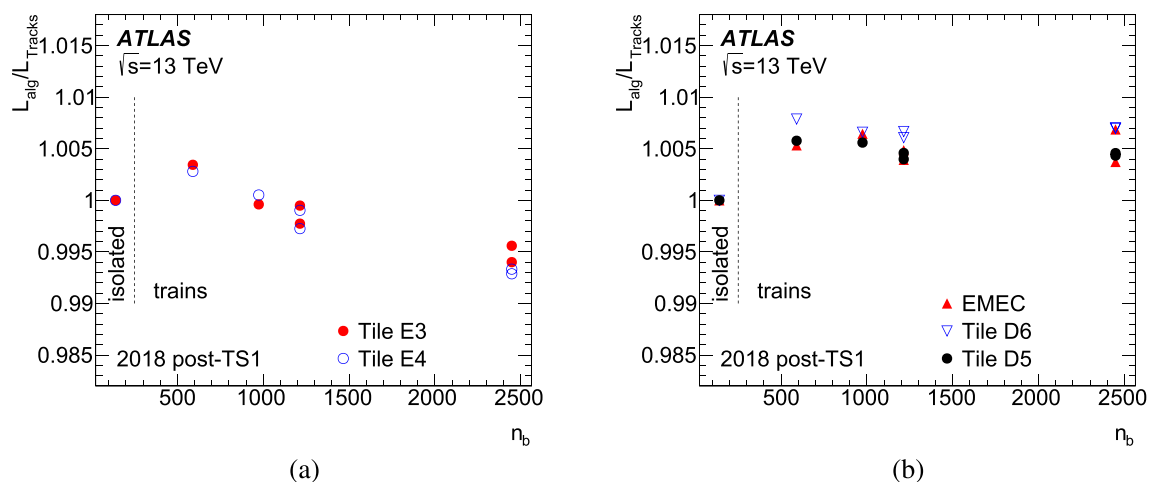


Fig. 27 Ratios of integrated luminosity measured by (a) the TileCal E3 and E4 cells, and (b) the EMEC, TileCal D6 and D5 cells, to that measured by track-counting as a function of the number of colliding bunch pairs in high- μ fills in the period after the 2018 technical stop

TS1. The ratios are averaged over A- and C-side calorimeter measurements and normalised to the high- μ part of the 140 isolated-bunch CT fill 6847 (the leftmost point). All the other fills feature bunch trains with 25ns spacing

was taken as the ‘calibration anchoring’ uncertainty for that year, and is shown in Table 8.

The anchored calorimeter measurements were then compared with LUCID measurements in each run to assess the long-term stability uncertainty. Figure 29 shows the per-run integrated luminosity differences between each calorimeter measurement and LUCID as a function of the fractional cumulative integrated luminosity in each data-taking year, for runs with at least 500 colliding bunch pairs and 1 h of data-taking. Except in the early parts of the years, most of the variations are well within $\pm 1\%$ in 2015, and within $\pm 0.5\%$ in subsequent years. In some periods, correlated trends common to all of the calorimeter vs. LUCID comparisons are visible, suggesting that the differences are caused by variations in the LUCID luminosity measurements.

Figure 29 demonstrates the run-to-run spread between luminosity measurements and their relative trends as a function of time, but shows all runs with equal weight. Figure 30 shows an alternative presentation of the same data, showing histograms of the per-run integrated luminosity differences, weighted by the integrated luminosity of each run. The RMS values of these distributions reflect the spread also visible in Fig. 29, but with higher weight given to longer runs. The means represent the fractional difference in integrated luminosity over the entire year obtained from each calorimeter measurement compared to LUCID. Since physics analyses require the total integrated luminosity of the dataset, these differences in integrated luminosity represent the best metric for assessing the consistency of different luminosity measurements, and hence the potential error in the baseline LUCID luminosity measurement integrated over the whole year. The long-term stability uncertainty for each year

quoted in Table 8 was therefore defined as the largest difference in year-integrated luminosity between LUCID and any calorimeter measurement. These differences are in the range 0.1–0.2%, and originate from comparisons of LUCID with different detectors in the different years.

The calibration anchoring procedure, including the uncertainty from the RMS over ten runs, protects against a fortuitous choice of anchoring run leading to an accidentally small difference in the total integrated luminosities. The track-counting luminosity measurements (shown in Fig. 20) were not considered in these comparisons, as the correction of LUCID to track-counting performed with multiple epochs per year makes them not fully independent. A comparison of the trends seen in Fig. 29 with those in Fig. 20 also suggests that the residual differences between LUCID and the calorimeters are rather similar to those between LUCID and track-counting.

The calibrations of the different luminosity measurements are in principle sensitive to shifts of the mean longitudinal position of the luminous region with respect to the nominal ATLAS interaction point. Studies from a test made in 2016, where the mean z -position was moved over the range $|z| < 300$ mm, showed that these effects vary across the different detectors, but that they are all negligible for the mean z -shifts of up to $\pm O(10)$ mm seen in physics conditions, especially for algorithms that average measurements from both sides of the ATLAS detector.

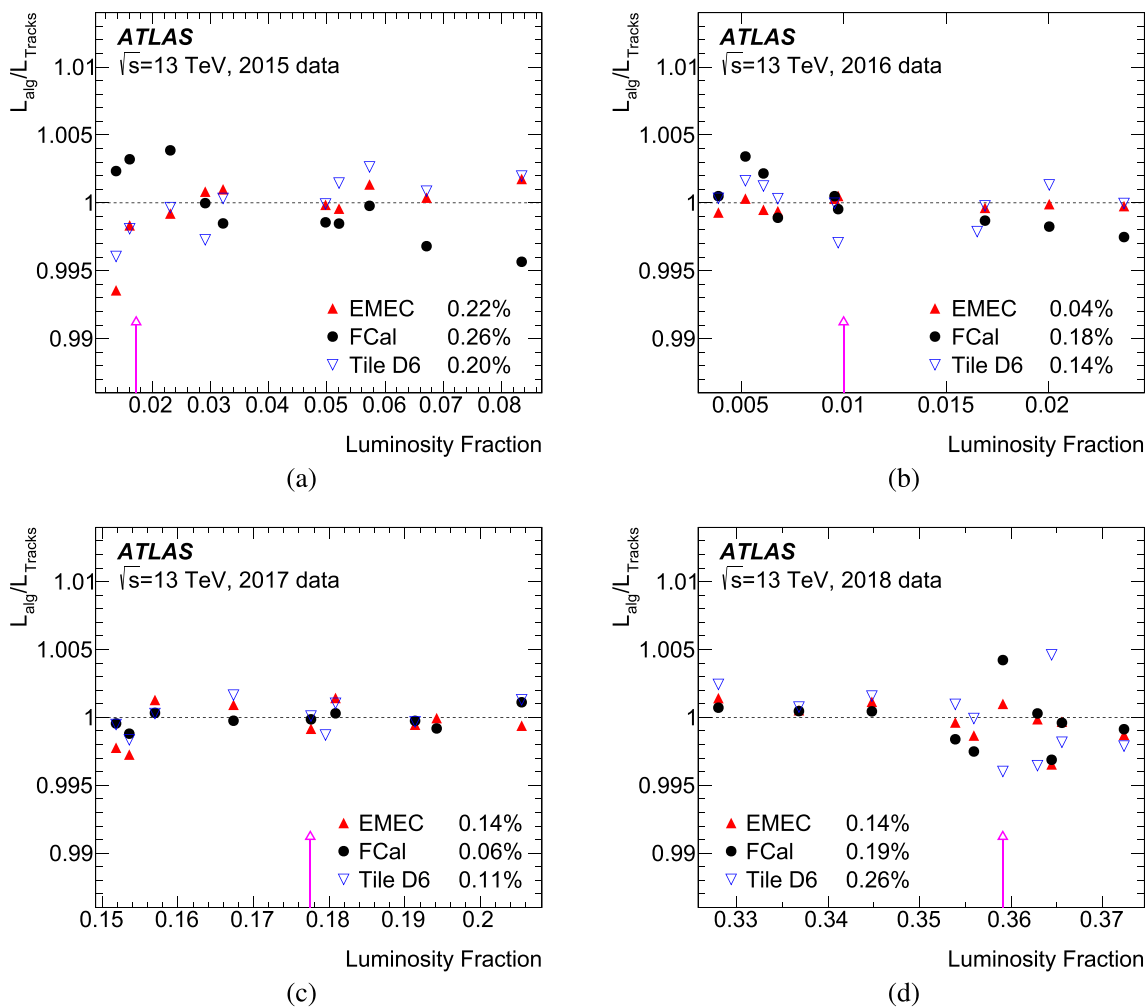


Fig. 28 Ratios of the per-run integrated luminosity measured by the EMEC, FCal and TileCal D6 algorithms to that measured by track-counting in the ten physics runs surrounding the vdM run, plotted as functions of the fractional cumulative integrated luminosity in each data-taking year. The positions of the vdM fills are shown by the purple

arrows. The ratios are each normalised so that the unweighted average over all ten runs is unity, and the legends show the RMS difference between the calorimeter and track-counting measurements in each case. Ratios which are not available for a particular detector and run are not plotted and removed from the average

8 Uncertainties and results

The various sources of uncertainty in the Run 2 luminosity calibration have been discussed in Sects. 4–7, in terms of the separate datasets from each data-taking year, each with its own absolute vdM calibration. However, most ATLAS physics analyses treat the full Run 2 $\sqrt{s} = 13$ TeV pp collision data sample as a single dataset, and therefore require the uncertainty in the total integrated luminosity of this combined dataset. The uncertainty correlations between years are discussed in Sect. 8.1, and the final uncertainties are derived and tabulated in Sect. 8.2. The consistency between the different years, and the stability as a function of $\langle\mu\rangle$, have been studied via comparisons with relative luminosity measurements derived from the rates of reconstructed $Z \rightarrow ee$ and $Z \rightarrow \mu\mu$

events (Z -counting). These comparisons are described in Sect. 8.3.

8.1 Uncertainty correlations between years

Since the absolute luminosity scale was calibrated separately for each year with an independent vdM scan session, a large part of the associated uncertainty is uncorrelated between years. The bunch-by-bunch consistency, scan-to-scan reproducibility and reference specific luminosity uncertainties are driven by the internal consistency of each set of vdM scans, and were considered to be uncorrelated, as were the beam position jitter and orbit-drift correction uncertainties, which depend on the specifics of the jitter and drifts observed in each scan session. The uncertainties in the FBCT and DCCT cal-

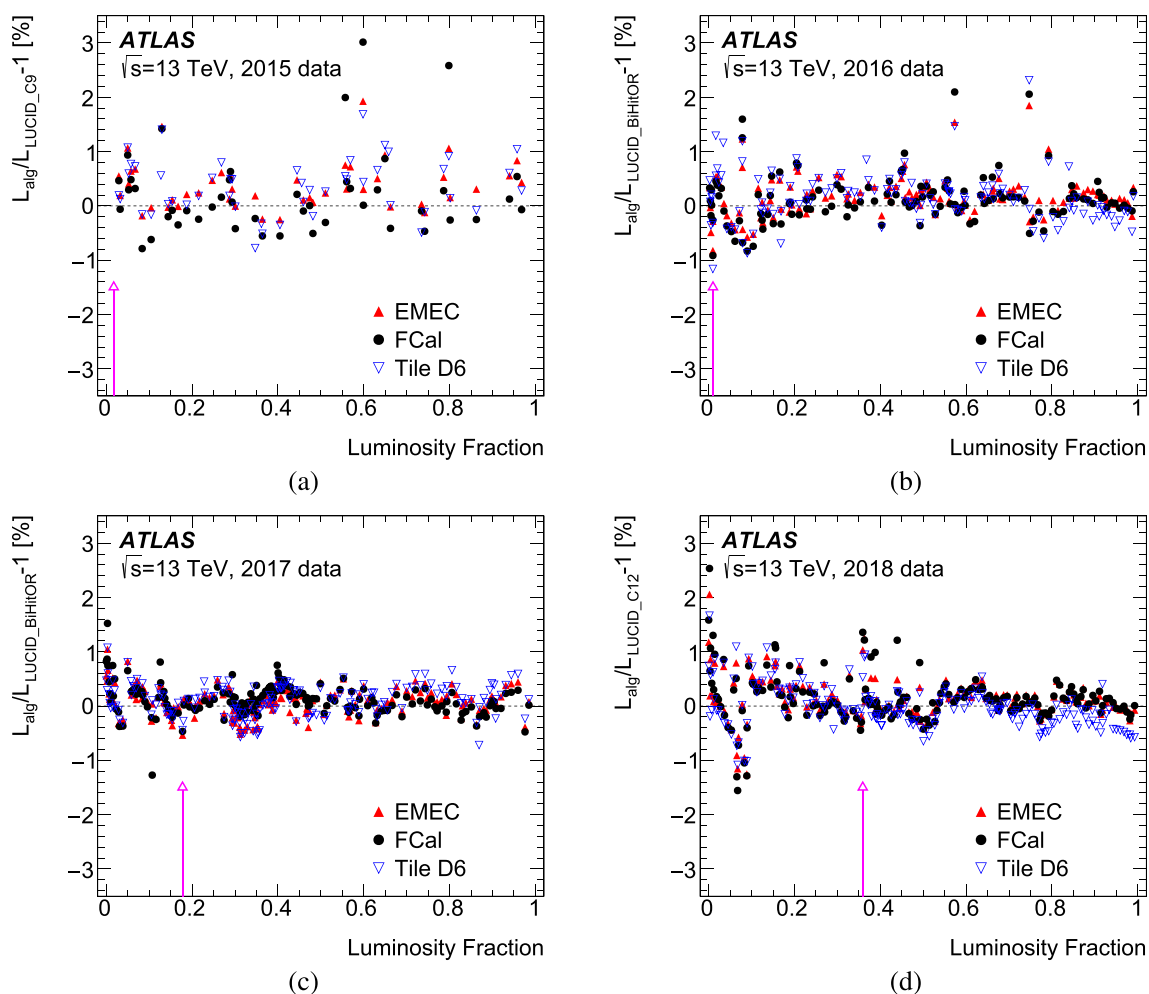


Fig. 29 Fractional differences in run-integrated luminosity between the EMEC, FCal and TileCal D6 luminosity measurements and the baseline LUCID luminosity measurement, plotted as functions of the fractional cumulative integrated luminosity in each data-taking year.

ibration and ghost/satellite measurements are dominated by systematic instrumental effects and were considered correlated. The non-factorisation uncertainty was taken to be correlated, because the same methodology was used to evaluate it in each year, and a common underlying cause is likely. For the same reasons, the beam–beam effects, emittance growth correction, background subtraction, fit model and ID length scale uncertainties were treated as correlated between years. The results of the non-linear length scale fits accounting for magnetic non-linearity vary significantly between years, with no consistent trend or bias being visible in Fig. 11, so the magnetic non-linearity uncertainty was treated as uncorrelated between years. An alternative treatment, applying the baseline magnetic non-linearity fit results shown in Fig. 11 as correlated corrections to the σ_{vis} values in each year, gives a shift in the total Run 2 integrated luminosity which is smaller than the uncertainty from treating the years as uncorrelated,

The positions of the vdM fills are shown by the purple arrows. Only runs with at least 500 colliding-bunch pairs and 1 h of data-taking are shown

due to the non-linearity correction for 2018 having the opposite sign to those for 2015–2017. Applying the same procedure to the alternative magnetic non-linearity fits discussed in Sect. 4.10 also gives smaller uncertainties than the uncorrelated treatment. The separate uncertainty in the linear length scale calibration is statistical in nature and hence uncorrelated between years.

The calibration transfer uncertainty was derived from comparisons of TileCal E-cell and track-counting data at multiple points throughout 2016–2018, and the resulting uncertainty was taken to be correlated between years, as discussed at the end of Sect. 6. The calibration anchoring and long-term stability uncertainties were obtained by taking the largest difference between a reference measurement from LUCID or track-counting and any calorimeter-based measurement. These comparisons exhibit significant scatter, with the largest differences having different signs and

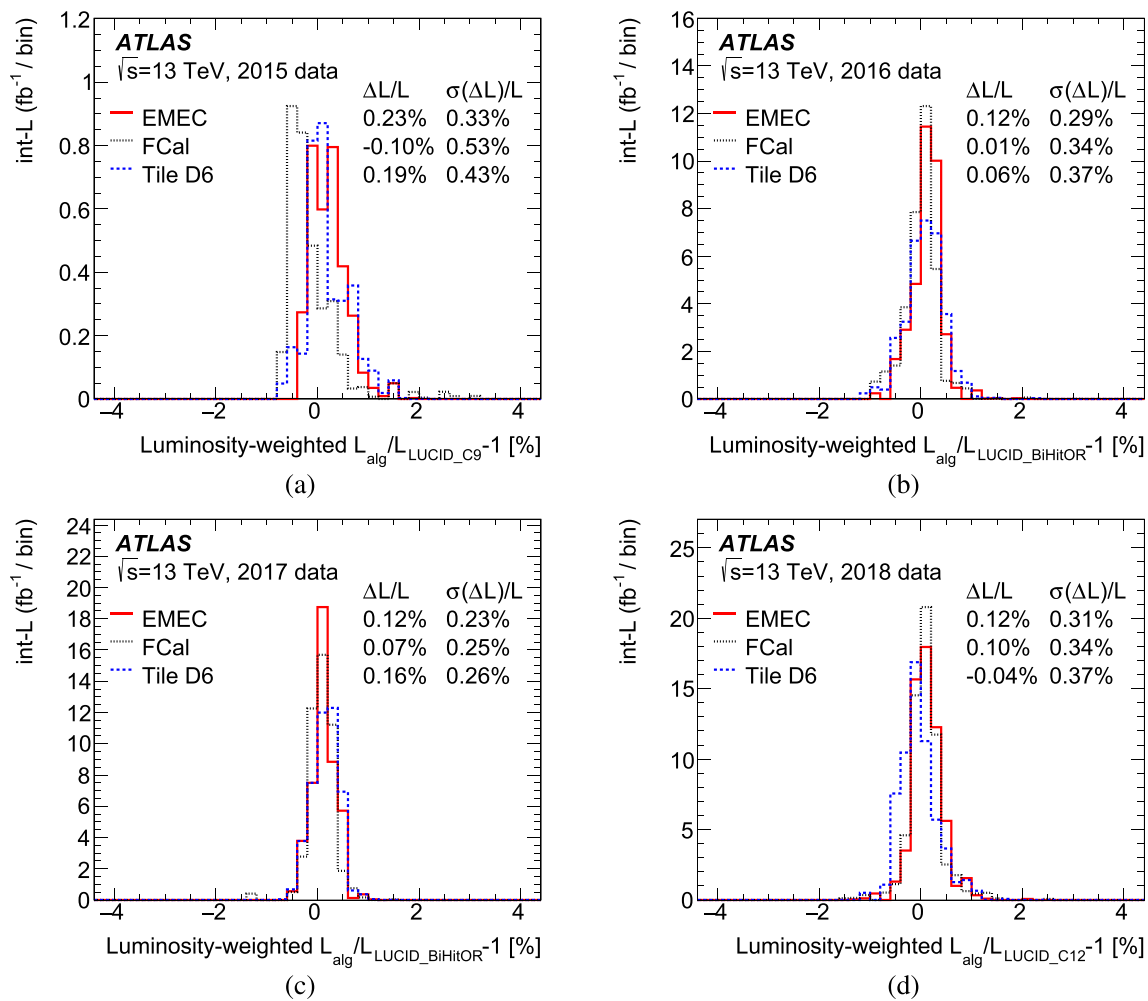


Fig. 30 Distributions of relative differences in run-integrated luminosity between the EMEC, FCal and TileCal D6 luminosity measurements and the baseline LUCID luminosity measurement, weighted by the inte-

grated luminosity in each run, for each data-taking year. The mean and RMS of each of the distributions are given in the legend

coming from different calorimeter measurements across the years, and the corresponding uncertainties were taken to be uncorrelated between years.

The sensitivity of the final combined uncertainty to the above assumptions was further investigated by separately considering the beam position jitter, reference specific luminosity, calibration anchoring and long-term stability uncertainties to be correlated rather than uncorrelated between years. None of these variations increased the size of the total Run 2 luminosity uncertainty by more than 4% of its original value. Taking the non-factorisation uncertainty to be uncorrelated rather than correlated reduced the total uncertainty by 2%. The total uncertainty is therefore rather insensitive to the correlations assumed for these contributions.

8.2 Results for the $\sqrt{s} = 13$ TeV Run 2 dataset

The integrated luminosities and associated uncertainties for the high-pileup pp collision data sample at $\sqrt{s} = 13$ TeV from each year of Run 2 data-taking are summarised in Table 8. The data samples are those recorded by ATLAS and passing the standard data quality requirements for ATLAS physics analyses [7], and are significantly smaller than those for the luminosity delivered to ATLAS shown in Table 1. In 2017 and 2018, they do not include the 338.1 pb^{-1} of low-pileup data discussed in Sect. 9.

The total Run 2 integrated luminosity \mathcal{L}_{tot} is the sum of the integrated luminosities \mathcal{L}_i for each individual year:

$$\mathcal{L}_{\text{tot}} = \sum_i \mathcal{L}_i$$

Table 8 Summary of the integrated luminosities (after standard data-quality requirements) and uncertainties for the calibration of each individual year of the Run 2 pp data sample at $\sqrt{s} = 13$ TeV and the full combined sample. As well as the integrated luminosities and total uncertainties, the table gives the breakdown and total of contributions to the

absolute vdM calibration, the additional uncertainties for the physics data sample, and the total relative uncertainty in percent. Contributions marked * are considered fully correlated between years, and the other uncertainties are considered uncorrelated

Data sample	2015	2016	2017	2018	Comb.
Integrated luminosity [fb^{-1}]	3.24	33.40	44.63	58.79	140.07
Total uncertainty [fb^{-1}]	0.04	0.30	0.50	0.64	1.17
Uncertainty contributions [%]					
Statistical uncertainty	0.07	0.02	0.02	0.03	0.01
Fit model*	0.14	0.08	0.09	0.17	0.12
Background subtraction*	0.06	0.11	0.19	0.11	0.13
FBCT bunch-by-bunch fractions*	0.07	0.09	0.07	0.07	0.07
Ghost-charge and satellite bunches*	0.04	0.04	0.02	0.09	0.05
DCCT calibration*	0.20	0.20	0.20	0.20	0.20
Orbit-drift correction	0.05	0.02	0.02	0.01	0.01
Beam position jitter	0.20	0.22	0.20	0.23	0.13
Non-factorisation effects*	0.60	0.30	0.10	0.30	0.24
Beam–beam effects*	0.27	0.25	0.26	0.26	0.26
Emittance growth correction*	0.04	0.02	0.09	0.02	0.04
Length scale calibration	0.03	0.06	0.04	0.04	0.03
Inner detector length scale*	0.12	0.12	0.12	0.12	0.12
Magnetic non-linearity	0.37	0.07	0.34	0.60	0.27
Bunch-by-bunch σ_{vis} consistency	0.44	0.28	0.19	0.00	0.09
Scan-to-scan reproducibility	0.09	0.18	0.71	0.30	0.26
Reference specific luminosity	0.13	0.29	0.30	0.31	0.18
Subtotal vdM calibration	0.96	0.70	0.99	0.93	0.65
Calibration transfer*	0.50	0.50	0.50	0.50	0.50
Calibration anchoring	0.22	0.18	0.14	0.26	0.13
Long-term stability	0.23	0.12	0.16	0.12	0.08
Total uncertainty [%]	1.13	0.89	1.13	1.10	0.83

and the absolute uncertainty in the total luminosity, $\sigma_{\mathcal{L}_{\text{tot}}}$, is given by standard error propagation as

$$\sigma_{\mathcal{L}_{\text{tot}}}^2 = \mathbf{e}^T \mathbf{V}_L \mathbf{e}.$$

Here, \mathbf{V}_L is the covariance matrix of the absolute luminosity uncertainties for the different years, and \mathbf{e} is a column vector with unit entries.¹³ The covariance matrix is made up of the sum of terms corresponding to each uncertainty source in Table 8; uncorrelated uncertainties give rise to terms on the diagonal, whilst correlated sources are represented by terms with non-zero off-diagonal entries.

The results of the combination are shown in the right-most column in Table 8. The integrated luminosity of the full Run 2 sample is $140.1 \pm 1.2 \text{ fb}^{-1}$, corresponding to a relative uncertainty of 0.83%. This uncertainty is smaller than that

for any individual year, reflecting the fact that the total uncertainty is not dominated by effects that are correlated between years. The covariance matrix \mathbf{V}_L can also be expressed as $\mathbf{V}_L = \sigma_L \mathbf{C} \sigma_L^T$, where the vector σ_L of total absolute uncertainties on \mathcal{L}_i and (symmetric) correlation matrix \mathbf{C} are given by

$$\sigma_L = \begin{pmatrix} 0.0367 \\ 0.296 \\ 0.504 \\ 0.644 \end{pmatrix} \text{fb}^{-1}$$

$$\mathbf{C} = \begin{pmatrix} 1.000 & & & \\ 0.579 & 1.000 & & \\ 0.368 & 0.437 & 1.000 & \\ 0.480 & 0.510 & 0.362 & 1.000 \end{pmatrix}.$$

The off-diagonal elements of the correlation matrix are all smaller than 0.6, and the relative error of 0.83% in the total luminosity is significantly smaller than that for any individ-

¹³ In general, $\sigma_{\mathcal{L}_{\text{tot}}}^2 = \mathbf{D}^T \mathbf{V}_L \mathbf{D}$ where the i entries of \mathbf{D} are $d\mathcal{L}_{\text{tot}}/d\mathcal{L}_i$, but since these derivatives are all unity, $\mathbf{D} = \{1, 1, 1, 1\}$.

Table 9 Increase in the integrated luminosity (after standard data-quality requirements) of the $\sqrt{s} = 13\text{TeV}$ pp data sample recorded in each year of Run 2 ATLAS data-taking, comparing the results of this analysis with the preliminary calibration reported in Ref. [40]

Year	2015	2016	2017	2018	Comb.
$\Delta\mathcal{L}/\mathcal{L}$ [%]	+0.93	+1.23	+0.73	+0.59	+0.80

ual year. The largest single uncertainty in the total luminosity is 0.5% from calibration transfer. The total uncertainty from the absolute vdM calibration is 0.65%, and the largest contributions come from non-factorisation corrections, beam–beam effects, magnetic non-linearity and scan-to-scan reproducibility, all four of which contribute at a comparable level. The beam–beam correction and the evaluation of potential biases from magnetic non-linearity have been refined significantly since the Run 1 luminosity measurements [2,3] and the preliminary Run 2 luminosity calibration [40] used for most ATLAS Run 2 physics analyses to date. However, the total uncertainty in the integrated luminosity is significantly smaller than those achieved previously.

The changes to the integrated luminosities of the standard Run 2 physics samples in each year compared to the preliminary calibration are listed in Table 9. The largest contributions come from the refinements in the vdM calibration, but changes in the calibration transfer procedure and other effects also contribute. The increase for the full Run 2 sample is 0.8%, and that for the 2015–2016 sample is 1.2%. The uncertainty has been reduced by a factor two compared with the preliminary calibration, thanks to improvements in the calibration transfer and long-term stability analyses, as well as the changes to the vdM calibration. If the refinements in the absolute vdM calibration (in particular the revised beam–beam interaction treatment and the GP4+G fit model) were applied to the Run 1 analyses, the corresponding integrated luminosities would increase by 0.5–1.0%, well within the uncertainties assigned to these measurements.

8.3 Comparison with Z -counting measurements

The continuous monitoring of high-rate physics processes, such as the production of Z bosons, provides another potential luminosity measurement. The leptonic decays $Z \rightarrow ee$ and $Z \rightarrow \mu\mu$ are particularly attractive, as the distinctive signature is easy to trigger on and reconstruct, has less than 1% background [41], and the two lepton channels can be compared for internal consistency checks. The lepton trigger and reconstruction efficiencies can be measured in-situ using tag-and-probe techniques exploiting the two leptons in each event [38,42], and the rate of about 10Hz of reconstructed events per lepton flavour at $\sqrt{s} = 13\text{TeV}$ and $\mathcal{L}_{\text{inst}} = 10^{34}\text{cm}^{-2}\text{s}^{-1}$ gives a statistical precision well

below 1% for runs lasting several hours. However, the Z production cross-section is only predicted to a precision of 3–4% due to uncertainties in the proton parton distribution functions [43], so this method is most useful as a relative luminosity measurement, after normalisation to an absolutely calibrated reference. In this mode, it can be used to study the stability with time, or with respect to other parameters such as pileup $\langle\mu\rangle$.

Within ATLAS, Z -counting has been used both within the offline data-quality framework for giving fast feedback on the delivered luminosity (for example in comparisons with CMS), and for offline studies. The method is described in detail in Ref. [44], where the results are compared with the preliminary baseline Run 2 luminosity measurement. A brief overview of the Z -counting luminosity measurement is given here, together with a comparison of the results with the updated luminosity calibration described in this paper. This serves as a validation of the stability of the calibration with time and pileup $\langle\mu\rangle$.

Selected events were required to contain two identified leptons (electrons or muons) of the same flavour and opposite charge, each having $p_T > 27\text{GeV}$ and $|\eta| < 2.4$, and satisfying track-based isolation criteria, and with at least one lepton matched to a corresponding trigger signature. The dilepton invariant mass $m_{\ell\ell}$ was required to lie in the range $66 < m_{\ell\ell} < 116\text{GeV}$. The resulting samples are around 99.5% pure in $Z \rightarrow \ell\ell$ events, and the small background was estimated using simulation and subtracted. Within each luminosity block, the lepton trigger and reconstruction efficiencies were estimated from data, automatically accounting for variations due to transient detector problems or the variation of efficiencies with pileup, for example. Corrections to account for effects not included in the tag-and-probe formalism were estimated using simulation. These corrections amount to 1–2% for $Z \rightarrow \mu\mu$, and up to about 10% for $Z \rightarrow ee$, where a larger fraction of the lepton inefficiencies are not captured by the tag-and-probe procedure. The resulting measurements have a statistical precision of 2–5% per 20 min period, and show excellent consistency between electron and muon channels, both as a function of time and $\langle\mu\rangle$. The ratios of same-year-integrated luminosities estimated from $Z \rightarrow ee$ and $Z \rightarrow \mu\mu$ (where the Z production cross-section cancels out) are around 0.992–0.993 for all years, consistent with unity within the residual uncertainties in the lepton reconstruction and trigger efficiencies.

Ratios of the run-integrated Z -counting luminosity measurements from $Z \rightarrow ee$ and $Z \rightarrow \mu\mu$ events to the corresponding ATLAS baseline luminosity measurements are shown in Fig. 31. The Z -counting measurements are each normalised to the year-integrated baseline measurement. The ratios for the two channels are similar, and show little residual structure, confirming that the calibration of the baseline luminosity measurement is stable in time. Figure 32 shows

a comparison of the combined Z -counting ($Z \rightarrow ee$ and $Z \rightarrow \mu\mu$) and baseline luminosity measurements over the complete Run 2 data-taking period, where the Z -counting measurement has been normalised to the baseline integrated luminosity of the full sample. This comparison is therefore sensitive to differences in the baseline luminosity calibration between years, and tests the consistency of the absolute vdM calibrations performed in each year. Year-averaged systematic differences of -0.5% , 0.2% , 0.4% and -0.4% for 2015, 2016, 2017 and 2018 are visible between the Z -counting and baseline luminosity measurements. The consistency of these differences with the uncertainties detailed in Sect. 8.2 was quantified using a χ^2 defined as

$$\chi^2 = \mathbf{\Delta}^T (\mathbf{V}_L)^{-1} \mathbf{\Delta}$$

where $\mathbf{\Delta}$ is the vector of per-year differences in the absolute integrated luminosity measured by Z -counting and the baseline method, and \mathbf{V}_L is the covariance matrix of the baseline luminosity measurements (neglecting statistical and systematic uncertainties in the Z -counting result). The resulting χ^2 is 0.8 for three degrees of freedom, confirming the good compatibility of baseline and Z -counting luminosity measurements.

The Z -counting and baseline luminosity measurements have also been compared as a function of pileup $\langle\mu\rangle$, as shown in Fig. 33. In 2015, 2016 and 2018, these ratios show very little pileup dependence, except at the extreme ends of the distributions, which contain only a very small fraction of the data. In 2017, a trend is visible, with the Z -counting luminosity measurement being higher than the baseline at low μ and lower at high μ . However, the size of these variations does not exceed the $\pm 0.5\%$ calibration transfer uncertainty, and this trend is not visible in other years. The distributions are presented separately for each year and not combined, as the year-dependence visible in Fig. 32 combined with the different $\langle\mu\rangle$ profile in each year would produce a spurious correlation, not connected to μ -dependence within an individual year.

In summary, the comparisons with Z -counting do not reveal any unexpected time- or $\langle\mu\rangle$ -dependence in the baseline luminosity calibration, and serve as an important validation of the calibration transfer procedures and overall uncertainty estimates presented above.

9 Luminosity calibration for low-pileup datasets

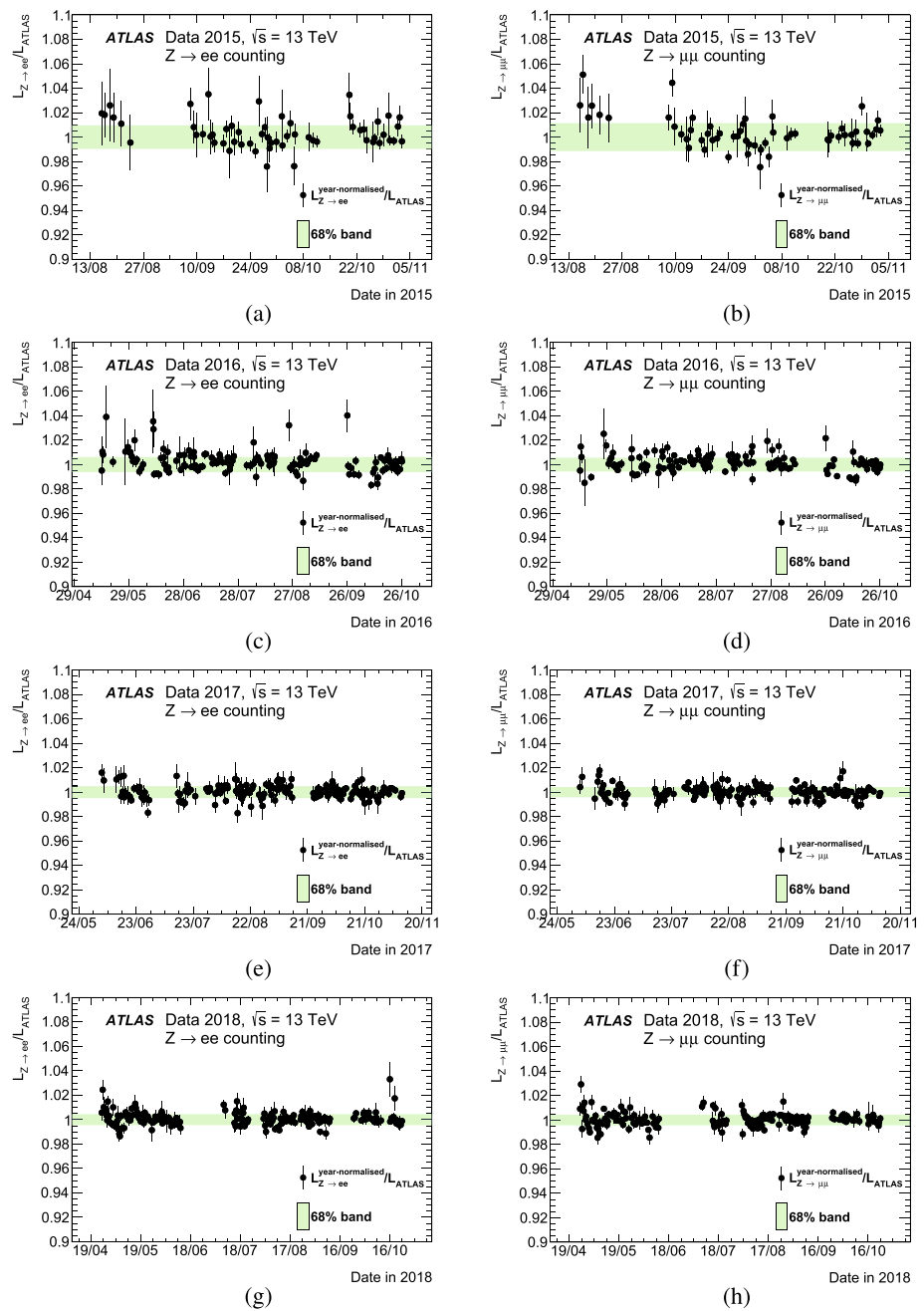
During Run 2, five-day periods in both November 2017 and July 2018 were devoted to recording $\sqrt{s} = 13$ TeV pp collisions with reduced instantaneous luminosity in ATLAS. In these periods, the beams were partially separated in the transverse plane at the ATLAS interaction point to give $\langle\mu\rangle \approx 2$, and the separation was adjusted continuously to maintain this

level of pileup throughout the fills, which had durations of up to 29 h. The lower level of pileup significantly improves the resolution of the ATLAS missing transverse momentum and hadronic recoil measurements, making these data samples particularly useful for precision measurements of single W/Z boson production [45].

The luminosity calibration for these data samples was derived in a similar way as for the $\sqrt{s} = 13$ TeV high-pileup data, using the LUCID BiHitOR algorithm in 2017 and the single-PMT C12 algorithm in 2018. The absolute calibrations were obtained from the vdM analysis described in Sect. 4. A dedicated calibration transfer correction was determined from the ratio of LUCID to track-counting luminosities in long reference fills within each low-pileup period. As the $\langle\mu\rangle$ values were approximately constant throughout these fills, the p_1 parameter of Eq. (16) was fixed to zero, reducing the correction to a simple scaling of the LUCID luminosity by p_0 . The values of p_0 were determined to be 0.987 for the 2017 dataset and 1.009 for 2018. The larger value in 2018 compared to 2017 reflects the LHC beam crossing angle dependence of the response of individual LUCID PMTs, which depends on the azimuthal ϕ -position of the PMT around the beam pipe (see Sect. 3.1). Since the HitOR algorithm used in 2017 combines PMTs which are distributed approximately ϕ -symmetrically around the beam pipe, the crossing-angle effect mostly averages out. In 2018, the sign of the vertical boost from the crossing angle was such that it downwardly biased the response of the single-PMT C12 algorithm, necessitating a positive correction. The remaining correction is dominated by the effect of running with bunch trains at $\langle\mu\rangle \approx 2$, rather than isolated bunches with $\langle\mu\rangle \approx 0.5$ as in the vdM fills.

This correction procedure assumes that the track-counting luminosity response does not change between the vdM regime and $\langle\mu\rangle \approx 2$ physics running with bunch trains. In the same way as discussed for the high-pileup calibration transfer correction in Sect. 6, this assumption was probed via comparisons of luminosity measurements from TileCal E3 and E4 cells with those from track-counting. The last LHC fill of the June 2018 intensity ramp-up described in Sect. 6 (fill 6860, with 2448 colliding bunch pairs) was recorded two days before the 2018 vdM run, and included 6 h of running at $\langle\mu\rangle \approx 2$ after 1 h of high-pileup running and a μ -scan. This high-luminosity running resulted in a slowly decaying activation contribution to the TileCal luminosity signal (amounting to 1–2% of the actual luminosity at the start of the $\langle\mu\rangle \approx 2$ period), which was corrected using the activation model described in Sect. 6.1. The resulting ratios of TileCal E-cell to track-counting luminosity measurements as a function of luminosity block number in the $\langle\mu\rangle \approx 2$ physics and vdM fills are shown in Fig. 34(a). The average ratios are about 0.5% higher in the physics fill for E3, and somewhat

Fig. 31 Ratios of the run-integrated Z-counting and baseline ATLAS luminosity measurements as a function of run date within each year of Run 2 data-taking, showing (a, c, e, g) $Z \rightarrow ee$ and (b, d, f, h) $Z \rightarrow \mu\mu$ measurements separately. The Z-counting measurements within each year and lepton channel are each normalised to the year-integrated baseline luminosity measurement. The error bars show statistical uncertainties only, and the green bands contain 68% of all runs centred around the mean



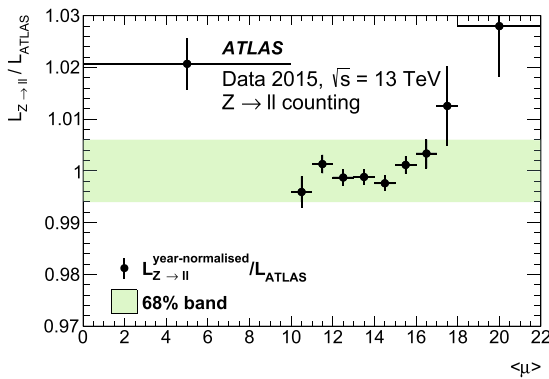
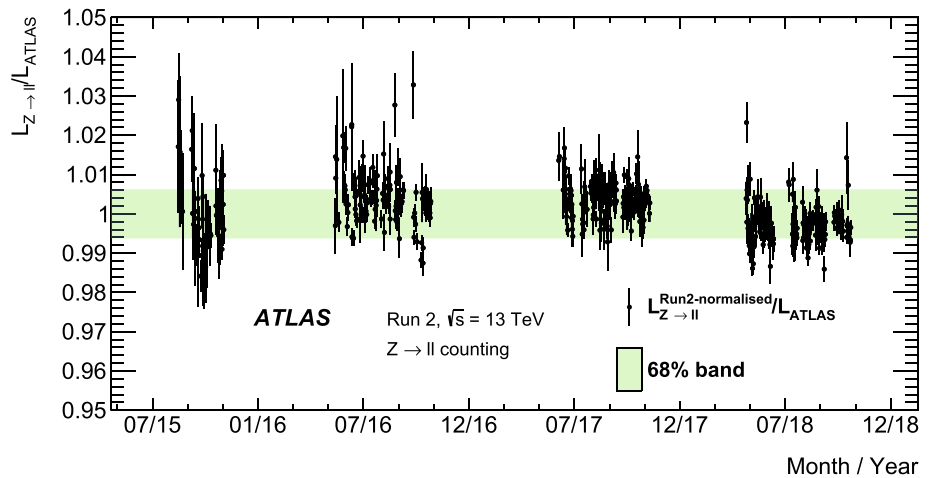
smaller for E4, suggesting that the change in track-counting response between these two regimes is at most 0.5%.

A second constraint was obtained from a μ -scan in the earlier fill 6854 with 1214 colliding bunch pairs, which was recorded two days after the 140 bunch calibration transfer fill 6847 with vdM-like conditions discussed in Sect. 6. Figure 34(b) shows the ratio of activation-corrected TileCal E3A to track-counting luminosities as a function of $\langle\mu\rangle$ in this scan, normalised to the ratio measured in the $\langle\mu\rangle = 0.5$ part of fill 6847. Although the statistical precision of the ratios at low $\langle\mu\rangle$ is limited (as only a few minutes were spent at each scan point), the intercept p_0 of the linear fit of the ratio as a function of $\langle\mu\rangle$ can be interpreted as a measurement

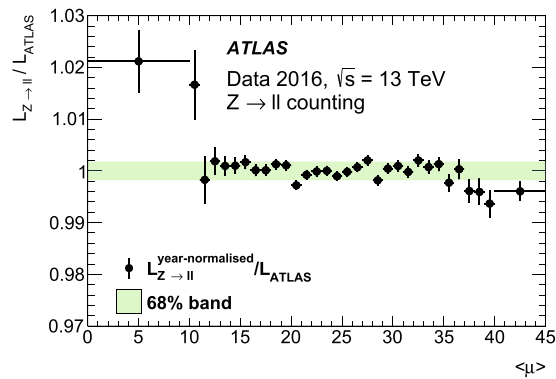
of the ratio at low $\langle\mu\rangle$, giving a ratio 0.2% below unity for the E3A TileCal cell family. The corresponding values for E4A and the C-side measurements are all within $\pm 0.5\%$ of unity, again suggesting that any changes in track-counting response between the vdM and $\langle\mu\rangle \approx 2$ physics regime is at most $\pm 0.5\%$. An uncertainty of 0.5% was therefore assigned to the calibration transfer correction of the LUCID luminosity scale in 2018. Given the similar performance of track-counting seen in the high-pileup datasets across all years, this uncertainty was also assigned for the 2017 low-pileup dataset.

Using a reference run within the low-pileup period in each year also ensures that the calibration transfer procedure cor-

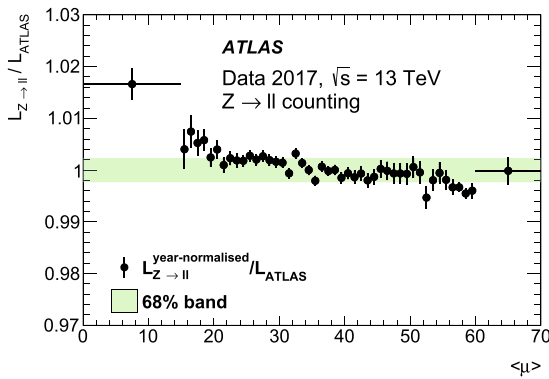
Fig. 32 Ratios of the run-integrated Z-counting (combining $Z \rightarrow ee$ and $Z \rightarrow \mu\mu$) and baseline ATLAS luminosity measurements as a function of run date. The Z-counting measurements are normalised to the baseline luminosity measurement integrated over the entire Run 2 data-taking period. The error bars show statistical uncertainties only, and the green bands contain 68% of all runs centred around the mean



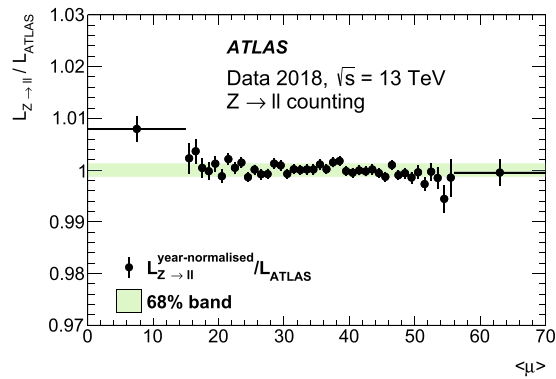
(a)



(b)



(c)



(d)

Fig. 33 Ratios of the Z-counting (combining $Z \rightarrow ee$ and $Z \rightarrow \mu\mu$) and baseline ATLAS luminosity measurements as a function of pileup $\langle \mu \rangle$ determined from the baseline measurement, separately for each year of Run 2 data-taking. The Z-counting measurements are normalised

separately in each year to the baseline luminosity measurement integrated over the entire year. The error bars show statistical uncertainties only, and the green bands contain 68% of the points centred around the mean

rects for any time drifts of the LUCID calibration between the vdM run and the low-pileup period, but it introduces a dependency on any drifts of the track-counting measurements. The studies shown in Sects. 5.2 and 7 suggest that these are small, but an independent check can be obtained from the EMEC measurements, absolutely calibrated to track-counting in high-pileup physics runs close to the vdM run using the anchoring procedure described in Sect. 7. Compar-

ison of the run-integrated luminosity measured by EMEC and LUCID in each of the low-pileup physics runs is sensitive to time drifts of either detector, and also further probes the calibration transfer correction applied to LUCID, assuming that the EMEC luminosity response does not change between high- and low-pileup data-taking with bunch trains. The FCAL data cannot be used in the same way, because of its strongly non-linear response with instantaneous luminosity, leading

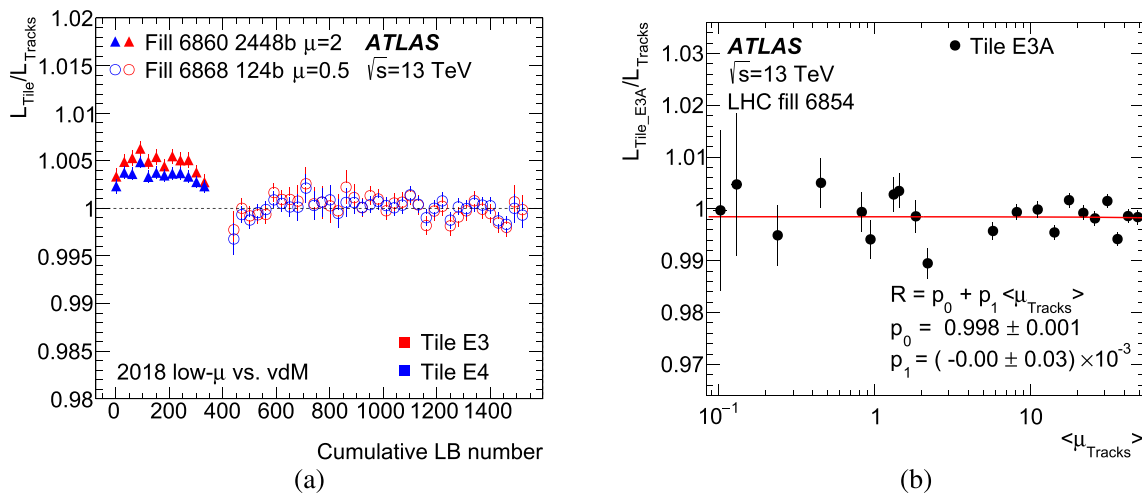


Fig. 34 (a) Ratios of luminosity measured by the TileCal E-cells to that measured by track-counting for the $\langle\mu\rangle = 2$ part of fill 6860 with 2448 colliding bunch pairs, followed by that in the head-on part of the vdM fill 6868 with 124 isolated colliding bunch pairs. The ratios are averaged over the A- and C-side measurements and over 30 luminosity blocks, separately for the E3 (red) and E4 (blue) cells, and are shown as a function of luminosity block number, renumbered to give a continuous sequence over both fills. The ratios have been normalised separately for E3 and E4 cells so that the integrated ratios in the vdM fill

are unity. (b) Ratios of luminosity measured by the TileCal E3A-cells to that measured by track-counting as a function of $\langle\mu\rangle$ in the μ -scan of fill 6854, with 1214 colliding bunch pairs in bunch trains. The ratios are normalised so that the integrated ratio in the low- μ part of the nearby 140 colliding bunch fill 6847 is unity, as in Fig. 23(e). The red line shows a linear fit (as a function of $\langle\mu\rangle$) through the points, and the fit parameters are shown in the legend. In both plots, the error bars show the uncertainties in the ratios, dominated by the statistical uncertainties of the track-counting measurements

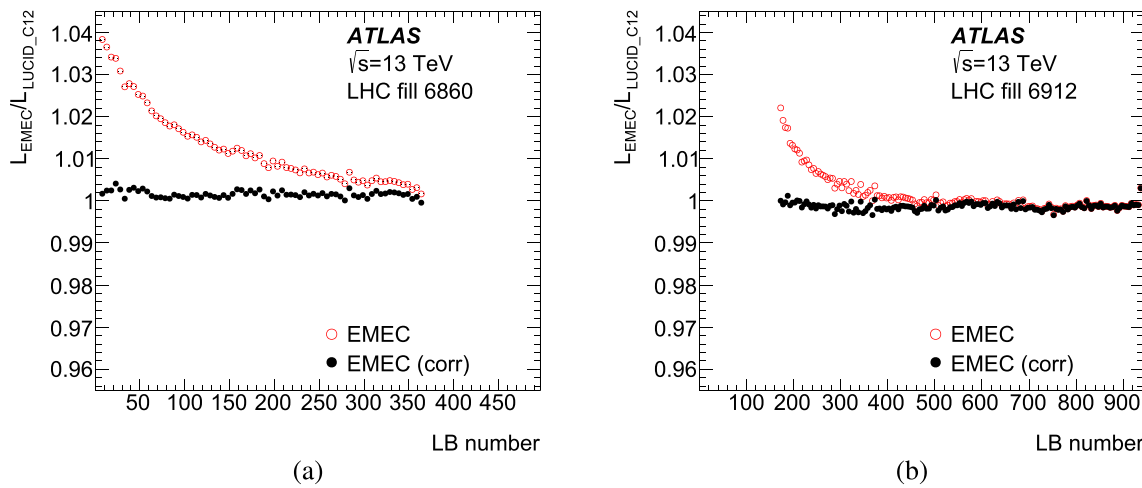


Fig. 35 Examples of the activation corrections applied to the EMEC luminosity data in low-pileup runs with $\langle\mu\rangle \approx 2$ in 2018, showing LHC fills lasting (a) 6 and (b) 13 h. The red open points show the ratios of uncorrected EMEC luminosity measurements to those from LUCID

as a function of luminosity block number, and the black filled points show the corresponding ratios after correcting for activation effects as discussed in the text. The ratios have each been averaged over five consecutive luminosity blocks

to an offset of several percent in the FCal to LUCID luminosity ratios at $\langle\mu\rangle \approx 2$ if the FCal calibration is taken from the high-pileup anchoring. The FCal luminosity measurements were therefore anchored in the $\langle\mu\rangle \approx 2$ reference runs used to determine the LUCID calibration transfer correction, and used only for stability checks within each low-pileup dataset. The same procedure was followed for the TileCal D-cell data; although this detector is linear in the relevant lumi-

nosity range, changes in the pedestal procedures and TileCal gain settings between high- and low-pileup running meant that the absolute calibration from the high-pileup anchoring could not be transferred to the $\langle\mu\rangle \approx 2$ datasets.

The LHC operation sequence followed at the start of physics fills in these data-taking periods separated the beams at the ATLAS interaction point only after head-on collisions had been established and optimised at all four IPs, leading

to periods of typically 10–30 min at high luminosity before the start of low-pileup data-taking in each 2018 fill. In 2017, the high-pileup periods were even longer in the first two fills, but much shorter in the subsequent ones. Activation from this high-luminosity running biases the EMEC, FCal and TileCal D-cell luminosity measurements upwards by several percent, in the same way as discussed above for the TileCal E-cell measurements. The open red points in Fig. 35 illustrate this effect for two fills in 2018, showing a ratio of EMEC to LUCID instantaneous luminosity which asymptotically approaches a constant value as the activation from the initial high-luminosity period decays away. Assuming that the instantaneous luminosity in the low-pileup period is constant, the ratio $R(t)$ of calorimeter to LUCID luminosity as a function of time t can be modelled as

$$R(t) = R_0 + \sum_{i=1}^2 a_i e^{-t/\tau_i} \quad (21)$$

i.e. as the sum of a constant asymptotic value R_0 and two activation terms whose contributions a_i decay exponentially with lifetime τ_i . The values of τ_i depend on the lifetimes of the contributing isotopes, and are constant, whereas the values of a_i depend on the luminosity profile and duration of the initial high-pileup running, and are thus different for each fill. This model was fitted simultaneously to the ratios of EMEC to LUCID luminosities in all five fills in the 2018 low-pileup period, determining values of R_0 for each fill (representing the activation-corrected run-integrated luminosity ratios for the two detectors), together with the lifetimes $\tau_1 \approx 900$ s and $\tau_2 \approx 8000$ s and separate a_1 and a_2 values for each fill. The black points in Fig. 35 show the EMEC to LUCID ratios after subtracting the fitted activation contributions; these ratios are much flatter, indicating that the two-component model of Eq. (21) provides a reasonable description of the activation. In the 2017 dataset, the fills with large activation contributions are short, making it hard to constrain the longer-lifetime component, so the six fills were fitted using fixed lifetimes taken from the 2018 dataset. The same procedure was applied to the FCal data, which was found to be well described with two components with $\tau_1 \approx 600$ s and $\tau_2 \approx 39000$ s, and to the TileCal D6 data, giving components with $\tau_1 \approx 1700$ s and $\tau_2 \approx 29000$ s.

Figure 36(a, b) show the resulting differences in run-integrated luminosity between each activation-corrected calorimeter measurement and LUCID, together with the corresponding track-counting vs. LUCID differences. The track-counting, FCal and TileCal D6 measurements agree with LUCID by construction in the two reference runs, shown by the purple arrows. LUCID and EMEC agree in the reference runs within 0.2% in 2017 and within 0.05% in 2018, providing a strong validation of the calibration transfer correction applied to LUCID. The per-run differences for other

runs and detectors are typically within $\pm 0.5\%$ for 2017 and $\pm 0.2\%$ for 2018. The FCal measurement for fill 6404 in 2017 is 1.8% higher than LUCID; however this fill has only 644 colliding bunch pairs rather than 1866 as for the other fills, and only one third of the instantaneous luminosity, giving a significantly different FCal response due to its non-linearity. In 2018, the activation-corrected TileCal D6 measurement in the 6 h fill 6860 is 2% lower than all the other measurements, but the relatively short length of this fill compared with the long lifetime of the second activation component makes it difficult to establish the activation correction precisely. These two measurements were therefore considered outliers and not used to assess the run-to-run stability of the LUCID measurement.

Following the approach described for high-pileup data in Sect. 7, the long-term stability uncertainty was defined as the largest difference in integrated luminosity between LUCID and any calorimeter measurement, evaluated over the entire low-pileup dataset, separately for 2017 and 2018. The corresponding plots of fractional differences in per-run integrated luminosity, weighted by the integrated luminosity of each run, are shown in Fig. 36(c, d); these distributions do not include the two outlier measurements discussed above.

The integrated luminosities and uncertainty breakdowns for the 2017 and 2018 low-pileup datasets are summarised in Table 10. The vdM uncertainties are the same as in Table 8, and only the total vdM uncertainties are shown here. Since the EMEC luminosity measurements are anchored in high-pileup runs close to the vdM scans as described in Sect. 7, the EMEC calibration anchoring uncertainties (as shown in Fig. 28(c, d)) are also included. No additional uncertainty is included for FCal and TileCal measurements, because they are normalised within the low-pileup periods, and are therefore not sensitive to drifts between the vdM run and the low-pileup data-taking. The long-term stability uncertainties are defined from the largest differences in fractional integrated luminosity shown in Fig. 36(c, d), and are set by the EMEC measurement in 2017 and TileCal D6 in 2018. The long-term stability uncertainty is larger in 2017 than 2018, reflecting the long extrapolation in 2017 between the vdM run (July) and low-pileup runs (November). In 2018, the last low-pileup run was recorded only two weeks after the vdM run.

The rightmost column in Table 10 shows the combination of the 2017 and 2018 low-pileup datasets, with the same correlation assumptions as made for the high-pileup sample. The total integrated luminosity of the $\langle \mu \rangle \approx 2$ sample is $338.1 \pm 3.1 \text{ pb}^{-1}$, corresponding to a relative uncertainty of 0.92%. The covariance matrix is $\mathbf{V}_L = \sigma_L \mathbf{C} \sigma_L^T$, where

$$\sigma_L = \begin{pmatrix} 1.69 \\ 2.05 \end{pmatrix} \text{ pb}^{-1} \quad \mathbf{C} = \begin{pmatrix} 1.000 & \\ 0.363 & 1.000 \end{pmatrix}.$$

The total luminosity uncertainty for the low-pileup data sample is slightly larger than for the high-pileup sample, mainly

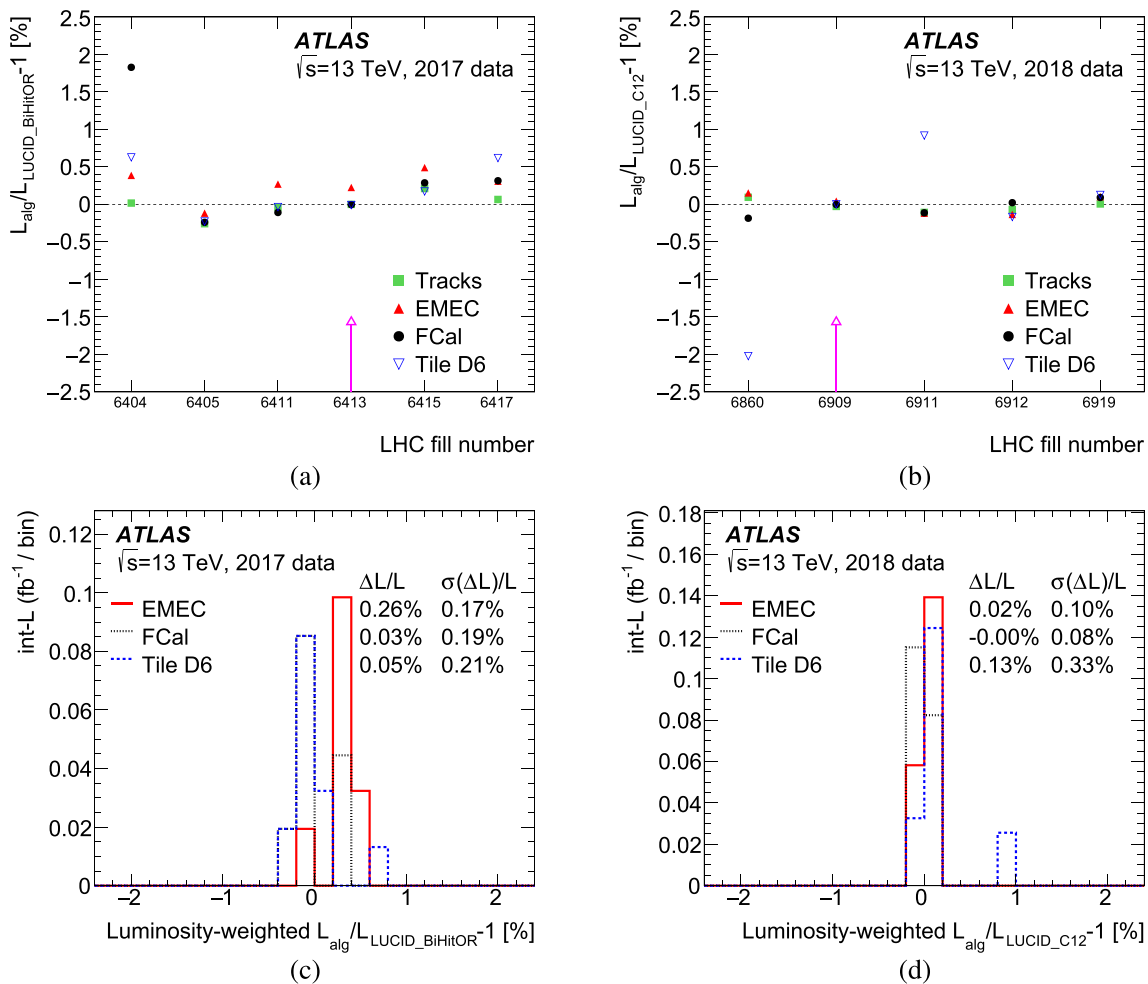


Fig. 36 (a, b) Fractional differences in run-integrated luminosity between the track-counting, EMEC, FCal and TileCal D6 luminosity measurements and the baseline LUCID luminosity measurements, for each LHC fill in the 2017 and 2018 ($\mu \approx 2$) datasets. The reference fills, used to normalise LUCID to track-counting, and FCal and TileCal to LUCID, are indicated by the purple arrows in each year. The EMEC measurements are normalised in high-pileup runs close to the

vdM run, as shown in Fig. 28. (c, d) Distributions of relative differences in run-integrated luminosity between the EMEC, FCal and TileCal D6 measurements and the baseline LUCID measurement, weighted by the integrated luminosity in each run for the two datasets, excluding fill 6404 for the FCal measurement in 2017 and fill 6860 for the TileCal measurement in 2018 (see text). The mean and RMS of each of the distributions are given in the legend

because it contains data from only two years, normalised using only two vdM calibration sessions.

10 Conclusions

The luminosity scale for the Run 2 $\sqrt{s} = 13$ TeV pp collision data recorded by the ATLAS experiment at the LHC during the years 2015–2018 has been calibrated using dedicated van der Meer scans in each year, and extrapolated to the physics regime using complementary measurements from several luminosity-sensitive detectors. The total uncertainties in the integrated luminosities for each individual year vary from 0.9–1.1%, and the uncertainty in the combined Run 2 dataset is $\delta\mathcal{L}/\mathcal{L} = \pm 0.83\%$. The largest contributions to the uncertainty come from the extrapolation of the calibration from the low-luminosity vdM scans to the high-luminosity

physics data-taking regime, followed by the effects of magnetic non-linearity, beam–beam interactions and scan-to-scan reproducibility on the absolute vdM calibration. Overall, the uncertainties related to the vdM calibration are larger than those from other sources in the final uncertainty. This final calibration implies that previously published ATLAS $\sqrt{s} = 13$ TeV pp cross-section values should be decreased by about 1%, depending on the data sample used.

This calibration is significantly more precise than those achieved by ATLAS for Run 1 (1.8% at $\sqrt{s} = 7$ TeV [2] and 1.9% at $\sqrt{s} = 8$ TeV [3]), and is the most precise luminosity measurement at any hadron collider to date, apart from some of the second-generation total cross-section experiments at the CERN ISR which achieved a comparable precision of 0.9% using the vdM calibration technique [5,46]. The 2015 and 2016 calibrations are more precise than the 1.6% and

Table 10 Summary of the integrated luminosities (after standard data-quality requirements) and uncertainties for the calibration of the $\langle\mu\rangle \approx 2$ low-pileup pp collision data samples at $\sqrt{s} = 13$ TeV in 2017 and 2018, and for the combined sample. As well as the integrated luminosities and total uncertainties, the table gives the absolute vdM calibration uncertainty and the additional uncertainties for the physics data sample, and the total relative uncertainty in percent. The calibration transfer contributions, marked *, are considered fully correlated between years, whilst the calibration anchoring and long-term stability uncertainties are considered uncorrelated. A detailed breakdown of the vdM calibration uncertainties for each year is given in Table 8

Data sample	2017	2018	Comb.
Integrated luminosity [pb^{-1}]	147.1	191.1	338.1
Total uncertainty [pb^{-1}]	1.7	2.1	3.1
Uncertainty contributions [%]:			
Subtotal vdM calibration	0.99	0.93	0.75
Calibration transfer*	0.50	0.50	0.50
Calibration anchoring	0.14	0.14	0.10
Long-term stability	0.26	0.13	0.13
Total uncertainty [%]	1.15	1.08	0.92

1.2% achieved by the CMS Collaboration for their corresponding datasets [47].

The same techniques have been used to calibrate the small $\sqrt{s} = 13$ TeV pp collision datasets with pileup of $\langle\mu\rangle \approx 2$ recorded in 2017 and 2018 for the precision Standard Model physics programme. This sample has an integrated luminosity of 338.1 pb^{-1} with an uncertainty of 0.92%. This calibration does not apply to the even smaller samples recorded in Run 2 at high β^* for the ALFA forward-physics programme, which require dedicated analyses appropriate to their specific experimental conditions.

Acknowledgements We thank CERN for the very successful operation of the LHC, as well as the support staff from our institutions without whom ATLAS could not be operated efficiently. We also thank the LHC operations team, and the LHC machine and programme coordinators, for their collaboration in planning and performing the vdM scans and other dedicated LHC fills used to calibrate the ATLAS luminosity measurement. We acknowledge the support of ANPCyT, Argentina; YerPhI, Armenia; ARC, Australia; BMWFW and FWF, Austria; ANAS, Azerbaijan; CNPq and FAPESP, Brazil; NSERC, NRC and CFI, Canada; CERN; ANID, Chile; CAS, MOST and NSFC, China; Minciencias, Colombia; MEYS CR, Czech Republic; DNRF and DNSRC, Denmark; IN2P3-CNRS and CEA-DRF/IRFU, France; SRNSFG, Georgia; BMBF, HGF and MPG, Germany; GSRI, Greece; RGC and Hong Kong SAR, China; ISF and Benozio Center, Israel; INFN, Italy; MEXT and JSPS, Japan; CNRST, Morocco; NWO, Netherlands; RCN, Norway; MEIN, Poland; FCT, Portugal; MNE/IFA, Romania; MESTD, Serbia; MSSR, Slovakia; ARRS and MIZŠ, Slovenia; DSI/NRF, South Africa; MICINN, Spain; SRC and Wallenberg Foundation, Sweden; SERI, SNSF and Cantons of Bern and Geneva, Switzerland; MOST, Taiwan; TENMAK, Türkiye; STFC, United Kingdom; DOE and NSF, United States of America. In addition, individual groups and members have received support from BCKDF, CANARIE, Compute Canada and CRC, Canada; PRIMUS 21/SCI/017 and UNCE SCI/013, Czech Republic; COST, ERC, ERDF, Horizon 2020 and Marie Skłodowska-Curie Actions, European Union; Investissements d’Avenir Labex, Investisse-

ments d’Avenir Idex and ANR, France; DFG and AvH Foundation, Germany; Herakleitos, Thales and Aristeia programmes co-financed by EU-ESF and the Greek NSRF, Greece; BSF-NSF and MINERVA, Israel; Norwegian Financial Mechanism 2014–2021, Norway; NCN and NAWA, Poland; La Caixa Banking Foundation, CERCA Programme Generalitat de Catalunya and PROMETEO and GenT Programmes Generalitat Valenciana, Spain; Göran Gustafssons Stiftelse, Sweden; The Royal Society and Leverhulme Trust, United Kingdom. The crucial computing support from all WLCG partners is acknowledged gratefully, in particular from CERN, the ATLAS Tier-1 facilities at TRIUMF (Canada), NDGF (Denmark, Norway, Sweden), CC-IN2P3 (France), KIT/GridKA (Germany), INFN-CNAF (Italy), NL-T1 (Netherlands), PIC (Spain), ASGC (Taiwan), RAL (UK) and BNL (USA), the Tier-2 facilities worldwide and large non-WLCG resource providers. Major contributors of computing resources are listed in Ref. [48].

Data Availability Statement This manuscript has no associated data or the data will not be deposited. [Authors’ comment: All ATLAS scientific output is published in journals, and preliminary results are made available in Conference Notes. All are openly available, without restriction on use by external parties beyond copyright law and the standard conditions agreed by CERN. Data associated with journal publications are also made available: tables and data from plots (e.g. cross section values, likelihood profiles, selection efficiencies, cross section limits, ...) are stored in appropriate repositories such as HEPDATA (<http://hepdata.cedar.ac.uk/>). ATLAS also strives to make additional material related to the paper available that allows a reinterpretation of the data in the context of new theoretical models. For example, an extended encapsulation of the analysis is often provided for measurements in the framework of RIVET (<http://rivet.hepforge.org/>). This information is taken from the ATLAS Data Access Policy, which is a public document that can be downloaded from <http://opendata.cern.ch/record/413> [opendata.cern.ch].]

Open Access This article is licensed under a Creative Commons Attribution 4.0 International License, which permits use, sharing, adaptation, distribution and reproduction in any medium or format, as long as you give appropriate credit to the original author(s) and the source, provide a link to the Creative Commons licence, and indicate if changes were made. The images or other third party material in this article are included in the article’s Creative Commons licence, unless indicated otherwise in a credit line to the material. If material is not included in the article’s Creative Commons licence and your intended use is not permitted by statutory regulation or exceeds the permitted use, you will need to obtain permission directly from the copyright holder. To view a copy of this licence, visit <http://creativecommons.org/licenses/by/4.0/>.

Funded by SCOAP³. SCOAP³ supports the goals of the International Year of Basic Sciences for Sustainable Development.

References

1. ATLAS Collaboration, Luminosity determination in pp collisions at $\sqrt{s} = 7$ TeV using the ATLAS detector at the LHC. *Eur. Phys. J. C* **71**, 1630 (2011). <https://doi.org/10.1140/epjc/s10052-011-1630-5>. arXiv:1101.2185 [hep-ex]
2. ATLAS Collaboration, Improved luminosity determination in pp collisions at $\sqrt{s} = 7$ TeV using the ATLAS detector at the LHC. *Eur. Phys. J. C* **73**, 2518 (2013). <https://doi.org/10.1140/epjc/s10052-013-2518-3>. arXiv:1302.4393 [hep-ex]
3. ATLAS Collaboration, Luminosity determination in pp collisions at $\sqrt{s} = 7$ TeV using the ATLAS detector at the LHC. *Eur. Phys. J. C* **76**, 653 (2016). <https://doi.org/10.1140/epjc/s10052-016-4466-1>. arXiv:1608.03953 [hep-ex]

4. S. van der Meer, Calibration of the effective beam height in the ISR, CERN-ISR-PO-68-31 (1968). <https://cds.cern.ch/record/296752>
5. P. Grafström, W. Kozanecki, Luminosity determination at proton colliders. Prog. Part. Nucl. Phys. **81**, 97 (2015). <https://doi.org/10.1016/j.pnpnp.2014.11.002>
6. M. Böhler et al., Evolution of ATLAS conditions data and its management for LHC Run-2. J. Phys. Conf. Ser. **664**, 042005 (2015). <https://doi.org/10.1088/1742-6596/664/4/042005>
7. ATLAS Collaboration, ATLAS data quality operations and performance for 2015–2018 data-taking. JINST **15**, P04003 (2020). <https://doi.org/10.1088/1748-0221/15/04/P04003>. [arXiv:1911.04632](https://arxiv.org/abs/1911.04632) [physics.ins-det]
8. ATLAS Collaboration, Operation of the ATLAS trigger system in Run 2. JINST **15**, P10004 (2020). <https://doi.org/10.1088/1748-0221/15/10/P10004>. [arXiv:2007.12539](https://arxiv.org/abs/2007.12539) [hep-ex]
9. H. Wiedemann, *Particle Accelerator Physics, Graduate Texts in Physics* (Springer, 2015). https://www.springer.com/us/book/9783319183169?wt_mc=ThirdParty.SpringerLink.3.EPR653>About_eBook
10. ATLAS Collaboration, The ATLAS experiment at the CERN Large Hadron Collider. JINST **3**, S08003 (2008). <https://doi.org/10.1088/1748-0221/3/08/S08003>
11. B. Abbott et al., Production and integration of the ATLAS Insertable B-Layer. JINST **13**, T05008 (2018). <https://doi.org/10.1088/1748-0221/13/05/T05008>. [arXiv:1803.00844](https://arxiv.org/abs/1803.00844) [physics.ins-det]
12. ATLAS Collaboration, ATLAS Insertable B-Layer Technical Design Report, ATLAS-TDR-19 (2010) <https://cds.cern.ch/record/1291633>, ATLAS Insertable B-Layer Technical Design Report Addendum, ATLAS-TDR-19-ADD-1 (2012). <https://cds.cern.ch/record/1451888>
13. ATLAS Collaboration, The ATLAS Collaboration Software and Firmware, ATL-SOFT-PUB-2021-001 (2021). <https://cds.cern.ch/record/2767187>
14. G. Avoni et al., The new LUCID-2 detector for luminosity measurement and monitoring in ATLAS. JINST **13**, P07017 (2018). <https://doi.org/10.1088/1748-0221/13/07/P07017>
15. V. Cindro et al., The ATLAS beam conditions monitor. JINST **3**, P02004 (2008). <https://doi.org/10.1088/1748-0221/3/02/P02004>
16. ATLAS Collaboration, Early inner detector tracking performance in the 2015 data at $\sqrt{s} = 13$ TeV, ATL-PHYS-PUB-2015-051 (2015). <https://cds.cern.ch/record/2110140>
17. ATLAS Collaboration, Drift time measurement in the ATLAS liquid argon electromagnetic calorimeter using cosmic muons. Eur. Phys. J. C **70**, 755 (2010). <https://doi.org/10.1140/epjc/s10052-010-1403-6>. [arXiv:1002.4189](https://arxiv.org/abs/1002.4189) [hep-ex]
18. ATLAS Collaboration, Readiness of the ATLAS tile calorimeter for LHC collisions. Eur. Phys. J. C **70**, 1193 (2010). <https://doi.org/10.1140/epjc/s10052-010-1508-y>. [arXiv:1007.5423](https://arxiv.org/abs/1007.5423) [hep-ex]
19. H. Bartosik, G. Rumolo, Production of single Gaussian bunches for Van der Meer scans in the LHC injector chain, CERN-ACC-Note-2013-0008 (2013). <https://cds.cern.ch/record/1590405>
20. G. Anders et al., Study of the relative LHC bunch populations for luminosity calibration, CERN-ATS-Note-2013-028 PERF (2013). <https://cds.cern.ch/record/1427726>
21. LHCb Collaboration, Precision luminosity measurements at LHCb. JINST **9**, P12005 (2014). <https://doi.org/10.1088/1748-0221/9/12/P12005>. [arXiv:1410.0149](https://arxiv.org/abs/1410.0149) [hep-ex]
22. A. Boccardi, E. Bravin, M. Ferro-Luzzi, S. Mazzoni, M. Palm, LHC Luminosity calibration using the Longitudinal Density Monitor, CERN-ATS-Note-2013-034 TECH (2013). <https://cds.cern.ch/record/1556087>
23. C. Barschel et al., Results of the LHC DCCT Calibration Studies, CERN-ATS-Note-2012-026 PERF (2012). <https://cds.cern.ch/record/1425904>
24. G. Anders, Absolute luminosity determination for the ATLAS experiment, CERN-THESIS-2013-111 (2013). <https://cds.cern.ch/record/1595219>
25. ATLAS Collaboration, Reconstruction of primary vertices at the ATLAS experiment in Run 1 proton–proton collisions at the LHC. Eur. Phys. J. C **77**, 332 (2017). <https://doi.org/10.1140/epjc/s10052-017-4887-5>. [arXiv:1611.10235](https://arxiv.org/abs/1611.10235) [hep-ex]
26. P. Bambade et al., Observation of beam-beam deflections at the interaction point of the SLAC Linear Collider. Phys. Rev. Lett. **62**, 2949 (1989). <https://doi.org/10.1103/PhysRevLett.62.2949>
27. M. Bassetti, G. Erskine, Closed expression for the electrical field of a two-dimensional Gaussian charge, CERN-ISR-TH-80-06 (1980). <https://cds.cern.ch/record/122227>
28. CERN Accelerator Beam Physics Group, MAD—Methodical Accelerator Design. <https://mad.web.cern.ch/mad>
29. A. Babaev et al., Impact of beam-beam effects on absolute luminosity calibrations at the CERN Large Hadron Collider (2023). [arXiv:2306.10394](https://arxiv.org/abs/2306.10394) [physics.acc-ph]
30. V. Balagura, Van der Meer scan luminosity measurement and beam-beam correction. Eur. Phys. J. C **81**, 26 (2021). <https://doi.org/10.1140/epjc/s10052-021-08837-y>. [arXiv:2012.07752](https://arxiv.org/abs/2012.07752) [hep-ex]
31. F.W. Jones, W. Herr, T. Pieloni, Parallel beam-beam simulation incorporating multiple bunches and multiple interaction regions, CERN-LHC-PROJECT-Report-1038 (2007). <https://cds.cern.ch/record/1058519>
32. ATLAS Collaboration, Alignment of the ATLAS Inner Detector in Run-2. Eur. Phys. J. C **80**, 1194 (2020). <https://doi.org/10.1140/epjc/s10052-020-08700-6>. [arXiv:2007.07624](https://arxiv.org/abs/2007.07624) [hep-ex]
33. A. Chmieleńska et al., Magnetization in superconducting corrector magnets and impact on luminosity-calibration scans in the Large Hadron Collider (2023). [arXiv:2304.06559](https://arxiv.org/abs/2304.06559) [physics.acc-ph]
34. ATLAS Collaboration, The ATLAS simulation infrastructure. Eur. Phys. J. C **70**, 823 (2010). <https://doi.org/10.1140/epjc/s10052-010-1429-9>. [arXiv:1005.4568](https://arxiv.org/abs/1005.4568) [physics.ins-det]
35. S. Agostinelli et al., GEANT4-A simulation toolkit. Nucl. Instrum. Methods A **506**, 250 (2003). [https://doi.org/10.1016/S0168-9002\(03\)01368-8](https://doi.org/10.1016/S0168-9002(03)01368-8)
36. T. Sjöstrand, S. Mrenna, P.Z. Skands, A brief introduction to PYTHIA 8.1. Comput. Phys. Commun. **178**, 852 (2008). <https://doi.org/10.1016/j.cpc.2008.01.036>. [arXiv:0710.3820](https://arxiv.org/abs/0710.3820) [hep-ph]
37. ATLAS Collaboration, The Pythia 8 A3 tune description of ATLAS minimum bias and inelastic measurements incorporating the Donnachie–Landshoff diffractive model, ATL-PHYS-PUB-2016-017 (2016). <https://cds.cern.ch/record/2206965>
38. ATLAS Collaboration, Muon reconstruction and identification efficiency in ATLAS using the full Run 2 pp collision data set at $\sqrt{s} = 13$ TeV. Eur. Phys. J. C **81**, 578 (2021). <https://doi.org/10.1140/epjc/s10052-021-09233-2>. [arXiv:2012.00578](https://arxiv.org/abs/2012.00578) [hep-ex]
39. ATLAS Collaboration, Muon reconstruction performance of the ATLAS detector in proton–proton collision data at $\sqrt{s} = 13$ TeV. Eur. Phys. J. C **76**, 292 (2016). <https://doi.org/10.1140/epjc/s10052-016-4120-y>. [arXiv:1603.05598](https://arxiv.org/abs/1603.05598) [hep-ex]
40. ATLAS Collaboration, Luminosity determination in pp collisions at $\sqrt{s} = 13$ TeV using the ATLAS detector at the LHC, ATLAS-CONF-2019-021 (2019). <https://cds.cern.ch/record/2677054>
41. ATLAS Collaboration, Measurement of the transverse momentum distribution of Drell–Yan lepton pairs in proton–proton collisions at $\sqrt{s} = 13$ TeV with the ATLAS detector. Eur. Phys. J. C **80**, 616 (2020). <https://doi.org/10.1140/epjc/s10052-020-8001-z>. [arXiv:1912.02844](https://arxiv.org/abs/1912.02844) [hep-ex]

42. ATLAS Collaboration, Electron reconstruction and identification in the ATLAS experiment using the 2015 and 2016 LHC proton–proton collision data at $\sqrt{s} = 13$ TeV. *Eur. Phys. J. C* **79**, 639 (2019). <https://doi.org/10.1140/epjc/s10052-019-7140-6>. [arXiv:1902.04655](https://arxiv.org/abs/1902.04655) [hep-ex]
43. ATLAS Collaboration, Measurements of top-quark pair to Z-boson cross-section ratios at $\sqrt{s} = 13, 8, 7$ TeV with the ATLAS detector. *JHEP* **02**, 117 (2017). [https://doi.org/10.1007/JHEP02\(2017\)117](https://doi.org/10.1007/JHEP02(2017)117). [arXiv:1612.03636](https://arxiv.org/abs/1612.03636) [hep-ex]
44. ATLAS Collaboration, Luminosity monitoring using $Z \rightarrow \ell^+ \ell^-$ events at $\sqrt{s} = 13$ TeV with the ATLAS detector, ATL-DAPR-PUB-2021-001 (2021). <https://cds.cern.ch/record/2752951>
45. ATLAS Collaboration, Prospects for the measurement of the Z-boson transverse momentum with a low pileup data sample at $\sqrt{s} = 13$ TeV with the ATLAS detector, ATL-PHYS-PUB-2017-021 (2017). <https://cds.cern.ch/record/2298152>
46. U. Amaldi et al., Precision measurement of proton-proton total cross section at the CERN intersecting storage rings. *Nucl. Phys. B* **145**, 367 (1978). [https://doi.org/10.1016/0550-3213\(78\)90090-1](https://doi.org/10.1016/0550-3213(78)90090-1)
47. CMS Collaboration, Precision luminosity measurement in proton-proton collisions at $\sqrt{s} = 13$ TeV in 2015 and 2016 at CMS. *Eur. Phys. J. C* **81**, 800 (2021). <https://doi.org/10.1140/epjc/s10052-021-09538-2>. [arXiv:2104.01927](https://arxiv.org/abs/2104.01927) [hep-ex]
48. ATLAS Collaboration, ATLAS Computing Acknowledgements, ATL-SOFT-PUB-2021-003 (2021). <https://cds.cern.ch/record/2776662>

ATLAS Collaboration*

G. Aad¹⁰², B. Abbott¹²⁰, K. Abeling⁵⁵, S. H. Abidi²⁹, A. Aboulhorma^{35e}, H. Abramowicz¹⁵¹, H. Abreu¹⁵⁰, Y. Abulaiti¹¹⁷, A. C. Abusleme Hoffman^{137a}, B. S. Acharya^{69a,69b,p}, C. Adam Bourdarios⁴, L. Adamczyk^{85a}, L. Adamek¹⁵⁵, S. V. Addepalli²⁶, J. Adelman¹¹⁵, A. Adiguzel^{21c}, S. Adorni⁵⁶, T. Adye¹³⁴, A. A. Affolder¹³⁶, Y. Afik³⁶, M. N. Agaras¹³, J. Agarwala^{73a,73b}, A. Aggarwal¹⁰⁰, C. Agheorghiesei^{27c}, J. A. Aguilar-Saavedra^{130f}, A. Ahmad³⁶, F. Ahmadov^{38,aa}, W. S. Ahmed¹⁰⁴, S. Ahuja⁹⁵, X. Ai⁴⁸, G. Aielli^{76a,76b}, M. Ait Tamlihat^{35e}, B. Aitbenkhik^{35a}, I. Aizenberg¹⁶⁹, M. Akbiyik¹⁰⁰, T. P. A. Åkesson⁹⁸, A. V. Akimov³⁷, N. N. Akolkar²⁴, K. Al Khoury⁴¹, G. L. Alberghi^{23b}, J. Albert¹⁶⁵, P. Albicocco⁵³, S. Alderweireldt⁵², M. Aleksa³⁶, I. N. Aleksandrov³⁸, C. Alexa^{27b}, T. Alexopoulos¹⁰, A. Alfonsi¹¹⁴, F. Alfonsi^{23b}, M. Alhroob¹²⁰, B. Ali¹³², S. Ali¹⁴⁸, M. Aliev³⁷, G. Alimonti^{71a}, W. Alkakh⁵⁵, C. Allaire⁶⁶, B. M. M. Allbrooke¹⁴⁶, C. A. Allendes Flores^{137f}, P. P. Allport²⁰, A. Aloisio^{72a,72b}, F. Alonso⁹⁰, C. Alpigiani¹³⁸, M. Alvarez Estevez⁹⁹, A. Alvarez Fernandez¹⁰⁰, M. G. Alviggi^{72a,72b}, M. Aly¹⁰¹, Y. Amaral Coutinho^{82b}, A. Ambler¹⁰⁴, C. Amelung³⁶, M. Ameri¹⁰¹, C. G. Ames¹⁰⁹, D. Amidei¹⁰⁶, S. P. Amor Dos Santos^{130a}, K. R. Amos¹⁶³, V. Ananiev¹²⁵, C. Anastopoulos¹³⁹, T. Andeen¹¹, J. K. Anders³⁶, S. Y. Andreev^{47a,47b}, A. Andreazza^{71a,71b}, S. Angelidakis⁹, A. Angerami^{41,ad}, A. V. Anisenkov³⁷, A. Annovi^{74a}, C. Antel⁵⁶, M. T. Anthony¹³⁹, E. Antipov¹⁴⁵, M. Antonelli⁵³, D. J. A. Antrim^{17a}, F. Anulli^{75a}, M. Aoki⁸³, T. Aoki¹⁵³, J. A. Aparisi Pozo¹⁶³, M. A. Aparo¹⁴⁶, L. Aperio Bella⁴⁸, C. Appelt¹⁸, N. Aranzabal³⁶, V. Araujo Ferraz^{82a}, C. Arcangeletti⁵³, A. T. H. Arce⁵¹, E. Arena⁹², J.-F. Arguin¹⁰⁸, S. Argyropoulos⁵⁴, J.-H. Arling⁴⁸, A. J. Armbruster³⁶, O. Arnaez⁴, H. Arnold¹¹⁴, Z. P. Arrubarrena Tame¹⁰⁹, G. Artoni^{75a,75b}, H. Asada¹¹¹, K. Asai¹¹⁸, S. Asai¹⁵³, N. A. Asbah⁶¹, J. Assahsah^{35d}, K. Assamagan²⁹, R. Astalos^{28a}, R. J. Atkin^{33a}, M. Atkinson¹⁶², N. B. Atlay¹⁸, H. Atmani^{62b}, P. A. Atmasiddha¹⁰⁶, K. Augsten¹³², S. Auricchio^{72a,72b}, A. D. Aurioi²⁰, V. A. Austrup¹⁷¹, G. Avner¹⁵⁰, G. Avolio³⁶, K. Axiotis⁵⁶, G. Azuelos^{108,ai}, D. Babal^{28b}, H. Bachacou¹³⁵, K. Bachas^{152,s}, A. Bachi³⁴, F. Backman^{47a,47b}, A. Badae⁶¹, P. Bagnaia^{75a,75b}, M. Bahmani¹⁸, A. J. Bailey¹⁶³, V. R. Bailey¹⁶², J. T. Baines¹³⁴, C. Bakalis¹⁰, O. K. Baker¹⁷², E. Bakos¹⁵, D. Bakshi Gupta⁸, R. Balasubramanian¹¹⁴, E. M. Baldin³⁷, P. Balek¹³³, E. Ballabene^{71a,71b}, F. Balli¹³⁵, L. M. Baltés^{63a}, W. K. Balunas³², J. Balz¹⁰⁰, E. Banas⁸⁶, M. Bandieramonte¹²⁹, A. Bandyopadhyay²⁴, S. Bansal²⁴, L. Barak¹⁵¹, E. L. Barberio¹⁰⁵, D. Barberis^{57a,57b}, M. Barbero¹⁰², G. Barbour⁹⁶, K. N. Barends^{33a}, T. Barillari¹¹⁰, M.-S. Barisits³⁶, T. Barklow¹⁴³, P. Baron¹²², D. A. Baron Moreno¹⁰¹, A. Baroncelli^{62a}, G. Barone²⁹, A. J. Barr¹²⁶, L. Barranco Navarro^{47a,47b}, F. Barreiro⁹⁹, J. Barreiro Guimarães da Costa^{14a}, U. Barron¹⁵¹, M. G. Barros Teixeira^{130a}, S. Barsov³⁷, F. Bartels^{63a}, R. Bartoldus¹⁴³, A. E. Barton⁹¹, P. Bartos^{28a}, A. Basan¹⁰⁰, M. Baselga⁴⁹, I. Bashta^{77a,77b}, A. Bassalat^{66,b}, M. J. Basso¹⁵⁵, C. R. Basson¹⁰¹, R. L. Bates⁵⁹, S. Batlamous^{35e}, J. R. Batley³², B. Batool¹⁴¹, M. Battaglia¹³⁶, D. Battulga¹⁸, M. Bauce^{75a,75b}, P. Bauer²⁴, J. B. Beacham⁵¹, T. Beau¹²⁷, P. H. Beauchemin¹⁵⁸, F. Becherer⁵⁴, P. Bechtel²⁴, H. P. Beck^{19,r}, K. Becker¹⁶⁷, A. J. Beddall^{21d}, V. A. Bednyakov³⁸, C. P. Bee¹⁴⁵, L. J. Beemster¹⁵, T. A. Beerma³⁶, M. Begalli^{82d}, M. Begel²⁹, A. Behera¹⁴⁵, J. K. Behr⁴⁸, C. Beirao Da Cruz E Silva³⁶, J. F. Beirer^{36,55}, F. Beisiegel²⁴, M. Belfkir¹⁵⁹, G. Bella¹⁵¹, L. Bellagamba^{23b}, A. Bellerive³⁴, P. Bellos²⁰, K. Beloborodov³⁷, N. L. Belyaev³⁷, D. Benckekroun^{35a}, F. Bendebba^{35a}, Y. Benhammou¹⁵¹, M. Benoit²⁹,

J. R. Bensinger²⁶, S. Bentvelsen¹¹⁴, L. Beresford⁴⁸, M. Beretta⁵³, E. Bergeaas Kuutmann¹⁶¹, N. Berger⁴,
 B. Bergmann¹³², J. Beringer^{17a}, S. Berlendis⁷, G. Bernardi⁵, C. Bernius¹⁴³, F. U. Bernlochner²⁴,
 T. Berry⁹⁵, P. Berta¹³³, A. Berthold⁵⁰, I. A. Bertram⁹¹, S. Bethke¹¹⁰, A. Betti^{75a,75b}, A. J. Bevan⁹⁴,
 M. Bhamjee^{33c}, S. Bhatta¹⁴⁵, D. S. Bhattacharya¹⁶⁶, P. Bhattacharai²⁶, V. S. Bhopatkar¹²¹, R. Bi^{29.ak},
 R. M. Bianchi¹²⁹, O. Biebel¹⁰⁹, R. Bielski¹²³, M. Biglietti^{77a}, T. R. V. Billoud¹³², M. Bindi⁵⁵,
 A. Bingul^{21b}, C. Bini^{75a,75b}, A. Biondini⁹², C. J. Birch-sykes¹⁰¹, G. A. Bird^{20,134}, M. Birman¹⁶⁹,
 M. Biros¹³³, T. Bisanz³⁶, E. Bisceglie^{43a,43b}, D. Biswas¹⁷⁰, A. Bitadze¹⁰¹, K. Bjørke¹²⁵, I. Bloch⁴⁸,
 C. Blocker²⁶, A. Blue⁵⁹, U. Blumenschein⁹⁴, J. Blumenthal¹⁰⁰, G. J. Bobbink¹¹⁴, V. S. Bobrovnikov³⁷,
 M. Boehler⁵⁴, D. Bogavac³⁶, A. G. Bogdanchikov³⁷, C. Bohm^{47a}, V. Boisvert⁹⁵, P. Bokan⁴⁸, T. Bold^{85a},
 M. Bomben⁵, M. Bona⁹⁴, M. Boonekamp¹³⁵, C. D. Booth⁹⁵, A. G. Borbely⁵⁹, H. M. Borecka-Bielska¹⁰⁸,
 L. S. Borgna⁹⁶, G. Borissov⁹¹, D. Bortoletto¹²⁶, D. Boscherini^{23b}, M. Bosman¹³, J. D. Bossio Sola³⁶,
 K. Bouaouda^{35a}, N. Bouchhar¹⁶³, J. Boudreau¹²⁹, E. V. Bouhova-Thacker⁹¹, D. Boumediene⁴⁰,
 R. Bouquet⁵, A. Boveia¹¹⁹, J. Boyd³⁶, D. Boye²⁹, I. R. Boyko³⁸, J. Bracinik²⁰, N. Brahim^{62d},
 G. Brandt¹⁷¹, O. Brandt³², F. Braren⁴⁸, B. Brau¹⁰³, J. E. Brau¹²³, K. Brendlinger⁴⁸, R. Brenner¹⁶⁹,
 L. Brenner¹¹⁴, R. Brenner¹⁶¹, S. Bressler¹⁶⁹, D. Britton⁵⁹, D. Britzger¹¹⁰, I. Brock²⁴, G. Brooijmans⁴¹,
 W. K. Brooks^{137f}, E. Brost²⁹, L. M. Brown¹⁶⁵, T. L. Bruckler¹²⁶, P. A. Bruckman de Renstrom⁸⁶,
 B. Brüers⁴⁸, D. Bruncko^{28b,*}, A. Bruni^{23b}, G. Bruni^{23b}, M. Bruschi^{23b}, N. Brusino^{75a,75b}, T. Buanes¹⁶,
 Q. Buat¹³⁸, A. G. Buckley⁵⁹, I. A. Budagov^{38,*}, M. K. Bugge¹²⁵, O. Bulekov³⁷, B. A. Bullard¹⁴³,
 S. Burdin⁹², C. D. Burgard⁴⁹, A. M. Burger⁴⁰, B. Burghgrave⁸, O. Burlayenko⁵⁴, J. T. P. Burr³²,
 C. D. Burton¹¹, J. C. Burzynski¹⁴², E. L. Busch⁴¹, V. Büscher¹⁰⁰, P. J. Bussey⁵⁹, J. M. Butler²⁵,
 C. M. Buttar⁵⁹, J. M. Butterworth⁹⁶, W. Buttinger¹³⁴, C. J. Buxo Vazquez¹⁰⁷, A. R. Buzykaev³⁷,
 G. Cabras^{23b}, S. Cabrera Urbán¹⁶³, D. Caforio⁵⁸, H. Cai¹²⁹, Y. Cai^{14a,14d}, V. M. M. Cairo³⁶,
 O. Cakir^{3a}, N. Calace³⁶, P. Calafiura^{17a}, G. Calderini¹²⁷, P. Calfayan⁶⁸, G. Callea⁵⁹, L. P. Caloba^{82b},
 D. Calvet⁴⁰, S. Calvet⁴⁰, T. P. Calvet¹⁰², M. Calvetti^{74a,74b}, R. Camacho Toro¹²⁷, S. Camarda³⁶,
 D. Camarero Munoz²⁶, P. Camarri^{76a,76b}, M. T. Camerlingo^{72a,72b}, D. Cameron¹²⁵, C. Camincher¹⁶⁵,
 M. Campanelli⁹⁶, A. Camplani⁴², V. Canale^{72a,72b}, A. Canesse¹⁰⁴, M. Cano Bret⁸⁰, J. Cantero¹⁶³, Y. Cao¹⁶²,
 F. Capocasa²⁶, M. Capua^{43a,43b}, A. Carbone^{71a,71b}, R. Cardarelli^{76a}, J. C. J. Cardenas⁸, F. Cardillo¹⁶³,
 T. Carli³⁶, G. Carlino^{72a}, J. I. Carlotto¹³, B. T. Carlson^{129,t}, E. M. Carlson^{156a,165}, L. Carminati^{71a,71b},
 M. Carnesale^{75a,75b}, S. Caron¹¹³, E. Carquin^{137f}, S. Carrá^{71a,71b}, G. Carratta^{23a,23b}, F. Carri Argos^{33g},
 J. W. S. Carter¹⁵⁵, T. M. Carter⁵², M. P. Casado^{13j}, A. F. Casha¹⁵⁵, M. Caspar⁴⁸, E. G. Castiglia¹⁷²,
 F. L. Castillo^{63a}, L. Castillo Garcia¹³, V. Castillo Gimenez¹⁶³, N. F. Castro^{130a,130c}, A. Catinaccio³⁶,
 J. R. Catmore¹²⁵, V. Cavaliere²⁹, N. Cavalli^{23a,23b}, V. Cavasinni^{74a,74b}, E. Celebi^{21a}, F. Celli¹²⁶,
 M. S. Centonze^{70a,70b}, K. Cerny¹²², A. S. Cerqueira^{82a}, A. Cerri¹⁴⁶, L. Cerrito^{76a,76b}, F. Cerutti^{17a},
 A. Cervelli^{23b}, G. Cesarini⁵³, S. A. Cetin^{21d}, Z. Chadi^{35a}, D. Chakraborty¹¹⁵, M. Chala^{130f}, J. Chan¹⁷⁰,
 W. Y. Chan¹⁵³, J. D. Chapman³², B. Chargeishvili^{149b}, D. G. Charlton²⁰, T. P. Charman⁹⁴, M. Chatterjee¹⁹,
 C. Chauhan¹³³, S. Chekanov⁶, S. V. Chekulaev^{156a}, G. A. Chelkov^{38,a}, A. Chen¹⁰⁶, B. Chen¹⁵¹, B. Chen¹⁶⁵,
 H. Chen^{14c}, H. Chen²⁹, J. Chen^{62c}, J. Chen¹⁴², S. Chen¹⁵³, S. J. Chen^{14c}, X. Chen^{62c}, X. Chen^{14b,ab},
 Y. Chen^{62a}, C. L. Cheng¹⁷⁰, H. C. Cheng^{64a}, S. Cheong¹⁴³, A. Cheplakov³⁸, E. Cheremushkina⁴⁸,
 E. Cherepanova¹¹⁴, R. Cherkaoui El Moursli^{35e}, E. Cheu⁷, K. Cheung⁶⁵, L. Chevalier¹³⁵, V. Chiarella⁵³,
 G. Chiarelli^{74a}, N. Chiedde¹⁰², G. Chiodini^{70a}, A. S. Chisholm²⁰, A. Chitan^{27b}, M. Chitishvili¹⁶³,
 M. V. Chizhov³⁸, K. Choi¹¹, A. R. Chomont^{75a,75b}, Y. Chou¹⁰³, E. Y. S. Chow¹¹⁴, T. Chowdhury^{33g},
 L. D. Christopher^{33g}, K. L. Chu^{64a}, M. C. Chu^{64a}, X. Chu^{14a,14d}, J. Chudoba¹³¹, J. J. Chwastowski⁸⁶,
 D. Cieri¹¹⁰, K. M. Ciesla^{85a}, V. Cindro⁹³, A. Ciocio^{17a}, F. Ciroto^{72a,72b}, Z. H. Citron^{169,m}, M. Citterio^{71a},
 D. A. Ciubotaru^{27b}, B. M. Ciungu¹⁵⁵, A. Clark⁵⁶, P. J. Clark⁵², J. M. Clavijo Columbie⁴⁸, S. E. Clawson¹⁰¹,
 C. Clement^{47a,47b}, J. Clercx⁴⁸, L. Clissa^{23a,23b}, Y. Coadou¹⁰², M. Cobal^{69a,69c}, A. Coccaro^{57b},
 R. F. Coelho Barrue^{130a}, R. Coelho Lopes De Sa¹⁰³, S. Coelli^{71a}, H. Cohen¹⁵¹, A. E. C. Coimbra^{71a,71b},
 B. Cole⁴¹, J. Collot⁶⁰, P. Conde Muiño^{130a,130g}, M. P. Connell^{33c}, S. H. Connell^{33c}, I. A. Connelly⁵⁹,
 E. I. Conroy¹²⁶, F. Conventi^{72a,aj}, H. G. Cooke²⁰, A. M. Cooper-Sarkar¹²⁶, F. Cormier¹⁶⁴, L. D. Corpe³⁶,
 M. Corradi^{75a,75b}, F. Corriveau^{104,y}, A. Cortes-Gonzalez¹⁸, M. J. Costa¹⁶³, F. Costanza⁴, D. Costanzo¹³⁹,
 B. M. Cote¹¹⁹, G. Cowan⁹⁵, K. Cranmer¹¹⁷, S. Crépe-Renaudin⁶⁰, F. Crescioli¹²⁷, M. Cristinziani¹⁴¹,
 M. Cristoforetti^{78a,78b,d}, V. Croft¹¹⁴, G. Crosetti^{43a,43b}, A. Cueto³⁶, T. Cuhadar Donszelmann¹⁶⁰,
 H. Cui^{14a,14d}, Z. Cui⁷, W. R. Cunningham⁵⁹, F. Curcio^{43a,43b}, P. Czodrowski³⁶, M. M. Czurylo^{63b},
 M. J. Da Cunha Sargedas De Sousa^{62a}, J. V. Da Fonseca Pinto^{82b}, C. Da Via¹⁰¹, W. Dabrowski^{85a},

T. Dado⁴⁹, S. Dahbi^{33g}, T. Dai¹⁰⁶, C. Dallapiccola¹⁰³, M. Dam⁴², G. D'amen²⁹, V. D'Amico¹⁰⁹, J. Damp¹⁰⁰, J. R. Dandoy¹²⁸, M. F. Daneri³⁰, M. Danninger¹⁴², V. Dao³⁶, G. Darbo^{57b}, S. Darmora⁶, S. J. Das^{29.ak}, S. D'Auria^{71a,71b}, C. David^{156b}, T. Davidek¹³³, B. Davis-Purcell³⁴, I. Dawson⁹⁴, K. De⁸, R. De Asmundis^{72a}, N. De Biase⁴⁸, S. De Castro^{23a,23b}, N. De Groot¹¹³, P. de Jong¹¹⁴, H. De la Torre¹⁰⁷, A. De Maria^{14c}, A. De Salvo^{75a}, U. De Sanctis^{76a,76b}, A. De Santo¹⁴⁶, J. B. De Vivie De Regie⁶⁰, D. V. Dedovich³⁸, J. Degens¹¹⁴, A. M. Deiana⁴⁴, F. Del Corso^{23a,23b}, J. Del Peso⁹⁹, F. Del Rio^{63a}, F. Deliot¹³⁵, C. M. Delitzsch⁴⁹, M. Della Pietra^{72a,72b}, D. Della Volpe⁵⁶, A. Dell'Acqua³⁶, L. Dell'Asta^{71a,71b}, M. Delmastro⁴, P. A. Delsart⁶⁰, S. Demers¹⁷², M. Demichev³⁸, S. P. Denisov³⁷, L. D'Eramo¹¹⁵, D. Derendarz⁸⁶, F. Derue¹²⁷, P. Dervan⁹², K. Desch²⁴, K. Dette¹⁵⁵, C. Deutsch²⁴, F. A. Di Bello^{57a,57b}, A. Di Ciaccio^{76a,76b}, L. Di Ciaccio⁴, A. Di Domenico^{75a,75b}, C. Di Donato^{72a,72b}, A. Di Girolamo³⁶, G. Di Gregorio⁵, A. Di Luca^{78a,78b}, B. Di Micco^{77a,77b}, R. Di Nardo^{77a,77b}, C. Diaconu¹⁰², F. A. Dias¹¹⁴, T. Dias Do Vale¹⁴², M. A. Diaz^{137a,137b}, F. G. Diaz Capriles²⁴, M. Didenko¹⁶³, E. B. Diehl¹⁰⁶, L. Diehl⁵⁴, S. Díez Cornell⁴⁸, C. Díez Pardos¹⁴¹, C. Dimitriadi^{24,161}, A. Dimitrievska^{17a}, J. Dingfelder²⁴, I.-M. Dinu^{27b}, S. J. Dittmeier^{63b}, F. Dittus³⁶, F. Djama¹⁰², T. Djobava^{149b}, J. I. Djuvsland¹⁶, C. Doglioni^{98,101}, J. Dolejsi¹³³, Z. Dolezal¹³³, M. Donadelli^{82c}, B. Dong¹⁰⁷, J. Donini⁴⁰, A. D'Onofrio^{77a,77b}, M. D'Onofrio⁹², J. Dopke¹³⁴, A. Doria^{72a}, M. T. Dova⁹⁰, A. T. Doyle⁵⁹, M. A. Dragnet¹²⁶, E. Drechsler¹⁴², E. Dreyer¹⁶⁹, I. Drivas-koulouris¹⁰, A. S. Drobac¹⁵⁸, M. Drozdova⁵⁶, D. Du^{62a}, T. A. du Pree¹¹⁴, F. Dubinin³⁷, M. Dubovsky^{28a}, E. Duchovni¹⁶⁹, G. Duckeck¹⁰⁹, O. A. Ducu^{27b}, D. Duda¹¹⁰, A. Dudarev³⁶, E. R. Duden²⁶, M. D'uffizi¹⁰¹, L. Dufflot⁶⁶, M. Dührssen³⁶, C. Dülsen¹⁷¹, A. E. Dumitriu^{27b}, M. Dunford^{63a}, S. Dungs⁴⁹, K. Dunne^{47a,47b}, A. Duperrin¹⁰², H. Duran Yildiz^{3a}, M. Düren⁵⁸, A. Durglishvili^{149b}, B. L. Dwyer¹¹⁵, G. I. Dyckes^{17a}, M. Dyndal^{85a}, S. Dysch¹⁰¹, B. S. Dziedzic⁸⁶, Z. O. Earnshaw¹⁴⁶, B. Eckerova^{28a}, S. Eggebrecht⁵⁵, M. G. Eggleston⁵¹, E. Egidio Purcino De Souza¹²⁷, L. F. Ehrke⁵⁶, G. Eigen¹⁶, K. Einsweiler^{17a}, T. Ekelof¹⁶¹, P. A. Ekman⁹⁸, Y. El Ghazali^{35b}, H. El Jarrari^{35e,148}, A. El Moussaouy^{35a}, V. Ellajosyula¹⁶¹, M. Ellert¹⁶¹, F. Ellinghaus¹⁷¹, A. A. Elliot⁹⁴, N. Ellis³⁶, J. Elmsheuser²⁹, M. Elsing³⁶, D. Emelianov¹³⁴, Y. Enari¹⁵³, I. Ene^{17a}, S. Epari¹³, J. Erdmann⁴⁹, P. A. Erland⁸⁶, M. Errenst¹⁷¹, M. Escalier⁶⁶, C. Escobar¹⁶³, E. Etzion¹⁵¹, G. Evans^{130a}, H. Evans⁶⁸, M. O. Evans¹⁴⁶, A. Ezhilov³⁷, S. Ezzarqtouni^{35a}, F. Fabbri⁵⁹, L. Fabbri^{23a,23b}, G. Facini⁹⁶, V. Fadeyev¹³⁶, R. M. Fakhruddinov³⁷, S. Falciano^{75a}, L. F. Falda Ulhoa Coelho³⁶, P. J. Falke²⁴, S. Falke³⁶, J. Faltova¹³³, Y. Fan^{14a}, Y. Fang^{14a,14d}, M. Fanti^{71a,71b}, M. Faraj^{69a,69b}, Z. Farazpay⁹⁷, A. Farbin⁸, A. Farilla^{77a}, T. Farooque¹⁰⁷, S. M. Farrington⁵², F. Fassi^{35c}, D. Fassouliotis⁹, M. Fauci Giannelli^{76a,76b}, W. J. Fawcett³², L. Fayard⁶⁶, P. Federic¹³³, P. Federicova¹³¹, O. L. Fedin^{37.a}, G. Fedotov³⁷, M. Feickert¹⁷⁰, L. Feligioni¹⁰², A. Fell¹³⁹, D. E. Fellers¹²³, C. Feng^{62b}, M. Feng^{14b}, Z. Feng¹¹⁴, M. J. Fenton¹⁶⁰, A. B. Fenyuk³⁷, L. Ferencz⁴⁸, R. A. M. Ferguson⁹¹, S. I. Fernandez Luengo^{137f}, J. Ferrando⁴⁸, A. Ferrari¹⁶¹, P. Ferrari^{113,114}, R. Ferrari^{73a}, D. Ferrere⁵⁶, C. Ferretti¹⁰⁶, F. Fiedler¹⁰⁰, A. Filipčić⁹³, E. K. Filmer¹, F. Filthaut¹¹³, M. C. N. Fiolhais^{130a,130c.c}, L. Fiorini¹⁶³, W. C. Fisher¹⁰⁷, T. Fitschen¹⁰¹, I. Fleck¹⁴¹, P. Fleischmann¹⁰⁶, T. Flick¹⁷¹, L. Flores¹²⁸, M. Flores^{33d,ae}, L. R. Flores Castillo^{64a}, F. M. Follega^{78a,78b}, N. Fomin¹⁶, J. H. Foo¹⁵⁵, B. C. Forland⁶⁸, A. Formica¹³⁵, A. C. Forti¹⁰¹, E. Fortin³⁶, A. W. Fortman⁶¹, M. G. Foti^{17a}, L. Fountas^{9,k}, D. Fournier⁶⁶, H. Fox⁹¹, P. Francavilla^{74a,74b}, S. Francescato⁶¹, S. Franchellucci⁵⁶, M. Franchini^{23a,23b}, S. Franchino^{63a}, D. Francis³⁶, L. Franco¹¹³, L. Franconi¹⁹, M. Franklin⁶¹, G. Frattari²⁶, A. C. Freegard⁹⁴, W. S. Freund^{82b}, Y. Y. Frid¹⁵¹, N. Fritzsche⁵⁰, A. Froch⁵⁴, D. Froidevaux³⁶, J. A. Frost¹²⁶, Y. Fu^{62a}, M. Fujimoto¹¹⁸, E. Fullana Torregrosa^{163,*}, E. Furtado De Simas Filho^{82b}, J. Fuster¹⁶³, A. Gabrielli^{23a,23b}, A. Gabrielli¹⁵⁵, P. Gadow⁴⁸, G. Gagliardi^{57a,57b}, L. G. Gagnon^{17a}, E. J. Gallas¹²⁶, B. J. Gallop¹³⁴, K. K. Gan¹¹⁹, S. Ganguly¹⁵³, J. Gao^{62a}, Y. Gao⁵², F. M. Garay Walls^{137a,137b}, B. Garcia^{29.ak}, C. García¹⁶³, J. E. García Navarro¹⁶³, M. Garcia-Sciveres^{17a}, R. W. Gardner³⁹, D. Garg⁸⁰, R. B. Garg^{143,q}, C. A. Garner¹⁵⁵, S. J. Gasiorowski¹³⁸, P. Gaspar^{82b}, G. Gaudio^{73a}, V. Gautam¹³, P. Gauzzi^{75a,75b}, I. L. Gavrilenko³⁷, A. Gavriluk³⁷, C. Gay¹⁶⁴, G. Gaycken⁴⁸, E. N. Gazis¹⁰, A. A. Geanta^{27b,27e}, C. M. Gee¹³⁶, K. Gellerstedt^{47b}, C. Gemme^{57b}, M. H. Genest⁶⁰, S. Gentile^{75a,75b}, S. George⁹⁵, W. F. George²⁰, T. Geralis⁴⁶, L. O. Gerlach⁵⁵, P. Gessinger-Befurt³⁶, M. E. Geyik¹⁷¹, M. Ghneimat¹⁴¹, K. Ghorbanian⁹⁴, A. Ghosal¹⁴¹, A. Ghosh¹⁶⁰, A. Ghosh⁷, B. Giacobbe^{23b}, S. Giagu^{75a,75b}, P. Giannetti^{74a}, A. Giannini^{62a}, S. M. Gibson⁹⁵, M. Gignac¹³⁶, D. T. Gil^{85b}, A. K. Gilbert^{85a}, B. J. Gilbert⁴¹, D. Gillberg³⁴, G. Gilles¹¹⁴, N. E. K. Gillwald⁴⁸, L. Ginabat¹²⁷, D. M. Gingrich^{2.ai}, M. P. Giordani^{69a,69c}, P. F. Giraud¹³⁵, G. Giugliarelli^{69a,69c}, D. Giugni^{71a}, F. Giuli³⁶, I. Gkialas^{9,k}, L. K. Gladilin³⁷, C. Glasman⁹⁹, G. R. Gledhill¹²³, M. Glisic¹²³, I. Gnesi^{43b,g}, Y. Go^{29.ak}, M. Goblirsch-Kolb³⁶

B. Gocke⁴⁹, D. Godin¹⁰⁸, B. Gokturk^{21a}, S. Goldfarb¹⁰⁵, T. Golling⁵⁶, M. G. D. Gololo^{33g}, D. Golubkov³⁷, J. P. Gombas¹⁰⁷, A. Gomes^{130a,130b}, G. Gomes Da Silva¹⁴¹, A. J. Gomez Delegido¹⁶³, R. Gonalo^{130a,130c}, G. Gonella¹²³, L. Gonella²⁰, A. Gongadze³⁸, F. Gonnella²⁰, J. L. Gonski⁴¹, R. Y. Gonzalez Andana⁵², S. Gonzalez de la Hoz¹⁶³, S. Gonzalez Fernandez¹³, R. Gonzalez Lopez⁹², C. Gonzalez Renteria^{17a}, R. Gonzalez Suarez¹⁶¹, S. Gonzalez-Sevilla⁵⁶, G. R. Gonzalvo Rodriguez¹⁶³, L. Goossens³⁶, P. A. Gorbounov³⁷, B. Gorini³⁶, E. Gorini^{70a,70b}, A. Gorišek⁹³, T. C. Gosart¹²⁸, A. T. Goshaw⁵¹, M. I. Gostkin³⁸, S. Goswami¹²¹, C. A. Gottardo³⁶, M. Gouighri^{35b}, V. Goumarre⁴⁸, A. G. Goussiou¹³⁸, N. Govender^{33c}, I. Grabowska-Bold^{85a}, K. Graham³⁴, E. Gramstad¹²⁵, S. Grancagnolo^{70a,70b}, M. Grandi¹⁴⁶, V. Gratchev^{37,*}, P. M. Gravila^{27f}, F. G. Gravili^{70a,70b}, H. M. Gray^{17a}, M. Greco^{70a,70b}, C. Grefe²⁴, I. M. Gregor⁴⁸, P. Grenier¹⁴³, C. Grieco¹³, A. A. Grillo¹³⁶, K. Grimm^{31,n}, S. Grinstein^{13,v}, J.-F. Grivaz⁶⁶, E. Gross¹⁶⁹, J. Grosse-Knetter⁵⁵, C. Grud¹⁰⁶, J. C. Grundy¹²⁶, L. Guan¹⁰⁶, W. Guan¹⁷⁰, C. Gubbels¹⁶⁴, J. G. R. Guerrero Rojas¹⁶³, G. Guerrieri^{69a,69b}, F. Guescini¹¹⁰, R. Gugel¹⁰⁰, J. A. M. Guhit¹⁰⁶, A. Guida⁴⁸, T. Guillemain⁴, E. Guillon^{134,167}, S. Guindon³⁶, F. Guo^{14a,14d}, J. Guo^{62c}, L. Guo⁶⁶, Y. Guo¹⁰⁶, R. Gupta⁴⁸, S. Gurbuz²⁴, S. S. Gurdasani⁵⁴, G. Gustavino³⁶, M. Guth⁵⁶, P. Gutierrez¹²⁰, L. F. Gutierrez Zagazeta¹²⁸, C. Gutsche⁹⁶, C. Gwenlan¹²⁶, C. B. Gwilliam⁹², E. S. Haaland¹²⁵, A. Haas¹¹⁷, M. Habedank⁴⁸, C. Haber^{17a}, H. K. Hadavand⁸, A. Hader¹⁰⁰, S. Hadzic¹¹⁰, E. H. Haines⁹⁶, M. Haleem¹⁶⁶, J. Haley¹²¹, J. J. Hall¹³⁹, G. D. Hallowell¹⁰², L. Halser¹⁹, K. Hamano¹⁶⁵, H. Hamdaoui^{35c}, M. Hamer²⁴, G. N. Hamity⁵², E. J. Hampshire⁹⁵, J. Han^{62b}, K. Han^{62a}, L. Han^{14c}, L. Han^{62a}, S. Han^{17a}, Y. F. Han¹⁵⁵, K. Hanagaki⁸³, M. Hance¹³⁶, D. A. Hangal^{41,ad}, H. Hani¹⁴², M. D. Hank¹²⁸, R. Hankache¹⁰¹, J. B. Hansen⁴², J. D. Hansen⁴², P. H. Hansen⁴², K. Hara¹⁵⁷, D. Harada⁵⁶, T. Harenberg¹⁷¹, S. Harkusha³⁷, Y. T. Harris¹²⁶, N. M. Harrison¹¹⁹, P. F. Harrison¹⁶⁷, N. M. Hartman¹⁴³, N. M. Hartmann¹⁰⁹, Y. Hasegawa¹⁴⁰, A. Hasib⁵², S. Haug¹⁹, R. Hauser¹⁰⁷, M. Havranek¹³², C. M. Hawkes²⁰, R. J. Hawkins³⁶, S. Hayashida¹¹¹, D. Hayden¹⁰⁷, C. Hayes¹⁰⁶, R. L. Hayes¹¹⁴, C. P. Hays¹²⁶, J. M. Hays⁹⁴, H. S. Hayward⁹², F. He^{62a}, Y. He¹⁵⁴, Y. He¹²⁷, N. B. Heatley⁹⁴, V. Hedberg⁹⁸, A. L. Heggelund¹²⁵, N. D. Hehir⁹⁴, C. Heidegger⁵⁴, K. K. Heidegger⁵⁴, W. D. Heidorn⁸¹, J. Heilman³⁴, S. Heim⁴⁸, T. Heim^{17a}, B. Heinemann^{48,af}, J. G. Heinlein¹²⁸, J. J. Heinrich¹²³, L. Heinrich^{110,ag}, J. Hejbal¹³¹, L. Helary⁴⁸, A. Held¹⁷⁰, S. Hellesund¹⁶, C. M. Helling¹⁶⁴, S. Hellman^{47a,47b}, C. Helsens³⁶, R. C. W. Henderson⁹¹, L. Henkelmann³², A. M. Henriques Correia³⁶, H. Herde⁹⁸, Y. Hernandez Jimenez¹⁴⁵, L. M. Herrmann²⁴, T. Herrmann⁵⁰, G. Herten⁵⁴, R. Hertenberger¹⁰⁹, L. Hervas³⁶, N. P. Hessey^{156a}, H. Hibi⁸⁴, S. J. Hillier²⁰, F. Hinterkeuser²⁴, M. Hirose¹²⁴, S. Hirose¹⁵⁷, D. Hirschbuehl¹⁷¹, T. G. Hitchings¹⁰¹, B. Hiti⁹³, J. Hobbs¹⁴⁵, R. Hobincu^{27e}, N. Hod¹⁶⁹, M. C. Hodgkinson¹³⁹, B. H. Hodgkinson³², A. Hoecker³⁶, J. Hofer⁴⁸, T. Holm²⁴, M. Holzbock¹¹⁰, L. B. A. H. Hommels³², B. P. Honan¹⁰¹, J. Hong^{62c}, T. M. Hong¹²⁹, J. C. Honig⁵⁴, B. H. Hooberman¹⁶², W. H. Hopkins⁶, Y. Horii¹¹¹, S. Hou¹⁴⁸, A. S. Howard⁹³, J. Howarth⁵⁹, J. Hoya⁶, M. Hrabovsky¹²², A. Hrynevich⁴⁸, T. Hryn'ova⁴, P. J. Hsu⁶⁵, S.-C. Hsu¹³⁸, Q. Hu⁴¹, Y. F. Hu^{14a,14d}, D. P. Huang⁹⁶, S. Huang^{64b}, X. Huang^{14c}, Y. Huang^{62a}, Y. Huang^{14a}, Z. Huang¹⁰¹, Z. Hubacek¹³², M. Huebner²⁴, F. Huegging²⁴, T. B. Huffman¹²⁶, M. Huhtinen³⁶, S. K. Huiberts¹⁶, R. Hulsken¹⁰⁴, N. Huseynov^{12,a}, J. Huston¹⁰⁷, J. Huth⁶¹, R. Hyneman¹⁴³, G. Iacobucci⁵⁶, G. Iakovidis²⁹, I. Ibragimov¹⁴¹, L. Iconomidou-Fayard⁶⁶, P. Iengo^{72a,72b}, R. Iguchi¹⁵³, T. Iizawa⁵⁶, Y. Ikegami⁸³, A. Ilg¹⁹, N. Ilic¹⁵⁵, H. Imam^{35a}, T. Ingebretsen Carlson^{47a,47b}, G. Introzzi^{73a,73b}, M. Iodice^{77a}, V. Ippolito^{75a,75b}, M. Ishino¹⁵³, W. Islam¹⁷⁰, C. Issever^{18,48}, S. Istin^{21a,am}, H. Ito¹⁶⁸, J. M. Iturbe Ponce^{64a}, R. Iuppa^{78a,78b}, A. Ivina¹⁶⁹, J. M. Izen⁴⁵, V. Izzo^{72a}, P. Jacka^{131,132}, P. Jackson¹, R. M. Jacobs⁴⁸, B. P. Jaeger¹⁴², C. S. Jagfeld¹⁰⁹, P. Jain⁵⁴, G. Jakel¹⁷¹, K. Jakobs⁵⁴, T. Jakoubek¹⁶⁹, J. Jamieson⁵⁹, K. W. Janas^{85a}, A. E. Jaspan⁹², M. Javurkova¹⁰³, F. Jeanneau¹³⁵, L. Jeanty¹²³, J. Jejelava^{149a,ab}, P. Jenni^{54,h}, C. E. Jessiman³⁴, S. Jezequel⁴, C. Jia^{62b}, J. Jia¹⁴⁵, X. Jia⁶¹, X. Jia^{14a,14d}, Z. Jia^{14c}, Y. Jiang^{62a}, S. Jiggins⁴⁸, J. Jimenez Pena¹¹⁰, S. Jin^{14c}, A. Jinaru^{27b}, O. Jinnouchi¹⁵⁴, P. Johansson¹³⁹, K. A. Johns⁷, J. W. Johnson¹³⁶, D. M. Jones³², E. Jones¹⁶⁷, P. Jones³², R. W. L. Jones⁹¹, T. J. Jones⁹², R. Joshi¹¹⁹, J. Jovicevic¹⁵, X. Ju^{17a}, J. J. Junggeburth³⁶, T. Junkermann^{63a}, A. Juste Rozas^{13,v}, S. Kabana^{137e}, A. Kaczmarzka⁸⁶, M. Kado¹¹⁰, H. Kagan¹¹⁹, M. Kagan¹⁴³, A. Kahn⁴¹, A. Kahn¹²⁸, C. Kahra¹⁰⁰, T. Kaji¹⁶⁸, E. Kajomovitz¹⁵⁰, N. Kakati¹⁶⁹, C. W. Kalderon²⁹, A. Kamenshchikov¹⁵⁵, S. Kanayama¹⁵⁴, N. J. Kang¹³⁶, D. Kar^{33g}, K. Karava¹²⁶, M. J. Kareem^{156b}, E. Karentzos⁵⁴, I. Karkanias^{152,f}, S. N. Karpov³⁸, Z. M. Karpova³⁸, V. Kartvelishvili⁹¹, A. N. Karyukhin³⁷, E. Kasimi^{152,f}, J. Katzy⁴⁸, S. Kaur³⁴, K. Kawade¹⁴⁰, T. Kawamoto¹³⁵, G. Kawamura⁵⁵, E. F. Kay¹⁶⁵, F. I. Kaya¹⁵⁸, S. Kazakos¹³, V. F. Kazanin³⁷, Y. Ke¹⁴⁵, J. M. Keaveney^{33a}, R. Keeler¹⁶⁵, G. V. Kehris⁶¹, J. S. Keller³⁴, A. S. Kelly⁹⁶, D. Kelsey¹⁴⁶

J. J. Kempster¹⁴⁶, K. E. Kennedy⁴¹, P. D. Kennedy¹⁰⁰, O. Kepka¹³¹, B. P. Kerridge¹⁶⁷, S. Kersten¹⁷¹, B. P. Kerševan⁹³, S. Keshri⁶⁶, L. Keszeghova^{28a}, S. Ketabchi Haghighat¹⁵⁵, M. Khandoga¹²⁷, A. Khanov¹²¹, A. G. Kharlamov³⁷, T. Kharlamova³⁷, E. E. Khoda¹³⁸, T. J. Khoo¹⁸, G. Khorauli¹⁶⁶, J. Khubua^{149b}, Y. A. R. Khwaira⁶⁶, M. Kiehn³⁶, A. Kilgallon¹²³, D. W. Kim^{47a,47b}, Y. K. Kim³⁹, N. Kimura⁹⁶, A. Kirchhoff⁵⁵, C. Kirfel²⁴, J. Kirk¹³⁴, A. E. Kiryunin¹¹⁰, T. Kishimoto¹⁵³, D. P. Kisliuk¹⁵⁵, C. Kitsaki¹⁰, O. Kivernyk²⁴, M. Klassen^{63a}, C. Klein³⁴, L. Klein¹⁶⁶, M. H. Klein¹⁰⁶, M. Klein⁹², S. B. Klein⁵⁶, U. Klein⁹², P. Klimek³⁶, A. Klimentov²⁹, T. Klioutchnikova³⁶, P. Kluit¹¹⁴, S. Kluth¹¹⁰, E. Kneringer⁷⁹, T. M. Knight¹⁵⁵, A. Knue⁵⁴, R. Kobayashi⁸⁷, M. Kocian¹⁴³, P. Kodyš¹³³, D. M. Koeck¹²³, P. T. Koenig²⁴, T. Koffas³⁴, M. Kolb¹³⁵, I. Koletsou⁴, T. Komarek¹²², K. Köneke⁵⁴, A. X. Y. Kong¹, T. Kono¹¹⁸, N. Konstantinidis⁹⁶, B. Konya⁹⁸, R. Kopeliansky⁶⁸, S. Koperny^{85a}, K. Korcyl⁸⁶, K. Kordas^{152.f}, G. Koren¹⁵¹, A. Korn⁹⁶, S. Korn⁵⁵, I. Korolkov¹³, N. Korotkova³⁷, B. Kortman¹¹⁴, O. Kortner¹¹⁰, S. Kortner¹¹⁰, W. H. KostECKa¹¹⁵, V. V. Kostyukhin¹⁴¹, A. Kotsokchagia¹³⁵, A. Kotwal⁵¹, A. Koulouris³⁶, A. Kourkoumeli-Charalampidi^{73a,73b}, C. Kourkoumelis⁹, E. Kourlitis⁶, O. Kovanda¹⁴⁶, R. Kowalewski¹⁶⁵, W. Kozanecki¹³⁵, A. S. Kozhin³⁷, V. A. Kramarenko³⁷, G. Kramberger⁹³, P. Kramer¹⁰⁰, M. W. Krasny¹²⁷, A. Krasznahorkay³⁶, J. A. Kremer¹⁰⁰, T. Kresse⁵⁰, J. Kretschmar⁹², K. Kreul¹⁸, P. Krieger¹⁵⁵, S. Krishnamurthy¹⁰³, M. Krivos¹³³, K. Krizka²⁰, K. Kroeninger⁴⁹, H. Kroha¹¹⁰, J. Kroll¹³¹, J. Kroll¹²⁸, K. S. Krowpman¹⁰⁷, U. Kruchonak³⁸, H. Krüger²⁴, N. Krumnack⁸¹, M. C. Kruse⁵¹, J. A. Krzysiak⁸⁶, O. Kuchinskaia³⁷, S. Kuday^{3a}, J. T. Kuechler⁴⁸, S. Kuehn³⁶, R. Kuesters⁵⁴, T. Kuhl⁴⁸, V. Kukhtin³⁸, Y. Kulchitsky^{37.a}, S. Kuleshov^{137b,137d}, M. Kumar^{33g}, N. Kumari¹⁰², A. Kupco¹³¹, T. Kupfer⁴⁹, A. Kupich³⁷, O. Kuprash⁵⁴, H. Kurashige⁸⁴, L. L. Kurchaninov^{156a}, O. Kurdyshev⁶⁶, Y. A. Kurochkin³⁷, A. Kurova³⁷, M. Kuze¹⁵⁴, A. K. Kvam¹⁰³, J. Kvita¹²², T. Kwan¹⁰⁴, N. G. Kyriacou¹⁰⁶, L. A. O. Laatu¹⁰², C. Lacasta¹⁶³, F. Lacava^{75a,75b}, H. Lacker¹⁸, D. Lacour¹²⁷, N. N. Lad⁹⁶, E. Ladygin³⁸, B. Laforge¹²⁷, T. Lagouri^{137e}, S. Lai⁵⁵, I. K. Lakomic^{85a}, N. Lalloue⁶⁰, J. E. Lambert¹²⁰, S. Lammers⁶⁸, W. Lampl⁷, C. Lampoudis^{152.f}, A. N. Lancaster¹¹⁵, E. Lançon²⁹, U. Landgraf⁵⁴, M. P. J. Landon⁹⁴, V. S. Lang⁵⁴, R. J. Langenberg¹⁰³, A. J. Lankford¹⁶⁰, F. Lanni³⁶, K. Lantzsch²⁴, A. Lanza^{73a}, A. Lapertosa^{57a,57b}, J. F. Laporte¹³⁵, T. Lari^{71a}, F. Lasagni Manghi^{23b}, M. Lassnig³⁶, V. Latonova¹³¹, A. Laudrain¹⁰⁰, A. Laurier¹⁵⁰, S. D. Lawlor⁹⁵, Z. Lawrence¹⁰¹, M. Lazzaroni^{71a,71b}, B. Le¹⁰¹, E. M. Le Boulicaut⁵¹, B. Leban⁹³, A. Lebedev⁸¹, M. LeBlanc³⁶, F. Ledroit-Guillon⁶⁰, A. C. A. Lee⁹⁶, G. R. Lee¹⁶, S. C. Lee¹⁴⁸, S. Lee^{47a,47b}, T. F. Lee⁹², L. L. Leeuw^{33c}, H. P. Lefebvre⁹⁵, M. Lefebvre¹⁶⁵, C. Leggett^{17a}, K. Lehmann¹⁴², G. Lehmann Miotto³⁶, M. Leigh⁵⁶, W. A. Leight¹⁰³, A. Leisos^{152.u}, M. A. L. Leite^{82c}, C. E. Leitgeb⁴⁸, R. Leitner¹³³, K. J. C. Leney⁴⁴, T. Lenz²⁴, S. Leone^{74a}, C. Leonidopoulos⁵², A. Leopold¹⁴⁴, C. Leroy¹⁰⁸, R. Les¹⁰⁷, C. G. Lester³², M. Levchenko³⁷, J. Levêque⁴, D. Levin¹⁰⁶, L. J. Levinson¹⁶⁹, M. P. Lewicki⁸⁶, D. J. Lewis⁴, A. Li⁵, B. Li^{62b}, C. Li^{62a}, C.-Q. Li^{62c}, H. Li^{62a}, H. Li^{62b}, H. Li^{14c}, H. Li^{62b}, J. Li^{62c}, K. Li¹³⁸, L. Li^{62c}, M. Li^{14a,14d}, Q. Y. Li^{62a}, S. Li^{14a,14d}, S. Li^{62c,62d,e}, T. Li^{62b}, X. Li¹⁰⁴, Z. Li^{62b}, Z. Li¹²⁶, Z. Li¹⁰⁴, Z. Li⁹², Z. Li^{14a,14d}, Z. Liang^{14a}, M. Liberatore⁴⁸, B. Liberti^{76a}, K. Lie^{64c}, J. Lieber Marin^{82b}, H. Lien⁶⁸, K. Lin¹⁰⁷, R. A. Linck⁶⁸, R. E. Lindley⁷, J. H. Lindon², A. Linss⁴⁸, E. Lipeles¹²⁸, A. Lipniacka¹⁶, A. Lister¹⁶⁴, J. D. Little⁴, B. Liu^{14a}, B. X. Liu¹⁴², D. Liu^{62c,62d}, J. B. Liu^{62a}, J. K. K. Liu³², K. Liu^{62c,62d}, M. Liu^{62a}, M. Y. Liu^{62a}, P. Liu^{14a}, Q. Liu^{62c,62d,138}, X. Liu^{62a}, Y. Liu^{14c,14d}, Y. L. Liu¹⁰⁶, Y. W. Liu^{62a}, J. Llorente Merino¹⁴², S. L. Lloyd⁹⁴, E. M. Lobodzinska⁴⁸, P. Loch⁷, S. Loffredo^{76a,76b}, T. Lohse¹⁸, K. Lohwasser¹³⁹, E. Loiacono⁴⁸, M. Lokajicek^{131,*}, J. D. Long¹⁶², I. Longarini¹⁶⁰, L. Longo^{70a,70b}, R. Longo¹⁶², I. Lopez Paz⁶⁷, A. Lopez Solis⁴⁸, J. Lorenz¹⁰⁹, N. Lorenzo Martinez⁴, A. M. Lory¹⁰⁹, X. Lou^{47a,47b}, X. Lou^{14a,14d}, A. Lounis⁶⁶, J. Love⁶, P. A. Love⁹¹, G. Lu^{14a,14d}, M. Lu⁸⁰, S. Lu¹²⁸, Y. J. Lu⁶⁵, H. J. Lubatti¹³⁸, C. Luci^{75a,75b}, F. L. Lucio Alves^{14c}, A. Lucotte⁶⁰, F. Luehring⁶⁸, I. Luise¹⁴⁵, O. Lukianchuk⁶⁶, O. Lundberg¹⁴⁴, B. Lund-Jensen¹⁴⁴, N. A. Luongo¹²³, M. S. Lutz¹⁵¹, D. Lynn²⁹, H. Lyons⁹², R. Lysak¹³¹, E. Lytken⁹⁸, V. Lyubushkin³⁸, T. Lyubushkina³⁸, M. M. Lyukova¹⁴⁵, H. Ma²⁹, L. L. Ma^{62b}, Y. Ma⁹⁶, D. M. Mac Donell¹⁶⁵, G. Maccarrone⁵³, J. C. MacDonald¹³⁹, R. Madar⁴⁰, W. F. Mader⁵⁰, J. Maeda⁸⁴, T. Maeno²⁹, M. Maerker⁵⁰, H. Maguire¹³⁹, A. Maio^{130a,130b,130d}, K. Maj^{85a}, O. Majersky⁴⁸, S. Majewski¹²³, N. Makovec⁶⁶, V. Maksimovic¹⁵, B. Malaescu¹²⁷, Pa. Malecki⁸⁶, V. P. Maleev³⁷, F. Malek⁶⁰, D. Malito^{43a,43b}, U. Mallik⁸⁰, C. Malone³², S. Maltezos¹⁰, S. Malyukov³⁸, J. Mamuzic¹³, G. Mancini⁵³, G. Manco^{73a,73b}, J. P. Mandalia⁹⁴, I. Mandić⁹³, L. Manhaes de Andrade Filho^{82a}, I. M. Maniatis¹⁶⁹, J. Manjarres Ramos^{102.ac}, D. C. Mankad¹⁶⁹, A. Mann¹⁰⁹, B. Mansoulie¹³⁵, S. Manzoni³⁶, A. Marantis^{152.u}, G. Marchiori⁵, M. Marcisovsky¹³¹, C. Marcon^{71a,71b}, M. Marinescu²⁰, M. Marjanovic¹²⁰, E. J. Marshall⁹¹, Z. Marshall^{17a}, S. Marti-Garcia¹⁶³, T. A. Martin¹⁶⁷, V. J. Martin⁵², B. Martin dit Latour¹⁶

L. Martinelli^{75a,75b}^{ID}, M. Martinez^{13,y}^{ID}, P. Martinez Agullo¹⁶³^{ID}, V. I. Martinez Outschoorn¹⁰³^{ID}, P. Martinez Suarez¹³^{ID}, S. Martin-Haugh¹³⁴^{ID}, V. S. Martoiu^{27b}^{ID}, A. C. Martyniuk⁹⁶^{ID}, A. Marzin³⁶^{ID}, S. R. Maschek¹¹⁰^{ID}, D. Mascione^{78a,78b}^{ID}, L. Masetti¹⁰⁰^{ID}, T. Mashimo¹⁵³^{ID}, J. Masik¹⁰¹^{ID}, A. L. Maslennikov³⁷^{ID}, L. Massa^{23b}^{ID}, P. Massarotti^{72a,72b}^{ID}, P. Mastrandrea^{74a,74b}^{ID}, A. Mastroberardino^{43a,43b}^{ID}, T. Masubuchi¹⁵³^{ID}, T. Mathisen¹⁶¹^{ID}, N. Matsuzawa¹⁵³^{ID}, J. Maurer^{27b}^{ID}, B. Maček⁹³^{ID}, D. A. Maximov³⁷^{ID}, R. Mazini¹⁴⁸^{ID}, I. Maznas^{152,f}^{ID}, M. Mazza¹⁰⁷^{ID}, S. M. Mazza¹³⁶^{ID}, C. Mc Ginn^{29,ak}^{ID}, J. P. Mc Gowan¹⁰⁴^{ID}, S. P. Mc Kee¹⁰⁶^{ID}, E. F. McDonald¹⁰⁵^{ID}, A. E. McDougall¹¹⁴^{ID}, J. A. Mcfayden¹⁴⁶^{ID}, R. P. McGovern¹²⁸^{ID}, G. Mchedlidze^{149b}^{ID}, R. P. McKenzie^{33g}^{ID}, T. C. McLachlan⁴⁸^{ID}, D. J. McLaughlin⁹⁶^{ID}, K. D. McLean¹⁶⁵^{ID}, S. J. McMahon¹³⁴^{ID}, P. C. McNamara¹⁰⁵^{ID}, C. M. Mcpartland⁹²^{ID}, R. A. McPherson^{165,y}^{ID}, T. Megy⁴⁰^{ID}, S. Mehlhase¹⁰⁹^{ID}, A. Mehta⁹²^{ID}, D. Melini¹⁵⁰^{ID}, B. R. Mellado Garcia^{33g}^{ID}, A. H. Melo⁵⁵^{ID}, F. Meloni⁴⁸^{ID}, S. B. Menary¹⁰¹^{ID}, A. M. Mendes Jacques Da Costa¹⁰¹^{ID}, H. Y. Meng¹⁵⁵^{ID}, L. Meng⁹¹^{ID}, S. Menke¹¹⁰^{ID}, M. Mentink³⁶^{ID}, E. Meoni^{43a,43b}^{ID}, C. Merlassino¹²⁶^{ID}, L. Merola^{72a,72b}^{ID}, C. Meroni^{71a,71b}^{ID}, G. Merz¹⁰⁶^{ID}, O. Meshkov³⁷^{ID}, J. Metcalfe⁶^{ID}, A. S. Mete⁶^{ID}, C. Meyer⁶⁸^{ID}, J.-P. Meyer¹³⁵^{ID}, R. P. Middleton¹³⁴^{ID}, L. Mijović⁵²^{ID}, G. Mikenberg¹⁶⁹^{ID}, M. Mikesikova¹³¹^{ID}, M. Mikuz⁹³^{ID}, H. Mildner¹³⁹^{ID}, A. Milic³⁶^{ID}, C. D. Milke⁴⁴^{ID}, D. W. Miller³⁹^{ID}, L. S. Miller³⁴^{ID}, A. Milov¹⁶⁹^{ID}, D. A. Milstead^{47a,47b}^{ID}, T. Min^{14c}^{ID}, A. A. Minaenko³⁷^{ID}, I. A. Minashvili^{149b}^{ID}, L. Mince⁵⁹^{ID}, A. I. Mincer¹¹⁷^{ID}, B. Mindur^{85a}^{ID}, M. Mineev³⁸^{ID}, Y. Mino⁸⁷^{ID}, L. M. Mir¹³^{ID}, M. Miralles Lopez¹⁶³^{ID}, M. Mironova^{17a}^{ID}, M. C. Missio¹¹³^{ID}, T. Mitani¹⁶⁸^{ID}, A. Mitra¹⁶⁷^{ID}, V. A. Mitsou¹⁶³^{ID}, O. Miu¹⁵⁵^{ID}, P. S. Miyagawa⁹⁴^{ID}, Y. Miyazaki⁸⁹^{ID}, A. Mizukami⁸³^{ID}, T. Mkrtchyan^{63a}^{ID}, M. Mlinarevic⁹⁶^{ID}, T. Mlinarevic⁹⁶^{ID}, M. Mlynarikova³⁶^{ID}, S. Mobius⁵⁵^{ID}, K. Mochizuki¹⁰⁸^{ID}, P. Moder⁴⁸^{ID}, P. Mogg¹⁰⁹^{ID}, A. F. Mohammed^{14a,14d}^{ID}, S. Mohapatra⁴¹^{ID}, G. Mokgatitswane^{33g}^{ID}, B. Mondal¹⁴¹^{ID}, S. Mondal¹³²^{ID}, K. Mönig⁴⁸^{ID}, E. Monnier¹⁰²^{ID}, L. Monsonis Romero¹⁶³^{ID}, J. Montejo Berlingen⁸³^{ID}, M. Montella¹¹⁹^{ID}, F. Monticelli⁹⁰^{ID}, N. Morange⁶⁶^{ID}, A. L. Moreira De Carvalho^{130a}^{ID}, M. Moreno Llácer¹⁶³^{ID}, C. Moreno Martinez⁵⁶^{ID}, P. Morettini^{57b}^{ID}, S. Morgenstern³⁶^{ID}, M. Morii⁶¹^{ID}, M. Morinaga¹⁵³^{ID}, A. K. Morley³⁶^{ID}, F. Morodei^{75a,75b}^{ID}, L. Morvaj³⁶^{ID}, P. Moschovakos³⁶^{ID}, B. Moser³⁶^{ID}, M. Mosidze^{149b}^{ID}, T. Moskalets⁵⁴^{ID}, P. Moskvitina¹¹³^{ID}, J. Moss^{31,o}^{ID}, E. J. W. Moyse¹⁰³^{ID}, O. Mtintsilana^{33g}^{ID}, S. Muanza¹⁰²^{ID}, J. Mueller¹²⁹^{ID}, D. Muenstermann⁹¹^{ID}, R. Müller¹⁹^{ID}, G. A. Mullier¹⁶¹^{ID}, J. J. Mullin¹²⁸^{ID}, D. P. Mungo¹⁵⁵^{ID}, J. L. Munoz Martinez¹³^{ID}, D. Munoz Perez¹⁶³^{ID}, F. J. Munoz Sanchez¹⁰¹^{ID}, M. Murin¹⁰¹^{ID}, W. J. Murray^{134,167}^{ID}, A. Murrone^{71a,71b}^{ID}, J. M. Muse¹²⁰^{ID}, M. Muškinja^{17a}^{ID}, C. Mwewa²⁹^{ID}, A. G. Myagkov^{37,a}^{ID}, A. J. Myers⁸^{ID}, A. A. Myers¹²⁹^{ID}, G. Myers⁶⁸^{ID}, M. Myska¹³²^{ID}, B. P. Nachman^{17a}^{ID}, O. Nackenhorst⁴⁹^{ID}, A. Nag⁵⁰^{ID}, K. Nagai¹²⁶^{ID}, K. Nagano⁸³^{ID}, J. L. Nagle^{29,ak}^{ID}, E. Nagy¹⁰²^{ID}, A. M. Nairz³⁶^{ID}, Y. Nakahama⁸³^{ID}, K. Nakamura⁸³^{ID}, H. Nanjo¹²⁴^{ID}, R. Narayan⁴⁴^{ID}, E. A. Narayanan¹¹²^{ID}, I. Naryshkin³⁷^{ID}, M. Naseri³⁴^{ID}, C. Nass²⁴^{ID}, G. Navarro^{22a}^{ID}, J. Navarro-Gonzalez¹⁶³^{ID}, R. Nayak¹⁵¹^{ID}, A. Nayaz¹⁸^{ID}, P. Y. Nechaeva³⁷^{ID}, F. Nechansky⁴⁸^{ID}, L. Nedic¹²⁶^{ID}, T. J. Neep²⁰^{ID}, A. Negri^{73a,73b}^{ID}, M. Negrini^{23b}^{ID}, C. Nellist¹¹⁴^{ID}, C. Nelson¹⁰⁴^{ID}, K. Nelson¹⁰⁶^{ID}, S. Nemecek¹³¹^{ID}, M. Nessi^{36,i}^{ID}, M. S. Neubauer¹⁶²^{ID}, F. Neuhaus¹⁰⁰^{ID}, J. Neundorfer⁴⁸^{ID}, R. Newhouse¹⁶⁴^{ID}, P. R. Newman²⁰^{ID}, C. W. Ng¹²⁹^{ID}, Y. W. Y. Ng⁴⁸^{ID}, B. Ngair^{35e}^{ID}, H. D. N. Nguyen¹⁰⁸^{ID}, R. B. Nickerson¹²⁶^{ID}, R. Nicolaidou¹³⁵^{ID}, J. Nielsen¹³⁶^{ID}, M. Niemeyer⁵⁵^{ID}, N. Nikiforou³⁶^{ID}, V. Nikolaenko^{37,a}^{ID}, I. Nikolic-Audit¹²⁷^{ID}, K. Nikolopoulos²⁰^{ID}, P. Nilsson²⁹^{ID}, I. Ninca⁴⁸^{ID}, H. R. Nindhito⁵⁶^{ID}, G. Ninio¹⁵¹^{ID}, A. Nisati^{75a}^{ID}, N. Nishu²^{ID}, R. Nisius¹¹⁰^{ID}, J.-E. Nitschke⁵⁰^{ID}, E. K. Nkadimeng^{33g}^{ID}, S. J. Noacco Rosende⁹⁰^{ID}, T. Nobe¹⁵³^{ID}, D. L. Noel³²^{ID}, T. Nommensen¹⁴⁷^{ID}, M. A. Nomura²⁹^{ID}, M. B. Norfolk¹³⁹^{ID}, R. R. B. Norisam⁹⁶^{ID}, B. J. Norman³⁴^{ID}, J. Novak⁹³^{ID}, T. Novak⁴⁸^{ID}, L. Novotny¹³²^{ID}, R. Novotny¹¹²^{ID}, L. Nozka¹²²^{ID}, K. Ntekas¹⁶⁰^{ID}, N. M. J. Nunes De Moura Junior^{82b}^{ID}, E. Nurse⁹⁶^{ID}, J. Ocariz¹²⁷^{ID}, A. Ochi⁸⁴^{ID}, I. Ochoa^{130a}^{ID}, S. Oerdek¹⁶¹^{ID}, J. T. Offermann³⁹^{ID}, A. Ogrodnik^{85a}^{ID}, A. Oh¹⁰¹^{ID}, C. C. Ohm¹⁴⁴^{ID}, H. Oide⁸³^{ID}, R. Oishi¹⁵³^{ID}, M. L. Ojeda⁴⁸^{ID}, Y. Okazaki⁸⁷^{ID}, M. W. O'Keefe⁹²^{ID}, Y. Okumura¹⁵³^{ID}, L. F. Oleiro Seabra^{130a}^{ID}, S. A. Olivares Pino^{137d}^{ID}, D. Oliveira Damazio²⁹^{ID}, D. Oliveira Goncalves^{82a}^{ID}, J. L. Oliver¹⁶⁰^{ID}, M. J. R. Olsson¹⁶⁰^{ID}, A. Olszewski⁸⁶^{ID}, J. Olszowska^{86,*}^{ID}, Ö. O. Öncel⁵⁴^{ID}, D. C. O'Neil¹⁴²^{ID}, A. P. O'Neill¹⁹^{ID}, A. Onofre^{130a,130c}^{ID}, P. U. E. Onyisi¹¹^{ID}, M. J. Oreglia³⁹^{ID}, G. E. Orellana⁹⁰^{ID}, D. Orestano^{77a,77b}^{ID}, N. Orlando¹³^{ID}, R. S. Orr¹⁵⁵^{ID}, V. O'Shea⁵⁹^{ID}, R. Ospanov^{62a}^{ID}, G. Otero y Garzon³⁰^{ID}, H. Otono⁸⁹^{ID}, P. S. Ott^{63a}^{ID}, G. J. Ottino^{17a}^{ID}, M. Ouchrif^{35d}^{ID}, J. Ouellette²⁹^{ID}, F. Ould-Saada¹²⁵^{ID}, M. Owen⁵⁹^{ID}, R. E. Owen¹³⁴^{ID}, K. Y. Oyulmaz^{21a}^{ID}, V. E. Ozcan^{21a}^{ID}, N. Ozturk⁸^{ID}, S. Ozturk^{21d}^{ID}, H. A. Pacey³²^{ID}, A. Pacheco Pages¹³^{ID}, C. Padilla Aranda¹³^{ID}, G. Padovano^{75a,75b}^{ID}, S. Pagan Griso^{17a}^{ID}, G. Palacino⁶⁸^{ID}, A. Palazzo^{70a,70b}^{ID}, S. Palestini³⁶^{ID}, J. Pan¹⁷²^{ID}, T. Pan^{64a}^{ID}, D. K. Panchal¹¹^{ID}, C. E. Pandini¹¹⁴^{ID}, J. G. Panduro Vazquez⁹⁵^{ID}, H. Pang^{14b}^{ID}, P. Pani⁴⁸^{ID}, G. Panizzo^{69a,69c}^{ID}, L. Paolozzi⁵⁶^{ID}, C. Papadatos¹⁰⁸^{ID}, S. Parajuli⁴⁴^{ID}, A. Paramonov⁶^{ID}, C. Paraskevopoulos¹⁰^{ID}, D. Paredes Hernandez^{64b}^{ID}, T. H. Park¹⁵⁵^{ID}, M. A. Parker³²^{ID}, F. Parodi^{57a,57b}^{ID}, E. W. Parrish¹¹⁵^{ID}, V. A. Parrish⁵²^{ID}, J. A. Parsons⁴¹^{ID}, U. Parzefall⁵⁴^{ID}, B. Pascual Dias¹⁰⁸^{ID}, L. Pascual Dominguez¹⁵¹^{ID}, F. Pasquali¹¹⁴^{ID}, E. Pasqualucci^{75a}^{ID}, S. Passaggio^{57b}^{ID}, F. Pastore⁹⁵^{ID}, P. Pasuwan^{47a,47b}^{ID}, P. Patel⁸⁶^{ID}, U. M. Patel⁵¹^{ID}, J. R. Pater¹⁰¹^{ID}, T. Pauly³⁶^{ID}, J. Pearkes¹⁴³^{ID}, M. Pedersen¹²⁵^{ID}, R. Pedro^{130a}^{ID}, S. V. Peleganchuk³⁷^{ID}, O. Penc³⁶^{ID}, E. A. Pender⁵²^{ID},

H. Peng^{62a}, K. E. Penski¹⁰⁹, M. Penzin³⁷, B. S. Peralva^{82d}, A. P. Pereira Peixoto⁶⁰, L. Pereira Sanchez^{47a,47b}, D. V. Perpelitsa^{29,ak}, E. Perez Codina^{156a}, M. Perganti¹⁰, L. Perini^{71a,71b,*}, H. Pernegger³⁶, S. Perrella³⁶, A. Perrevoort¹¹³, O. Perrin⁴⁰, K. Peters⁴⁸, R. F. Y. Peters¹⁰¹, B. A. Petersen³⁶, T. C. Petersen⁴², E. Petit¹⁰², V. Petousis¹³², C. Petridou^{152,f}, A. Petrukhin¹⁴¹, M. Pettee^{17a}, N. E. Pettersson³⁶, A. Petukhov³⁷, K. Petukhova¹³³, A. Peyaud¹³⁵, R. Pezoa^{137f}, L. Pezzotti³⁶, G. Pezzullo¹⁷², T. M. Pham¹⁷⁰, T. Pham¹⁰⁵, P. W. Phillips¹³⁴, M. W. Phipps¹⁶², G. Piacquadio¹⁴⁵, E. Pianori^{17a}, F. Piazza^{71a,71b}, R. Piegaia³⁰, D. Pietreanu^{27b}, A. D. Pilkington¹⁰¹, M. Pinamonti^{69a,69c}, J. L. Pinfold², B. C. Pinheiro Pereira^{130a}, C. Pitman Donaldson⁹⁶, D. A. Pizzi³⁴, L. Pizzimento^{76a,76b}, A. Pizzini¹¹⁴, M.-A. Pleier²⁹, V. Plesanovs⁵⁴, V. Pleskot¹³³, E. Plotnikova³⁸, G. Poddar⁴, R. Poettgen⁹⁸, L. Poggioli¹²⁷, D. Pohl²⁴, I. Pokharel⁵⁵, S. Polacek¹³³, G. Polesello^{73a}, A. Poley^{142,156a}, R. Polifka¹³², A. Polini^{23b}, C. S. Pollard¹⁶⁷, Z. B. Pollock¹¹⁹, V. Polychronakos²⁹, E. Pompa Pacchi^{75a,75b}, D. Ponomarenko¹¹³, L. Pontecorvo³⁶, S. Popa^{27a}, G. A. Popeneciu^{27d}, D. M. Portillo Quintero^{156a}, S. Pospisil¹³², P. Postolache^{27c}, K. Potamianos¹²⁶, P. A. Potepa^{85a}, I. N. Potrap³⁸, C. J. Potter³², H. Potti¹, T. Poulsen⁴⁸, J. Poveda¹⁶³, M. E. Pozo Astigarraga³⁶, A. Prades Ibanez¹⁶³, M. M. Prapa⁴⁶, J. Pretel⁵⁴, D. Price¹⁰¹, M. Primavera^{70a}, M. A. Principe Martin⁹⁹, R. Privara¹²², M. L. Proffitt¹³⁸, N. Proklova¹²⁸, K. Prokofiev^{64c}, G. Proto^{76a,76b}, S. Protopopescu²⁹, J. Proudfoot⁶, M. Przybycien^{85a}, W. W. Przygoda^{85b}, J. E. Puddefoot¹³⁹, D. Pudzha³⁷, D. Pyatiizbyantseva³⁷, J. Qian¹⁰⁶, D. Qichen¹⁰¹, Y. Qin¹⁰¹, T. Qiu⁵², A. Quadt⁵⁵, M. Queitsch-Maitland¹⁰¹, G. Quetant⁵⁶, G. Rabanal Bolanos⁶¹, D. Rafanoharana⁵⁴, F. Ragusa^{71a,71b}, J. L. Rainbolt³⁹, J. A. Raine⁵⁶, S. Rajagopalan²⁹, E. Ramakoti³⁷, K. Ran^{14d,48}, N. P. Rapheeha^{33g}, V. Raskina¹²⁷, D. F. Rassloff^{63a}, S. Rave¹⁰⁰, B. Ravina⁵⁵, I. Ravinovich¹⁶⁹, M. Raymond³⁶, A. L. Read¹²⁵, N. P. Readoff¹³⁹, D. M. Rebuzzi^{73a,73b}, G. Redlinger²⁹, K. Reeves²⁶, J. A. Reidelsturz¹⁷¹, D. Reikher¹⁵¹, A. Rej¹⁴¹, C. Rembser³⁶, A. Renardi⁴⁸, M. Renda^{27b}, M. B. Rendel¹¹⁰, F. Renner⁴⁸, A. G. Rennie⁵⁹, S. Resconi^{71a}, M. Ressegotti^{57a,57b}, E. D. Resseguie^{17a}, S. Rettie³⁶, J. G. Reyes Rivera¹⁰⁷, B. Reynolds¹¹⁹, E. Reynolds^{17a}, M. Rezaei Estabragh¹⁷¹, O. L. Rezanova³⁷, P. Reznicek¹³³, N. Ribaric⁹¹, E. Ricci^{78a,78b}, R. Richter¹¹⁰, S. Richter^{47a,47b}, E. Richter-Was^{85b}, M. Ridel¹²⁷, S. Ridouani^{35d}, P. Rieck¹¹⁷, P. Riedler³⁶, M. Rijssenbeek¹⁴⁵, A. Rimoldi^{73a,73b}, M. Rimoldi⁴⁸, L. Rinaldi^{23a,23b}, T. T. Rinn²⁹, M. P. Rinnagel¹⁰⁹, G. Ripellino¹⁶¹, I. Riu¹³, P. Rivadeneira⁴⁸, J. C. Rivera Vergara¹⁶⁵, F. Rizatdinova¹²¹, E. Rizvi⁹⁴, C. Rizzi⁵⁶, B. A. Roberts¹⁶⁷, B. R. Roberts^{17a}, S. H. Robertson^{104,y}, M. Robin⁴⁸, D. Robinson³², C. M. Robles Gajardo^{137f}, M. Robles Manzano¹⁰⁰, A. Robson⁵⁹, A. Rocchi^{76a,76b}, C. Roda^{74a,74b}, S. Rodriguez Bosca^{63a}, Y. Rodriguez Garcia^{22a}, A. Rodriguez Rodriguez⁵⁴, A. M. Rodríguez Vera^{156b}, S. Roe³⁶, J. T. Roemer¹⁶⁰, A. R. Roepe-Gier¹³⁶, J. Roggel¹⁷¹, O. Røhne¹²⁵, R. A. Rojas¹⁰³, C. P. A. Roland⁶⁸, J. Roloff²⁹, A. Romaniouk³⁷, E. Romano^{73a,73b}, M. Romano^{23b}, A. C. Romero Hernandez¹⁶², N. Rompotis⁹², L. Roos¹²⁷, S. Rosati^{75a}, B. J. Rosser³⁹, E. Rossi⁴, E. Rossi^{72a,72b}, L. P. Rossi^{57b}, L. Rossini⁴⁸, R. Rosten¹¹⁹, M. Rotaru^{27b}, B. Rottler⁵⁴, C. Rougier^{102,ac}, D. Rousseau⁶⁶, D. Rousso³², A. Roy¹⁶², S. Roy-Garand¹⁵⁵, A. Rozanov¹⁰², Y. Rozen¹⁵⁰, X. Ruan^{33g}, A. Rubio Jimenez¹⁶³, A. J. Ruby⁹², V. H. Ruelas Rivera¹⁸, T. A. Ruggeri¹, A. Ruiz-Martinez¹⁶³, A. Rummler³⁶, Z. Rurikova⁵⁴, N. A. Rusakovich³⁸, H. L. Russell¹⁶⁵, J. P. Rutherford⁷, K. Rybacki⁹¹, M. Rybar¹³³, E. B. Rye¹²⁵, A. Ryzhov³⁷, J. A. Sabater Iglesias⁵⁶, P. Sabatini¹⁶³, L. Sabetta^{75a,75b}, H. F.-W. Sadrozinski¹³⁶, F. Safai Tehrani^{75a}, B. Safarzadeh Samani¹⁴⁶, M. Safdari¹⁴³, S. Saha¹⁰⁴, M. Sahinsky¹¹⁰, M. Saimpert¹³⁵, M. Saito¹⁵³, T. Saito¹⁵³, D. Salamani³⁶, A. Salmikov¹⁴³, J. Salt¹⁶³, A. Salvador Salas¹³, D. Salvatore^{43a,43b}, F. Salvatore¹⁴⁶, A. Salzburger³⁶, D. Sammel⁵⁴, D. Sampsonidis^{152,f}, D. Sampsonidou^{62c,123}, J. Sánchez¹⁶³, A. Sanchez Pineda⁴, V. Sanchez Sebastian¹⁶³, H. Sandaker¹²⁵, C. O. Sander⁴⁸, J. A. Sandesara¹⁰³, M. Sandhoff¹⁷¹, C. Sandoval^{22b}, D. P. C. Sankey¹³⁴, T. Sano⁸⁷, A. Sansoni⁵³, L. Santi^{75a,75b}, C. Santoni⁴⁰, H. Santos^{130a,130b}, S. N. Santpur^{17a}, A. Santra¹⁶⁹, K. A. Saoucha¹³⁹, J. G. Saraiva^{130a,130d}, J. Sardain⁷, O. Sasaki⁸³, K. Sato¹⁵⁷, C. Sauer^{63b}, F. Sauerburger⁵⁴, E. Sauvan⁴, P. Savard^{155,ai}, R. Sawada¹⁵³, C. Sawyer¹³⁴, L. Sawyer⁹⁷, I. Sayago Galvan¹⁶³, C. Sbarra^{23b}, A. Sbrizzi^{23a,23b}, T. Scanlon⁹⁶, J. Schaarschmidt¹³⁸, P. Schacht¹¹⁰, D. Schaefer³⁹, U. Schäfer¹⁰⁰, A. C. Schaffer^{44,66}, D. Schaile¹⁰⁹, R. D. Schamberger¹⁴⁵, E. Schanet¹⁰⁹, C. Scharf¹⁸, M. M. Schefer¹⁹, V. A. Schegelsky³⁷, D. Scheirich¹³³, F. Schenck¹⁸, M. Schernau¹⁶⁰, C. Scheulen⁵⁵, C. Schiavi^{57a,57b}, E. J. Schioppa^{70a,70b}, M. Schioppa^{43a,43b}, B. Schlag^{143,q}, K. E. Schleicher⁵⁴, S. Schlenker³⁶, J. Schmeing¹⁷¹, M. A. Schmidt¹⁷¹, K. Schmieden¹⁰⁰, C. Schmitt¹⁰⁰, S. Schmitt⁴⁸, L. Schoeffel¹³⁵, A. Schoening^{63b}, P. G. Scholer⁵⁴, E. Schopf¹²⁶, M. Schott¹⁰⁰, J. Schovancova³⁶, S. Schramm⁵⁶, F. Schroeder¹⁷¹, H.-C. Schultz-Coulon^{63a}, M. Schumacher⁵⁴, B. A. Schumm¹³⁶, Ph. Schune¹³⁵, H. R. Schwartz¹³⁶, A. Schwartzman¹⁴³, T. A. Schwarz¹⁰⁶, Ph. Schwemling¹³⁵, R. Schwienhorst¹⁰⁷

A. Sciandra¹³⁶, G. Sciolla²⁶, F. Scuri^{74a}, F. Scutti¹⁰⁵, C. D. Sebastiani⁹², K. Sedlaczek⁴⁹, P. Seema¹⁸, S. C. Seidel¹¹², A. Seiden¹³⁶, B. D. Seidlitz⁴¹, C. Seitz⁴⁸, J. M. Seixas^{82b}, G. Sekhniaidze^{72a}, S. J. Sekula⁴⁴, L. Selem⁴, N. Semprini-Cesari^{23a,23b}, S. Sen⁵¹, D. Sengupta⁵⁶, V. Senthilkumar¹⁶³, L. Serin⁶⁶, L. Serkin^{69a,69b}, M. Sessa^{77a,77b}, H. Severini¹²⁰, F. Sforza^{57a,57b}, A. Sfyrla⁵⁶, E. Shabalina⁵⁵, R. Shaheen¹⁴⁴, J. D. Shahinian¹²⁸, D. Shaked Renous¹⁶⁹, L. Y. Shan^{14a}, M. Shapiro^{17a}, A. Sharma³⁶, A. S. Sharma¹⁶⁴, P. Sharma⁸⁰, S. Sharma⁴⁸, P. B. Shatalov³⁷, K. Shaw¹⁴⁶, S. M. Shaw¹⁰¹, Q. Shen^{5,62c}, P. Sherwood⁹⁶, L. Shi⁹⁶, C. O. Shimmin¹⁷², Y. Shimogama¹⁶⁸, J. D. Shinner⁹⁵, I. P. J. Shipsey¹²⁶, S. Shirabe⁶⁰, M. Shiyakova³⁸, J. Shlomi¹⁶⁹, M. J. Shochet³⁹, J. Shojaii¹⁰⁵, D. R. Shope¹²⁵, S. Shrestha^{119,al}, E. M. Shrif^{33g}, M. J. Shroff¹⁶⁵, P. Sicho¹³¹, A. M. Sickles¹⁶², E. Sideras Haddad^{33g}, A. Sidoti^{23b}, F. Siegert⁵⁰, Dj. Sijacki¹⁵, R. Sikora^{85a}, F. Sili⁹⁰, J. M. Silva²⁰, M. V. Silva Oliveira³⁶, S. B. Silverstein^{47a}, S. Simion⁶⁶, R. Simoniello³⁶, E. L. Simpson⁵⁹, H. Simpson¹⁴⁶, L. R. Simpson¹⁰⁶, N. D. Simpson⁹⁸, S. Simsek^{21d}, S. Sindhu⁵⁵, P. Sinervo¹⁵⁵, S. Singh¹⁴², S. Singh¹⁵⁵, S. Sinha⁴⁸, S. Sinha^{33g}, M. Sioli^{23a,23b}, I. Siral³⁶, S. Yu. Sivoklov^{37,*}, J. Sjölín^{47a,47b}, A. Skaf⁵⁵, E. Skorda⁹⁸, P. Skubic¹²⁰, M. Slawinska⁸⁶, V. Smakhtin¹⁶⁹, B. H. Smart¹³⁴, J. Smiesko³⁶, S. Yu. Smirnov³⁷, Y. Smirnov³⁷, L. N. Smirnova^{37,a}, O. Smirnova⁹⁸, A. C. Smith⁴¹, E. A. Smith³⁹, H. A. Smith¹²⁶, J. L. Smith⁹², R. Smith¹⁴³, M. Smizanska⁹¹, K. Smolek¹³², A. A. Snesarev³⁷, H. L. Snoek¹¹⁴, S. Snyder²⁹, R. Sobie^{165,y}, A. Soffer¹⁵¹, C. A. Solans Sanchez³⁶, E. Yu. Soldatov³⁷, U. Soldevila¹⁶³, A. A. Solodkov³⁷, S. Solomon⁵⁴, A. Soloshenko³⁸, K. Solovieva⁵⁴, O. V. Solovyanov⁴⁰, V. Solovyev³⁷, P. Sommer³⁶, A. Sonay¹³, W. Y. Song^{156b}, J. M. Sonneveld¹¹⁴, A. Sopczak¹³², A. L. Sopio⁹⁶, F. Sopkova^{28b}, V. Sothilingam^{63a}, S. Sottocornola⁶⁸, R. Soualah^{116b}, Z. Soumami^{35c}, D. South⁴⁸, S. Spagnolo^{70a,70b}, M. Spalla¹¹⁰, D. Sperlich⁵⁴, G. Spigo³⁶, M. Spina¹⁴⁶, S. Spinali⁹¹, D. P. Spiteri⁵⁹, M. Spousta¹³³, E. J. Staats³⁴, A. Stabile^{71a,71b}, R. Stamen^{63a}, M. Stamenkovic¹¹⁴, A. Stampekis²⁰, M. Standke²⁴, E. Stanecka⁸⁶, M. V. Stange⁵⁰, B. Stanislaus^{17a}, M. M. Stanitzki⁴⁸, M. Stankaityte¹²⁶, B. Stapf⁴⁸, E. A. Starchenko³⁷, G. H. Stark¹³⁶, J. Stark^{102,ac}, D. M. Starcko^{156b}, P. Staroba¹³¹, P. Starovoitov^{63a}, S. Stärz¹⁰⁴, R. Staszewski⁸⁶, G. Stavropoulos⁴⁶, J. Steentoft¹⁶¹, P. Steinberg²⁹, B. Stelzer^{142,156a}, H. J. Stelzer¹²⁹, O. Stelzer-Chilton^{156a}, H. Stenzel⁵⁸, T. J. Stevenson¹⁴⁶, G. A. Stewart³⁶, J. R. Stewart¹²¹, M. C. Stockton³⁶, G. Stoicea^{27b}, M. Stolarski^{130a}, S. Stonjek¹¹⁰, A. Straessner⁵⁰, J. Strandberg¹⁴⁴, S. Strandberg^{47a,47b}, M. Strauss¹²⁰, T. Strebler¹⁰², P. Striznec^{28b}, R. Ströhmer¹⁶⁶, D. M. Strom¹²³, L. R. Strom⁴⁸, R. Stroynowski⁴⁴, A. Strubig^{47a,47b}, S. A. Stucci²⁹, B. Stugu¹⁶, J. Stupak¹²⁰, N. A. Styles⁴⁸, D. Su¹⁴³, S. Su^{62a}, W. Su^{62c,62d,138}, X. Su^{62a,66}, K. Sugizaki¹⁵³, V. V. Sulín³⁷, M. J. Sullivan⁹², D. M. S. Sultan^{78a,78b}, L. Sultanaliev³⁷, S. Sultansoy^{3b}, T. Sumida⁸⁷, S. Sun¹⁰⁶, S. Sun¹⁷⁰, O. Sunneborn Gudnadottir¹⁶¹, M. R. Sutton¹⁴⁶, M. Svatos¹³¹, M. Swiatlowski^{156a}, T. Swirski¹⁶⁶, I. Sykora^{28a}, M. Sykora¹³³, T. Sykora¹³³, D. Ta¹⁰⁰, K. Tackmann^{48,w}, A. Taffard¹⁶⁰, R. Tafirout^{156a}, J. S. Tafoya Vargas⁶⁶, R. H. M. Taibah¹²⁷, R. Takashima⁸⁸, E. P. Takeva⁵², Y. Takubo⁸³, M. Talby¹⁰², A. A. Talyshev³⁷, K. C. Tam^{64b}, N. M. Tamir¹⁵¹, A. Tanaka¹⁵³, J. Tanaka¹⁵³, R. Tanaka⁶⁶, M. Tanasini^{57a,57b}, J. Tang^{62c}, Z. Tao¹⁶⁴, S. Tapia Araya^{137f}, S. Tapprogge¹⁰⁰, A. Tarek Abouelfadl Mohamed¹⁰⁷, S. Tarem¹⁵⁰, K. Tariq^{62b}, G. Tarna^{27b,102}, G. F. Tartarelli^{71a}, P. Tas¹³³, M. Tasevsky¹³¹, E. Tassi^{43a,43b}, A. C. Tate¹⁶², G. Tateno¹⁵³, Y. Tayalati^{35e,x}, G. N. Taylor¹⁰⁵, W. Taylor^{156b}, H. Teagle⁹², A. S. Tee¹⁷⁰, R. Teixeira De Lima¹⁴³, P. Teixeira-Dias⁹⁵, J. J. Teoh¹⁵⁵, K. Terashi¹⁵³, J. Terron⁹⁹, S. Terzo¹³, M. Testa⁵³, R. J. Teuscher^{155,y}, A. Thaler⁷⁹, O. Theiner⁵⁶, N. Themistokleous⁵², T. Theveneaux-Pelzer¹⁰², O. Thielmann¹⁷¹, D. W. Thomas⁹⁵, J. P. Thomas²⁰, E. A. Thompson^{17a}, P. D. Thompson²⁰, E. Thomson¹²⁸, Y. Tian⁵⁵, V. Tikhomirov^{37,a}, Yu. A. Tikhonov³⁷, S. Timoshenko³⁷, E. X. L. Ting¹, P. Tipton¹⁷², S. H. Tlou^{33g}, A. Tnourji⁴⁰, K. Todome^{23a,23b}, S. Todorova-Nova¹³³, S. Todt⁵⁰, M. Togawa⁸³, J. Tojo⁸⁹, S. Tokár^{28a}, K. Tokushuku⁸³, O. Toldaiev⁶⁸, R. Tombs³², M. Tomoto^{83,111}, L. Tompkins^{143,q}, K. W. Topolnicki^{85b}, E. Torrence¹²³, H. Torres^{102,ac}, E. Torró Pastor¹⁶³, M. Toscani³⁰, C. Tosciri³⁹, M. Tost¹¹, D. R. Tovey¹³⁹, A. Traet¹⁶, I. S. Trandafir^{27b}, T. Trefzger¹⁶⁶, A. Tricoli²⁹, I. M. Trigger^{156a}, S. Trincaz-Duvoid¹²⁷, D. A. Trischuk²⁶, B. Trocme⁶⁰, C. Troncon^{71a}, L. Truong^{33c}, M. Trzebinski⁸⁶, A. Trzupek⁸⁶, F. Tsai¹⁴⁵, M. Tsai¹⁰⁶, A. Tsiamis^{152,f}, P. V. Tsiarehka³⁷, S. Tsigaridas^{156a}, A. Tsigotis^{152,u}, V. Tsiskaridze¹⁴⁵, E. G. Tskhadadze^{149a}, M. Tsopoulou^{152,f}, Y. Tsujikawa⁸⁷, I. I. Tsukerman³⁷, V. Tsulaia^{17a}, S. Tsuno⁸³, O. Tsur¹⁵⁰, D. Tsybychev¹⁴⁵, Y. Tu^{64b}, A. Tudorache^{27b}, V. Tudorache^{27b}, A. N. Tuna³⁶, S. Turchikhin³⁸, I. Turk Cakir^{3a}, R. Turra^{71a}, T. Turtuvshin^{38,z}, P. M. Tuts⁴¹, S. Tzamarias^{152,f}, P. Tzani¹⁰, E. Tzovara¹⁰⁰, K. Uchida¹⁵³, F. Ukegawa¹⁵⁷, P. A. Ulloa Poblete^{137c}, E. N. Umaka²⁹, G. Unal³⁶, M. Unal¹¹, A. Undrus²⁹, G. Unel¹⁶⁰, J. Urban^{28b}, P. Urquijo¹⁰⁵, G. Usal⁸, R. Ushioda¹⁵⁴

M. Usman¹⁰⁸ , Z. Uysal^{21b} , L. Vacavant¹⁰² , V. Vacek¹³² , B. Vachon¹⁰⁴ , K. O. H. Vadla¹²⁵ , T. Vafeiadis³⁶ , A. Vaitkus⁹⁶ , C. Valderanis¹⁰⁹ , E. Valdes Santurio^{47a,47b} , M. Valente^{156a} , S. Valentini^{23a,23b} , A. Valero¹⁶³ , E. Valiente Moreno¹⁶³ , A. Vallier^{102.ac} , J. A. Valls Ferrer¹⁶³ , D. R. Van Arnhem¹¹⁴ , T. R. Van Daalen¹³⁸ , P. Van Gemmeren⁶ , M. Van Rijnbach^{36,125} , S. Van Stroud⁹⁶ , I. Van Vulpen¹¹⁴ , M. Vanadia^{76a,76b} , W. Vandelli³⁶ , M. Vandenbroucke¹³⁵ , E. R. Vandewall¹²¹ , D. Vannicola¹⁵¹ , L. Vannoli^{57a,57b} , R. Vari^{75a} , E. W. Varnes⁷ , C. Varni^{17a} , T. Varol¹⁴⁸ , D. Varouchas⁶⁶ , L. Varriale¹⁶³ , K. E. Varvell¹⁴⁷ , M. E. Vasile^{27b} , L. Vaslin⁴⁰ , G. A. Vasquez¹⁶⁵ , F. Vazeille⁴⁰ , T. Vazquez Schroeder³⁶ , J. Veatch³¹ , V. Vecchio¹⁰¹ , M. J. Veen¹⁰³ , I. Veliscek¹²⁶ , L. M. Veloce¹⁵⁵ , F. Veloso^{130a,130c} , S. Veneziano^{75a} , A. Ventura^{70a,70b} , A. Verbytskyi¹¹⁰ , M. Verducci^{74a,74b} , C. Vergis²⁴ , M. Verissimo De Araujo^{82b}

, W. Verkerke¹¹⁴ , J. C. Vermeulen¹¹⁴ , C. Vernieri¹⁴³ , P. J. Verschuuren⁹⁵ , M. Vessella¹⁰³ , M. C. Vetterli^{142.ai} , A. Vgenopoulos^{152.f} , N. Viaux Maira^{137f} , T. Vickey¹³⁹ , O. E. Vickey Boeriu¹³⁹ , G. H. A. Viehhauser¹²⁶ , L. Vigani^{63b} , M. Villa^{23a,23b} , M. Villaplana Perez¹⁶³ , E. M. Villhauer⁵² , E. Vilucchi⁵³ , M. G. Vinciter³⁴ , G. S. Virdee²⁰ , A. Vishwakarma⁵² , C. Vittori³⁶ , I. Vivarelli¹⁴⁶ , V. Vladimirov¹⁶⁷ , E. Voevodina¹¹⁰ , F. Vogel¹⁰⁹ , P. Vokac¹³² , J. Von Ahnen⁴⁸ , E. Von Toerne²⁴ , B. Vormwald³⁶ , V. Vorobel¹³³ , K. Vorobev³⁷ , M. Vos¹⁶³ , K. Voss¹⁴¹ , J. H. Vossebeld⁹² , M. Vozak¹¹⁴ , L. Vozdecky⁹⁴ , N. Vranjes¹⁵ , M. Vranjes Milosavljevic¹⁵ , M. Vreeswijk¹¹⁴ , R. Vuillermet³⁶ , O. Vujanovic¹⁰⁰ , I. Vukotic³⁹ , S. Wada¹⁵⁷ , C. Wagner¹⁰³ , J. M. Wagner^{17a} , W. Wagner¹⁷¹ , S. Wahdan¹⁷¹ , H. Wahlberg⁹⁰ , R. Wakasa¹⁵⁷ , M. Wakida¹¹¹ , J. Walder¹³⁴ , R. Walker¹⁰⁹ , W. Walkowiak¹⁴¹

, A. Z. Wang¹⁷⁰ , C. Wang¹⁰⁰ , C. Wang^{62c} , H. Wang^{17a} , J. Wang^{64a} , R.-J. Wang¹⁰⁰ , R. Wang⁶¹ , R. Wang⁶ , S. M. Wang¹⁴⁸ , S. Wang^{62b} , T. Wang^{62a} , W. T. Wang⁸⁰ , X. Wang^{14c} , X. Wang¹⁶² , X. Wang^{62c} , Y. Wang^{62d} , Y. Wang^{14c} , Z. Wang¹⁰⁶ , Z. Wang^{51,62c,62d} , Z. Wang¹⁰⁶ , A. Warburton¹⁰⁴ , R. J. Ward²⁰ , N. Warrack⁵⁹ , A. T. Watson²⁰ , H. Watson⁵⁹ , M. F. Watson²⁰ , G. Watts¹³⁸ , B. M. Waugh⁹⁶ , C. Weber²⁹ , H. A. Weber¹⁸ , M. S. Weber¹⁹ , S. M. Weber^{63a} , C. Wei^{62a} , Y. Wei¹²⁶ , A. R. Weidberg¹²⁶ , E. J. Weik¹¹⁷ , J. Weingarten⁴⁹ , M. Weirich¹⁰⁰ , C. Weiser⁵⁴ , C. J. Wells⁴⁸ , T. Wenaus²⁹ , B. Wendland⁴⁹ , T. Wengler³⁶ , N. S. Wenke¹¹⁰ , N. Wermes²⁴ , M. Wessels^{63a} , K. Whalen¹²³ , A. M. Wharton⁹¹ , A. S. White⁶¹ , A. White⁸ , M. J. White¹ , D. Whiteson¹⁶⁰ , L. Wickremasinghe¹²⁴

, W. Wiedenmann¹⁷⁰ , C. Wiel⁵⁰ , M. Wielers¹³⁴ , C. Wiglesworth⁴² , L. A. M. Wiik-Fuchs⁵⁴ , D. J. Wilbern¹²⁰ , H. G. Wilkens³⁶ , D. M. Williams⁴¹ , H. H. Williams¹²⁸ , S. Williams³² , S. Willocq¹⁰³ , B. J. Wilson¹⁰¹ , P. J. Windischhofer³⁹ , F. Winklmeier¹²³ , B. T. Winter⁵⁴ , J. K. Winter¹⁰¹ , M. Wittgen¹⁴³ , M. Wobisch⁹⁷ , R. Wölker¹²⁶ , J. Wollrath¹⁶⁰ , M. W. Wolter⁸⁶ , H. Wolters^{130a,130c} , V. W. S. Wong¹⁶⁴ , A. F. Wongel⁴⁸ , S. D. Worm⁴⁸ , B. K. Wosiek⁸⁶ , K. W. Woźniak⁸⁶ , K. Wraight⁵⁹ , J. Wu^{14a,14d} , M. Wu^{64a} , M. Wu¹¹³ , S. L. Wu¹⁷⁰ , X. Wu⁵⁶ , Y. Wu^{62a} , Z. Wu^{62a,135} , J. Wuerzinger¹¹⁰ , T. R. Wyatt¹⁰¹ , B. M. Wynne⁵² , S. Xella⁴² , L. Xia^{14c} , M. Xia^{14b} , J. Xiang^{64c} , X. Xiao¹⁰⁶ , M. Xie^{62a} , X. Xie^{62a} , S. Xin^{14a,14d} , J. Xiong^{17a} , I. Xiotidis¹⁴⁶ , D. Xu^{14a} , H. Xu^{62a} , H. Xu^{62a} , L. Xu^{62a} , R. Xu¹²⁸

, T. Xu¹⁰⁶ , Y. Xu^{14b} , Z. Xu^{62b} , Z. Xu^{14a} , B. Yabsley¹⁴⁷ , S. Yacob^{33a} , N. Yamaguchi⁸⁹ , Y. Yamaguchi¹⁵⁴ , H. Yamauchi¹⁵⁷ , T. Yamazaki^{17a} , Y. Yamazaki⁸⁴ , J. Yan^{62c} , S. Yan¹²⁶ , Z. Yan²⁵ , H. J. Yang^{62c,62d} , H. T. Yang^{62a} , S. Yang^{62a} , T. Yang^{64c} , X. Yang^{62a} , X. Yang^{14a} , Y. Yang⁴⁴ , Y. Yang^{62a} , Z. Yang^{62a,106} , W.-M. Yao^{17a} , Y. C. Yap⁴⁸ , H. Ye^{14c} , H. Ye⁵⁵ , J. Ye⁴⁴ , S. Ye²⁹ , X. Ye^{62a} , Y. Yeh⁹⁶ , I. Yeletskikh³⁸ , B. K. Yeo^{17a} , M. R. Yexley⁹¹ , P. Yin⁴¹ , K. Yorita¹⁶⁸ , S. Younas^{27b} , C. J. S. Young⁵⁴ , C. Young¹⁴³ , Y. Yu^{62a} , M. Yuan¹⁰⁶ , R. Yuan^{62b.1} , L. Yue⁹⁶ , M. Zaazoua^{35e} , B. Zabinski⁸⁶ , E. Zaid⁵² , T. Zakareishvili^{149b} , N. Zakharchuk³⁴ , S. Zambito⁵⁶ , J. A. Zamora Saa^{137b,137d} , J. Zang¹⁵³ , D. Zanzi⁵⁴ , O. Zaplatilek¹³²

, C. Zeitnitz¹⁷¹ , H. Zeng^{14a} , J. C. Zeng¹⁶² , D. T. Zenger Jr²⁶ , O. Zenin³⁷ , T. Ženiš^{28a} , S. Zenz⁹⁴ , S. Zerradi^{35a} , D. Zerwas⁶⁶ , M. Zhai^{14a,14d} , B. Zhang^{14c} , D. F. Zhang¹³⁹ , J. Zhang^{62b} , J. Zhang⁶ , K. Zhang^{14a,14d} , L. Zhang^{14c} , P. Zhang^{14a,14d} , R. Zhang¹⁷⁰ , S. Zhang¹⁰⁶ , T. Zhang¹⁵³ , X. Zhang^{62c} , X. Zhang^{62b} , Y. Zhang^{5,62c} , Z. Zhang^{17a} , Z. Zhang⁶⁶

- ⁵ APC, Université Paris Cité, CNRS/IN2P3, Paris, France
- ⁶ High Energy Physics Division, Argonne National Laboratory, Argonne, IL, USA
- ⁷ Department of Physics, University of Arizona, Tucson, AZ, USA
- ⁸ Department of Physics, University of Texas at Arlington, Arlington, TX, USA
- ⁹ Physics Department, National and Kapodistrian University of Athens, Athens, Greece
- ¹⁰ Physics Department, National Technical University of Athens, Zografou, Greece
- ¹¹ Department of Physics, University of Texas at Austin, Austin, TX, USA
- ¹² Institute of Physics, Azerbaijan Academy of Sciences, Baku, Azerbaijan
- ¹³ Institut de Física d'Altes Energies (IFAE), Barcelona Institute of Science and Technology, Barcelona, Spain
- ¹⁴ ^(a)Institute of High Energy Physics, Chinese Academy of Sciences, Beijing, China; ^(b)Physics Department, Tsinghua University, Beijing, China; ^(c)Department of Physics, Nanjing University, Nanjing, China; ^(d)University of Chinese Academy of Science (UCAS), Beijing, China
- ¹⁵ Institute of Physics, University of Belgrade, Belgrade, Serbia
- ¹⁶ Department for Physics and Technology, University of Bergen, Bergen, Norway
- ¹⁷ ^(a)Physics Division, Lawrence Berkeley National Laboratory, Berkeley, CA, USA; ^(b)University of California, Berkeley, CA, USA
- ¹⁸ Institut für Physik, Humboldt Universität zu Berlin, Berlin, Germany
- ¹⁹ Albert Einstein Center for Fundamental Physics and Laboratory for High Energy Physics, University of Bern, Bern, Switzerland
- ²⁰ School of Physics and Astronomy, University of Birmingham, Birmingham, UK
- ²¹ ^(a)Department of Physics, Bogazici University, Istanbul, Türkiye; ^(b)Department of Physics Engineering, Gaziantep University, Gaziantep, Türkiye; ^(c)Department of Physics, Istanbul University, Istanbul, Türkiye; ^(d)Istinye University, Sariyer, Istanbul, Türkiye
- ²² ^(a)Facultad de Ciencias y Centro de Investigaciones, Universidad Antonio Nariño, Bogotá, Colombia; ^(b)Departamento de Física, Universidad Nacional de Colombia, Bogotá, Colombia
- ²³ ^(a)Dipartimento di Fisica e Astronomia A. Righi, Università di Bologna, Bologna, Italy; ^(b)INFN Sezione di Bologna, Bologna, Italy
- ²⁴ Physikalisches Institut, Universität Bonn, Bonn, Germany
- ²⁵ Department of Physics, Boston University, Boston, MA, USA
- ²⁶ Department of Physics, Brandeis University, Waltham, MA, USA
- ²⁷ ^(a)Transilvania University of Brasov, Brasov, Romania; ^(b)Horia Hulubei National Institute of Physics and Nuclear Engineering, Bucharest, Romania; ^(c)Department of Physics, Alexandru Ioan Cuza University of Iasi, Iasi, Romania; ^(d)National Institute for Research and Development of Isotopic and Molecular Technologies, Physics Department, Cluj-Napoca, Romania; ^(e)University Politehnica Bucharest, Bucharest, Romania; ^(f)West University in Timisoara, Timisoara, Romania; ^(g)Faculty of Physics, University of Bucharest, Bucharest, Romania
- ²⁸ ^(a)Faculty of Mathematics, Physics and Informatics, Comenius University, Bratislava, Slovak Republic; ^(b)Department of Subnuclear Physics, Institute of Experimental Physics of the Slovak Academy of Sciences, Kosice, Slovak Republic
- ²⁹ Physics Department, Brookhaven National Laboratory, Upton, NY, USA
- ³⁰ Departamento de Física, y CONICET, Facultad de Ciencias Exactas y Naturales, Instituto de Física de Buenos Aires (IFIBA), Universidad de Buenos Aires, Buenos Aires, Argentina
- ³¹ California State University, Los Angeles, CA, USA
- ³² Cavendish Laboratory, University of Cambridge, Cambridge, UK
- ³³ ^(a)Department of Physics, University of Cape Town, Cape Town, South Africa; ^(b)iThemba Labs, Western Cape, South Africa; ^(c)Department of Mechanical Engineering Science, University of Johannesburg, Johannesburg, South Africa; ^(d)National Institute of Physics, University of the Philippines, Diliman, Philippines; ^(e)Department of Physics, University of South Africa, Pretoria, South Africa; ^(f)University of Zululand, KwaDlangezwa, South Africa; ^(g)School of Physics, University of the Witwatersrand, Johannesburg, South Africa
- ³⁴ Department of Physics, Carleton University, Ottawa, ON, Canada
- ³⁵ ^(a)Faculté des Sciences Ain Chock, Réseau Universitaire de Physique des Hautes Energies-Université Hassan II, Casablanca, Morocco; ^(b)Faculté des Sciences, Université Ibn-Tofail, Kenitra, Morocco; ^(c)Faculté des Sciences Semlalia, Université Cadi Ayyad, LPHEA-Marrakech, Morocco; ^(d)LPMR, Faculté des Sciences, Université Mohamed

- Premier, Oujda, Morocco; ^(e)Faculté des sciences, Université Mohammed V, Rabat, Morocco; ^(f)Institute of Applied Physics, Mohammed VI Polytechnic University, Ben Guerir, Morocco
- ³⁶ CERN, Geneva, Switzerland
- ³⁷ Affiliated with an institute covered by a cooperation agreement with CERN, Geneva, Switzerland
- ³⁸ Affiliated with an international laboratory covered by a cooperation agreement with CERN, Geneva, Switzerland
- ³⁹ Enrico Fermi Institute, University of Chicago, Chicago, IL, USA
- ⁴⁰ LPC, Université Clermont Auvergne, CNRS/IN2P3, Clermont-Ferrand, France
- ⁴¹ Nevis Laboratory, Columbia University, Irvington, NY, USA
- ⁴² Niels Bohr Institute, University of Copenhagen, Copenhagen, Denmark
- ⁴³ ^(a)Dipartimento di Fisica, Università della Calabria, Rende, Italy; ^(b)INFN Gruppo Collegato di Cosenza, Laboratori Nazionali di Frascati, Frascati, Italy
- ⁴⁴ Physics Department, Southern Methodist University, Dallas, TX, USA
- ⁴⁵ Physics Department, University of Texas at Dallas, Richardson, TX, USA
- ⁴⁶ National Centre for Scientific Research “Demokritos”, Agia Paraskevi, Greece
- ⁴⁷ ^(a)Department of Physics, Stockholm University, Stockholm, Sweden; ^(b)Oskar Klein Centre, Stockholm, Sweden
- ⁴⁸ Deutsches Elektronen-Synchrotron DESY, Hamburg and Zeuthen, Germany
- ⁴⁹ Fakultät Physik, Technische Universität Dortmund, Dortmund, Germany
- ⁵⁰ Institut für Kern- und Teilchenphysik, Technische Universität Dresden, Dresden, Germany
- ⁵¹ Department of Physics, Duke University, Durham, NC, USA
- ⁵² SUPA-School of Physics and Astronomy, University of Edinburgh, Edinburgh, UK
- ⁵³ INFN e Laboratori Nazionali di Frascati, Frascati, Italy
- ⁵⁴ Physikalisches Institut, Albert-Ludwigs-Universität Freiburg, Freiburg, Germany
- ⁵⁵ II. Physikalisches Institut, Georg-August-Universität Göttingen, Göttingen, Germany
- ⁵⁶ Département de Physique Nucléaire et Corpusculaire, Université de Genève, Geneva, Switzerland
- ⁵⁷ ^(a)Dipartimento di Fisica, Università di Genova, Genoa, Italy; ^(b)INFN Sezione di Genova, Genoa, Italy
- ⁵⁸ II. Physikalisches Institut, Justus-Liebig-Universität Giessen, Giessen, Germany
- ⁵⁹ SUPA-School of Physics and Astronomy, University of Glasgow, Glasgow, UK
- ⁶⁰ LPSC, Université Grenoble Alpes, CNRS/IN2P3, Grenoble INP, Grenoble, France
- ⁶¹ Laboratory for Particle Physics and Cosmology, Harvard University, Cambridge, MA, USA
- ⁶² ^(a)Department of Modern Physics and State Key Laboratory of Particle Detection and Electronics, University of Science and Technology of China, Hefei, China; ^(b)Institute of Frontier and Interdisciplinary Science and Key Laboratory of Particle Physics and Particle Irradiation (MOE), Shandong University, Qingdao, China; ^(c)School of Physics and Astronomy, Shanghai Jiao Tong University, Key Laboratory for Particle Astrophysics and Cosmology (MOE), SKLPPC, Shanghai, China; ^(d)Tsung-Dao Lee Institute, Shanghai, China
- ⁶³ ^(a)Kirchhoff-Institut für Physik, Ruprecht-Karls-Universität Heidelberg, Heidelberg, Germany; ^(b)Physikalisches Institut, Ruprecht-Karls-Universität Heidelberg, Heidelberg, Germany
- ⁶⁴ ^(a)Department of Physics, Chinese University of Hong Kong, Shatin, N.T., Hong Kong, China; ^(b)Department of Physics, University of Hong Kong, Hong Kong, China; ^(c)Department of Physics and Institute for Advanced Study, Hong Kong University of Science and Technology, Clear Water Bay, Kowloon, Hong Kong, China
- ⁶⁵ Department of Physics, National Tsing Hua University, Hsinchu, Taiwan
- ⁶⁶ IJCLab, Université Paris-Saclay, CNRS/IN2P3, 91405 Orsay, France
- ⁶⁷ Centro Nacional de Microelectrónica (IMB-CNM-CSIC), Barcelona, Spain
- ⁶⁸ Department of Physics, Indiana University, Bloomington, IN, USA
- ⁶⁹ ^(a)INFN Gruppo Collegato di Udine, Sezione di Trieste, Udine, Italy; ^(b)ICTP, Trieste, Italy; ^(c)Dipartimento Politecnico di Ingegneria e Architettura, Università di Udine, Udine, Italy
- ⁷⁰ ^(a)INFN Sezione di Lecce, Lecce, Italy; ^(b)Dipartimento di Matematica e Fisica, Università del Salento, Lecce, Italy
- ⁷¹ ^(a)INFN Sezione di Milano, Milan, Italy; ^(b)Dipartimento di Fisica, Università di Milano, Milan, Italy
- ⁷² ^(a)INFN Sezione di Napoli, Naples, Italy; ^(b)Dipartimento di Fisica, Università di Napoli, Naples, Italy
- ⁷³ ^(a)INFN Sezione di Pavia, Pavia, Italy; ^(b)Dipartimento di Fisica, Università di Pavia, Pavia, Italy
- ⁷⁴ ^(a)INFN Sezione di Pisa, Pisa, Italy; ^(b)Dipartimento di Fisica E. Fermi, Università di Pisa, Pisa, Italy
- ⁷⁵ ^(a)INFN Sezione di Roma, Rome, Italy; ^(b)Dipartimento di Fisica, Sapienza Università di Roma, Rome, Italy
- ⁷⁶ ^(a)INFN Sezione di Roma Tor Vergata, Rome, Italy; ^(b)Dipartimento di Fisica, Università di Roma Tor Vergata, Rome, Italy

- 77 (a) INFN Sezione di Roma Tre, Rome, Italy; (b) Dipartimento di Matematica e Fisica, Università Roma Tre, Rome, Italy
- 78 (a) INFN-TIFPA, Trento, Italy; (b) Università degli Studi di Trento, Trento, Italy
- 79 Department of Astro and Particle Physics, Universität Innsbruck, Innsbruck, Austria
- 80 University of Iowa, Iowa City, IA, USA
- 81 Department of Physics and Astronomy, Iowa State University, Ames, IA, USA
- 82 (a) Departamento de Engenharia Elétrica, Universidade Federal de Juiz de Fora (UFJF), Juiz de Fora, Brazil; (b) Universidade Federal do Rio de Janeiro COPPE/EE/IF, Rio de Janeiro, Brazil; (c) Instituto de Física, Universidade de São Paulo, São Paulo, Brazil; (d) Rio de Janeiro State University, Rio de Janeiro, Brazil
- 83 KEK, High Energy Accelerator Research Organization, Tsukuba, Japan
- 84 Graduate School of Science, Kobe University, Kobe, Japan
- 85 (a) Faculty of Physics and Applied Computer Science, AGH University of Science and Technology, Krakow, Poland; (b) Marian Smoluchowski Institute of Physics, Jagiellonian University, Krakow, Poland
- 86 Institute of Nuclear Physics, Polish Academy of Sciences, Krakow, Poland
- 87 Faculty of Science, Kyoto University, Kyoto, Japan
- 88 Kyoto University of Education, Kyoto, Japan
- 89 Research Center for Advanced Particle Physics and Department of Physics, Kyushu University, Fukuoka, Japan
- 90 Instituto de Física La Plata, Universidad Nacional de La Plata and CONICET, La Plata, Argentina
- 91 Physics Department, Lancaster University, Lancaster, UK
- 92 Oliver Lodge Laboratory, University of Liverpool, Liverpool, UK
- 93 Department of Experimental Particle Physics, Jožef Stefan Institute and Department of Physics, University of Ljubljana, Ljubljana, Slovenia
- 94 School of Physics and Astronomy, Queen Mary University of London, London, UK
- 95 Department of Physics, Royal Holloway University of London, Egham, UK
- 96 Department of Physics and Astronomy, University College London, London, UK
- 97 Louisiana Tech University, Ruston, LA, USA
- 98 Fysiska institutionen, Lunds universitet, Lund, Sweden
- 99 Departamento de Física Teórica C-15 and CIAFF, Universidad Autónoma de Madrid, Madrid, Spain
- 100 Institut für Physik, Universität Mainz, Mainz, Germany
- 101 School of Physics and Astronomy, University of Manchester, Manchester, UK
- 102 CPPM, Aix-Marseille Université, CNRS/IN2P3, Marseille, France
- 103 Department of Physics, University of Massachusetts, Amherst, MA, USA
- 104 Department of Physics, McGill University, Montreal, QC, Canada
- 105 School of Physics, University of Melbourne, Victoria, Australia
- 106 Department of Physics, University of Michigan, Ann Arbor, MI, USA
- 107 Department of Physics and Astronomy, Michigan State University, East Lansing, MI, USA
- 108 Group of Particle Physics, University of Montreal, Montreal, QC, Canada
- 109 Fakultät für Physik, Ludwig-Maximilians-Universität München, Munich, Germany
- 110 Max-Planck-Institut für Physik (Werner-Heisenberg-Institut), Munich, Germany
- 111 Graduate School of Science and Kobayashi-Maskawa Institute, Nagoya University, Nagoya, Japan
- 112 Department of Physics and Astronomy, University of New Mexico, Albuquerque, NM, USA
- 113 Institute for Mathematics, Astrophysics and Particle Physics, Radboud University/Nikhef, Nijmegen, The Netherlands
- 114 Nikhef National Institute for Subatomic Physics and University of Amsterdam, Amsterdam, The Netherlands
- 115 Department of Physics, Northern Illinois University, DeKalb, IL, USA
- 116 (a) New York University Abu Dhabi, Abu Dhabi, United Arab Emirates; (b) University of Sharjah, Sharjah, United Arab Emirates
- 117 Department of Physics, New York University, New York, NY, USA
- 118 Ochanomizu University, Otsuka, Bunkyo-ku, Tokyo, Japan
- 119 Ohio State University, Columbus, OH, USA
- 120 Homer L. Dodge Department of Physics and Astronomy, University of Oklahoma, Norman, OK, USA
- 121 Department of Physics, Oklahoma State University, Stillwater, OK, USA
- 122 Joint Laboratory of Optics, Palacký University, Olomouc, Czech Republic
- 123 Institute for Fundamental Science, University of Oregon, Eugene, OR, USA
- 124 Graduate School of Science, Osaka University, Osaka, Japan

- 125 Department of Physics, University of Oslo, Oslo, Norway
- 126 Department of Physics, Oxford University, Oxford, UK
- 127 LPNHE, Sorbonne Université, Université Paris Cité, CNRS/IN2P3, Paris, France
- 128 Department of Physics, University of Pennsylvania, Philadelphia, PA, USA
- 129 Department of Physics and Astronomy, University of Pittsburgh, Pittsburgh, PA, USA
- 130 ^(a)Laboratório de Instrumentação e Física Experimental de Partículas-LIP, Lisbon, Portugal; ^(b)Departamento de Física, Faculdade de Ciências, Universidade de Lisboa, Lisbon, Portugal; ^(c)Departamento de Física, Universidade de Coimbra, Coimbra, Portugal; ^(d)Centro de Física Nuclear da Universidade de Lisboa, Lisbon, Portugal; ^(e)Departamento de Física, Universidade do Minho, Braga, Portugal; ^(f)Departamento de Física Teórica y del Cosmos, Universidad de Granada, Granada, Spain; ^(g)Departamento de Física, Instituto Superior Técnico, Universidade de Lisboa, Lisbon, Portugal
- 131 Institute of Physics of the Czech Academy of Sciences, Prague, Czech Republic
- 132 Czech Technical University in Prague, Prague, Czech Republic
- 133 Faculty of Mathematics and Physics, Charles University, Prague, Czech Republic
- 134 Particle Physics Department, Rutherford Appleton Laboratory, Didcot, UK
- 135 IRFU, CEA, Université Paris-Saclay, Gif-sur-Yvette, France
- 136 Santa Cruz Institute for Particle Physics, University of California Santa Cruz, Santa Cruz, CA, USA
- 137 ^(a)Departamento de Física, Pontificia Universidad Católica de Chile, Santiago, Chile; ^(b)Millennium Institute for Subatomic Physics at High Energy Frontier (SAPHIR), Santiago, Chile; ^(c)Instituto de Investigación Multidisciplinario en Ciencia y Tecnología y Departamento de Física, Universidad de La Serena, La Serena, Chile; ^(d)Department of Physics, Universidad Andres Bello, Santiago, Chile; ^(e)Instituto de Alta Investigación, Universidad de Tarapacá, Arica, Chile; ^(f)Departamento de Física, Universidad Técnica Federico Santa María, Valparaíso, Chile
- 138 Department of Physics, University of Washington, Seattle, WA, USA
- 139 Department of Physics and Astronomy, University of Sheffield, Sheffield, UK
- 140 Department of Physics, Shinshu University, Nagano, Japan
- 141 Department Physik, Universität Siegen, Siegen, Germany
- 142 Department of Physics, Simon Fraser University, Burnaby, BC, Canada
- 143 SLAC National Accelerator Laboratory, Stanford, CA, USA
- 144 Department of Physics, Royal Institute of Technology, Stockholm, Sweden
- 145 Departments of Physics and Astronomy, Stony Brook University, Stony Brook, NY, USA
- 146 Department of Physics and Astronomy, University of Sussex, Brighton, UK
- 147 School of Physics, University of Sydney, Sydney, Australia
- 148 Institute of Physics, Academia Sinica, Taipei, Taiwan
- 149 ^(a)E. Andronikashvili Institute of Physics, Iv. Javakhishvili Tbilisi State University, Tbilisi, Georgia; ^(b)High Energy Physics Institute, Tbilisi State University, Tbilisi, Georgia; ^(c)University of Georgia, Tbilisi, Georgia
- 150 Department of Physics, Technion, Israel Institute of Technology, Haifa, Israel
- 151 Raymond and Beverly Sackler School of Physics and Astronomy, Tel Aviv University, Tel Aviv, Israel
- 152 Department of Physics, Aristotle University of Thessaloniki, Thessaloniki, Greece
- 153 International Center for Elementary Particle Physics and Department of Physics, University of Tokyo, Tokyo, Japan
- 154 Department of Physics, Tokyo Institute of Technology, Tokyo, Japan
- 155 Department of Physics, University of Toronto, Toronto, ON, Canada
- 156 ^(a)TRIUMF, Vancouver, BC, Canada; ^(b)Department of Physics and Astronomy, York University, Toronto, ON, Canada
- 157 Division of Physics and Tomonaga Center for the History of the Universe, Faculty of Pure and Applied Sciences, University of Tsukuba, Tsukuba, Japan
- 158 Department of Physics and Astronomy, Tufts University, Medford, MA, USA
- 159 United Arab Emirates University, Al Ain, United Arab Emirates
- 160 Department of Physics and Astronomy, University of California Irvine, Irvine, CA, USA
- 161 Department of Physics and Astronomy, University of Uppsala, Uppsala, Sweden
- 162 Department of Physics, University of Illinois, Urbana, IL, USA
- 163 Instituto de Física Corpuscular (IFIC), Centro Mixto Universidad de Valencia - CSIC, Valencia, Spain
- 164 Department of Physics, University of British Columbia, Vancouver, BC, Canada
- 165 Department of Physics and Astronomy, University of Victoria, Victoria, BC, Canada
- 166 Fakultät für Physik und Astronomie, Julius-Maximilians-Universität Würzburg, Würzburg, Germany
- 167 Department of Physics, University of Warwick, Coventry, UK

- ¹⁶⁸ Waseda University, Tokyo, Japan
- ¹⁶⁹ Department of Particle Physics and Astrophysics, Weizmann Institute of Science, Rehovot, Israel
- ¹⁷⁰ Physics Department, Brookhaven National Laboratory, Upton NY, United States of America
- ¹⁷¹ Fakultät für Mathematik und Naturwissenschaften, Fachgruppe Physik, Bergische Universität Wuppertal, Wuppertal, Germany
- ¹⁷² Department of Physics, Yale University, New Haven, CT, USA
- ^a Also Affiliated with an institute covered by a cooperation agreement with CERN, Geneva, Switzerland
- ^b Also at An-Najah National University, Nablus, Palestine
- ^c Also at Borough of Manhattan Community College, City University of New York, New York, NY, USA
- ^d Also at Bruno Kessler Foundation, Trento, Italy
- ^e Also at Center for High Energy Physics, Peking University, Beijing, China
- ^f Also at Center for Interdisciplinary Research and Innovation (CIRI-AUTH), Thessaloniki, Greece
- ^g Also at Centro Studi e Ricerche Enrico Fermi, Rome, Italy
- ^h Also at CERN, Geneva, Switzerland
- ⁱ Also at Département de Physique Nucléaire et Corpusculaire, Université de Genève, Geneva, Switzerland
- ^j Also at Departament de Física de la Universitat Autònoma de Barcelona, Barcelona, Spain
- ^k Also at Department of Financial and Management Engineering, University of the Aegean, Chios, Greece
- ^l Also at Department of Physics and Astronomy, Michigan State University, East Lansing, MI, USA
- ^m Also at Department of Physics, Ben Gurion University of the Negev, Beer Sheva, Israel
- ⁿ Also at Department of Physics, California State University, East Bay, USA
- ^o Also at Department of Physics, California State University, Sacramento, USA
- ^p Also at Department of Physics, King's College London, London, UK
- ^q Also at Department of Physics, Stanford University, Stanford, CA, USA
- ^r Also at Department of Physics, University of Fribourg, Fribourg, Switzerland
- ^s Also at Department of Physics, University of Thessaly, Thessaly, Greece
- ^t Also at Department of Physics, Westmont College, Santa Barbara, USA
- ^u Also at Hellenic Open University, Patras, Greece
- ^v Also at Institutio Catalana de Recerca i Estudis Avancats, ICREA, Barcelona, Spain
- ^w Also at Institut für Experimentalphysik, Universität Hamburg, Hamburg, Germany
- ^x Also at Institute of Applied Physics, Mohammed VI Polytechnic University, Ben Guerir, Morocco
- ^y Also at Institute of Particle Physics (IPP), Toronto, Canada
- ^z Also at Institute of Physics and Technology, Ulaanbaatar, Mongolia
- ^{aa} Also at Institute of Physics, Azerbaijan Academy of Sciences, Baku, Azerbaijan
- ^{ab} Also at Institute of Theoretical Physics, Ilia State University, Tbilisi, Georgia
- ^{ac} Also at L2IT, Université de Toulouse, CNRS/IN2P3, UPS, Toulouse, France
- ^{ad} Also at Lawrence Livermore National Laboratory, Livermore, USA
- ^{ae} Also at National Institute of Physics, University of the Philippines, Diliman, Philippines
- ^{af} Also at Physikalisches Institut, Albert-Ludwigs-Universität Freiburg, Freiburg, Germany
- ^{ag} Also at Technical University of Munich, Munich, Germany
- ^{ah} Also at The Collaborative Innovation Center of Quantum Matter (CICQM), Beijing, China
- ^{ai} Also at TRIUMF, Vancouver, BC, Canada
- ^{aj} Also at Università di Napoli Parthenope, Naples, Italy
- ^{ak} Also at Department of Physics, University of Colorado Boulder, Boulder, CO, USA
- ^{al} Also at Washington College, Chestertown, MD, USA
- ^{am} Also at Physics Department, Yeditepe University, Istanbul, Türkiye
- ^{an} Also at Institute for Nuclear Research and Nuclear Energy (INRNE) of the Bulgarian Academy of Sciences, Sofia, Bulgaria
- * Deceased